

# *Declaration*

I, **Mikhail Vasiliev**, declare that the thesis titled,

*“Low Coherence Fibre Interferometry With a Multi-Wavelength Light Source”*

is my own work and has not been submitted previously, in whole or in part, in respect of any other academic award.

Mikhail Vasiliev,

dated the 28th day of March, 2001.

# *Acknowledgements*

I would firstly like to thank my supervisors, Professor David Booth, Dr Andrew Stevenson and Associate Professor Stephen Collins for giving me the opportunity to undertake this research and for their constant guidance and encouraging discussions throughout the course of this work.

I am grateful to the School of Communications and Informatics, Victoria University, for providing me with a research scholarship during my studies.

I am very grateful to all members of academic, technical and administrative staff of the School of Communications and Informatics for their helpful assistance and friendly support. I would also like to thank all of my fellow post-graduate students for their friendship and assistance.

Finally, I would like to thank my parents for their constant inspiration and support during my studies in Australia away from my family.

# *Abstract*

This thesis describes the results of study of the multi-wavelength low coherence fibre interferometry. The development and performance of the all-fibre interferometric measurement systems utilising multi-wavelength combination sources are described.

Principal aspects of the low-coherence sensor interrogation scheme are analysed in order to substantiate the development of fibre sensors with a particular configuration that employs a reflection-type Fabry-Pérot as sensing interferometer and a reflection-type Michelson as receiver interferometer. The background on the choice of an optimised signal processing scheme and data processing algorithms is given. Predictions were made during this work regarding the achievable measurement resolution and speed, together with the analysis of the limitations of the chosen measurement scheme.

Double and triple combinations of broad spectral linewidth light sources were used in this work for illuminating the fibre interferometers in order to facilitate measurements that utilise an efficient signal processing technique based on the optimised combination of light source wavelengths. Methods for the analysis of multiple light source combinations and their application in the present research program are fully discussed.

Techniques for the manufacture of broad reflection bandwidth in-fibre Fabry-Pérot cavities based on the Bragg grating technology have been developed during the course of this project and are discussed in detail. A novel technique for the production of wavelength-tunable, broad-bandwidth chirped Bragg gratings was developed and patented during this project in order to facilitate economically efficient production of sensing elements for multi-wavelength low coherence interferometry. These fabrication techniques are, in their own right, a major contribution of this work, which may be useful to others working in the field of optical fibre technology.

Intrinsic fibre Fabry-Pérot sensing elements based on superimposed chirped Bragg gratings have been designed, fabricated and employed in fibre interferometers due to their potentially superior characteristics of suitability for a range of industrial and laboratory applications.

Approaches to optimisation of the white-light system performance are analysed for the chosen system configuration and scheme of signal processing. An efficient algorithm for the interferogram data processing that takes advantage of the source wavelength optimisation has been implemented during laboratory measurements. A moderately fast scanning technique for inducing the phase modulation in the receiver interferometer was employed, and that had facilitated the measurements of quasi-static and slowly-varying strain and temperature measurands. The characteristics of performance of low coherence fibre interferometers developed during this study are analysed, and the theory predictions are compared to the measurement data obtained from the operational fibre interferometers.

Some problems related to the development and operation of the described type of measurement systems are discussed and analysed in the context of system limitations and the achievable performance characteristics. Ways of improving these characteristics are suggested, with predictions based on the practical development results. The prospective industrial applications of low-coherence interferometers employing the multi-wavelength light sources and chirped grating-based sensor elements are suggested.

# *Table of Contents*

	<b>Page</b>
DECLARATION.....	i
ACKNOWLEDGEMENTS .....	ii
ABSTRACT .....	iii
TABLE OF CONTENTS .....	v
<b>CHAPTER 1. INTRODUCTION</b>	<b>1.1</b>
1.1 Background.....	1.1
1.1.1 Interferometric optical fibre sensors.....	1.2
1.1.2 Low coherence interferometry.....	1.4
1.1.3 Tracking the path matching condition for absolute sensing.....	1.4
1.1.4 Source synthesis - three wavelengths.....	1.7
1.2 Research objectives and major activities.....	1.10
1.3 Thesis overview.....	1.12
<b>CHAPTER 2. BACKGROUND</b>	<b>2.1</b>
2.1 Previous work in strain sensing.....	2.2
2.2 Interferometric optical fibre sensing schemes.....	2.5
2.2.1 Sensing applications based on low coherence interferometry.....	2.6
2.3 Sensing schemes based on Bragg grating technology.....	2.8

2.4 Sensors utilising in-line and extrinsic Fabry-Pérot interferometers.....	2.12
2.5 Strain and temperature responses of a fibre Fabry-Pérot cavity.....	2.13
2.6 Fabry-Pérot sensing elements in low coherence interferometry.....	2.19
<b>CHAPTER 3. THEORETICAL ANALYSIS OF LOW COHERENCE</b>	<b>3.1</b>
<b><i>OPTICAL FIBRE INTERFEROMETRY</i></b>	
3.1 Introduction.....	3.1
3.1.1 The principle of low-coherence interferometry.....	3.2
3.2 White-light interferometer transfer function.....	3.4
3.3 Design considerations for low coherence fibre sensors.....	3.11
3.4 Advantages and problems of WLI.....	3.13
3.4.1 Advantages of optical fibre low-coherence sensing.....	3.13
3.4.2 Technical challenges in optical fibre WLI and ways of improving performance.....	3.15
3.5 Signal processing techniques in WLI.....	3.16
3.5.1 Source coherence synthesis technique.....	3.17
3.5.2 Analysis of source synthesis technique and optimisation of central wavelength separation of two sources.....	3.18
3.5.3 Analysis and optimisation of multiple source combinations.....	3.24
3.6 Sensing elements based on fibre Bragg grating Fabry-Pérots.....	3.31
3.6.1 Properties of fibre Fabry-Pérot sensors. Optimisation of sensor performance.....	3.31
3.6.2 Transfer function of a low-coherence system using a chirped Bragg grating FP sensor and an optimised combination source.....	3.36
3.7 Central fringe identification and processing of output fringe patterns.....	3.41

## CHAPTER 4. *IN-FIBRE BRAGG GRATINGS AND THEIR*

### *APPLICATIONS IN OPTICAL FIBRE SENSORS*

	4.1
4.1 Introduction.....	4.1
4.2 Overview of properties and general theory of in-fibre Bragg gratings.....	4.2
4.2.1 General characteristics of fibre Bragg gratings. Approaches to the theoretical analysis of Bragg gratings.....	4.3
4.2.2 Coupled-mode theory analysis of uniform constant-periodicity Bragg gratings.....	4.5
4.2.3 Spectral properties of uniform constant-periodicity Bragg gratings.....	4.10
4.2.4 Analysis of chirped Bragg gratings.....	4.13
4.3 Manufacturing techniques and facilities for IFBG production.....	4.26
4.3.1 Photosensitivity in optical fibres.....	4.26
4.3.2 Experimental arrangements used for the production of Bragg gratings.....	4.29
4.3.3 Techniques for the production of chirped Bragg gratings.....	4.31
4.4 The prism interferometer chirping technique.....	4.37
4.4.1 Principle of the method.....	4.38
4.4.2 Analysis of the prism interferometer chirping technique .....	4.41
4.5 Modelling of UV-induced refractive index change and index saturation effects...	4.46
4.6 Analysis of multiple superimposed chirped Bragg grating structures.....	4.50
4.7 In-fibre Fabry-Pérot cavities produced by writing chirped Bragg gratings.....	4.53
4.7.1 Methods of fabrication of Fabry-Pérot cavities formed by pairs of superimposed chirped grating structures.....	4.54
4.7.2 Fabry-Pérot cavities formed by multiple superimposed sets of chirped Bragg gratings.....	4.56

<b>CHAPTER 5. DEVELOPMENT OF LOW-COHERENCE OPTICAL FIBRE FABRY-PÉROT SENSOR SYSTEMS</b>	<b>5.1</b>
5.1 Introduction.....	5.1
5.2 Scheme and description of a practical low-coherence sensing system.....	5.2
5.3 Low coherence optical sources.....	5.4
5.4 Sensor Fabry-Pérot properties. Advantages and disadvantages of sensing elements produced with the prism interferometer technique.....	5.7
5.5 Receiver electronics .....	5.10
5.6 Properties of the interferometer output signal and dispersion-induced signal distortion effects.....	5.12
5.6.1 Effect of stress-optic dispersion.....	5.12
5.6.2 Effect of chromatic dispersion in the system components.....	5.16
5.7 Summary .....	5.21
 <b>CHAPTER 6. MEASUREMENTS OF TEMPERATURE AND STRAIN WITH LOW-COHERENCE FIBRE FABRY-PÉROT SENSORS</b>	 <b>6.1</b>
6.1 Introduction.....	6.1
6.2 Temperature monitoring with end-coated Fabry-Pérot sensors.....	6.2
6.2.1 Measurements with a double combination source interferometer.....	6.3
6.2.2 Measurements with a triple combination source interferometer.....	6.8
6.3 Methods of calibration and testing used for strain monitoring.....	6.13
6.3.1 Mechanical characterisation of testing method.....	6.14
6.3.2 Monitoring of dynamic strain with grating-based Fabry-Pérot sensors.....	6.19

6.4 Results summary .....	6.26
6.5 Conclusion .....	6.27
 <b>CHAPTER 7. CONCLUSION AND FUTURE WORK</b>	<b>7.1</b>
 7.1 Conclusion .....	7.1
7.2 Future work .....	7.3
 <b>REFERENCES</b>	<b>R.1</b>
 <b>PUBLICATIONS</b>	<b>P.1</b>
 <b>APPENDICES</b>	<b>A.1</b>
A.1 List of symbols .....	A.1

## **Introduction**

### **1.1 Background.**

The field of optical fibre sensor (OFS) technology has been attracting significant research interest during the last three decades and research efforts have resulted in the successful development of a large number of sensing systems [Giallorenzi *et al.*, 1982, Grattan and Sun, 2000]. The fundamental reason for this growing interest in the development of OFS is the existence of a large range of industrial and laboratory applications for which these types of devices have proved to be particularly attractive and suitable. A variety of practical measurement and control applications exist that involve harsh environments, hard-to-reach measurement locations, or require a lightweight sensor element to be incorporated into a structure for monitoring its integrity non-destructively. Optical fibre sensor technology can offer the best up-to-date metrology solutions for a great number of situations requiring precise measurement of mechanical, thermal, chemical, acoustic, electrical or magnetic parameters [Culshaw and Dakin, 1989].

### 1.1.1 Interferometric optical fibre sensors.

Optical interferometry exploits the very short ( $\sim 10^{-6}$  m) wavelength of light by discriminating between dark and bright fringes produced when two light beams are superimposed at a detector. Optical path changes comparable to the wavelength of light between two or more interfering optical fields result in measurable changes in output, so that interferometers can discriminate sub-micron optical path changes, arising, for example, due to strain or refractive index variations.

Interferometric optical fibre sensors provide measurement systems that combine the advantages of high precision inherent to optical interferometry with the advantages of system flexibility, compact size and immunity to environmental perturbations characteristic of fibre optic systems. All-fibre interferometers are particularly attractive due to the absence of any bulk-optic components that require precise and stable alignment. This makes the overall system design more compact and portable, thus making measurement systems very suitable for both laboratory and field deployment.

Devices based on fibre interferometry utilise sensing elements that encode the influence of a measurand into a variation in the intensity, phase, state of polarisation, or spectrum of the output optical signal. The output signal itself results from the interference of beams propagating via different arms of an interferometer and it can be processed remotely due to the low propagation loss in optical fibres.

Systems based on optical fibre interferometry can be classified either according to the way the measurand modifies the sensor signal or according to a sensor being of intrinsic or extrinsic type. The former category of classification is further subdivided into classes of systems based on measurand-induced intensity, phase, polarisation, or spectrum modulation. The latter category subdivides types of optical fibre systems according to the way the signal information from the sensing element is carried to the detector and electronic processing unit. An intrinsic OFS utilises in-fibre sensing elements that enable the measurand to modify the optical properties of a lightwave propagating inside the fibre. Extrinsic OFS systems, on the other hand, form a class of devices in which an optical fibre is utilised as a waveguide that carries light to an external sensor, and directs the returned lightwave to the processing unit.

Intrinsic interferometric sensors offer the advantages of high sensitivity to all parameters that affect the refractive index or physical length of a section of fibre placed inside the measurand

field. This type of OFS also has the potential for utilising all of the advantages of compactness, ruggedness and measurement stability offered by all-fibre interferometers.

All types of OFS can also be categorised according to the working principle of a sensing element employed to encode measurand information, the interferometer configuration used, and according to the signal recovery scheme implemented in the system.

Interferometric systems employing fibre Fabry-Pérot sensing elements have been shown to possess great potential for measurement of many parameters with sensors employing various configurations, signal encoding and processing schemes [Yoshino *et al.*, 1982, Mitchell, 1991, Measures, 1992]. This is due to the structural simplicity, compactness and versatility of the in-fibre Fabry-Pérot interferometer. This sensor configuration ensures that light travels to and from the sensor within the same optical fibre, and therefore the problems of lead sensitivity and associated phase noise are reduced significantly. In-fibre Fabry-Pérot sensors have also been shown to possess a significant potential for sensor multiplexing, for example, in the case of low-coherence interrogation [Kaddu *et al.*, 1999]. In the case when an in-fibre Fabry-Pérot interferometer is illuminated with a highly coherent light source, measurements are possible only if the combined mirror reflectance of the Fabry-Pérot is low (for the case of low-finesse cavities). Otherwise, this type of sensor will return several lightwaves produced by multiple reflections within a Fabry-Pérot, and the signal processing schemes suitable for two-beam interferometers will not work. However, with low-coherence interrogation, when the optical path difference corresponding to just one round trip through the Fabry-Pérot cavity is much greater than the coherence length of the light source, higher mirror reflectances can be used. This can potentially improve the signal-to-noise performance characteristics and allows a system designer to vary Fabry-Pérot mirror reflectances over a large range in order to achieve optimised fringe visibility for the output signal.

During the course of this project, intrinsic all-fibre low-coherence interferometers with Fabry-Pérot sensing elements based on sets of superimposed chirped Bragg gratings were designed, built, and tested. The performance characteristics of this novel type of sensing system have been optimised through the investigation of system configuration, design and fabrication of a sensor element, and signal processing technique utilising a multi-wavelength combination source. The performance characteristics of this measurement system were investigated theoretically and tested experimentally.

### **1.1.2 Low coherence interferometry.**

Low coherence interferometry (LCI) is a technique that is well known in classical optics [Born and Wolf, 1980] and an interferometric measurement approach that employs broad spectral linewidth optical sources. The general approach to measurements in the case of low-coherence sensing is common to all other methods used in optical interferometry, since the value of measurand is recovered through the analysis of an interferometric fringe pattern that allows the measurand-induced change in the optical path length of the sensing element to be determined.

The application of low-coherence interferometry to optical fibre sensing was first reported in 1983 [Al-Chalabi *et al.*, 1983]. It was employed for interferometric systems based on single-mode fibres [Al-Chalabi *et al.*, 1983] and later the application of this sensing scheme was demonstrated with multimode fibre systems [Bosselman and Ulrich, 1984]. The progress in the field of low-coherence optical fibre sensing has been rapid in recent years and a wide variety of measurement systems have been developed [Rao and Jackson, 1996, Ning and Grattan, 1998].

The low-coherence sensor interrogation technique is a solution to the fundamental problem of limited unambiguous measurand range that is inherent in conventional laser interferometry due to the periodic nature of the output fringe signal. Moreover, this sensing technique offers the advantage of absolute sensing with potentially a very high range-to-resolution ratio and relaxed requirements for the stability of optical sources. Sensing systems using the low-coherence principle do not suffer loss of data after power cut-off events and feature self-initialisation.

### **1.1.3 Tracking the path matching condition for absolute sensing.**

Conventional interferometric optical fibre sensors usually employ a highly coherent light source that enables precise measurement within a limited operating range due to the periodic structure of the output interference signal. Such sensor systems also require highly stabilised light sources and are sensitive to optical power fluctuations. If measurements are interrupted due to a power cut-off event, loss of measurand information can occur.

White-light interferometry (WLI, the alternative terminology to LCI) is a measurement technique that is capable of overcoming the intrinsic difficulties of conventional interferometric sensing schemes. It uses a low-coherence light source and offers the possibility of absolute

position measurement. In addition, it offers such advantages as relative insensitivity to optical power fluctuations and light source wavelength instabilities. Measurand information is not lost when measurements are interrupted due to a power switch-off event. Therefore, white-light interferometric systems offer a practical solution to many sensing applications, especially in situations where long-term measurement or parameter monitoring is required.

A white-light interferometric system uses two interferometers linked in series, one of which is called the sensor interferometer and the second the receiver interferometer. Optical path imbalances of both the sensor and receiver interferometers are always greater than the coherence length of the optical source, so that interference effects could only be observed if the path difference in the receiver interferometer is matched closely to that of the sensor interferometer. The latter path difference is defined by the measurand. By scanning the optical path imbalance in the receiver interferometer, one can match its value with the value of the optical path imbalance of the sensor interferometer, and under this condition interference fringes can be seen at the output. Any physical quantity that affects the optical path length in the sensor interferometer can be measured using white-light interferometry [Culshaw and Dakin, 1989].

Unlike measurements made with conventional interferometers (utilising highly coherent light sources), the measurand-encoded output fringe pattern in the case of a low-coherence system is aperiodic. This follows from the character of the white-light interferometer transfer function (as is discussed in detail in Chapter 3), since phase and visibility of fringes are both dependent on the relative path imbalance between the two interferometers. This aperiodic but symmetrical (with respect to the point of zero relative path imbalance) character of white-light interference pattern leads to the existence of a unique central point in the transfer function of white-light systems termed the centre of the white-light interference pattern. This is the basis for the ability to perform absolute measurements.

Of particular interest within this sensing scheme is the problem of determination of the position of the centre of interference pattern, which is the value of relative path imbalance between the two interferometers corresponding to the maximum output fringe visibility. This unique point in the interference pattern provides information about the sensing interferometer path imbalance and hence about the value of the measurand. The precision of WLI sensing is determined by the achievable accuracy of determination of this path matching position. In a practical system, the position of the centre of the interference fringe pattern should be determined promptly, with maximum precision and without ambiguity, which is possible if the central fringe in a fringe pattern has dominant intensity with respect to the side-fringes. If noise considerations are taken into account, the system requires some minimum value of the signal-to-noise ratio (SNR) to

allow for unambiguous central point determination. A considerable amount of research effort has been dedicated, in recent years, to determining the conditions that provide the minimum signal-to-noise ratio required by the system for correct measurement. It was found that by employing synthetic low-coherence optical sources with different central wavelengths, the requirements for the minimum SNR could be substantially lowered [Chen *et al.*, 1993, Wang *et al.*, 1994a]. In the case of a double-wavelength combination source, the resultant interference fringe pattern is actually the beat pattern between the two interference signals, and the central fringe intensity is significantly higher than that of the side-fringes. This is due to the fact that two intensities are added in phase at the point of zero relative path imbalance. The value of minimum SNR required by the system for correct determination of the central point can be lowered using such a technique from about 50 dB to nearly 20 dB, giving significant improvement in the accuracy and applicability of the method [Wang *et al.*, 1994].

The minimum SNR required by the system for correct determination of the central point position in the case of dual-wavelength WLI is achieved when the central wavelength difference between two broadband sources is equal to an optimum value. The optimum condition in this case is determined by the fact that the normalised AC intensity (peak-to-peak value) of the first side fringe in the central fringe packet should be equal to the intensity of the central fringe in the first side fringe packet. This condition sets the minimum SNR value that can be used for a dual-wavelength combination system [Wang *et al.*, 1994]. However, it was reported that such a dual-wavelength combination source does not represent the optimum possible optical source for use in WLI systems. It was found that better interference patterns can be obtained using the product of two autocorrelation functions of two broadband sources instead of using their sum as described above. Although the use of this technique necessitates the introduction of switching between two optical sources (and hence the experimental setup is more complicated), such a sensing scheme improves the sensing accuracy by lowering the required SNR by approximately 6 dB when compared to the summation method [Rao and Jackson, 1994]. Further improvements in terms of measurement stability in the presence of noise effects are possible with multi-wavelength combination sources.

### 1.1.4 Source synthesis - three wavelengths.

Of particular research interest in the recent years has been the use of multiple-wavelength combination sources in low-coherence sensing. It has been shown, both theoretically and experimentally, that the use of a triple-wavelength combination source can further reduce the value of minimum signal-to-noise ratio required by the system for correct measurement [Wang *et al.*, 1994a] compared to double-wavelength systems. The concept of optimum wavelength combination remains applicable in this case and according to Wang *et al.*, correct determination of the zero path difference position is no longer a serious problem, provided that the optical sources to be used in the system are chosen correctly. Thus, a very short interference pattern with a dominant central fringe can be obtained using suitably optimised combinations of three broadband sources.

An example of central fringe enhancement due to interferogram superposition effects is presented in Figure 1.1. The interferograms shown are modelled taking into account the optimised set of central wavelengths employed for the construction of fibre sensors in this project.

Clearly, the interferograms shown in Figure 1.1 demonstrate the strength of the multi-wavelength approach in low coherence sensing. However, the efficient practical utilisation of combined sources in all-fibre sensing systems requires thorough analysis of all aspects of white-light interferometry and has been the principal motivation for this work.

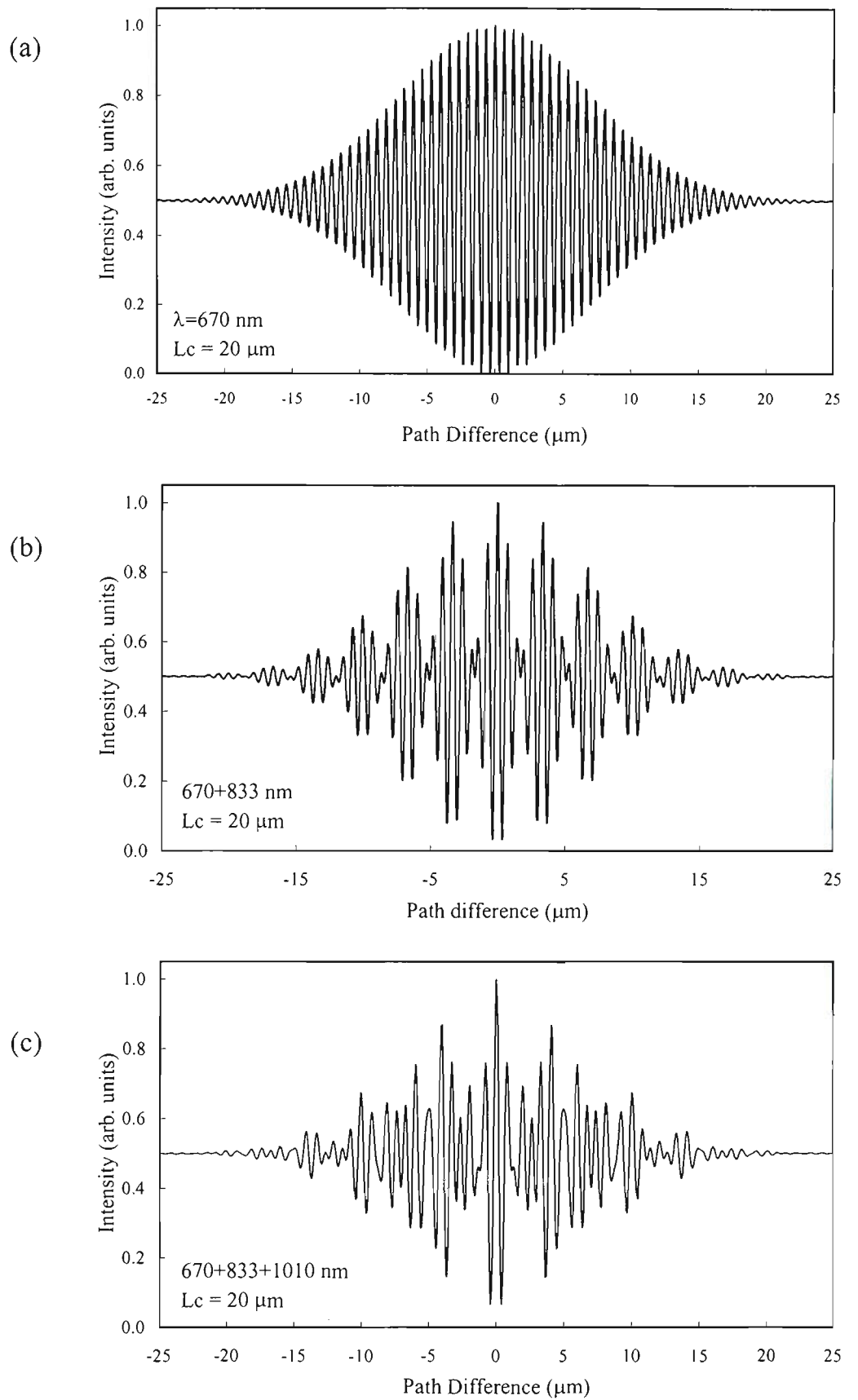


**Figure 1.1** *Low coherence interferograms obtained with (a) single light source, (b) double and (c) triple-wavelength combination source.*

Recent progress in optical fibre technology has allowed the use of novel fibre optic components such as in-fibre Bragg gratings (IFBG) for the construction of low coherence fibre Fabry-Pérot sensors capable of withstanding high tensile strains [Kaddu, 1995]. Therefore, the applicability of LCI-based fibre sensors for strain monitoring can be improved greatly due to superior mechanical properties of a sensing element allowing the measurement of strains of the order of 12,000 microstrain. This figure is far beyond the limits of fibre optic Fabry-Pérot sensors produced by conventional technologies. The usage of multiple Bragg gratings written onto a single section of fibre gives the opportunity to produce a synthesised low-coherence signal with improved characteristics for better precision and repeatability of measurements.

The principal motivation for this study has been to analyse low coherence fibre interferometry in order to utilise the latest developments in optical fibre technology for the construction of measurement systems that could serve as a prototype for future industrial fibre sensors with improved characteristics.

Literature searches indicate that, to the best of our knowledge, only the OTRL group has reported the use of the LCI sensing technique utilising multiple in-fibre Bragg grating reflectors for the formation of in-line Fabry-Pérot sensor cavities [Kaddu *et al.*, 1997]. No reports of practical white-light interferometers with sensor elements based on multiple superimposed chirped gratings have been produced to date, and therefore this study represents a new approach to low-coherence sensing.

During this research program, the optimised double-wavelength and triple-wavelength source combinations for use in a low-coherence sensor were calculated taking into account the sources' coherence length parameter and the commercial availability of broad-bandwidth fibre-coupled light sources. The sensor elements based on broad reflection bandwidth Bragg gratings were manufactured according to the calculations that optimised the source's central wavelength combination.

## 1.2 Research objectives and major activities.

The principal aim of this study has been to investigate the viability of the multi-wavelength low coherence interferometry scheme in a practical all-fibre sensor employing a novel type of sensing element based on chirped Bragg gratings.

The particular objectives of this research project have been:

- To investigate methods for the production of chirped Bragg gratings with broad reflection bandwidth.
- To model the spectral properties and characterise the performance of superimposed chirped grating structures.
- To design and fabricate fibre Fabry-Pérot interferometers based on sets of superimposed chirped Bragg gratings with characteristics suitable for the multi-wavelength low coherence application.
- To characterise the response function of a Fabry-Pérot interferometric sensor with superimposed chirped Bragg gratings.
- To investigate and characterise the effects of dispersion in the gratings and other optical components on the output white-light interferogram near the path matching condition.
- To design and construct a practical all-fibre sensor system utilising the principle of low coherence interferometry with multi-wavelength combination source interrogation.
- To perform measurements of strain and temperature with the sensor system constructed and to characterise its performance and potential.

A principal diagram of the low-coherence fibre Fabry-Pérot sensing system developed during this project is shown in Figure 1.2.

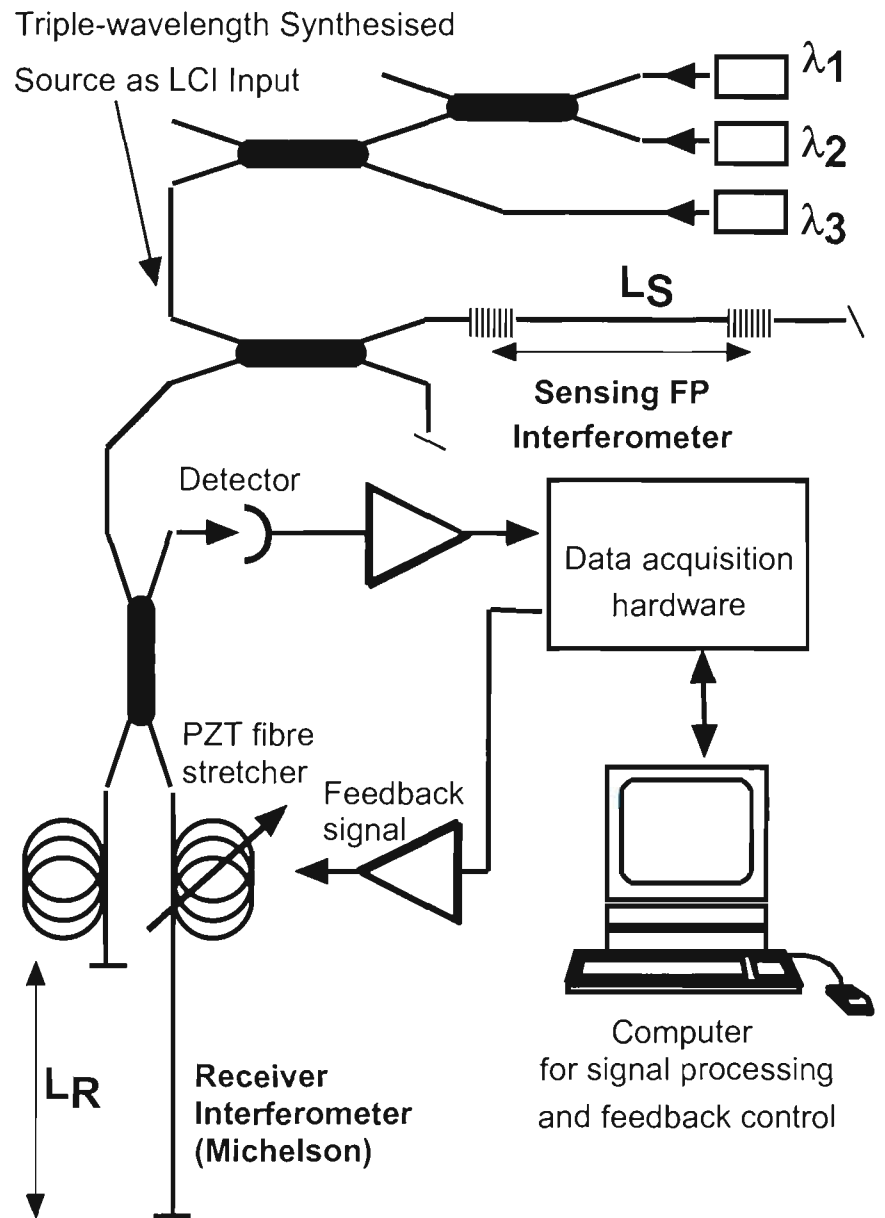


**Figure 1.2** *Schematic diagram of the multi-wavelength low coherence fibre interferometers developed during this study.*

The operation of this sensor system and all of its components are discussed in detail in the subsequent chapters of this thesis.

### **1.3 Thesis overview.**

This thesis reports a study of the principles of low-coherence optical fibre sensing and ways of utilising the current developments in optical technology for the construction of measurement systems with improved characteristics. Major attention was directed at obtaining a thorough understanding of the properties of fibre Bragg gratings, in particular, the methods for their design and fabrication. Analysis of chirped Bragg gratings (particularly multiple superimposed sets of chirped gratings) has enabled economically efficient production of the Fabry-Pérot sensor elements designed according to the specifications dictated by the low coherence sensing application.

Chapter 2 is a brief introduction into the field of optical fibre sensors and it focuses on the features of several previously developed approaches to optical fibre strain and temperature sensing. It contains a detailed overview of previous work in optical fibre low-coherence sensing and a discussion of recent progress in this field.

Chapter 3 contains theoretical analysis of the principles of optical fibre low-coherence interferometry. It provides theory background on the development of practical multi-wavelength low-coherence interferometers and explains the system configuration and signal processing methodology chosen during the course of this study. Predictions of the characteristics of system performance derived from theoretical analysis are given.

Chapter 4 provides a thorough analysis of the fundamental properties of optical fibre Bragg gratings. This part of the thesis also provides theoretical background on chirped gratings and the description of techniques for fabrication of in-fibre Fabry-Pérot interferometers with characteristics suitable for multi-wavelength low coherence interferometry. A detailed investigation of methods for the analysis, design and fabrication of multiple superimposed chirped grating structures is presented.

Chapter 5 presents a detailed technical description of the features and components of multi-wavelength low-coherence sensing systems developed during this study. It contains information on the practical aspects of the design and operation of these sensors. This links parts of the thesis describing the theory predictions and experimental results.

Chapter 6 presents the principal results of strain and temperature monitoring achieved with low coherence interferometers built during this study. It evaluates the performance characteristics of the systems developed and compares the performance of systems utilising double and triple source combinations. Approaches that would provide further improvements in strain and temperature monitoring are considered.

Chapter 7 is devoted to the critical analysis of the major contributions of this work and the significance of the principal results achieved. It concludes the thesis with suggestions on future improvements of the measurement technique studied in the context of the results obtained.

## **Background**

This chapter provides a summary of the current state of the field of optical fibre sensors. In particular, the background on strain sensing and optical fibre interferometry is presented. Techniques and approaches utilised for constructing efficient interferometric measurement systems are outlined together with the current trends in the design and operation of such systems. This chapter emphasises the applicability and advantages of optical fibre low coherence interferometry for applications involving strain and temperature measurement. Types of industrial applications within this field and their particular features related to the technology of measurement are described. Substantial attention is devoted to the potential of fibre optic Bragg grating-based sensors and fibre Fabry-Pérot interferometers for the measurement of strain and to the practical application of systems utilising these sensing elements. The purpose of this chapter is to review previous work and to introduce the principal features of low coherence fibre Fabry-Pérot sensors, their principal advantages and relation to other reported measurement schemes.

## 2.1 Previous work in strain sensing.

The requirement for the measurement of strain has originated with the advent of advanced machinery in industry and the development of modern technologies in civil infrastructure engineering. The growing demand for strain monitoring and characterisation is based on the necessity to ensure proper operation of appliances and safety of loaded structures. A large variety of technical approaches has been devised in response to the ever-growing demand for strain monitoring systems [Uttam *et al.*, 1985, Lesko *et al.*, 1992, Marshall *et al.*, 1998, Peters *et al.*, 2000]. Low coherence interferometry, due to its intrinsic feature of absolute measurement, possesses great potential for many applications involving strain and displacement monitoring. It is interesting to consider the theory background of strain measurements and practical approaches utilised in optical fibre sensing for the construction of strain monitoring systems.

### Stress and strain formalisms.

The notions of stress and strain are used in solid mechanics to describe the behaviour of structures under external loads. A solid structure subjected to an external loading force experiences deformation (a change in its dimensions), and internal forces develop within the deformed structure. Mechanical stress is defined as the internal force per unit cross-sectional area. Strain is the fractional change in the structure's dimensions caused by the application of stress.

A component of loading force perpendicular to the structure's cross-sectional area produces an axial (or normal) component of stress resulting in axial strain, which can be either tensile or compressional. A component of loading force parallel to the cross-sectional area produces a shear component of stress that results in shear strain. Since two directions (one associated with the loading force and the other associated with the plane of the structure cross-section) are used in the description of stress and strain, these quantities can be represented by second-rank tensors  $\sigma$  and  $\epsilon$  [Timoshenko and Goodier, 1970]:

$$\bar{\sigma} = [\sigma_{ij}] = \begin{bmatrix} \sigma_{xx} & \sigma_{xy} & \sigma_{xz} \\ \sigma_{yx} & \sigma_{yy} & \sigma_{yz} \\ \sigma_{zx} & \sigma_{zy} & \sigma_{zz} \end{bmatrix}, \quad (2.1)$$

$$\bar{\varepsilon} = [\varepsilon_{ij}] = \begin{bmatrix} \varepsilon_{xx} & \varepsilon_{xy} & \varepsilon_{xz} \\ \varepsilon_{yx} & \varepsilon_{yy} & \varepsilon_{yz} \\ \varepsilon_{zx} & \varepsilon_{zy} & \varepsilon_{zz} \end{bmatrix}, \quad (2.2)$$

where the diagonal elements of tensors represent the normal (axial) components of stress and strain and off-diagonal elements represent shear stresses and strains.

A typical (for most metals in the cases of axial and shear deformations) stress-strain relationship is represented in Figure 2.1.

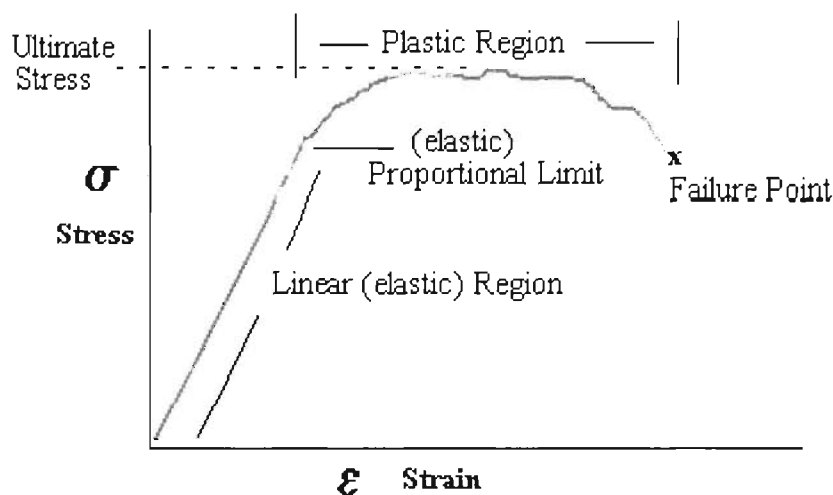


**Figure 2.1** Typical stress-strain relationship.

A principal feature of the stress-strain relationship shown in Figure 2.1 is the existence of an elastic region, in which the stress is directly proportional to strain. For linearly elastic materials, the relationship between the components of total stress and strain is governed by Hooke's law:

$$\sigma_{ij} = C_{ijkl} \varepsilon_{kl}, \text{ or} \quad (2.3)$$

$$\varepsilon_{ij} = S_{ijkl} \sigma_{kl}, \quad (2.4)$$

where  $C$  and  $S$  are the compliance and stiffness tensors, respectively, and Einstein's convention regarding the summation over all possible values of repetitive indices is used. The components of the compliance and stiffness tensors obey the following relationships:

$$C_{ijkl}^{-1} = S_{ijkl}, \text{ and} \quad (2.5)$$

$$C_{ijkl} = C_{jikl} = C_{ijlk} = C_{klij}. \quad (2.6)$$

The generalised Hooke's law can be rewritten in matrix form in the following way:

$$\begin{pmatrix} \varepsilon_{xx} \\ \varepsilon_{yy} \\ \varepsilon_{zz} \\ \gamma_{yz} \\ \gamma_{xz} \\ \gamma_{xy} \end{pmatrix} = \begin{pmatrix} S_{11} & S_{12} & S_{13} & S_{14} & S_{15} & S_{16} \\ S_{21} & S_{22} & S_{23} & S_{24} & S_{25} & S_{26} \\ S_{31} & S_{32} & S_{33} & S_{34} & S_{35} & S_{36} \\ S_{41} & S_{42} & S_{43} & S_{44} & S_{45} & S_{46} \\ S_{51} & S_{52} & S_{53} & S_{54} & S_{55} & S_{56} \\ S_{61} & S_{62} & S_{63} & S_{64} & S_{65} & S_{66} \end{pmatrix} \begin{pmatrix} \sigma_{xx} \\ \sigma_{yy} \\ \sigma_{zz} \\ \tau_{yz} \\ \tau_{xz} \\ \tau_{xy} \end{pmatrix}, \quad (2.7)$$

where  $(\varepsilon_{kk}, \gamma_{mn})$  are axial and shear strains, and  $(\sigma_{kk}, \tau_{mn})$  represent the axial and shear stresses respectively. In the case of a material possessing structural isotropic symmetry (as is the case for fused silica fibre), the stiffness matrix contains only three non-zero components, and Hooke's law can be rewritten in the form [Weber, 1986]:

$$\begin{pmatrix} \varepsilon_{xx} \\ \varepsilon_{yy} \\ \varepsilon_{zz} \\ \gamma_{yz} \\ \gamma_{xz} \\ \gamma_{xy} \end{pmatrix} = \begin{pmatrix} S_{11} & S_{12} & S_{12} & 0 & 0 & 0 \\ S_{12} & S_{11} & S_{12} & 0 & 0 & 0 \\ S_{12} & S_{12} & S_{11} & 0 & 0 & 0 \\ 0 & 0 & 0 & S_{44} & 0 & 0 \\ 0 & 0 & 0 & 0 & S_{44} & 0 \\ 0 & 0 & 0 & 0 & 0 & S_{44} \end{pmatrix} \begin{pmatrix} \sigma_{xx} \\ \sigma_{yy} \\ \sigma_{zz} \\ \tau_{yz} \\ \tau_{xz} \\ \tau_{xy} \end{pmatrix}, \quad (2.8)$$

where the three independent elastic constants of isotropic material are related to the Young's modulus  $Y$  and Poisson's ratio  $\mu$  of the material according to equations

$$\begin{aligned} S_{11} &= \frac{1}{Y}, \\ S_{12} &= -\frac{\mu}{Y}, \\ S_{44} &= \frac{2(1 + \mu)}{Y}, \end{aligned} \quad (2.9)$$

and the shear modulus of the material (constant factor in the proportional shear stress - shear strain relationship) can be expressed as  $G = 1/S_{44}$ .

Within this thesis, it is appropriate to distinguish between the so-called conventional types of strain sensing systems that currently occupy large segments of the market and are in general based on non-optical technologies, and sensing systems that utilise optical fibre technology. Conventional types of strain sensing systems commonly utilise transducers that convert the variations in the applied strain into measurable changes in the electrical resistance, capacitance or inductance of the transducer element. They are not suitable in environments where difficult measurement conditions exist, for example, in situations where electromagnetic interference effects, high temperatures or small dimensions of measurement locations may impede the successful operation of a sensor. The accuracy of transducer-based strain sensing technologies is also insufficient for many practical applications in modern industry.

Of particular interest within the class of devices utilising optical fibre technology are systems based on optical fibre interferometry that have inherent advantages of high accuracy, versatility and a wide range of applications. With the number of successful interferometric optical fibre sensors constantly increasing, this technology is poised to replace most of the conventional sensor technologies on the market in the future.

## **2.2 Interferometric optical fibre sensing schemes.**

Optical interferometry is one of the most accurate measurement techniques used in optical fibre sensor systems. During measurements with an interferometer, the measurand information is encoded through the action of the sensing element into the properties of the output optical signal that depend on the phase difference between interfering light waves. At the output of an interferometric sensing system, the optical interference signal is converted into an electrical signal (usually a voltage waveform) using a photodetector and signal processing circuitry. Optical fibre interferometry has proved to be one of the most versatile and promising measurement technologies within modern metrology due to its great potential to combine the advantages of the classical technique of optical interferometry with those of fibre-based systems. The success of optical fibre interferometers is due to their ability to provide accurate and reliable measurements in situations where other technologies are unsuitable or insufficient.

Interferometric optical fibre sensors can provide a very high level of measurand sensitivity, although in a number of situations, the cross-sensitivity problems may occur when the sensor elements cannot be isolated from undesirable measurement parameters - often these are temperature changes in the environment [Grattan and Sun, 2000]. A great number of optical fibre interferometers have been developed to date, from simple displacement sensors to the

multiplexed multi-parameter sensing systems employing various configurations and interrogation schemes [Giallorenzi *et al.*, 1982, Grattan and Sun, 2000]. Of particular importance is the application of the principle of white-light interferometry [Born and Wolf, 1980] to fibre systems that has resulted in the development of fibre interferometers capable of performing high-accuracy absolute measurements.

### **2.2.1 Sensing applications based on low coherence interferometry.**

Since the initial report of the application of low coherence interferometry to optical fibre sensing in 1983 [Al-Chalabi *et al.*, 1983], a large range of fibre sensors utilising this measurement principle has been developed. Practical systems for the measurement of displacement [Koch and Ulrich, 1991, Taplin *et al.*, 1994], strain [Gerges *et al.*, 1987, Belleville and Duplain, 1993], pressure [Velluet *et al.*, 1987, Rao *et al.*, 1994, Bock *et al.*, 1995], temperature [Marillier and Lequime, 1987, Lee and Taylor, 1991], refractive index [Trouchet *et al.*, 1992, Murphy and Flavin, 2000] and vibration amplitude [Weir *et al.*, 1992] have been reported.

Within the field of optical fibre low coherence interferometry, several principal approaches to measurement have been implemented. The processing of output fringe patterns in LCI can be performed in either the phase domain or the spectral domain. In each of these approaches, either the temporal or spatial fringe pattern formation can be implemented [Meggett, 1995].

In conventional LCI, measurements are performed in the phase domain, when the distance to be measured (optical path difference (OPD) of the sensing interferometer) is matched by the OPD of the processing interferometer. An alternative approach termed the spectral domain processing uses a spectrum analyser as the optical processing element for the measurement of the output power spectrum encoded by the sensor [Velluet *et al.*, 1987].

The changes in the OPD of the sensor interferometer can also be determined from the analysis of the channeled spectra produced by the sensor cavity. In this method, the light returned from the sensing cavity is being spatially dispersed using a diffractive optical element (a diffraction grating), and a linear CCD array can be used for monitoring the measurand-induced spectral changes of light returned from the sensor [Taplin *et al.*, 1994]. An advantageous feature of this technology is that no moving parts are required.

In electronically-scanned white-light interferometry, the spatial fringe formation principle is used [Koch and Ulrich, 1990, Chen *et al.*, 1990, Chen *et al.*, 1991]. A spatial fringe pattern is formed by expanding the beam in the receiving interferometer and by interfering beams reflected from the two mirrors, one of which is tilted. A photodetector array, such as a CCD, is used for recording the output interference pattern. Electronically-scanned LCI systems do not employ mechanical moving parts and therefore are compact, rigid, and stable. However, the operating range of such systems is limited by the number of pixels in a CCD array and the identification of the central fringe in electronically-scanned systems is more difficult than with the systems using other signal processing techniques due to the relatively high noise of the detector array [Rao and Jackson, 1996].

The application of chirped Bragg gratings for dual-wavelength pseudo-heterodyne signal processing in low coherence interferometry has been reported in 1997 [Brady *et al.*, 1997a]. In this system, an extrinsic Fizeau cavity was used as the sensor interferometer and two identical chirped gratings were used for synthesising two broadband sources through filtering the emission spectrum of a broad bandwidth superfluorescent fibre source. An unambiguous displacement sensing range of 270  $\mu\text{m}$  with a dynamic range of  $2.7 \times 10^5$  was reported. No reports of applications of broad reflection bandwidth chirped gratings for low coherence sensing with intrinsic fibre grating-based Fabry-Pérot cavities were found in the literature at present.

White-light interferometry has been used for multiplexing sensors, utilising the coherence multiplexing approach (coherence tuning) [Brooks *et al.*, 1985]. Low coherence fibre Fabry-Pérot sensors suitable for coherence multiplexing have been reported [Kaddu *et al.*, 1999]. Coherence-domain multiplexing was also reported for addressing arrays of fibre Bragg grating sensors [Dakin *et al.*, 1997]. Operation of networks of sensors addressed using LCI and utilising time division multiplexing has also been reported [Santos and Jackson, 1991].

Developments within the field of low coherence fibre interferometry have led to the emergence of new measurement technologies, such as optical coherence domain reflectometry (OCDR) and optical coherence tomography (OCT). OCDR was reported as a tool for measuring fault locations in optical waveguide devices and miniature optical elements with a typical resolution of a few tens of microns [Youngquist *et al.*, 1987]. Locations of polarisation cross-couplings in intrinsic interferometric fibre sensors, such as fibre gyroscopes, have been measured with the OCDR technique [Lefevre, 1990]. OCT was developed as a non-contact technique for imaging transparent and semi-transparent structures and found applications in the biomedical field, for example, in-vivo imaging of the human retina [Huang *et al.*, 1991]. In OCT, objects are scanned by laterally displacing the incident beam across the region of interest, with depth

information being obtained at each beam position through LCI measurement. Low coherence sensing schemes have also found applications in profilometry for imaging of surfaces with nanometric resolution [Sandoz and Tribillon, 1993].

## **2.3 Sensing schemes based on Bragg grating technology.**

It is important to note that the Bragg grating itself represents a strain and temperature sensor owing to the dependency of its reflection wavelength on ambient temperature and applied strain. This property of in-fibre Bragg gratings is now used extensively for the construction of practical strain and temperature sensors with wavelength-encoded operation [Rao, 1999, Zhang *et al.*, 1999]. Such sensors offer good sensitivity and stability of measurement but they normally require sophisticated wavelength demodulation technologies because of the small wavelength shift induced by the measurand. Typically, for gratings with nominal reflection wavelength of 1550 nm, the Bragg wavelength shift per unit perturbation is about 1 ppm/microstrain and 13 ppm/°C for temperature [Morey *et al.*, 1991]. The principal advantage of fibre Bragg grating sensors is their immunity to light power fluctuations and variations in polarization, due to their wavelength-encoded operation. Other advantages of Bragg grating sensors are their noise immunity, large measurement range, linearity of response, low insertion loss, simplicity and the ability to provide highly localised measurements at a number of points within a structure being monitored. At present, a large number of industrial applications exists for this type of strain or temperature gauges for safety monitoring of tunnels, bridges, power transformers, steam pipes and storage tanks. Bragg grating sensors therefore form a very important class of systems employed for the development of so-called "smart structures".

Of particular importance is the problem of cross-sensitivity of such sensors because both strain and temperature changes influence the output signal of the system [Xu *et al.*, 1994, Brady *et al.*, 1997]. An ideal strain gauge should respond to the changes in the applied strain only while exhibiting zero temperature sensitivity. In order to suppress the temperature sensitivity of in-fibre Bragg grating sensors, a thermal expansion compensating package has been developed [Yoffe *et al.*, 1995]. The wavelength-encoded sensing property of Bragg gratings can be used in white-light interferometric sensing systems to provide additional measurand information in order to decouple strain and temperature effects that affect the optical path in the sensor interferometer.

In white-light optical fibre sensors, ambient temperature changes cause variations in both the effective refractive index and physical path length in the sensor interferometer, and this may lead to the misinterpretation of the output data. This is the well-known phenomenon of thermally-induced strain or “apparent strain” [Kaddu, 1995]. In a practical system, it is necessary to minimise the influence of thermally induced path changes on the results of measurements. Several ways to solve this problem have been proposed, including the study of the thermal response of the system in order to correct the output data [Kaddu, 1995] and the utilisation of birefringent fibre interferometers [Sinha and Yoshino, 1998].

Applications of fibre Bragg gratings as sensor elements are based on the detection of the measurand-induced Bragg wavelength shift. Several detection schemes have been developed to date to interrogate Bragg grating sensors. These detection schemes are aimed at quantifying the value of the Bragg wavelength shift without the use of optical spectrum analysers in order to reduce the cost and complexity of sensor systems and to make them more suitable for field deployment. The measurement resolution achieved to date with most of the reported schemes for wavelength shift detection is limited by the minimum achievable spectral width of the reflection peak of sensor gratings [Zhang *et al.*, 1999].

One of the techniques used for interrogating Bragg grating sensors is the tunable receiving grating filter technique reported by [Jackson *et al.*, 1993] in which a fibre grating filter is used for tracking the changes in reflection wavelength of the sensor. The filter grating in this technique is tuned in wavelength using a PZT stretcher in order to match the reflection wavelength of the sensor. The output light intensity in this system is proportional to the product of reflection coefficients of the two Bragg gratings at the instantaneous wavelength of sensor grating. The maximum output light intensity is therefore achieved when the Bragg reflection wavelengths of the sensor and filter gratings are identical. The variations in strain applied to the sensor grating can be recovered from the measured variations of PZT voltage applied for tuning the filter grating. The strain sensing resolution achievable within this approach is limited by the finite values of the spectral width of grating reflection peaks and by the resolution of PZT scanner. A resolution of 4.12 microstrain was reported with this technique [Jackson *et al.*, 1993].

Another approach to interrogate the reflected wavelength shift uses a tunable in-fibre Fabry-Pérot filter [Kersey and Berkoff, 1993]. In this technique, the peak transmission passband of the fibre Fabry-Pérot (FFP) filter is tuned in and locked to the reflection peak of the sensor grating by modulating the Fabry-Pérot cavity length with a PZT driven by a dither signal generator. Dithering of the Fabry-Pérot cavity length modulates the Fabry-Pérot peak

transmission wavelength by 0.01 nm. The optical output of an FFP filter contains the fundamental frequency of the dither signal and its harmonics. The fundamental signal of the dither frequency disappears when the transmission peak of the Fabry-Pérot filter matches the reflection peak of the sensor grating, and therefore is used as an error signal for the PZT feedback loop. This allows the locking of the passband peak of the FFP to the peak of the reflection band of the sensor. The locking voltage of the PZT modulator is used as a measure of the reflection wavelength shift of the grating and therefore as a measure of applied strain. This technique allows interrogation of a multiplexed array of Bragg grating sensors in multi-point sensor applications since a ramp voltage can be applied to the PZT to tune the length of the FFP over its free spectral range. The resolution of less than 0.3 microstrain for a single sensor and of better than 3 microstrain for a system of four grating sensors has been achieved with this method [Kersey and Berkoff, 1993].

An alternative approach [Ball *et al.*, 1994] to recovering the measurand-induced wavelength shift uses a tunable fibre laser as a light source and a detection system for tracking the temperature-induced Bragg wavelength shift. The wavelength of the fibre laser is tuned by modulating the laser cavity length with a PZT in order to obtain a maximum output signal at the photodetector when the wavelength of the source is matched to the peak reflection wavelength of the sensor grating. Achieved resolution of 0.2°C was reported which is limited by the finite spectral width of the sensor grating reflection peak.

The Fourier transform spectroscopy technique has been used [Davis and Kersey, 1995] for simultaneous interrogation of an array of sensor gratings. A Fourier transform spectrometer used in this technique utilised a Michelson interferometer, one arm of which was linearly stretched with a PZT to produce a compound interferogram generated by all of the reflected wavelengths from an array of sensors. Fourier analysis of this interferogram produced the measurand-modulated compound source spectrum, which provided information on values of the wavelength shift for several sensors simultaneously. Resolution of about 12 microstrain has been achieved for three multiplexed sensor gratings having nominal reflection wavelengths of 1539, 1548 and 1551 nm.

An interferometric approach to the sensor wavelength shift detection has been reported by [Song *et al.*, 1997] that uses two concatenated Bragg gratings written onto fibres with different core diameters and a Mach-Zehnder interferometer in order to decouple the influences of strain and temperature measurands. The two in-fibre gratings used within a sensor element have the same values of temperature sensitivity due to the identical properties of the fibre material, but their strain sensitivity figures are different due to the difference in fibre core diameters. The

nominal reflection wavelength for gratings used in the system reported were 1549.3 and 1546.4 nm. A Mach-Zehnder interferometer with one of its arms modulated by a PZT is used to form an interference signal at the photodetector. When a linear length modulation is applied to one of the arms of the Mach-Zehnder interferometer, an interference signal is detected at the output, which is a mixture of two interference signals generated by reflections from the two sensor gratings. The difference in core diameters of the two concatenated grating sensors results in the phase difference of the two signals from gratings subjected to the same measurand. Therefore, the amplitude of this mixture signal depends on the phase difference between the two interference signals, and the amount of sensor wavelength shift can be determined from the amplitude of the interferometer signal. The reported strain resolution for this technique is about 2.6 microstrain within a measurement range corresponding to a reflection wavelength shift of 0.6 nm.

Zhang *et al.* have proposed a method for improving the strain sensing resolution of wavelength-encoded Bragg grating sensors. Since the main limiting factor for the measurement resolution achievable with these sensors is the finite spectral width of the grating peak, it has been suggested that fibre m $\acute{o}$ ire gratings containing very narrow-band (about 0.036 nm FWHM) spectral features can be employed for strain sensors based on the wavelength shift detection. Fibre m $\acute{o}$ ire gratings are grating structures formed within the fibre core by transverse holographic double exposure method and contain a very narrow spectral passband within a relatively narrow (about 0.3 nm FWHM) spectral stopband [Legoubin *et al.*, 1991].

This research project involved the application of fibre Bragg grating technology for the construction of broad bandwidth in-fibre mirrors forming an in-line Fabry-P $\acute{e}$ rot sensor cavity. The method of sensor interrogation used for the construction of the strain monitoring system in this project is based on the principle of white-light interferometry and does not directly involve the measurement of strain-induced Bragg wavelength shift. However, the mode of operation of this new sensor system can be potentially extended to include measurements with a Bragg grating reference sensor (or an array of grating sensors) illuminated by the same compound optical source. This additional reference sensor can be positioned in the unused arm of the sensor element coupler of the white-light system, in parallel with the Fabry-P $\acute{e}$ rot sensor cavity. This additional grating sensor can be protected from the influence of strain to provide information on the variations in ambient temperature.

Therefore, fibre Bragg grating technology offers unique advantages for optical fibre sensing applications and opens up numerous possibilities for the construction of multi-parameter fibre sensors based on a wide variety of sensor interrogation schemes. Bragg gratings have proved to be one of the most versatile optical fibre components currently used in the construction of sensing systems.

The white-light interferometric strain monitoring system developed during this project employs broad reflection bandwidth mirrors provided by sets of superimposed chirped gratings. The strain measurand can be arranged to either affect all of the Fabry-Pérot cavity length or only its part in between the grating mirrors. The difference between these two cases is that the cavity mirrors of the sensor element can be subjected to both strain and temperature variations, or to variations in temperature only. The slight measurand-induced variations in the central wavelength (and the shape of reflected spectrum) of the grating mirrors did not significantly affect the measurements since the spectral bandwidths of the low-coherence sources used for illuminating the system largely exceed the spectral bandwidths of the Fabry-Pérot reflectors. The response of the strain monitoring system to these measurand-induced variations in the properties of the Fabry-Pérot sensor element will be described in detail and backed with experimental data in the subsequent chapters of this thesis.

## **2.4 Sensors utilising in-line and extrinsic Fabry-Pérot interferometers.**

Numerous sensor configurations have been reported to date that utilise both extrinsic and intrinsic-type Fabry-Pérot interferometers [Lee and Taylor, 1995]. The extensive research interest in Fabry-Pérot sensors is due to their properties of robustness and versatility. The in-line Fabry-Pérot is a device that operates as a fibre-optic analogue of a classical bulk-optic Fabry-Pérot étalon. It can be utilised as an intrinsic sensor or as a device suitable for use in quasi-distributed systems [Grattan and Sun, 2000]. A fibre Fabry-Pérot can be produced, for example, by fusion splicing the end-coated fibres to form the interferometer [Lee and Taylor, 1988]. However, in order to fabricate an in-line Fabry-Pérot interferometer capable of withstanding higher levels of tensile strain, Bragg grating technology is preferable for the inscription of in-fibre mirrors [Kaddu, 1997]. Up to now, the in-fibre reflectors formed by Bragg gratings provide the most robust intrinsic fibre Fabry-Pérot, capable of withstanding levels of tensile strain of at least 12000 microstrain [Kaddu, 1995].

Among the sensor systems utilising Fabry-Pérot interferometers, of particular interest are sensors that employ an in-line Fabry-Pérot etalon [Singh and Sirkis, 1996, Jin and Sirkis, 1997] for simultaneous measurement of strain and temperature, and in-fibre Fabry-Pérots based on Bragg gratings [Kaddu, 1997] for the measurement of strain and temperature. The use of an extrinsic Fabry-Pérot sensor in combination with a fibre Bragg grating sensor has also been reported as a solution of the strain-temperature cross-sensitivity problem [Liu *et al.*, 1997].

Extrinsic fibre Fabry-Pérot interferometers can be formed by the air gap between two uncoated fibre faces in an arrangement where the fibres may be held using glue or epoxy resin, or positioned inside an outer alignment tube. These systems are used extensively for strain monitoring [Murphy, 1992]. Several electronic "read-out" techniques have been developed to overcome the ambiguity problem related to a cosine sensor response. Sensor interrogation schemes used for this type of extrinsic fibre Fabry-Pérots are based on the fringe counting technique and do not allow absolute measurements. Bhatia *et al.* reported the use of an absolute extrinsic Fabry-Pérot interferometer, in which the full reflectance spectrum of the sensor is analysed to determine the optical path difference [Bhatia *et al.*, 1994], and thus the measurand value. [Sirkis *et al.*, 1995] reported the development of an in-line fibre etalon made by fusion-splicing of the two fibres to a section of a hollow-core fibre of the same outside diameter. [Liu *et al.*, 1998] have reported sensors of an extrinsic Fabry-Pérot type for strain and temperature monitoring in concrete and composites.

## **2.5 Strain and temperature responses of a fibre Fabry-Pérot cavity.**

The operation of fibre Fabry-Pérot sensors is based on the effect of sensitivity of the optical length of the sensor cavity to external measurands. When illuminated with a low-coherence source, the Fabry-Pérot cavity acts as a two-beam interferometer with the optical length of one of its arms being modulated by the measurand. When a Fabry-Pérot is operated in reflection mode, this implies that the propagation time delay difference between the waves reflected from the front and the rear cavity mirrors is dependent on strain and temperature distribution along the sensing element. Changes in the optical length of the sensor cavity occur due to the measurand-induced variations in both the physical length and the effective core refractive index of the fibre section between the two Fabry-Pérot reflectors. We will consider the effects of strain and temperature measurands on the round-trip phase retardance of a guided fibre mode propagating through a Fabry-Pérot sensor cavity.

## The effect of axial tensile strain.

A light wave of a guided fibre mode propagating through a fibre Fabry-Pérot of length  $l$  and experiencing a single round trip acquires a phase delay with respect to the wave reflected by the front mirror of the cavity. This phase delay  $\varphi$  can be expressed as

$$\varphi = 2\beta l = \frac{4\pi n l}{\lambda}, \quad (2.10)$$

where  $\beta$  is the propagation constant of the mode,  $n$  is the effective refractive index of the fibre core and  $\lambda$  is the wavelength of light in vacuum. By differentiating equation (2.10), we can obtain an equation for the measurand-induced variation in the value of phase delay  $\varphi$ .

$$\Delta\varphi = 2(\beta\Delta l + l\Delta\beta), \quad (2.11)$$

where the first term accounts for the physical elongation of the fibre section under strain and the second term describes the phase effect of the variation in the propagation constant. The propagation constant  $\beta$  is affected by the applied strain in two ways, firstly through a stress-induced change in the effective refractive index of fibre, and secondly due to a variation in the fibre core radius  $r_{co}$ . The latter is caused by the induced lateral component of strain that is opposite in sign to the axial strain (Poisson's effect).

Consider a constant axial strain  $\varepsilon$  affecting a segment of length  $L_\varepsilon \leq l$  of the fibre Fabry-Pérot cavity. An induced change in the round-trip phase delay can be obtained from (2.11) and is represented by the relationship [Butter and Hocker, 1978]

$$\Delta\varphi = \frac{4\pi n L_\varepsilon}{\lambda} \left\{ \varepsilon + \frac{l}{n} \frac{\partial n}{\partial V} \frac{\partial V}{\partial r_{co}} \Delta r_{co} + \frac{l}{n} (\Delta n)_\varepsilon \right\}, \quad (2.12)$$

where  $V = (2\pi r_{co}/\lambda) (n_{co}^2 - n_{cl}^2)^{1/2}$  is the normalised frequency of the fibre with radius  $r_{co}$ , core and cladding refractive indices  $n_{co}$  and  $n_{cl}$  respectively, and  $(\Delta n)_\varepsilon$  is the elasto-optic change in the effective refractive index of the fibre core. In this equation, the first term represents the effect of physical elongation of fibre length  $L_\varepsilon$ , which usually is the dominant component of the total strain-induced phase change. The second term describes the contribution of waveguide dispersion (variations in the waveguide properties of fibre caused by a change in core radius) to

the total change in the core refractive index. The third term in (2.12) describes the elasto-optic component of the total change in the core refractive index.

Assuming that an isotropic and elastic optical fibre is oriented along the z-axis of a cartesian coordinate system and is subjected to a longitudinal tensile strain  $\varepsilon_z$ , we can apply elastic theory to describe all components of the resultant strain in the fibre (in a first order approximation) [Measures, 1992]. From (2.8), the total strain in the stretched fibre section is represented by the vector

$$\bar{\varepsilon} = \begin{bmatrix} -\mu\varepsilon_z \\ -\mu\varepsilon_z \\ \varepsilon_z \\ 0 \\ 0 \\ 0 \end{bmatrix}, \quad (2.13)$$

where  $\mu$  is the Poisson's ratio of the fibre core material and  $(-\mu\varepsilon_z)$  represents the value of the induced transverse strain. All shear strain components are zero since only the axial component of stress is present. From (2.13), the change in the fibre core radius is therefore

$$\Delta r_{co} = -\mu\varepsilon r_{co}, \quad (2.14)$$

so that equation (2.12) can be rewritten in the following way:

$$\Delta\varphi = \frac{4\pi n L \varepsilon}{\lambda} \left\{ \varepsilon(1 - \mu\chi_{co}) + \frac{1}{n}(\Delta n)_\varepsilon \right\}, \quad (2.15)$$

$$\text{where } \chi_{co} = \frac{r_{co}}{n} \frac{\partial n}{\partial V} \frac{\partial V}{\partial r_{co}}$$

is a parameter describing the effect of waveguide dispersion. This parameter can be determined from the normalised propagation constant  $b$  and normalised frequency  $V$  [Jeunhomme, 1990].

$$\chi_{co} = \frac{r_{co}}{n} \frac{\partial n}{\partial V} \frac{\partial V}{\partial r_{co}} = \frac{r_{co}}{n} \frac{\partial n}{\partial b} \frac{\partial b}{\partial V} \frac{\partial V}{\partial r_{co}} = \frac{V(n_{co}^2 - n_{cl}^2)}{2n^2} \frac{\partial b}{\partial V}, \quad \text{where} \quad (2.16)$$

$$b = \frac{n^2 - n_{co}^2}{n_{co}^2 - n_{cl}^2}.$$

For a weakly-guiding single mode fibre, the values of core and cladding refractive indices differ only slightly, so that  $(n_{co} - n_{cl})/n \approx 0.01$ . At around the single-mode cut-off, the value of normalised frequency is  $V \approx 2.405$ , and the partial derivative in (2.16) has a typical value of  $\partial b/\partial V \approx 0.5$  [Snyder & Love, 1983]. By substituting these values into (2.16), the waveguide dispersion parameter is found to have value of about  $\chi_{co} \approx 10^{-4}$ . This means that the fibre radius change has a practically negligible effect on the total stress-induced round-trip phase change  $\Delta\varphi$ .

The stress-optic contribution  $(\Delta n)_e$  to the total change in the effective core refractive index can be evaluated with elasto-optic theory that describes the stress-induced changes in the optical indicatrix tensor  $\left[\left(\frac{I}{n^2}\right)_i\right]$ . We will assume that the stress-optic changes in the effective core refractive index follow the changes in the refractive index of the core and cladding regions, since  $n_{co} \approx n_{cl}$  [Butter & Hocker, 1978]. The stress-optic variations in the optical indicatrix are represented by the tensor  $\mathbf{B} = \left[\Delta\left(\frac{I}{n^2}\right)_i\right]$ , the components of which are dependent on applied strain according to the relationship

$$B_i = p_{ij} \varepsilon_j, \quad (2.17)$$

where  $p_{ij}$  are the Pockels strain-optic coefficients (the components of the elasto-optic tensor of the medium) and  $\varepsilon_j$  are the components of strain vector defined in (2.13). The summation over all values of a repetitive index is assumed in this formula (Einstein's convention). Since fused silica fibre can be regarded as an isotropic medium, its elasto-optic tensor has the following form:

$$\bar{P} = [p_{ij}] = \begin{bmatrix} p_{11} & p_{12} & p_{12} & 0 & 0 & 0 \\ p_{12} & p_{11} & p_{12} & 0 & 0 & 0 \\ p_{12} & p_{12} & p_{11} & 0 & 0 & 0 \\ 0 & 0 & 0 & \frac{p_{11} - p_{12}}{2} & 0 & 0 \\ 0 & 0 & 0 & 0 & \frac{p_{11} - p_{12}}{2} & 0 \\ 0 & 0 & 0 & 0 & 0 & \frac{p_{11} - p_{12}}{2} \end{bmatrix}, \quad (2.18)$$

with two strain-optic Pockels coefficients  $p_{11}$  and  $p_{12}$  describing the fibre refractive index variations.

Using the relationships (2.17, 2.18), we can now derive all components of the strain-induced changes in the effective core refractive index and evaluate the stress-optic contribution to the cavity round-trip phase change. The variations in the components of tensor  $\mathbf{B}$  that are orthogonal to the fibre axis are given by

$$B_x = B_y = \varepsilon(p_{12} - \mu(p_{11} + p_{12})), \quad (2.19)$$

where  $\varepsilon = \varepsilon_z$  is the axial strain. Therefore, the elasto-optic change in the effective core refractive index in the direction perpendicular to axial strain is

$$(\Delta n)_\varepsilon = -\frac{n^3}{2} \Delta \left( \frac{1}{n^2} \right) = -\frac{n^3}{2} \varepsilon [p_{12} - \mu(p_{11} + p_{12})]. \quad (2.20)$$

Equation (2.20) allows simplification of relationship (2.15) for the strain-induced round-trip phase change and to obtain the following expression for the phase shift per unit strain (neglecting the waveguide dispersion effect):

$$\frac{\Delta \varphi}{\varepsilon} \cong \frac{4\pi n L_\varepsilon}{\lambda} \left\{ 1 - \frac{n^2}{2} (p_{12} - \mu(p_{11} + p_{12})) \right\}. \quad (2.21)$$

This equation (2.21) shows that the phase sensitivity of a fibre Fabry-Pérot cavity to applied axial strain is directly proportional to the length of cavity section under strain. This equation can be normalised with respect to the phase change acquired on round-trip propagation through the sensing length  $L_\varepsilon$  in order to derive an expression for the fractional round-trip phase shift per unit strain (phase sensitivity relationship that is independent of the sensing length). The resultant expression for the normalised phase-strain sensitivity of a fibre Fabry-Pérot cavity is given by

$$\frac{\Delta \varphi_\varepsilon}{\varphi_\varepsilon \varepsilon} \cong 1 - \frac{n^2}{2} [p_{12} - \mu(p_{11} + p_{12})] \quad (2.22)$$

Using the published data for the silica-based optical fibre parameters [Bertholds and Dändliker, 1988] we now can quantify the sensitivity of a fibre Fabry-Pérot cavity to applied strain and

obtain a value for the fractional round-trip phase shift per unit strain. By using values of  $n = 1.46$ ,  $\mu = 0.16$ ,  $p_{11} = 0.113$ , and  $p_{12} = 0.252$ , we obtain  $\Delta\phi_\varepsilon/(\phi_\varepsilon\varepsilon) \approx 0.80$ . This figure can be called the optical gauge factor for the strain sensitivity of a fibre Fabry-Pérot.

### Thermal response of a fibre Fabry-Pérot.

A fibre Fabry-Pérot cavity possesses sensitivity to variations in the ambient temperature, and so it is necessary to account for temperature-induced phase shifts during strain measurement. Alternatively, the thermal response property of a fibre Fabry-Pérot can be utilised for temperature measurement in cases when an interferometer is isolated from strain effects.

This temperature sensitivity originates from thermal dependencies of the effective core refractive index and fibre cavity length, resulting in changes to the cavity round-trip phase. The thermal response of the cavity can be characterised by the fractional phase shift per unit temperature change similarly to the characterisation of the strain response.

If a fraction  $L_T$  of the Fabry-Pérot cavity length is subjected to a temperature variation  $\Delta T$  and the fibre is able to expand thermally, the resultant variation in the round-trip phase can be obtained by differentiating equation (2.10):

$$\frac{d\phi}{dT} = \frac{4\pi}{\lambda} \frac{d(nl)}{dT} = \frac{4\pi}{\lambda} \left\{ \frac{\partial(nL_T)}{\partial n} \frac{dn}{dT} + \frac{\partial(nL_T)}{\partial L_T} \frac{dL_T}{dT} \right\} \quad (2.23)$$

Considering finite temperature changes and neglecting the waveguide effect of a change in fibre radius caused by the thermally-induced strain, the fractional phase shift per unit temperature change (for one-way propagation in fibre) can be expressed by [Lagakos *et al.*, 1981]:

$$\frac{\Delta\phi_T}{\phi_T\Delta T} = \frac{\Delta L_T}{L_T\Delta T} + \frac{\Delta n}{n\Delta T} = \alpha + \frac{1}{n} \frac{\Delta n}{\Delta T} \cong \alpha + \frac{1}{n} \frac{dn}{dT}, \quad (2.24)$$

where  $\alpha$  is the coefficient of linear thermal expansion of optical fibre ( $\alpha = 5.5 \times 10^{-7} \text{ }^\circ\text{C}^{-1}$  for silica-based fibre [Lagakos *et al.*, 1981]) and  $dn/dT$  is the thermo-optic coefficient ( $dn/dT = 10.93 \times 10^{-6} \text{ }^\circ\text{C}^{-1}$  for bulk silica at a wavelength of  $1 \text{ } \mu\text{m}$  [Barlow and Payne, 1983]).

Equation (2.24) provides a means for the characterisation of the Fabry-Pérot thermal response independently of the length of the sensing element. The sensitivity of round-trip phase to temperature depends on the wavelength of light due to dispersion of the effective refractive index and on the glass composition (as is the case for the strain sensitivity). Using the published data on the bulk-optic fused silica parameters, the value of the fractional cavity round-trip phase shift per unit temperature change can be calculated to be about  $\Delta\phi_r/(\phi_r\Delta T) \approx 1.6 \times 10^{-5} \text{ }^\circ\text{C}^{-1}$  for wavelengths near 780 nm. The contribution of the thermo-optic refractive index change is dominant for this effect of phase-temperature sensitivity.

## 2.6 Fabry-Pérot sensing elements in low coherence interferometry.

The construction of a fibre-optic low-coherence strain sensor can be made much more robust by using in-fibre Fabry-Pérot grating reflectors as a sensing element. Wavelength-selective reflection at an optical fibre Bragg grating normally has a narrow reflection bandwidth, and hence it is difficult to construct a broad reflection bandwidth in-fibre Fabry-Pérot cavity to be employed as a sensing interferometer in a WLI scheme. If a number of closely spaced Bragg gratings are written with equal spacing onto a single section of fibre and these Bragg grating pairs reflect incident light at different wavelengths, such a configuration will be equivalent to a set of in-fibre Fabry-Pérot interferometers. If operated with a suitable source (or multiple sources) emitting at all Bragg wavelengths, such an arrangement is equivalent to a compound source with broadband reflectors. Such a sensor can offer superior properties of high accuracy and repeatability of measurements provided that the sensor parameters are chosen correctly. The set of in-fibre Bragg gratings will act as a set of Fabry-Pérot interferometers [Kaddu *et al.*, 1997] and the structure of the interference pattern at the output of the receiver interferometer will be determined by the number of Bragg grating reflectors and by the values of reflected wavelengths and reflection bandwidths.

In-fibre Bragg grating reflectors with broad reflection bandwidths are difficult to make, and this problem is usually overcome by fabricating so-called chirped gratings when the periodicity of the refractive index modulation is varied over the length of a grating. Several methods of producing chirped gratings in optical fibres have been reported and these are reviewed in detail in chapter 4 of this thesis. During the course of this study, a novel technique for economically-efficient production of wavelength-tunable broad reflection bandwidth chirped gratings was developed [Garchev *et al.*, 1998]. This technique has been utilised for the production of in-line sensor Fabry-Pérot elements made of sets of colocated superimposed chirped reflectors written

at a set of central wavelengths pre-optimised for use in the low-coherence system. It was necessary to superimpose several chirped gratings for producing the suitable reflectors at each of the three source wavelengths in order to achieve the desired spectral properties of the sensing element.

## Theoretical analysis of low coherence optical fibre sensing systems

### 3.1 Introduction.

This chapter analyses the principal aspects of optical fibre low-coherence interferometry and provides a theoretical characterisation of the measurement systems developed during this study. The theory background for the chosen system configuration and signal processing methodology is given. The predicted performance characteristics and system limitations are analysed in the context of physical principles on which the operation of white-light interferometers relies. Particular attention is devoted to the characteristics of the sensing element consisting of an in-fibre Fabry-Pérot cavity formed by sets of chirped Bragg gratings. The characteristics and potential of this type of sensing systems are considered in the overall context of the low coherence sensor interrogation technique.

### 3.1.1 The principle of low-coherence interferometry.

The principle of low-coherence sensing technique is based on the fact that when an interferometer is illuminated by a broad linewidth optical source, the interference effects at the output of an interferometer are only observed when the optical path differences within the measurement system are well balanced. This approach to interferometric measurement is an alternative to conventional high-coherence laser interferometry since it involves measuring both the output signal phase and visibility, and which solves the problem of limited unambiguous measurement range and achieves high-precision absolute measurement of a wide range of parameters.

A schematic diagram of a fibre optic interferometric sensing system employing white-light interferometry (WLI) is shown in Figure 3.1. The overall system configuration shown in this figure represents the features of the fibre Fabry-Pérot strain sensor developed during this project. A more detailed system diagram of this sensor system is presented in Chapter 5.

A white-light measurement system is composed of two two-beam fibre interferometers linked in series forming the so-called “tandem” interferometer arrangement. This configuration employing a series combination of two interferometric sub-systems leads to elimination of the effects of lead sensitivity in the sensor interferometer. The phase and visibility parameters of the optical output signal are only sensitive to the variations in the optical path length within the sensor element. In principle, both sensor and receiver interferometers can have a variety of configurations and can be of a Fabry-Pérot, Mach-Zehnder, or a Michelson type.

A low-coherence source is used to illuminate the first interferometer, termed the sensor interferometer, since it is placed inside the measurand field and the optical path difference between its arms is directly affected by the measurand of interest. The optical path difference generated by the sensor interferometer is arranged to exceed at all times the value of the coherence length of an optical source in order to prevent any interference effects from occurring at the output of this sensor interferometer. The output of the sensor interferometer is linked via the optical fibre to the local receiver interferometer that is placed in a controlled environment outside the measurand field.

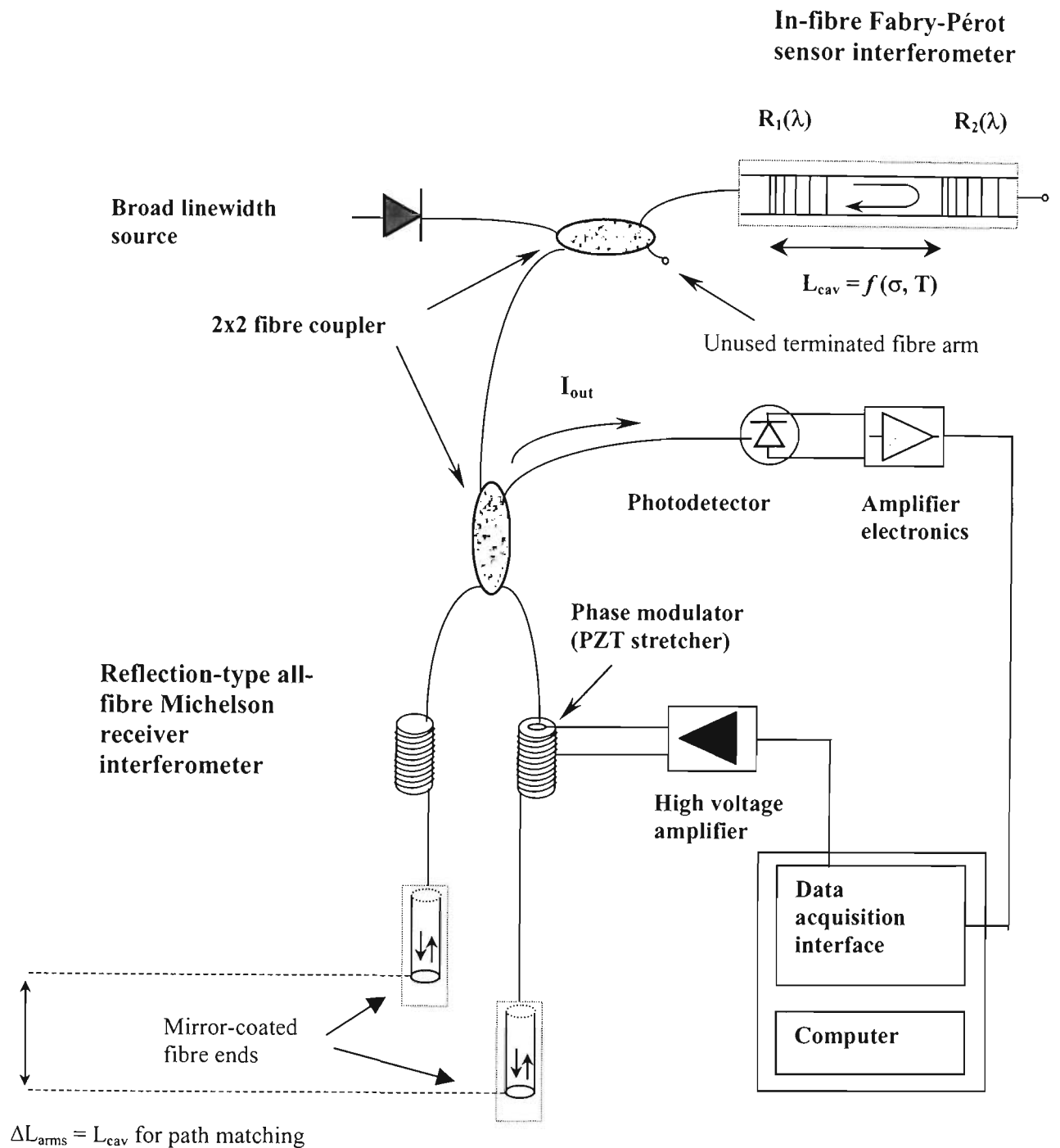


**Figure 3.1** Configuration of an all-fibre sensor system utilising a tandem interferometer arrangement.

The optical path difference between the arms of the receiver interferometer (RI) can be adjusted to match that of the sensor interferometer, so that the beams, initially separated in the sensor interferometer, are brought back into temporal coherence at the output of the system. Under the condition when the differential optical path imbalance between the two interferometers is within the coherence length of the source, a white-light interference fringe pattern is observed at the output of the receiver interferometer. The position of zero optical path imbalance of the system of two interferometers is a unique point in the interference pattern, where every spectral

component of light emitted by the source is added in phase, producing the point of maximum visibility. The absolute measurement of the optical path difference introduced by the sensor interferometer is achieved by scanning the optical path difference in the receiver interferometer until the position of the zero path imbalance point is reached and identified. Any measurand-induced change in the optical path difference (OPD) within the sensor interferometer will produce a change in the phase and visibility of the output signal resulting from the shift in the position of fringes within the output white-light interference pattern. Therefore, the effect of a measurand on the sensor's OPD can be sensed by determining the new position of the zero optical path imbalance point, which is done by scanning the OPD of the receiver interferometer. It can be seen from the operating principle of low-coherence interferometry that this technique can be applied to measurement of any physical parameter that affects the OPD in the sensor interferometer, including all parameters that are convertible into displacement.

### **3.2 White-light interferometer transfer function.**

In order to find the transfer function of a low-coherence tandem interferometer, we will consider a system in which the sensor interferometer is a reflection-type fibre Fabry-Pérot and the receiver interferometer is of Michelson type as shown in Figure 3.1. The two fibre interferometers are illuminated by a broad bandwidth source and are linked in series using four-port fibre couplers. The state of polarisation of the guided beam in the fibre is assumed to remain constant, and therefore all electric fields and amplitude coupling coefficients of fibre couplers can be treated as scalar quantities. We will denote the source electric field amplitude in the input arm of the sensor coupler  $E_0(0)$ . The electric field amplitude coupling coefficients of the two couplers are denoted as  $k_{ij}$  where the first index is the coupler number and the second index describes the directionality of coupling. We will choose  $i = 1$  for the sensor coupler,  $i = 2$  for the receiver coupler,  $j = 1$  for coupling in the straight-through direction and  $j = 2$  for the coupling into the diagonal opposite arm. The amplitude reflection and transmission coefficients of the Fabry-Pérot sensor cavity reflectors are  $r_1$ ,  $t_1$ ,  $r_2$  and  $t_2$  where indices relate to the reflector number starting from the light input end of the cavity. The light losses within all couplers and fibre links will be neglected and in addition we will assume a 100% reflection in both arms of the Michelson-type receiver interferometer.

The electric field of the light wave incident on a detector at the output of the receiver interferometer is given by [Culshaw and Dakin, 1989]

$$E = E_{11} + E_{12} + E_{21} + E_{22}, \quad (3.1)$$

where  $E_{ij}$  is the component of the total output electric field arising from light reflected by mirror  $i$  of the sensor cavity and propagated through arm  $j$  of the receiver interferometer. The values of these components of the total field are:

$$\begin{aligned} E_{11} &= E_0(\tau_{11}) k_{11} k_{12} k_{21} k_{22} r_1 \exp(i\omega \tau_{11}) = E_0(\tau_{11}) k r_1 \exp(i\omega \tau_{11}), \\ E_{12} &= E_0(\tau_{12}) k r_1 \exp(i\omega \tau_{12}), \\ E_{21} &= E_0(\tau_{21}) k t_1^2 r_2 \exp(i\omega \tau_{21}), \\ E_{22} &= E_0(\tau_{22}) k t_1^2 r_2 \exp(i\omega \tau_{22}), \end{aligned} \quad (3.2)$$

where  $k$  is the product of four amplitude coupling coefficients,  $\omega$  is the central frequency of the optical source and  $\tau_{ij}$  are the propagation delay times of the corresponding fields  $E_{ij}$ . The optical intensity  $I$  observed at the output of the receiver interferometer is a time average of the product of the total output electric field and its complex conjugate as represented by equation:

$$I = \left\langle (E_{11} + E_{12} + E_{21} + E_{22})(E_{11} + E_{12} + E_{21} + E_{22})^* \right\rangle. \quad (3.3)$$

Noting that a complex conjugate of a sum of terms equals the sum of complex conjugates and replacing a time average of a sum with the sum of time averages, we can rearrange the relationship (3.3) into the form

$$\begin{aligned} I &= \langle E_{11} E_{11}^* \rangle + \langle E_{12} E_{12}^* \rangle + \langle E_{21} E_{21}^* \rangle + \langle E_{22} E_{22}^* \rangle + \\ &\langle E_{12} E_{11}^* \rangle + \langle E_{21} E_{11}^* \rangle + \langle E_{22} E_{11}^* \rangle + \langle E_{11} E_{12}^* \rangle + \\ &\langle E_{21} E_{12}^* \rangle + \langle E_{22} E_{12}^* \rangle + \langle E_{11} E_{21}^* \rangle + \langle E_{12} E_{21}^* \rangle + \\ &\langle E_{22} E_{21}^* \rangle + \langle E_{11} E_{22}^* \rangle + \langle E_{12} E_{22}^* \rangle + \langle E_{21} E_{22}^* \rangle. \end{aligned} \quad (3.4)$$

The sum of the first four terms in (3.4) represents the total optical power at the output of the system, and each of the terms  $\langle E_{ij} E_{ij}^* \rangle$  stands for the fraction of the total optical power at the detector delivered by the wave propagating through arm  $i$  of the sensor interferometer and arm  $j$  of the receiver interferometer. The terms in equation (3.4) are evaluated using the definition of normalised source autocorrelation function (degree of coherence) [Born and Wolf, 1980]:

$$\gamma(\tau) = \frac{\langle E_0(t)E_0^*(t-\tau) \rangle}{\langle E_0(t)E_0^*(t) \rangle} = \frac{\langle E_0(t)E_0^*(t-\tau) \rangle}{I_0(t)}, \quad (3.5)$$

where  $I_0(t)$  stands for the source intensity at time  $t$ . We will consider the source intensity value to be stationary and will denote it  $I_0$ . The definition of  $\gamma(\tau)$  in (3.5) as a correlation between the two samples of a wave is equivalent (through the Wiener-Khinchine theorem) to the representation based on the Fourier transform of the source power spectrum  $I(\omega)$  [Guenther, 1990]

$$\gamma(\tau) = \frac{\int_{-\infty}^{\infty} I(\omega) e^{-i\omega\tau} d\omega}{\int_{-\infty}^{\infty} I(\omega) d\omega} \quad (3.6)$$

We will now evaluate all of the terms in (3.4) by using equations (3.2), starting from the constant intensity terms:

$$\begin{aligned} \langle E_{11}E_{11}^* \rangle &= k^2 r_1^2 \langle E_0^2(\tau_{11}) \rangle = KR_1 I_0, \\ \langle E_{12}E_{12}^* \rangle &= k^2 r_1^2 \langle E_0^2(\tau_{12}) \rangle = KR_1 I_0, \\ \langle E_{21}E_{21}^* \rangle &= k^2 t_1^4 r_2^2 \langle E_0^2(\tau_{21}) \rangle = K(1-R_1)^2 R_2 I_0, \\ \langle E_{22}E_{22}^* \rangle &= k^2 t_1^4 r_2^2 \langle E_0^2(\tau_{22}) \rangle = K(1-R_1)^2 R_2 I_0, \end{aligned} \quad (3.7)$$

where  $K$  is the product of four coupler power-splitting ratios,  $R_1$  and  $R_2$  are power reflectivities of the sensor cavity reflectors, and the relationship  $R_1 + T_1 = 1$  between the power reflection and transmission coefficients is accounted for.

Other terms in (3.4) are interference terms since they are propagation delay-dependent and include products of electric fields that have propagated through unequal optical paths in the system. At this stage, we will introduce the values of propagation time delays in the sensor interferometer and in the receiver interferometer  $\tau_{SI}$  and  $\tau_{RI}$ :

$$\begin{aligned} \tau_{SI} &= \tau_{11} - \tau_{21} = \tau_{12} - \tau_{22}, \\ \tau_{RI} &= \tau_{11} - \tau_{12} = \tau_{21} - \tau_{22}. \end{aligned} \quad (3.8)$$

The value of  $\tau_{SI}$  is negative according to our choice of arms numbering, and the value of  $\tau_{RI}$  can be negative, positive or zero depending on the physical arms length difference in the receiver interferometer.

By also noting that

$$\begin{aligned}\tau_{SI} - \tau_{RI} &= \tau_{I2} - \tau_{2I}, \\ \tau_{SI} + \tau_{RI} &= \tau_{I1} - \tau_{22},\end{aligned}\tag{3.9}$$

we now can analyse all terms in equation (3.4) in detail:

$$\begin{aligned}I &= 2I_0K\{R_1 + (1 - R_1)^2 R_2\} + KR_1I_0|\gamma(\tau_{RI})|\exp(-i\omega\tau_{RI}) + \\ &K(1 - R_1)\sqrt{R_1R_2}I_0|\gamma(\tau_{SI})|\exp(-i\omega\tau_{SI}) + K(1 - R_1)\sqrt{R_1R_2}I_0|\gamma(\tau_{SI} + \tau_{RI})|\exp[-i\omega(\tau_{SI} + \tau_{RI})] + \\ &KR_1I_0|\gamma(\tau_{RI})|\exp(i\omega\tau_{RI}) + K(1 - R_1)\sqrt{R_1R_2}I_0|\gamma(\tau_{SI} - \tau_{RI})|\exp[-i\omega(\tau_{SI} - \tau_{RI})] + \\ &K(1 - R_1)\sqrt{R_1R_2}I_0|\gamma(\tau_{SI})|\exp(-i\omega\tau_{SI}) + K(1 - R_1)\sqrt{R_1R_2}I_0|\gamma(\tau_{SI})|\exp(i\omega\tau_{SI}) + \\ &K(1 - R_1)\sqrt{R_1R_2}I_0|\gamma(\tau_{SI} - \tau_{RI})|\exp[i\omega(\tau_{SI} - \tau_{RI})] + K(1 - R_1)^2 R_2I_0|\gamma(\tau_{RI})|\exp(-i\omega\tau_{RI}) + \\ &K(1 - R_1)\sqrt{R_1R_2}I_0|\gamma(\tau_{SI} + \tau_{RI})|\exp[i\omega(\tau_{SI} + \tau_{RI})] + K(1 - R_1)\sqrt{R_1R_2}I_0|\gamma(\tau_{SI})|\exp(i\omega\tau_{SI}) + \\ &K(1 - R_1)^2 R_2I_0|\gamma(\tau_{RI})|\exp(i\omega\tau_{RI}).\end{aligned}$$

Since the normalised source autocorrelation function  $\gamma(\tau)$  can be related to the coherence time  $\tau_c$  of emitted radiation via the following relationship [Born and Wolf, 1980]

$$\gamma(\tau) = \exp(-|\tau|/\tau_c),\tag{3.10}$$

the interference at the output of this tandem interferometer arrangement is only observed when at least one of the following conditions is satisfied:

$$|\tau_{SI}| \leq \tau_c, \quad |\tau_{RI}| \leq \tau_c, \quad |\tau_{SI} + \tau_{RI}| \leq \tau_c, \quad \text{or} \quad |\tau_{SI} - \tau_{RI}| \leq \tau_c.\tag{3.11}$$

In a white-light interferometer system, the optical path difference in the sensor interferometer is made to be at least several times greater than the coherence length  $L_c$  of the optical source, in order to eliminate all interference effects at the output of the sensor interferometer. For this reason, all terms in the above equation for output intensity containing factors  $\gamma(\tau_{SI})$  are equal to zero. Let us first consider the variation of output optical intensity with the receiver

interferometer time delay  $\tau_{RI}$  for the case when optical paths in the receiver are closely matched, so that  $|\tau_{RI}| \leq \tau_c$ . For this case, we have  $0 \leq |\gamma(\tau_{RI})| \leq 1$ ,  $\gamma(\tau_{SI} - \tau_{RI}) = \gamma(\tau_{SI} + \tau_{RI}) = 0$ , and

$$I = I_{det} \left( 1 + |\gamma(\tau_{RI})| \cos(\omega\tau_{RI}) \right), \quad (3.12)$$

where  $I_{det} = 2I_0K(R_I + (1-R_I)^2R_2)$  is the total optical power arriving at the detector.

Equation (3.12) shows that if the receiver interferometer is balanced around its own path-matching condition, the set of cosine interference fringes modulated by the source autocorrelation function is produced. The fringes have unity visibility at the point of exact path matching, and the phase of fringes is dependent only on the optical path difference in the receiver interferometer. Therefore, the interference pattern in this case contains no information about the sensor interferometer.

Let us now consider the case when the optical path difference in the receiver interferometer  $X_{RI}$  is adjusted to satisfy one of the two following conditions:

$$|\tau_{SI} - \tau_{RI}| \leq \tau_c, \quad \text{or} \quad (3.13)$$

$$|\tau_{SI} + \tau_{RI}| \leq \tau_c \quad (3.14)$$

Condition (3.13) corresponds to the case when  $\tau_{RI} < 0$  and  $\Delta X = (X_{SI} - X_{RI}) \rightarrow 0$ .

Condition (3.14) is realised when  $\tau_{RI} > 0$  and  $\Delta X \rightarrow 0$ .

Both cases (3.13) and (3.14) represent an unbalanced state of the receiver interferometer adjusted so that the relative optical path mismatch between the sensor and receiver interferometers approaching zero. This can be achieved with either of the arms of the receiver interferometer introducing a greater propagation delay compared to the other arm.

In both cases, the optical path difference in the receiver interferometer is adjusted to match the optical path difference of the sensor interferometer, with the only difference in the choice of arm lengths in the receiver. For our chosen system configuration with a Fabry-Pérot type sensor interferometer and a Michelson-type RI, it is either arm 1 of the RI being shorter or longer than arm 2 by the value of the sensor cavity length. For both of the above situations, the white-light interference pattern is observed and the phase of fringes contains information about the differential optical path mismatch between the sensing and receiving interferometers.

Therefore, the optical path imbalance in the sensor interferometer can be found from measurements of the RI path imbalance and the phase of observed fringes.

We now can simplify the intensity equation for this particular case of interest when one of the conditions (3.13, 3.14) is satisfied and the white-light interference pattern is observed at the output of the system.

$$I = 2I_0K(R_1 + (1 - R_1)^2 R_2) \left[ I + \frac{(1 - R_1)\sqrt{R_1 R_2}}{R_1 + (1 - R_1)^2 R_2} |\gamma(\Delta\tau)| \cos(k\Delta X) \right], \quad (3.15)$$

where  $\Delta\tau$  is the propagation delay difference between the two interferometers,  $k$  is the wavenumber corresponding to the central wavelength of the source radiation, and  $\Delta X = X_{SI} - X_{RI}$  is the value of differential optical path imbalance of the two interferometers.

Using the fringe visibility function  $V(\Delta X)$ , we now can represent the optical intensity at the detector in the form

$$I = I_{det} [I + V(\Delta X) \cos(k\Delta X)], \quad (3.16)$$

where  $I_{det}$  is the total optical power arriving at the detector. The fringe visibility function  $V(\Delta X)$  is determined primarily by the source autocorrelation function that can be found from the Fourier transform of the source emission spectrum  $I(\omega)$ . Assuming a Gaussian spectrum for the low-coherence source as represented by the function

$$I(\omega) = I_0 \exp \left[ - \left( \frac{\omega - \omega_0}{\Delta\omega/2} \right)^2 \right], \quad (3.17)$$

where  $\Delta\omega$  is the spectral width of the source centered at frequency  $\omega_0$  at the level of  $1/e$  of the peak intensity, the Fourier transform of  $I(\omega)$  from (3.17) will then also be a Gaussian function. The normalised source autocorrelation function  $\gamma(\Delta\tau)$  can be represented via the differential value of optical path mismatch  $\Delta X$  and the source coherence length  $L_c$  so that finally for the fringe visibility function we have:

$$V(\Delta X) = \frac{(1 - R_1)\sqrt{R_1 R_2}}{R_1 + (1 - R_1)^2 R_2} \exp\left[-\left(\frac{2\Delta X}{L_c}\right)^2\right]. \quad (3.18)$$

The general character of a white-light interferometer transfer function is shown in Figure 3.2 and is represented by the dependency of the output fringe signal intensity on the optical path difference in the receiver interferometer. The white-light interference pattern observed in the case of path matching between the two interferometers is a cosine fringe pattern modulated by a Gaussian fringe visibility function, and is symmetrical with respect to the position of zero optical path imbalance. The shape of the envelope of the white-light fringe pattern is governed by the Fourier transform of the spectral distribution of the optical source, and the maximum visibility value is determined by the design parameters of the system that are related to the power splitting ratio of the interfering beams. As is seen from (3.18), for our chosen configuration of the system the maximum value of the visibility function depends on the values of reflectance of the sensor Fabry-Pérot cavity mirrors.

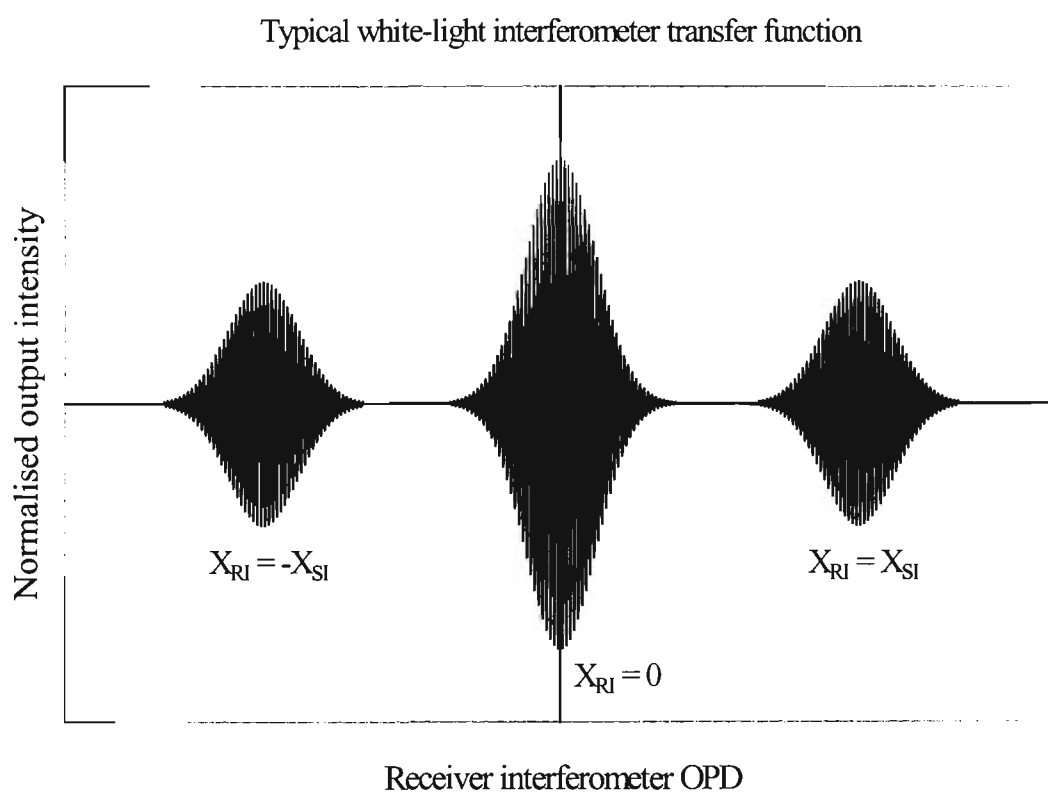


**Figure 3.2** *Transfer function of a WLI system.*

### 3.3 Design considerations for low coherence fibre sensors.

The performance characteristics of low-coherence interferometric sensing systems depend on the configuration of a tandem interferometer arrangement, design parameters of the sensor element and the local receiver interferometer, and on the signal processing method. Several configurations of WLI sensing systems have been reported and shown to be suitable for high-accuracy absolute measurements, both localised and remote [Rao and Jackson, 1996]. The choice of the overall sensor system configuration is application-specific and is governed by the properties of the sensing element, the character of the output interference pattern, the required operating range and the scanning speed of the receiver interferometer.

The choice of an optical source for a white-light sensor is of very high importance because it should satisfy the requirements of low coherence length, high output power and high efficiency of coupling into the fibre. The most commonly used broadband sources in WLI are light-emitting diodes (LEDs), superluminescent diodes (SLDs) and multimode laser diodes [Ning *et al.*, 1989]. LEDs are compact and inexpensive, but their output power is low and coupling efficiency into optical fibres is poor. Multimode laser diodes give a larger output power and offer high coupling efficiency into optical fibres, but their coherence lengths are longer than those of LEDs. Operation of a multimode laser diode in the regime close to the lasing threshold or below threshold can give a good compromise between the requirements of high optical power in the fibre and short coherence length.

In order to match the path imbalances in the sensing and the receiving interferometers, it is necessary to scan the receiving interferometer path imbalance until the interference pattern is produced. Therefore, an accurate and reliable phase modulating system is required in one of the arms of receiving interferometer. The scanning range of this system should be large enough to be able to scan through the whole interference pattern allowing for the accurate central fringe position determination. Piezoelectric transducers (PZT) can be used for fast and accurate scanning of the optical path in one arm of the receiving interferometer. The PZT scanning technique has distinct advantages when compared to the mechanical scanning techniques employing movable mirrors because it does not require moving parts, the signal does not exit the fibre and the scanning time is considerably shortened.

The optical interference signal in the receiver interferometer is converted to an electric signal (AC voltage) using a photodetector. Various types of photodetectors can be used for this purpose and the choice of optimum detecting device is defined by the desired sensitivity and

frequency response. PIN photodiodes are used quite frequently in optical fibre sensing applications due to their low noise levels and high efficiency. Instead of photodiodes, linear CCD arrays are used in the so-called electronically-scanned white-light interferometers [Chen *et al.*, 1990, Koch and Ulrich, 1990, Chen *et al.*, 1991] where it is possible to avoid the use of mechanical and piezoelectrical scanning elements, and such sensing configurations are often advantageous due to their potentially large dynamic range.

In order to simplify the correct determination of central fringe position, several digital signal processing techniques have been developed [Dändliker *et al.*, 1992, Chen *et al.*, 1992a, Rizk *et al.*, 1998]. In cases of high noise levels in the system (for example, caused by environmental perturbations), the central fringe position cannot be identified with enough accuracy by the visibility profile information. This difficulty is overcome by the use of such techniques as “centroid algorithm method” [Chen *et al.*, 1992] where the sampled data from the output interference signal is processed electronically to suppress the influence of noise deviations on the phase resolution and accuracy of the system. The use of digital signal processing can therefore improve the operating characteristics of the sensor and widen its applicability considerably.

One of the objectives of this study has been to develop a low-coherence sensor system providing high-accuracy absolute measurements of strain, temperature and other parameters convertible into displacement, both quasi-static and slowly-varying, suitable for remote monitoring of strain in civil structures and industrial appliances. A particular emphasis was made on the ability to measure and monitor relatively high levels of strain (in the range of up to 12000 microstrain, limited by the breaking strength of sensing elements) with maximum achievable resolution and speed. The desired features of the sensing system have been simplicity, ruggedness and low cost.

The white-light interferometer configuration chosen in accordance with the application requirements is represented by a reflection-type Fabry-Pérot sensor interferometer linked to a Michelson-type receiver interferometer. The ability of this system to monitor high levels of strain is provided by the high tensile strength of the sensing element, since the Fabry-Pérot sensor cavity consists of fibre Bragg gratings. This technology ensures ruggedness of the sensor element since fibres with photoinduced Bragg gratings are capable of withstanding high levels of tensile strain [Kaddu, 1995]. The advantages of using this type of sensor interferometer also include its simplicity, potential low cost, and relative ease of production, together with the ability to manufacture sensors with a wide range of lengths.

In order to provide sufficiently large scanning range within the receiver interferometer and at the same time avoid using moving parts (reflectors external to optical fibre), the Michelson receiver interferometer has two fibre arms with silver-coated cleaved ends and includes a PZT transducer in one of its arms to modulate fibre length. The PZT is a large diameter cylindrical pipe and the number of fibre turns wound around it is made sufficient to provide values of phase modulation that are adequate for the measurement of the desired strain levels. The speed of signal processing in the case of a PZT transducer driven by a waveform from a high voltage amplifier is substantially higher than in the case of using precision-moved external mirrors, and is only limited by the speed of processing fringe data with a computer. The all-fibre system configuration ensures sufficiently high signal-to-noise ratio achievable during measurement, which is limited only by the source powers, light coupling efficiency and the propagation loss within fibre components. This system configuration, together with the advanced signal processing technique based on using optimised multi-wavelength source combinations will be shown in chapters 5 and 6 to have potential for high-accuracy absolute measurement of strain required for a range of industrial applications. An all-fibre white-light interferometer system using a triple combination source developed during this study is presented in Chapter 5.

### **3.4 Advantages and problems of WLI.**

As is the case with any measurement technique, white-light interferometry possesses its own characteristic advantages, drawbacks, and limitations. In this section the unique features, advantages, and problems inherent to optical fibre low-coherence sensing technique are analysed.

#### **3.4.1 Advantages of optical fibre low-coherence sensing.**

Low coherence interferometry possesses several distinct advantages over conventional laser interferometry using highly coherent optical sources. The principal feature of the low-coherence technique is its ability to achieve absolute measurements within a large operating range and with high resolution. Low-coherence interferometry is an alternative to the conventional interferometry that offers a practical solution to the problems of limited unambiguous measurand range (within one wavelength for conventional interferometers) and the identification of the fringe order on initialisation that are not fully solved within conventional interferometry techniques.

The fundamental physical reason for the existence of those problems in high-coherence interferometry is the strictly periodic nature of the output signal (interferogram composed of identical fringes) that introduces uncertainty in phase measurement for any phase shifts exceeding  $2\pi$ . The identification of fringe order in a strictly periodic fringe pattern is difficult, and the reference point for phase measurement is lost when the system is switched off. With low-coherence systems, both of the above problems can be solved since the measurements of both fringe phase and visibility are made, and the centre of the white-light fringe pattern serves as a unique reference point that provides the ability to perform absolute measurements. In this case, measurements are not affected by any power failures.

Another important feature of optical fibre low-coherence systems is that the accuracy of phase measurements is practically unaffected by the fluctuations of optical power occurring along the fibre lead connecting the sensor interferometer and the local receiving interferometer [Culshaw and Dakin, 1989].

Due to the extended unambiguous measurand range and the achievable intra-fringe phase resolution, low-coherence interferometers can offer very high range-to-resolution ratio characteristics (of the order of  $10^5:1$  [Rao and Jackson, 1996]).

The next major advantage of white-light interferometry is associated with the relative immunity of the system to the source wavelength fluctuations. The levels of phase noise produced by the temperature-dependent source wavelength instabilities can be in the case of WLI reduced by more than three orders of magnitude when compared to the systems using pseudo-heterodyne single-mode laser diode interferometry [Grattan and Meggitt, 1995].

These features make the low-coherence-based systems very attractive and suitable for a wide variety of practical applications.

### 3.4.2 Technical challenges in optical fibre WLI and ways of improving performance.

The performance characteristics of optical fibre white-light interferometry systems ultimately depend on the system's ability to measure and sense the position of the centre of the central fringe in a white-light interference pattern accurately, reliably and quickly. Whilst the low-coherence sensing scheme possesses a number of unique advantages it also presents a number of specific problems. In order to identify the central fringe in the interference pattern reliably, it must be clearly distinguishable from other neighbouring fringes in the pattern through its larger peak-to-peak intensity value.

One of the principal problems in LCI measurements is due to the fact that the fringe visibility profile function is relatively flat near the centre of the fringe pattern generated by a broadband source. This leads to the possibility of misidentification of the central fringe caused by the presence of optical and electronic noise in the system and by the small value of visibility difference between the central fringe and its nearest neighbours. This problem is particularly important for optical fibre low-coherence sensors since the signal-to-noise ratio values achievable in fibre systems are generally less than those in bulk-optic interferometers.

The latter problem is caused by the following factors: the first is that there is a significant loss in optical power on coupling light into the fibre, and the second is that the availability of broad linewidth light sources suitable for efficient coupling of light into the fibre is limited. This leads to the necessity of developing special signal processing techniques for optical fibre low-coherence interferometers that enable the system to reliably operate in the presence of significant levels of noise. In recent years, a number of signal processing approaches have been developed [Rao and Jackson, 1996, Ning and Grattan, 1998] in order to relax the minimum signal-to-noise requirements for optical fibre WLI systems. There are several groups of techniques developed in order to solve this problem. The first group relates to the methods of producing an improved white-light interference pattern through enhancing the peak-to-peak intensity value of the central fringe by modifying the fringe visibility profile function. The development of the source coherence synthesis technique [Rao *et al.*, 1993, Chen *et al.*, 1993] was one of the most prominent advances in low-coherence interferometry made in recent years. This technique allows substantial reduction of the signal-to-noise ratio values required for the correct identification of the central fringe and therefore it has greatly widened the range of applicability of low-coherence optical fibre interferometers.

The second group of signal processing techniques are data processing methods that allow measurements with enhanced intra-fringe resolution through calculating the position of the centre of the central fringe after the central fringe itself has been identified. These techniques concentrate on the ability to extract the exact position of the path matching point in the interference pattern in the presence of noise with a minimum volume of calculations.

The performance characteristics of low-coherence optical fibre sensors also depend on the ability to perform a scan of the receiver interferometer within the required range of measurand-induced pathlength changes of the sensor. The main characteristics of the receiver interferometer are therefore the accuracy, range, repeatability and speed of scanning. There are several common approaches to the design of receiver interferometers. Among them are configurations with an external precision-moved scanning mirror [Weir *et al.*, 1994, Kaddu *et al.*, 1999] that offer the extended scanning range but involve bulky external elements and reduce the signal-to-noise ratio, and electronically-scanned systems that employ a CCD array for fringe signal detection [Chen *et al.*, 1990, Marshall *et al.*, 1998] that do not include any moving parts but the scanning range and resolution depends in this case on the number of pixels in a CCD array. Other systems including the one developed during this study use a PZT transducer for scanning the receiver interferometer by using phase modulation in one of its arms.

### **3.5 Signal processing techniques in WLI.**

In practical sensing applications of fibre optic low-coherence interferometry, the ability to accurately determine the value of a measurand depends critically on the correct determination of the position of zero optical path imbalance in the transfer function of the system. A variety of signal processing techniques has been developed in recent years in order to solve the problem of reliable identification of the central fringe of the white-light fringe pattern in the presence of optical and electronic noise.

These techniques are aimed at producing an interference pattern in which the central fringe is more pronounced due to its large peak-to-peak intensity and is more clearly distinguishable from neighbouring fringes in the central fringe packet due to the sharpness of the fringe visibility profile. The other component of the fringe signal processing is related to the task of accurate determination of the position of the centre of the central fringe (the unique point of exact path matching) after the central fringe itself has been identified. The most important criteria in the assessment of any WLI signal processing technique are its accuracy, resistance to

noise effects, and the achievable speed of signal processing that is related to the overall volume of calculations necessary to process the fringe data.

### **3.5.1 Source coherence synthesis technique.**

The introduction of the source coherence synthesis technique reported by [Chen *et al.*, 1993] has been one of the most important steps in the development of optical fibre low-coherence interferometry since it has significantly reduced the minimum signal-to-noise ratio requirements for practical measurement systems. This has widened the range of possible applications of the low-coherence sensing scheme.

The principle of the source coherence synthesis technique is based on the fact that when an interferometer is illuminated by a combination source composed of the two (or several) mutually incoherent optical sources of different central wavelengths, the output signal intensity distribution is represented by a sum of intensity distributions produced by each individual source. For sources with identical coherence lengths, this is equivalent to producing a synthetic light source with an autocorrelation function that equals the sum of the autocorrelation functions of individual sources. This intensity summation of the two or several individual fringe patterns leads to the production of a fringe beat pattern at the output of the WLI system. This fringe beating effect imposes modulation on the fringe visibility profile that leads to the spatial extent of a group of fringes inside the central fringe packet becoming effectively shorter with the central fringe becoming more easily identifiable due to increased visibility difference between the central fringe and its neighbours.

This is physically equivalent to producing a synthetic light source with a reduced value of the effective coherence length. The performance of this source autocorrelation function summation method (source coherence synthesis method) is dependent on the values of central wavelengths and coherence lengths of individual optical sources being used and on the number of sources employed. The combinations of sources can be optimised by comparing the fringe visibility profiles calculated from the resulting superposition of interference patterns.

### 3.5.2 Analysis of source synthesis technique and optimisation of central wavelength separation of two sources.

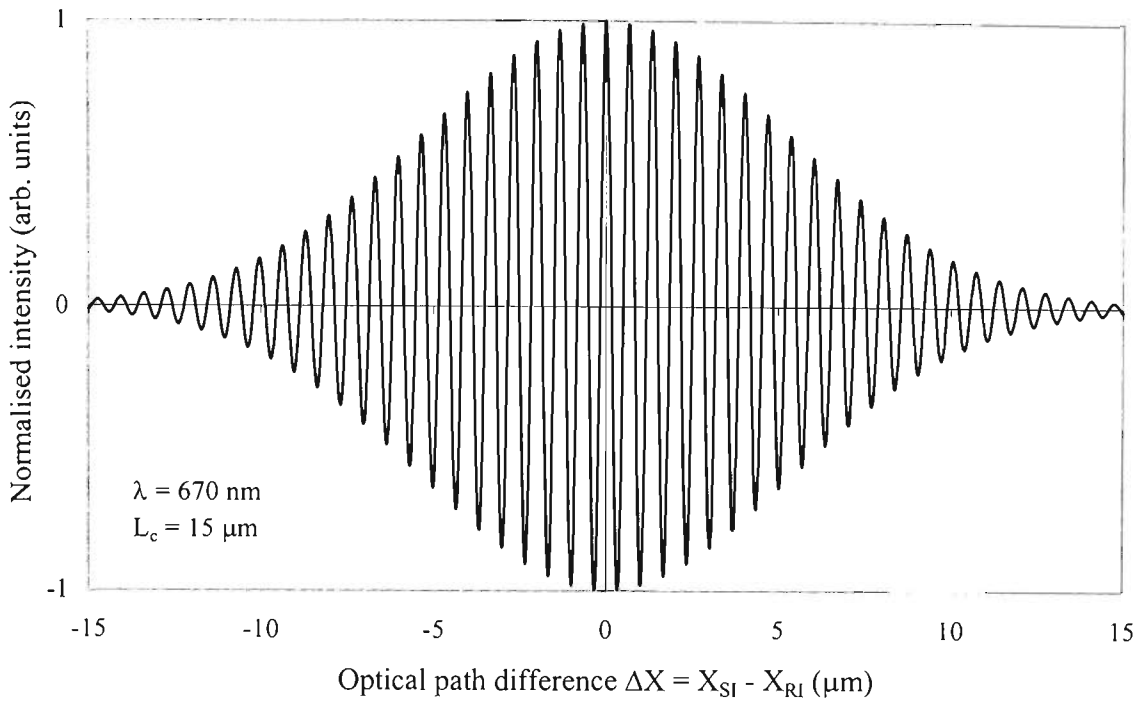
Let us consider the properties of synthesised light sources more in detail. The aim is to derive an expression for the minimum signal-to-noise ratio necessary for the correct identification of central fringe in cases of a single broadband source and a double synthetic source. The results of these calculations will illustrate the advantages associated with the source synthesising technique.

Consider a synthetic source composed of two low-coherence sources with a Gaussian spectral distribution, central wavelengths  $\lambda_1$  and  $\lambda_2$ , and coherence lengths  $L_{c1}$  and  $L_{c2}$ . The resultant normalised ac output fringe signal intensity produced at the output of a white-light interferometer can be represented by the function

$$I_{out}(\Delta X) = I_1 \exp\left[-\left(\frac{2\Delta X}{L_{c1}}\right)^2\right] \cos\left(\frac{2\pi\Delta X}{\lambda_1}\right) + I_2 \exp\left[-\left(\frac{2\Delta X}{L_{c2}}\right)^2\right] \cos\left(\frac{2\pi\Delta X}{\lambda_2}\right), \quad (3.19)$$

where  $I_1$  and  $I_2$  are maximum fringe amplitudes in the two individual fringe patterns and  $\Delta X$  is the optical path mismatch between the sensor interferometer and the receiver interferometer. The interference patterns produced by a single source and a double synthetic source are shown in Figure 3.3 for illustration and comparison.

Fringe pattern produced by a single low-coherence source



Fringe pattern produced by a double combination source

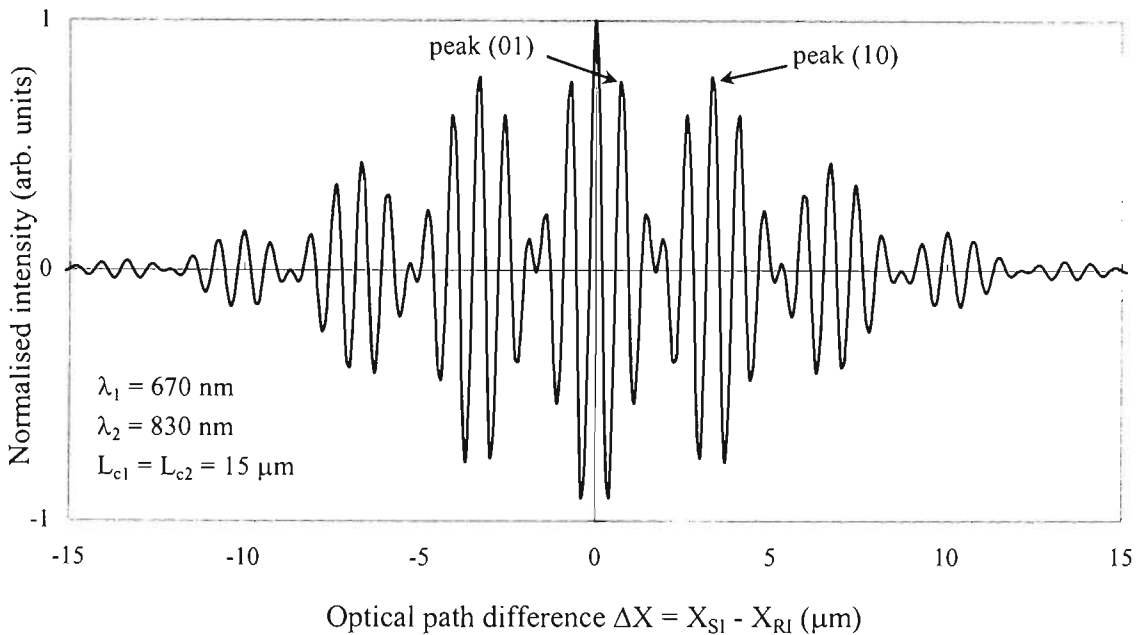


**Figure 3.3** *White-light interferograms produced by a single low-coherence source of central wavelength  $\lambda_1 = 670 \text{ nm}$  and by a double combination source with central wavelengths  $\lambda_1 = 670 \text{ nm}$  and  $\lambda_2 = 830 \text{ nm}$ . Coherence lengths of all sources are assumed to be equal to  $L_c = 15 \mu\text{m}$ .*

In order to calculate the value of normalised peak-to-peak intensity difference between the central fringe and its first adjacent side fringe in each case, we will simplify the normalised output signal function from (3.19) using the assumption of two sources producing equal zero-

order peak intensities in the fringe pattern and having identical coherence lengths. With these assumptions, the relationship (3.19) can be rewritten in the form [Wang *et al.*, 1994]

$$I_{out}(\Delta X) = \exp\left[-\left(\frac{2\Delta X}{L_c}\right)^2\right] \cos\left(\frac{2\pi\Delta X}{\lambda_a}\right) \cos\left(\frac{2\pi\Delta X}{\lambda_m}\right), \quad (3.20)$$

where  $\lambda_a = 2\lambda_1\lambda_2/(\lambda_1 + \lambda_2)$  is termed the average wavelength and  $\lambda_m = 2\lambda_1\lambda_2/(\lambda_2 - \lambda_1)$  is the modulation wavelength. It is also assumed that  $\Delta\lambda = \lambda_2 - \lambda_1 > 0$ .

The interference pattern produced by a double combination source is a cosine waveform of wavelength  $\lambda_a$  that is amplitude modulated by the signal of wavelength  $\lambda_m$  with the overall superimposed modulation provided by the Gaussian source coherence function. The presence of a beat pattern in the interferogram leads to the appearance of distinct packets of fringes with the visibility profile inside each packet being much sharper than that of the single source-generated interferogram. The normalised values of the peak-to-peak intensity difference between the central (zero-order) fringe and its adjacent side fringe for a single source of wavelength  $\lambda_1$  and a double synthetic source can be calculated from (3.20) and are given by

$$\begin{aligned} \Delta I_{single} &= I(0) - I(\lambda_1) = 1 - \exp\left[-\left(\frac{2\lambda_1}{L_c}\right)^2\right], \\ \Delta I_{double} &= I(0) - I(\lambda_a) = 1 - \exp\left[-\left(\frac{2\lambda_a}{L_c}\right)^2\right] \cos\left[2\pi\frac{\Delta\lambda}{\lambda_1 + \lambda_2}\right]. \end{aligned} \quad (3.21)$$

From equation (3.21), it can be seen that the intensity difference is always greater in the case of a double source since the average wavelength is greater than  $\lambda_1$  for any value of wavelength  $\lambda_2$  exceeding  $\lambda_1$ . Therefore, the central fringe of the white-light interference pattern becomes more distinguishable from its neighbours through the enhanced visibility difference. It can be shown mathematically [Wang *et al.*, 1994] that the value of the normalised peak-to-peak intensity of the first side fringe in the central fringe packet  $(I(\lambda_a) - I(\lambda_a/2))/(I(0) - I(\lambda_a/2))$  is a monotonically decreasing function of the central wavelength separation  $\Delta\lambda$  of the two sources. Hence, the central fringe becomes more dominant with respect to its nearest neighbour with increasing values of source wavelength separation.

However, as the source central wavelength separation increases, the intensity of the central fringe in the first side-fringe packet increases and may even exceed the intensity of the first

side-fringe in the central packet. The calculated behaviour of the normalised peak-to-peak intensity values for the first side-fringe in the central packet and the central fringe of the first side-packet with increasing wavelength separation shows that the intensity curves have only one point of intersection. The results of this analysis for a multimode laser diode of central wavelength  $\lambda_1 = 670$  nm and coherence length  $L_c = 25$   $\mu\text{m}$  are presented in Figure 3.4.

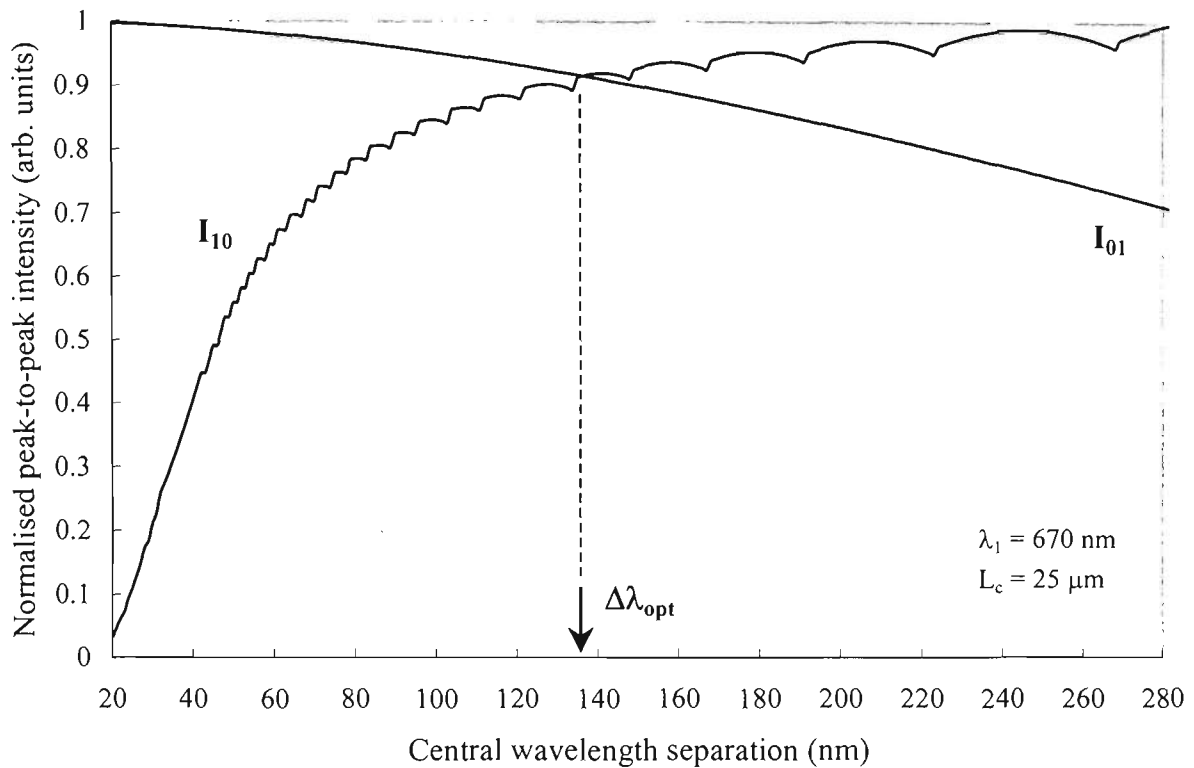


**Figure 3.4** *Determination of optimum central wavelength separation of the two low-coherence sources. Normalised values of peak-to-peak intensity are shown for the first side fringe in the central fringe packet ( $I_{01}$ ) and the central fringe in the first side packet ( $I_{10}$ ). Calculations were made for  $\lambda_1 = 670$  nm and  $L_c = 25$   $\mu\text{m}$ .*

At the point where the two intensities of competing large fringes are equal, the conditions for unambiguous determination of the central fringe position are optimal, since the normalised intensity difference between the central fringe and the largest possible side-fringe is maximised. The corresponding value of the central wavelength separation of the two sources is termed the optimum wavelength separation  $\Delta\lambda_{opt}$ , and the synthetic source formed by two sources of wavelengths  $\lambda_1$  and  $\lambda_2 = \lambda_1 + \Delta\lambda_{opt}$  will enable unambiguous identification of the central fringe with minimal possible value of the signal-to-noise ratio.

The minimum signal-to-noise ratio required for the correct identification of the central fringe is found from the condition when the effect of the peak-to-peak noise level present in the system equals the difference in the output electrical signal levels generated by the intensity difference

between the central fringe and the largest side fringe. The minimum SNR requirement for low-coherence interferometric measurement systems is represented by the relationship

$$SNR_{min} = \frac{I}{\Delta I_n}, \text{ or} \quad (3.22)$$

$$SNR_{min} (dB) = -20 \log_{10}(\Delta I_n),$$

where  $\Delta I_n = (I_{central} - I_{max\ side})/I_{central}$  is the peak-to-peak intensity difference between the central fringe and the largest side-fringe in the interference pattern normalised with respect to the peak-to-peak intensity of the central fringe.

Figure 3.5 shows the dependency of the optimum central wavelength separation  $\Delta\lambda_{opt}$  on wavelength  $\lambda_l$  for various coherence lengths.

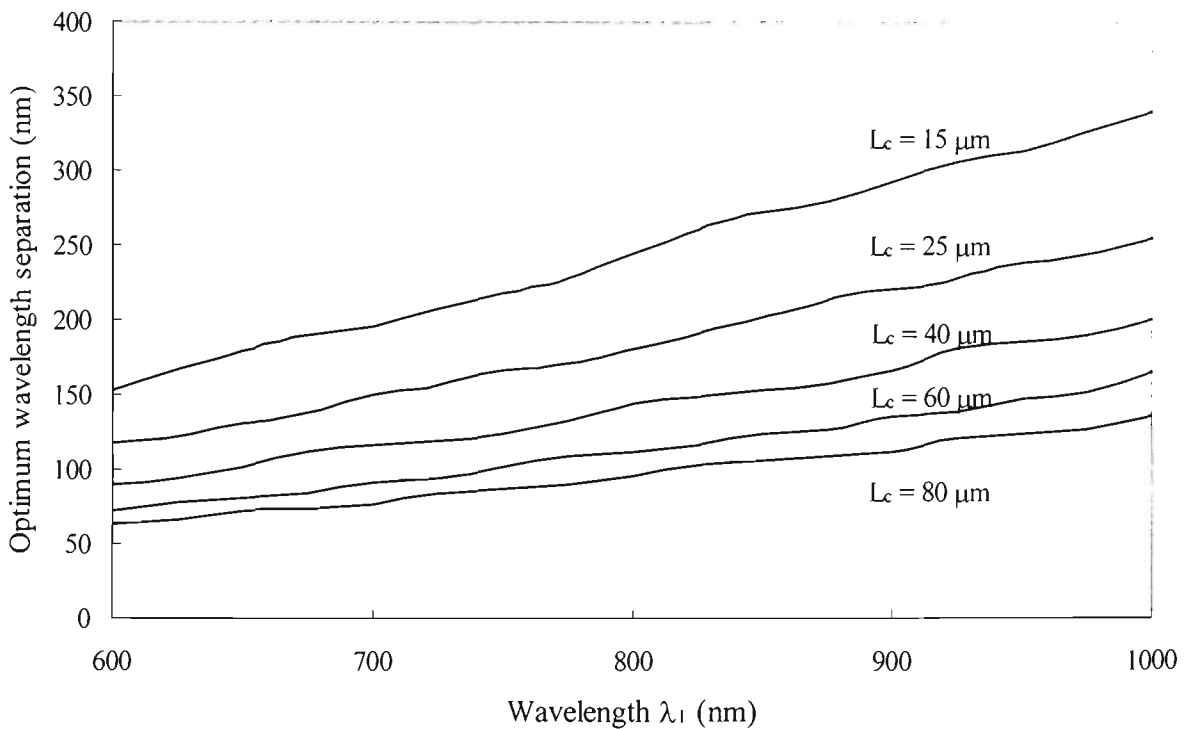


**Figure 3.5** Optimum central wavelength separation for a double combination source versus the wavelength  $\lambda_l$  of the first low-coherence source for various coherence lengths  $L_c$  (assumed equal for both sources).

It can be seen from Figure 3.5 that the coherence length of the light sources is a very important parameter for the optimisation of double source combinations, especially for sources with large central wavelength and short coherence length. For light sources emitting in the red part of the spectrum (600-700 nm) with relatively long coherence lengths (50-80  $\mu m$ , typical for SLD's),

optimisation of wavelength combinations is more stable with respect to slight variations in the sources' coherence length.

Figure 3.6 shows the results of calculations for the minimum signal-to-noise ratio in cases of a single source and a double synthetic source with an optimised wavelength combination. Minimum required signal-to-noise ratios are plotted versus wavelength of the first source  $\lambda_1$ . The plots illustrate clearly the reduction in the minimum signal-to-noise ratio requirement for a low-coherence system facilitated by the use of an optimised double source combination.

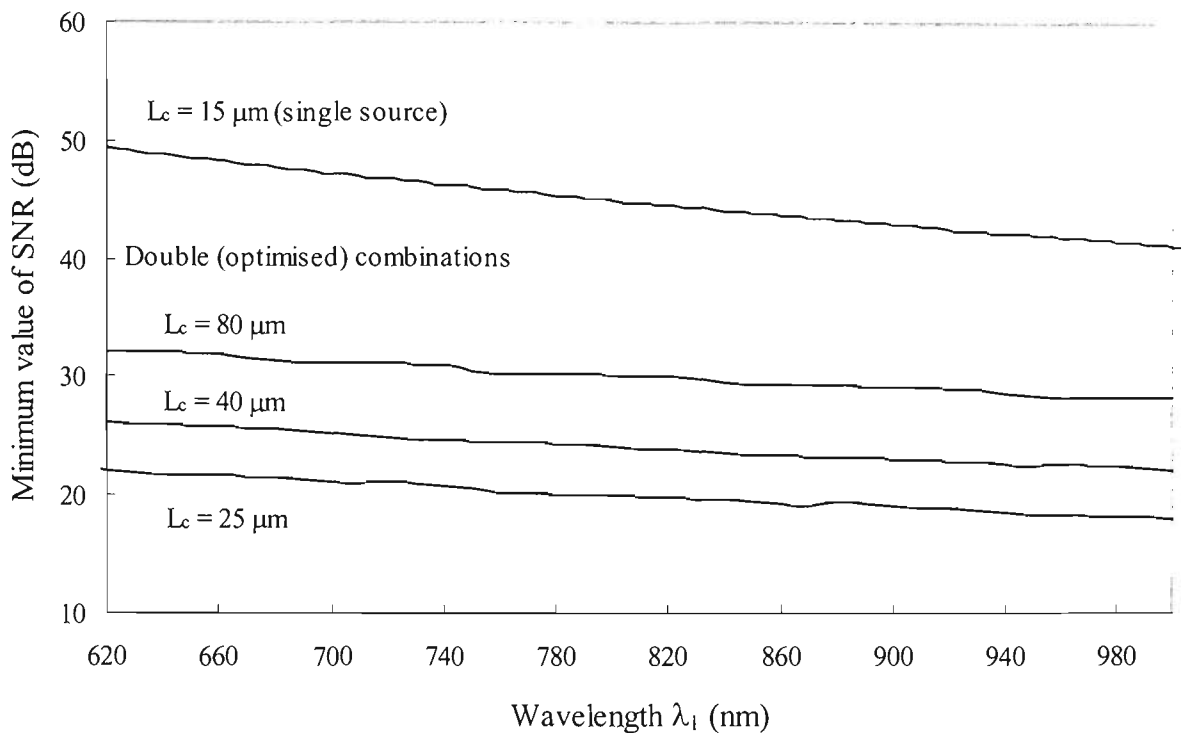


**Figure 3.6** Minimum signal-to-noise ratio requirement for a low-coherence sensing system in cases of a single broadband source of wavelength  $\lambda_1$  and coherence length  $L_c = 15 \mu\text{m}$  and a double combination source with an optimised central wavelength separation and wavelength of the first source  $\lambda_1$ . The two sources used in combination are assumed to have equal coherence lengths.

The plots in Figure 3.6 illustrate that optimisation of double combination sources is best in terms of the signal-to-noise ratio for sources in the infrared region with short coherence lengths. However, the availability of low-coherence sources with suitable emission characteristics and compatible for efficient fibre coupling remains an important limiting factor for the design of practical systems based on double source combinations. It is desirable to utilise optimised source combinations that guarantee low signal-to-noise ratio requirements and also low sensitivity of  $SNR_{min}$  to slight variations in the values of central wavelength and coherence length of sources. In a practical sensing system, an optimised source combination should be based on widely available sources in terms of central wavelength and coherence length, and

provide low SNR requirement even in the case of moderately large (and unequal) values of coherence length. Triple source combinations will be shown in this chapter to be more suitable for practical optimisation of output interference patterns.

### 3.5.3 Analysis and optimisation of multiple source combinations.

The performance of synthetic sources can be further improved with the use of multiple source combinations. The normalised output optical signal intensity observed within the white-light interference pattern in the case of  $n$  low-coherence sources producing equal zero-order peak intensities in the fringe pattern can be represented by the sum of  $n$  terms:

$$I_{out}(\Delta X) = \frac{I}{n} \sum_{i=1}^n \exp\left[-(2\Delta X/L_{ci})^2\right] \cos(2\pi\Delta X/\lambda_i), \quad (3.23)$$

where  $\lambda_1, \lambda_2, \dots, \lambda_n$  are the central wavelengths of the low-coherence sources, and their corresponding values of coherence length are termed  $L_{c1}, L_{c2}, \dots, L_{cn}$ . Equation (3.23) describes the general form of a white-light fringe beat pattern originating from the superposition of  $n$  independent interferograms produced by mutually incoherent broad bandwidth Gaussian light sources.

From the practical point of view, triple source combinations represent the most attractive subject for study since the overall system complexity and cost are increased with the number of optical sources employed. Triple sources can significantly improve the system performance since the addition of a third source can relax the requirements on the maximum coherence length of sources for a given minimum SNR, which makes the choice of optical sources more flexible. We will analyse the advantages associated with triple source combinations and methods of their optimisation.

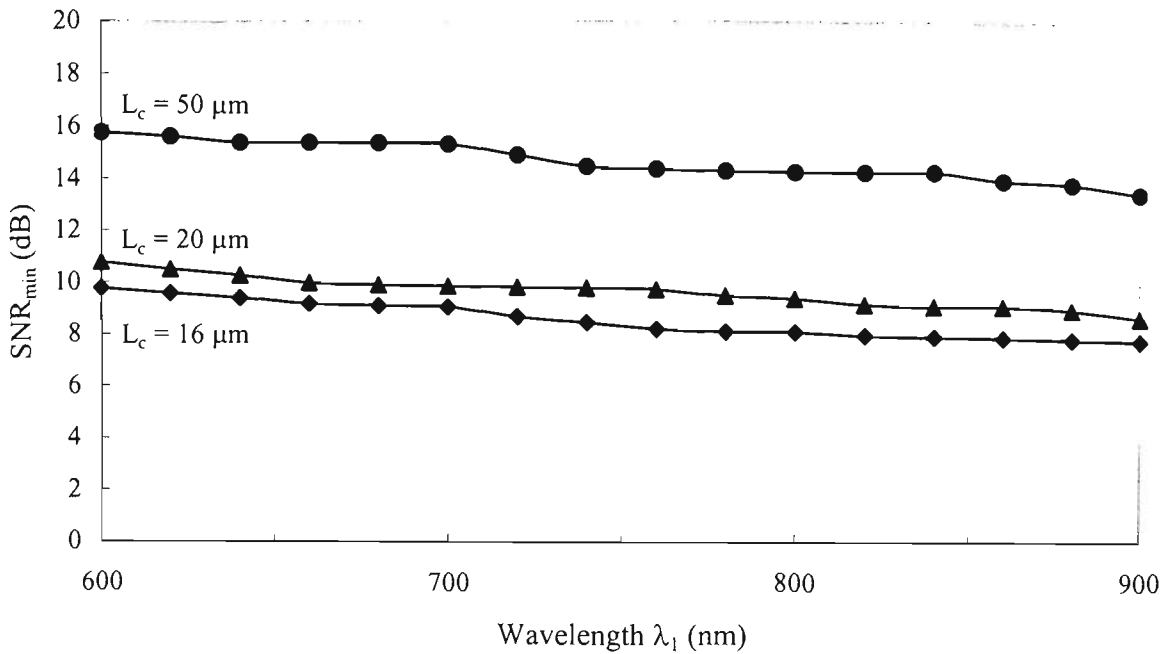
Following an approach represented in [Wang *et. al.*, 1994], assuming equal values of coherence length for all three sources, we can rearrange equation (3.23) into the form

$$I_{out}(\Delta X) = \frac{I}{3} \exp\left[-\left(\frac{2\Delta X}{L_c}\right)^2\right] \left\{ \cos\left(\frac{2\pi\Delta X}{\lambda_1}\right) + \cos\left(\frac{2\pi\Delta X}{a\lambda_1}\right) + \cos\left(\frac{2\pi\Delta X}{b\lambda_1}\right) \right\}, \quad (3.24)$$

where  $a$  and  $b$  are wavelength coefficients that satisfy the relationships  $a = \lambda_2/\lambda_1$ ,  $b = \lambda_3/\lambda_1$ , and  $1 < a < b$ . This relationship (3.24) cannot be further simplified in order to separate the visibility envelope terms, and therefore the interferogram envelope function in this case cannot be represented analytically. In order to optimise the choice of wavelength coefficients  $a$  and  $b$ , we must employ numerical methods and analyse computer-simulated interferograms produced by various source combinations.

The criterion for optimisation is the minimum possible value of the signal-to-noise requirement of the measurement system. The optimum values of wavelength coefficients are found by comparing the normalised peak-to-peak intensity differences between the central fringe and the largest side-fringe in any interferogram for a set of white-light fringe patterns generated with variable parameters  $a$  and  $b$ . The peak-to-peak values of all fringes in any possible interferogram are found by calculating the maxima and minima of the intensity function through finding the zeroes of its first derivative and inspecting the changes in the sign of the derivative in the vicinity of all peaks. The minimum signal-to-noise requirement can therefore be predicted for any given source combination, and the optimised wavelength coefficients can be found by sorting an array of minimum SNR values calculated using the above algorithm. The number of dimensions of that array of all possible SNR requirements is, for  $n$  sources, equal to  $(n-1)$ , or the number of wavelength coefficients considered for a multi-wavelength source. Therefore, as the number of sources increases, more "degrees of freedom" are available for the optimisation of the fringe beat pattern. However, in practice the choice of wavelength coefficients is limited by the availability of suitable light sources and the number of sources employed is limited by the considerations of system design and complexity. Optimised triple source combinations can provide a good trade-off between the desired ease of central fringe identification and the increased number of system components.

Figure 3.7 presents the results of numerical analysis of optimised triple source combinations and illustrates the advantages associated with triple combination sources in terms of the reduction in the minimum signal-to-noise ratio requirement.



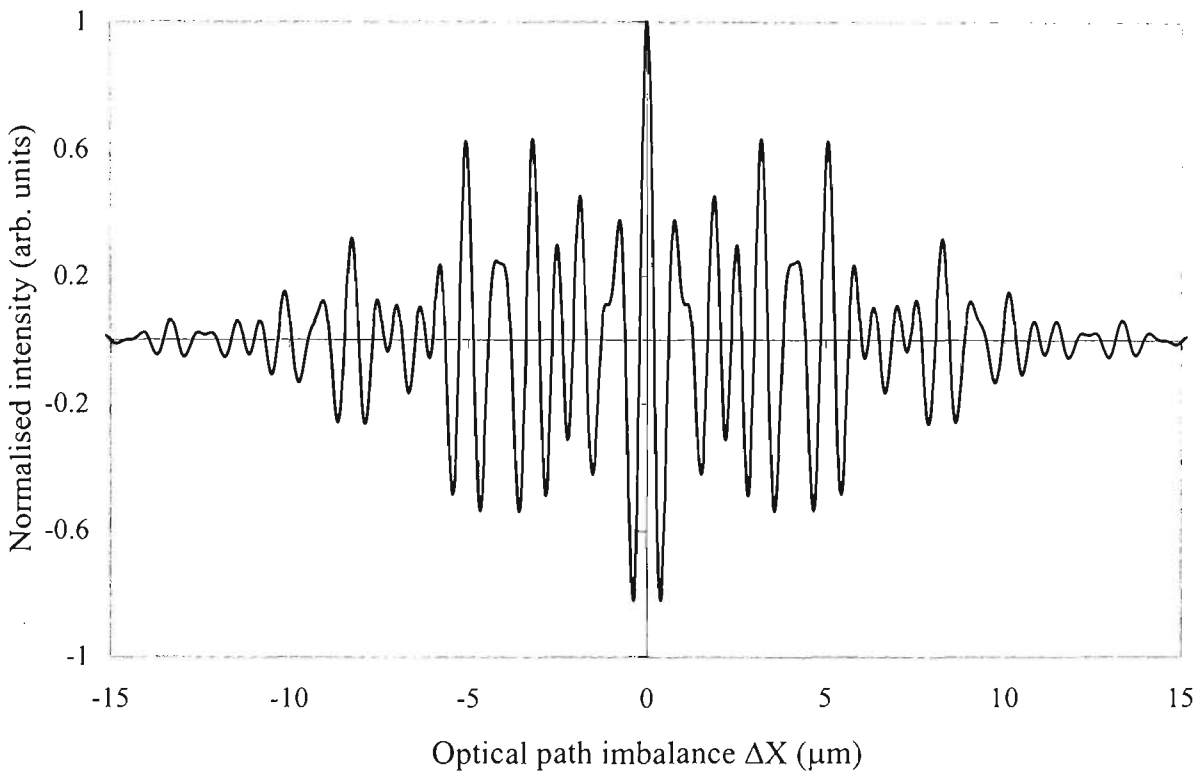
**Figure 3.7** Minimum signal-to-noise ratio requirement for a low-coherence sensing system in the case of a triple combination source with optimised separation of central wavelengths versus the wavelength of the first source  $\lambda_1$ . The three sources used in combination are assumed to have equal coherence lengths.

Figure 3.7 also shows that optimised triple source combinations significantly widen the range of choice of optical sources in terms of their coherence length. Even for sources with a relatively long coherence length of about  $50 \mu\text{m}$ , optimised source combinations allow unambiguous determination of the position of the central fringe with SNRs below 20 dB.

Figure 3.8 shows an example of a white-light interference pattern calculated for an optimised triple source combination with the central wavelength of the first source of 635 nm. Optimum wavelength coefficients for this combination have been calculated through the numerical analysis of white-light interferograms for a wide range of possible wavelength coefficients. The value of coherence length for all sources used in this combination was  $16 \mu\text{m}$ . Strong suppression of three fringes closest to the central fringe is shown, with further side-fringes being also suppressed due to phase mismatch between the three individual fringe patterns and the effect of the visibility envelope.

The interference pattern produced by the optimised source combination shown in Figure 3.8 illustrates how triple sources can be optimised without extensive numerical calculations. To choose three suitable optical sources, it is most convenient to investigate the phase interferogram of three superimposed fringe patterns and choose the three central wavelengths that provide efficient suppression of a maximum number of fringes closest to the central fringe.

This side-fringe suppression results from the difference in cycle lengths of the three interferograms that causes the anti-phase addition of at least one of them during a number of cycles starting from the position of central fringe where all three are in phase. The three fringe patterns will inevitably appear in phase again several fringes away from the central fringe, but the peak-to-peak intensity of the remote largest side-fringe will be reduced due to the effect of the visibility envelope function.



**Figure 3.8** *Theoretical optimised white-light interference fringe pattern produced by three sources with coherence length  $L_c = 16 \mu\text{m}$  and central wavelengths  $\lambda_1 = 635 \text{ nm}$ ,  $\lambda_2 = 831.85 \text{ nm}$ , and  $\lambda_3 = 1022.35 \text{ nm}$ . The minimum value of signal-to-noise ratio necessary for the correct identification of central fringe is 9.3 dB.*

The approach to triple source optimisation based on the analysis of the phase interferogram offers solutions for side-fringe suppression that are independent of variations in the individual coherence lengths of sources since only central wavelength information is used in modelling. An example of the application of the phase interferogram method for triple source optimisation is presented in Figure 3.9.

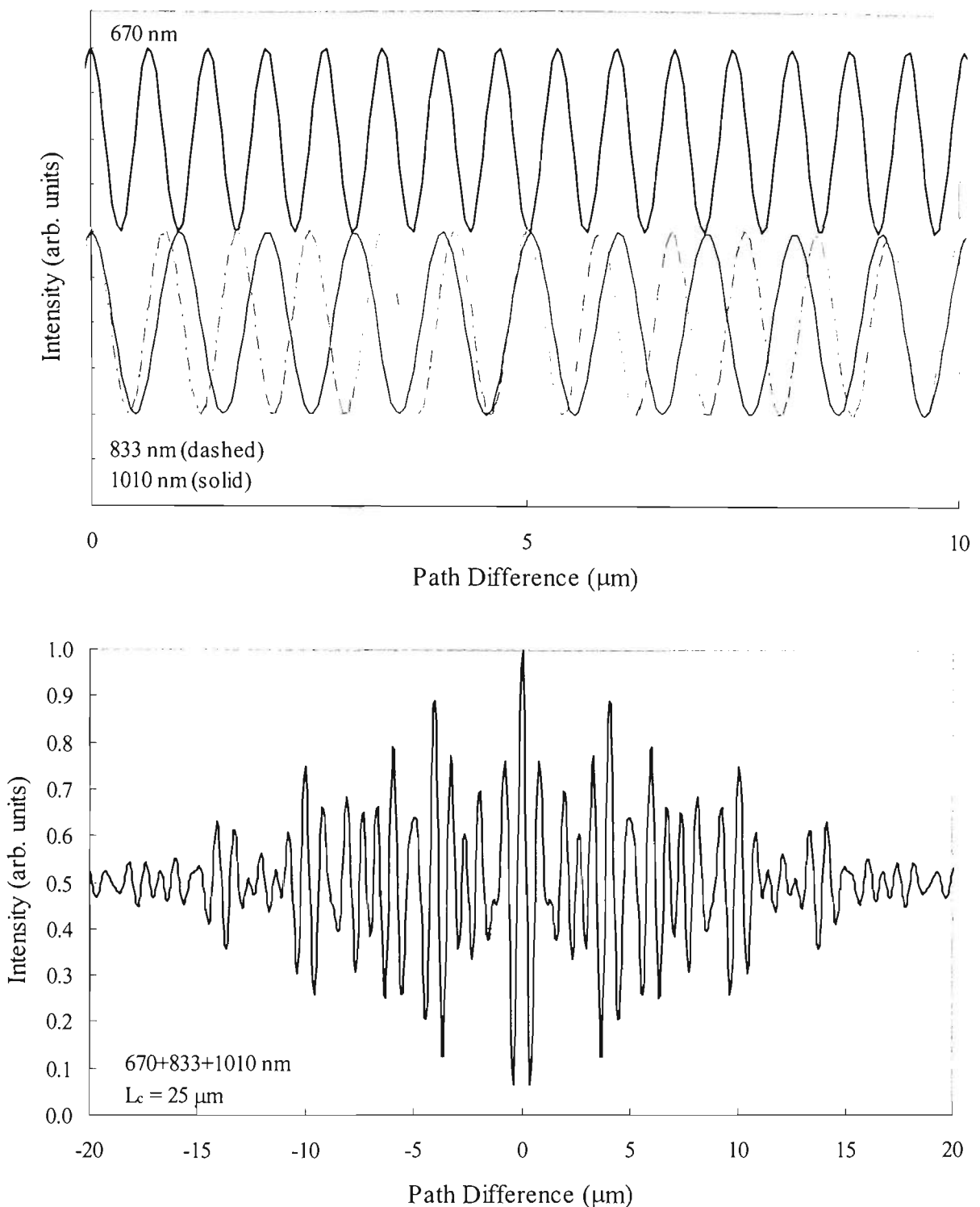


**Figure 3.9** *Phase interferogram of superimposed individual fringe patterns and an interference beat pattern produced with an optimised triple source combination. Central wavelengths of the sources are 670 nm, 833 nm and 1010 nm. A coherence length of 25  $\mu\text{m}$  is assumed for all sources.*

Consequently, this optimisation method will work for a large variety of optical sources with different emission characteristics. Even though the optimised source combinations found through the analysis of phase interferograms may require slightly larger SNRs compared to the corresponding theoretical minima for a given coherence length, this method is practically useful

since variations in the source coherence lengths will not alter the principal character of the beat interferogram.

The phase interferogram of Figure 3.9 shows that the three individual fringe patterns are phase-matched to produce the largest side-fringe after six cycles of minimum wavelength, five cycles of intermediate wavelength and four cycles of longest wavelength. This results in suppression of five fringes neighbouring the central fringe and a reduced peak-to-peak intensity of the largest side-fringe. In addition, this combination is composed of central wavelengths that correspond to the emission spectra of widely available types of semiconductor optical sources.

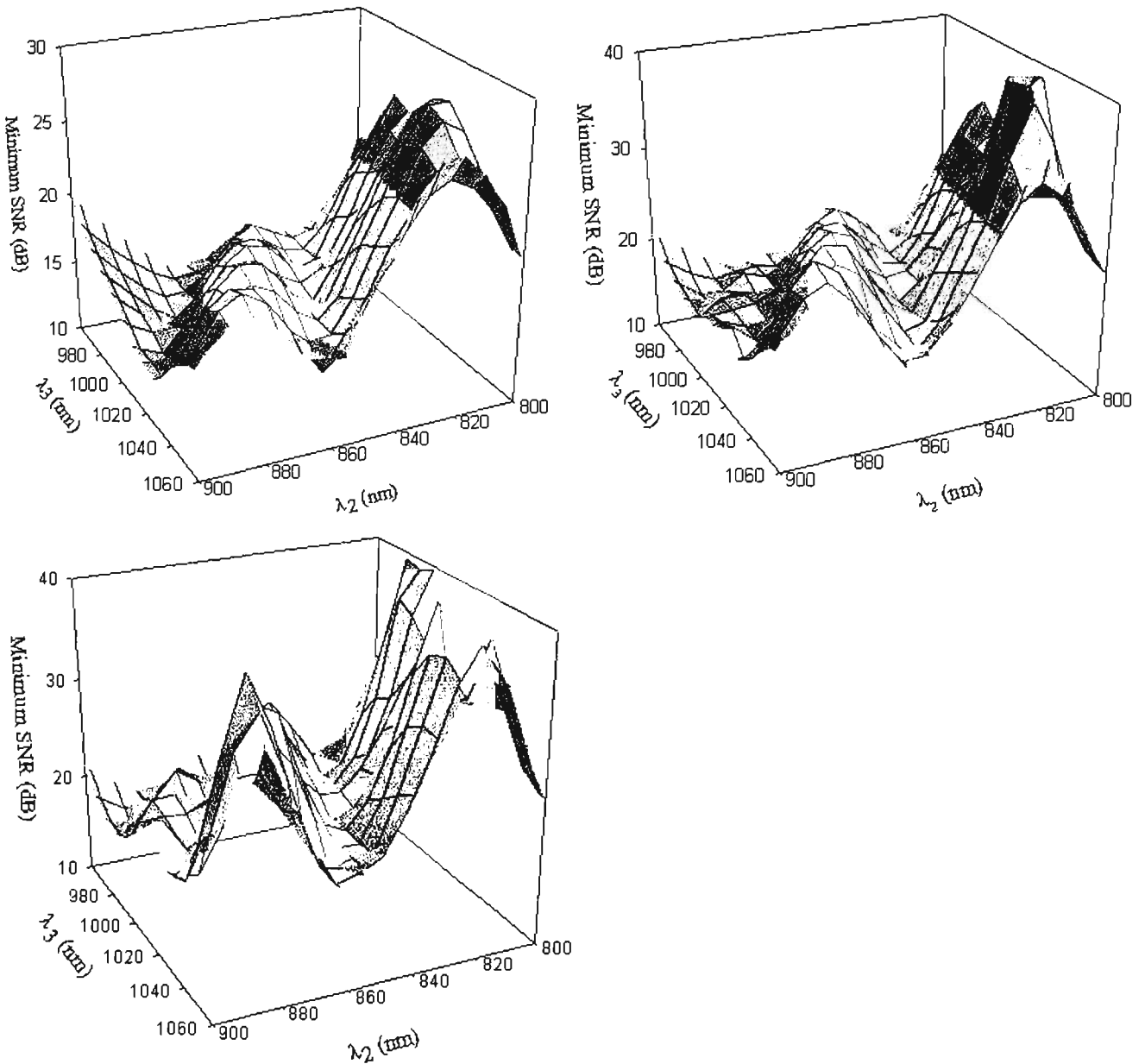


**Figure 3.10** *Calculated minimum signal-to-noise ratio requirements for a low-coherence system using a triple combination source with the minimum central wavelength of 670 nm. Coherence lengths of all three sources are assumed equal. Top left graph:  $L_c = 30 \mu\text{m}$ ; top right:  $L_c = 40 \mu\text{m}$ ; bottom graph:  $L_c = 50 \mu\text{m}$ .*

The calculated distribution of minimum SNR requirements for triple source combinations with a shortest central wavelength of 670 nm versus the intermediate and longest wavelength is shown in Figure 3.10 for three different values of source coherence length.

The optimised triple source combination of Figure 3.9 (central wavelengths of 670, 833 and 1010 nm) corresponds to a point on the surfaces of Figure 3.10 lying within a "valley" region of signal-to-noise ratios for each of the three values of coherence length. The appearance of this "valley" region in the signal-to-noise ratio surfaces is due to the character of the phase interferogram of Figure 3.9 that guarantees suppression of fringes immediately neighbouring the central fringe. The presence of a sizeable region of surface with minimised values of SNR implies that fringe pattern optimisation based on the analysis of phase interferogram is a reliable way of choosing the appropriate low-coherence light sources. Slight variations in the central wavelengths and coherence lengths of sources will not significantly affect the SNR requirement since the character of the fringe beating pattern is determined only by the ratio of central wavelengths and the ratio of peak-to-peak intensities in the central fringes of each individual pattern. For the surface in Figure 3.10 corresponding to a coherence length of 50  $\mu\text{m}$ , the SNR requirements are all below 24 dB for ranges of choice of central wavelengths of between 825-845 nm and 985-1020 nm, with the majority of combinations requiring less than 20 dB SNR for the correct identification of the central fringe. Comparison of the minimum SNR requirements for double and triple sources with first wavelength of 670 nm (figures 3.6 and 3.7) shows that a triple source with a moderately long coherence length of 50  $\mu\text{m}$  can be optimised to perform better than any double combination having a coherence length of 25  $\mu\text{m}$ .

## 3.6 Sensing elements based on fibre Bragg grating Fabry-Pérot.

The characteristics of the white-light interference pattern produced at the output of a low-coherence measurement system depend on the properties of the sensing element employed in the sensor interferometer. Fibre Fabry-Pérot sensors produced by writing sets of superimposed Bragg gratings can significantly affect the transfer function of the interferometer system since the sensor cavity mirrors in this case are not ideal plane mirrors. The spectrum of each light source in a combination-source system is modified on reflection due to the spectral response characteristics of the cavity reflectors. The ratio of intensities of the two beams returned from the sensor is determined by the reflectivity of each mirror in the fibre Fabry-Pérot cavity. In addition, the reflection of each spectral component of light from a distributed mirror provided by a set of superimposed chirped gratings occurs effectively at some distinct point within the grating structure, the position of which depends on the wavelength of that component and the internal structure of the mirror. Therefore, the visibility profile and spatial extent of the resultant white-light fringes are dependent on the characteristics of Bragg grating Fabry-Pérot cavity.

The effect of the chirped grating mirrors of the fibre Fabry-Pérot must be analysed to facilitate the design of sensors that provide optimum output signal properties. The spectral characteristics and structural composition of these grating mirrors are factors of prime importance that largely determine the overall performance characteristics of the low-coherence measurement system.

### 3.6.1 Properties of fibre Fabry-Pérot sensors. Optimisation of sensor performance.

Bragg grating fibre Fabry-Pérot sensing elements produced during this work have been utilised as two-beam interferometers operated in reflection mode. In order to exploit the advantages of low-coherence sensing with a combination source, the cavity mirrors have been designed to reflect the broad emission spectra of three light sources and maximise the power and fringe visibility in the output optical signal. Another design requirement has been to ensure that the effective Fabry-Pérot cavity length was identical for every spectral component of incident light. These requirements have been met by producing cavity mirrors made of identical (to the degree limited by manufacturing precision) superimposed grating structures with the techniques described in chapter 4. Cavity mirrors of the Fabry-Pérot sensors are distributed reflectors of about 4 mm length that can be described as sequences of ideal plane mirrors, each of which is positioned at a particular point within the reflector structure and is designed to reflect a

particular spectral component of incident light. The separation of effective points of reflection at the cavity ends has to be identical for all combination source wavelengths to ensure the same effective Fabry-Pérot lengths.

The reflection coefficients of Fabry-Pérot cavity mirrors determine the optical power and visibility of fringes in the white-light interference signal. In order to obtain an output fringe signal with optimised visibility, the intensities of interfering beams at the detector have to be equal. Considering the losses within the two arms of the receiver interferometer to be equal, the optimised sensor Fabry-Pérot should provide a 1:1 power splitting ratio for the two reflected beams.

From equation (3.18), the maximum visibility in the white-light interference pattern is observed near the path matching condition ( $\Delta X = 0$ ), and is dependent on cavity mirror reflection coefficients according to the relationship

$$V_{max} = \frac{(1 - R_1)\sqrt{R_1 R_2}}{R_1 + (1 - R_1)^2 R_2}. \quad (3.25)$$

The analysis of power splitting for the beams reflected from Fabry-Pérot shows that a 1:1 power splitting ratio is achieved when the reflectances of cavity mirrors are bound by the relationship

$$R_2 = \frac{R_1}{(1 - R_1)^2}. \quad (3.26)$$

If condition (3.26) is satisfied, the visibility of the central fringe in the white-light pattern reaches its theoretical maximum value of 0.5. The values of the second mirror reflectance (optimised for maximum output signal visibility) are plotted versus the reflectance of first mirror  $R_1$  in Figure 3.11.

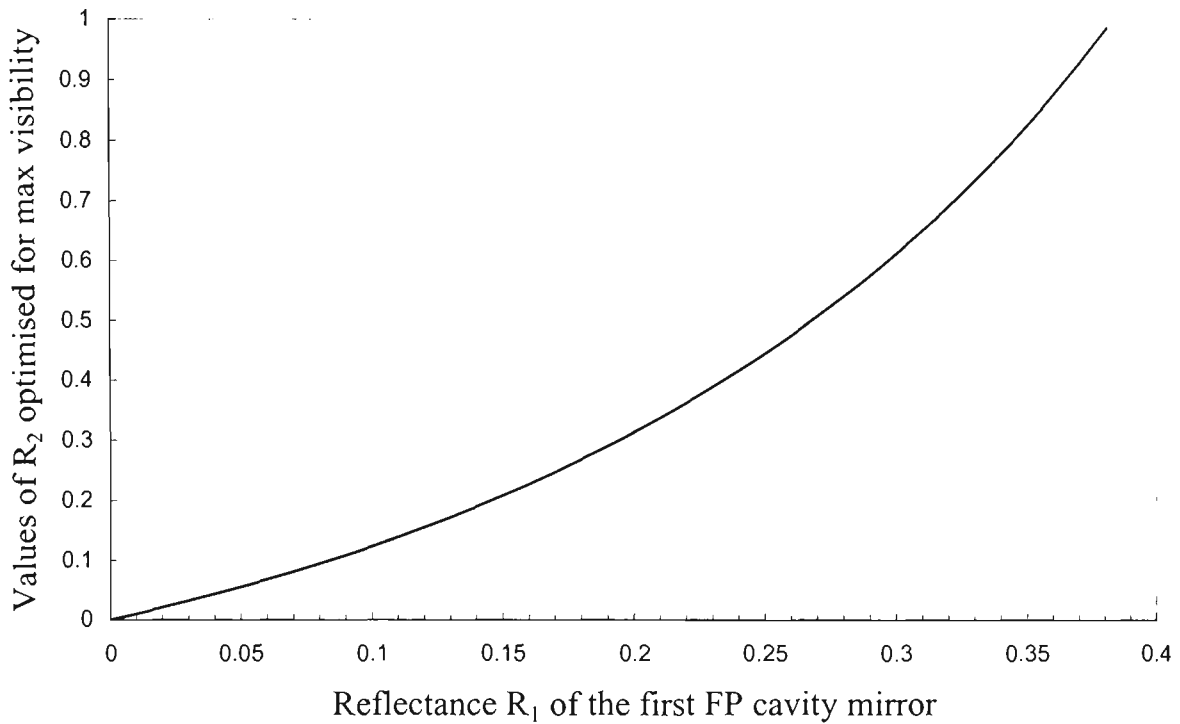


**Figure 3.11** *Optimisation of the Fabry-Pérot sensor mirror reflectances for maximum visibility of fringes in the white-light interference pattern.*

Figure 3.11 shows that a Fabry-Pérot sensor can only provide a 1:1 power splitting ratio for the signal beams if the reflectance of the cavity front mirror is less than about 38%.

If the sensor mirror reflectances are equal, the visibility of fringes in the output interference pattern is reduced with increased reflectance even though the amount of optical power arriving at the system output is increased. The fringe visibility function versus mirror reflectance  $R$  is shown in Figure 3.12. A mirror reflectance of 50% corresponds to visibility of about 0.4, which shows the trade-off between the optimum fringe visibility and the amount of signal power returned from the sensor. In the case when mirror reflectances approach zero, the visibility function peaks at  $V = 0.5$ ; however, this point also corresponds to the limiting case of zero optical power in the signal reflected from sensor.

Fabry-Pérot sensors can be optimised for maximum achievable signal-to-noise ratio by finding the mirror reflectances that provide maximum peak-to-peak intensity of the central fringe. Using equation (3.16) and considering the value of the source autocorrelation function to be unity near the path matching condition, the maximum peak-to-peak intensity of the central fringe can be approximated by

$$I_{00} = 2I_{det}V. \quad (3.27)$$

Therefore, the product of the total power arriving at the detector  $I_{det}$  and visibility  $V$  has to be maximised to achieve the optimum signal-to-noise ratio.

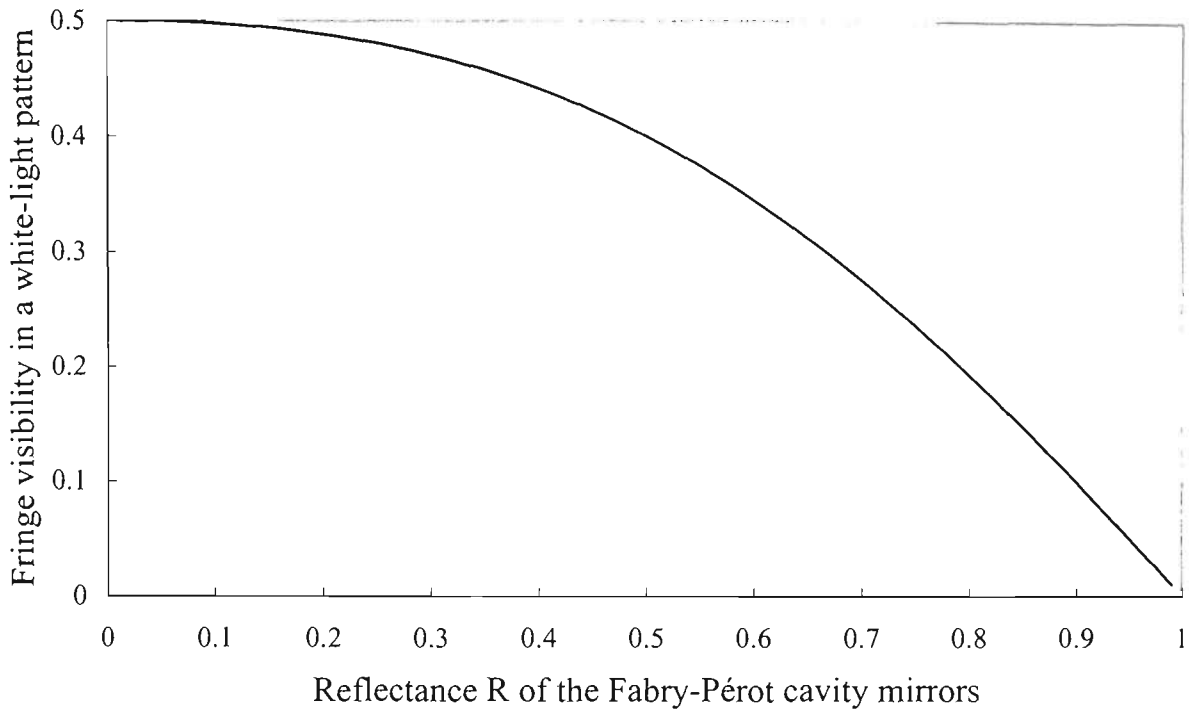


**Figure 3.12** Fringe visibility near the path matching condition versus the Fabry-Pérot sensor mirror reflectance for identical cavity mirrors.

From equation (3.15), the product  $I_{det}V$  is proportional to  $(1-R_1)(R_1R_2)^{1/2}$ , and therefore the optimum (for maximum signal-to-noise ratio) value of mirror reflectance  $R$  can be found for sensors with identical mirrors. It is found to be 0.5 through finding the maximum of the corresponding function  $R_1(1-R_1)$ . The dependency of the central fringe peak-to-peak intensity (normalised with respect to its maximum possible value for a given system) on cavity mirror reflectance is shown in Figure 3.13.

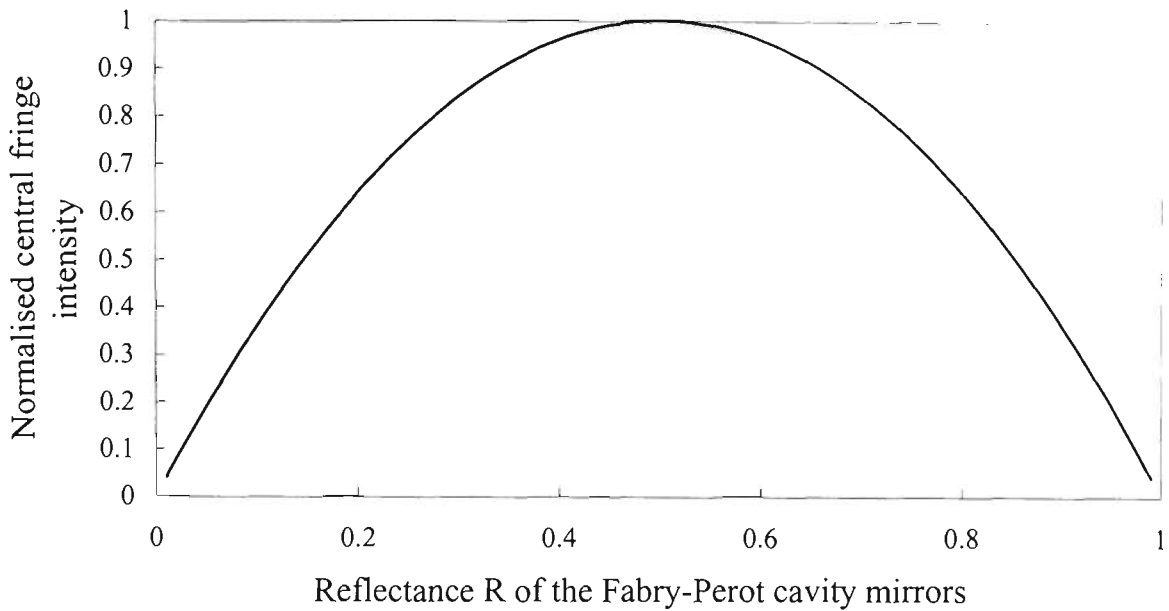


**Figure 3.13** *Normalised peak-to-peak intensity of the central fringe versus the Fabry-Pérot sensor mirror reflectance.*

For Fabry-Pérot sensors with non-identical mirrors, the sensor can be optimised by calculating the front mirror reflectance providing the maximum signal-to-noise ratio and the back mirror reflectance for equal power splitting ratio. The function  $(1-R_1)(R_1)^{1/2}$  peaks at the value of  $R_1 = 1/3 = 0.33$ , and the corresponding value of second mirror reflectance for maximum visibility is  $R_2 = 0.735$  from equation (3.26).

It is practically difficult to achieve large spectrally uniform reflectances over a wide bandwidth using sensor mirrors made of chirped Bragg gratings. Therefore, optimisation of a grating-based Fabry-Pérot sensor is practically performed by designing mirrors with spectral response characteristics matching the emission spectra of light sources and containing the minimum number of narrow-bandwidth features in the reflected spectrum. The reflectivity of broad bandwidth grating mirrors is limited by the degree of fibre photosensitivity. Average mirror reflectances of the order of 30% have been achieved over spectral widths of about 20 nm with superimposed chirped grating mirrors during this work. These sensor elements have been proven to generate output signals with signal-to-noise and visibility characteristics suitable for reliable central fringe identification.

### **3.6.2 Transfer function of a low-coherence system using a chirped Bragg grating FP sensor and an optimised combination source.**

Bragg grating Fabry-Pérot sensors modify the spectra of light sources on reflection from cavity mirrors. This changes the character of the transfer function of the white-light interferometer system since the spectral composition of interfering light beams determines the properties of the interferogram. Since Bragg grating mirrors can contain narrow-bandwidth features in their reflected spectrum, the effective coherence length of source light is inevitably increased on reflection from this type of sensor. This leads to the appearance of elongated white-light interferograms that contain groups of fringes positioned well away from the point of zero path imbalance. The properties of the central group of fringes are changed only slightly due to source spectrum modification, since these are primarily determined by the overall broadband spectral composition of the light source.

The effect of source spectrum modification on the properties of white-light interferograms can be illustrated by modelling the white-light interferograms using the measured spectral data for the combined source light returned from a Fabry-Pérot sensor. The interferogram is obtained by performing a discrete cosine Fourier transform of the spectrum of the interfering light beams. Figures 3.14 and 3.15 show the emission spectra of low-coherence light sources and a fringe pattern modelled for the case of an ideal Fabry-Pérot sensor (no source spectrum modification assumed). Figures 3.16 and 3.17 illustrate the spectral composition of source light returned from one of the chirped grating Fabry-Pérot sensors made during this project, and the effect of source spectrum modification on the interferogram.

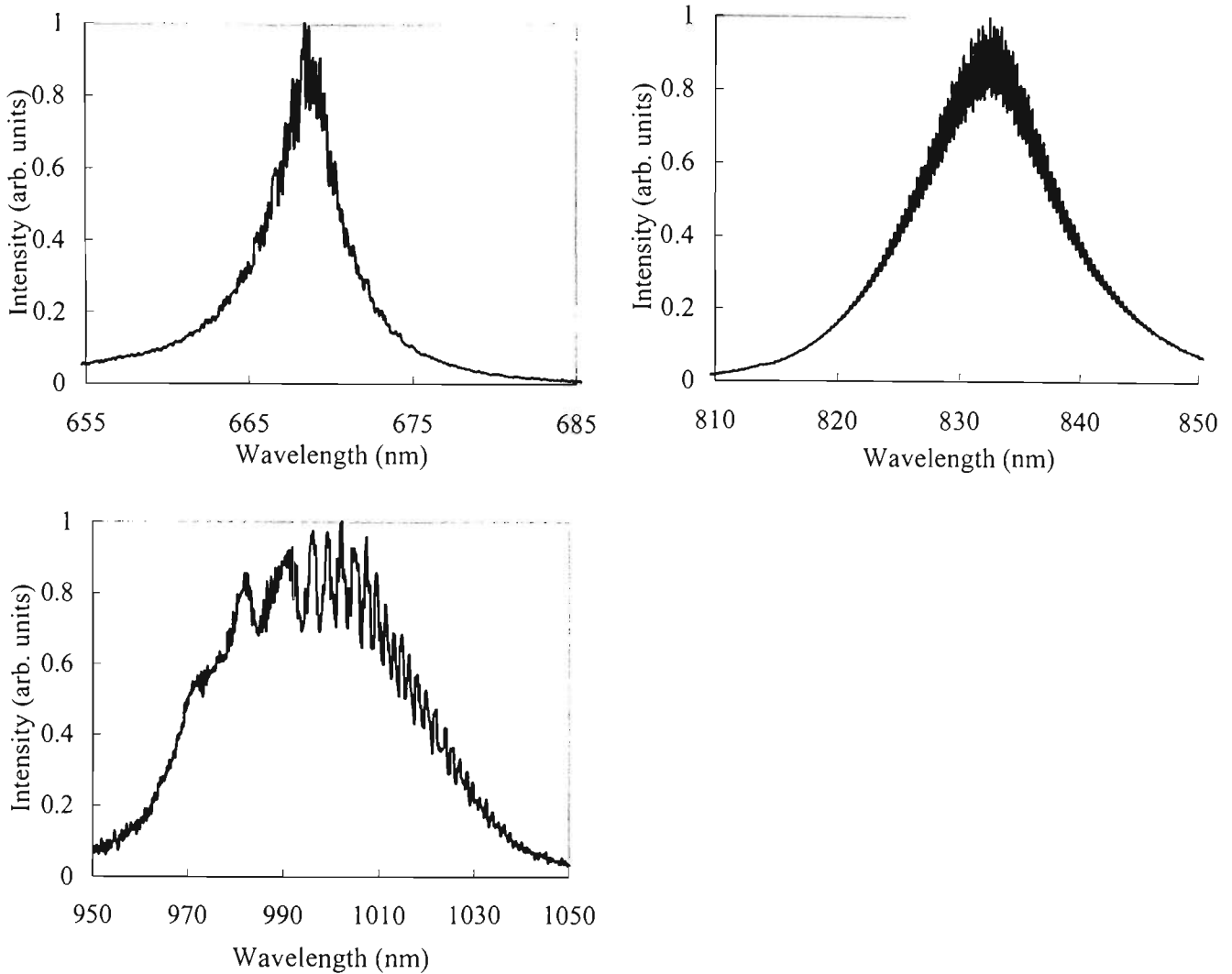


**Figure 3.14** *Emission spectra of low-coherence sources used for modelling the white-light fringe pattern of Figure 3.15.*

The spectral characteristics shown in Figure 3.14 have been measured experimentally using the low-coherence sources employed initially during this project. The sources chosen for an optimised source combination were: Toshiba TOLD 9225 laser diode with central wavelength of 670 nm running below threshold, Hamamatsu superluminescent diode with central wavelength of 833 nm, and a 980 nm fibre pigtailed laser diode running below threshold.

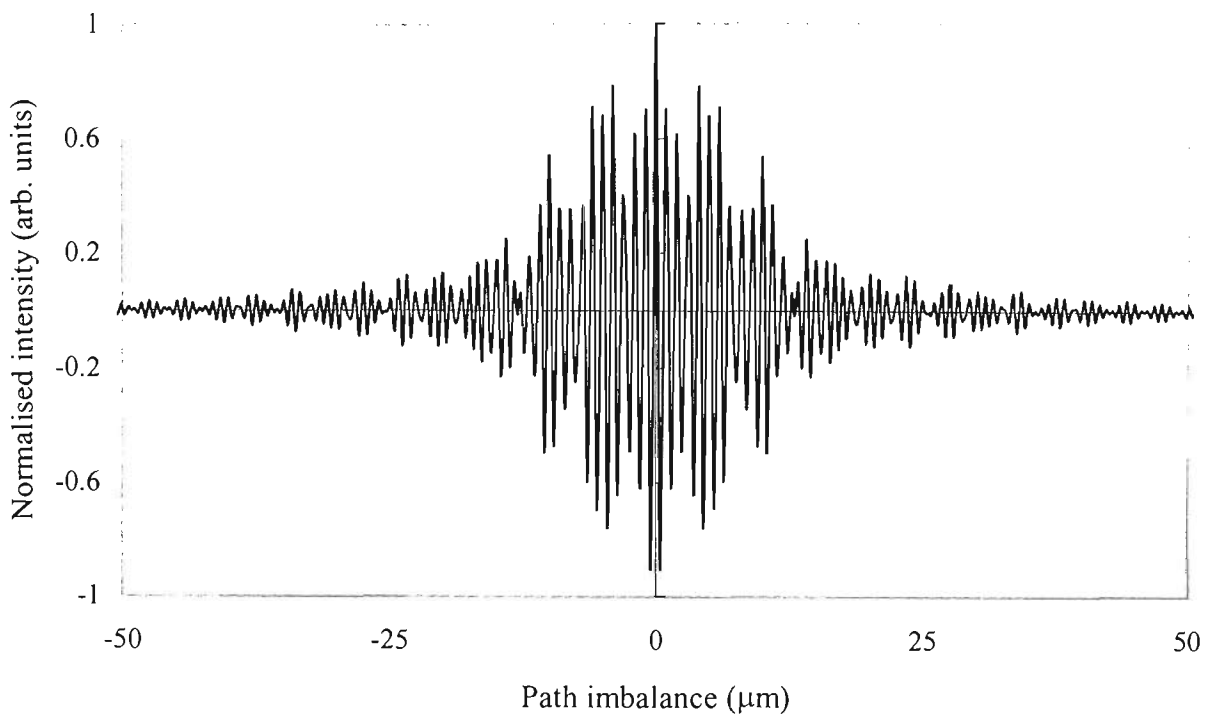


**Figure 3.15** *Modelled white-light interference signal at the output of a sensor system using an optimised triple-wavelength (670, 833 and 1000 nm) source combination and a FP sensor cavity made of ideal plane mirrors. The interferogram was obtained through a discrete Fourier transform of the measured combination source spectrum.*

The fringe pattern of Figure 3.15 was modelled using the spectral data of the low-coherence sources used during the initial stages of this project. The analysis of peak-to-peak intensity distribution within this pattern shows that the minimum signal-to-noise ratio requirement for correct identification of the central fringe is approximately 15.7 dB. This confirms the usefulness of the optimisation of source wavelength combination since a low signal-to-noise ratio is required in this case despite the relatively long and unequal coherence lengths. The 15.7 dB SNR requirement is close to its theoretical minimum value for the shortest wavelength of 670 nm and the range of coherence lengths matching that of the sources used in this model.

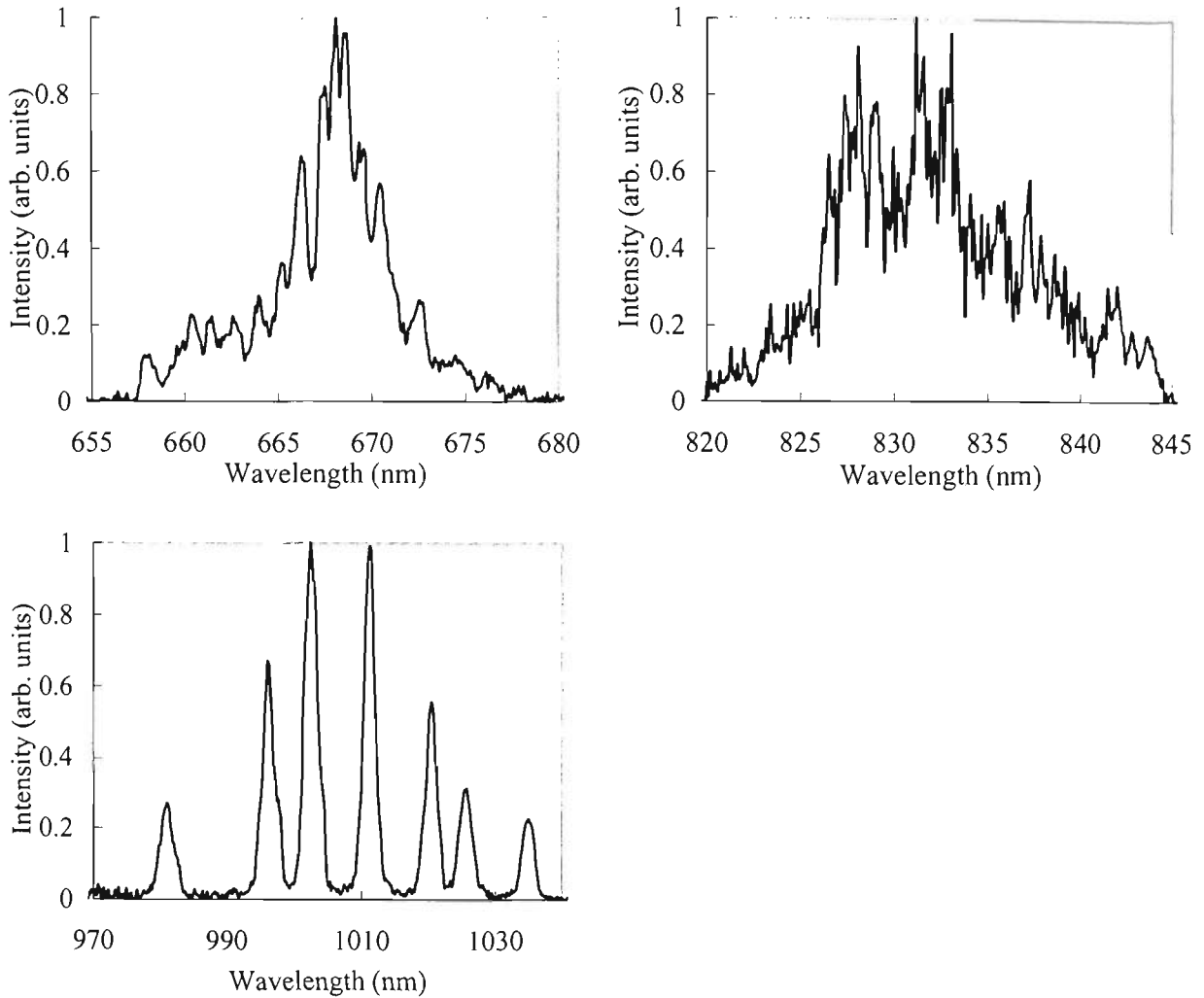


**Figure 3.16** *Measured spectral composition of the combined low-coherence source light reflected from a FP sensor made of superimposed chirped gratings.*

The presence of narrow-bandwidth spectral peaks in the measured spectrum of light reflected from a FP sensor (shown in Figure 3.16) is due to spectrally narrow features in the emission spectrum of light sources and in the spectral response of chirped gratings.

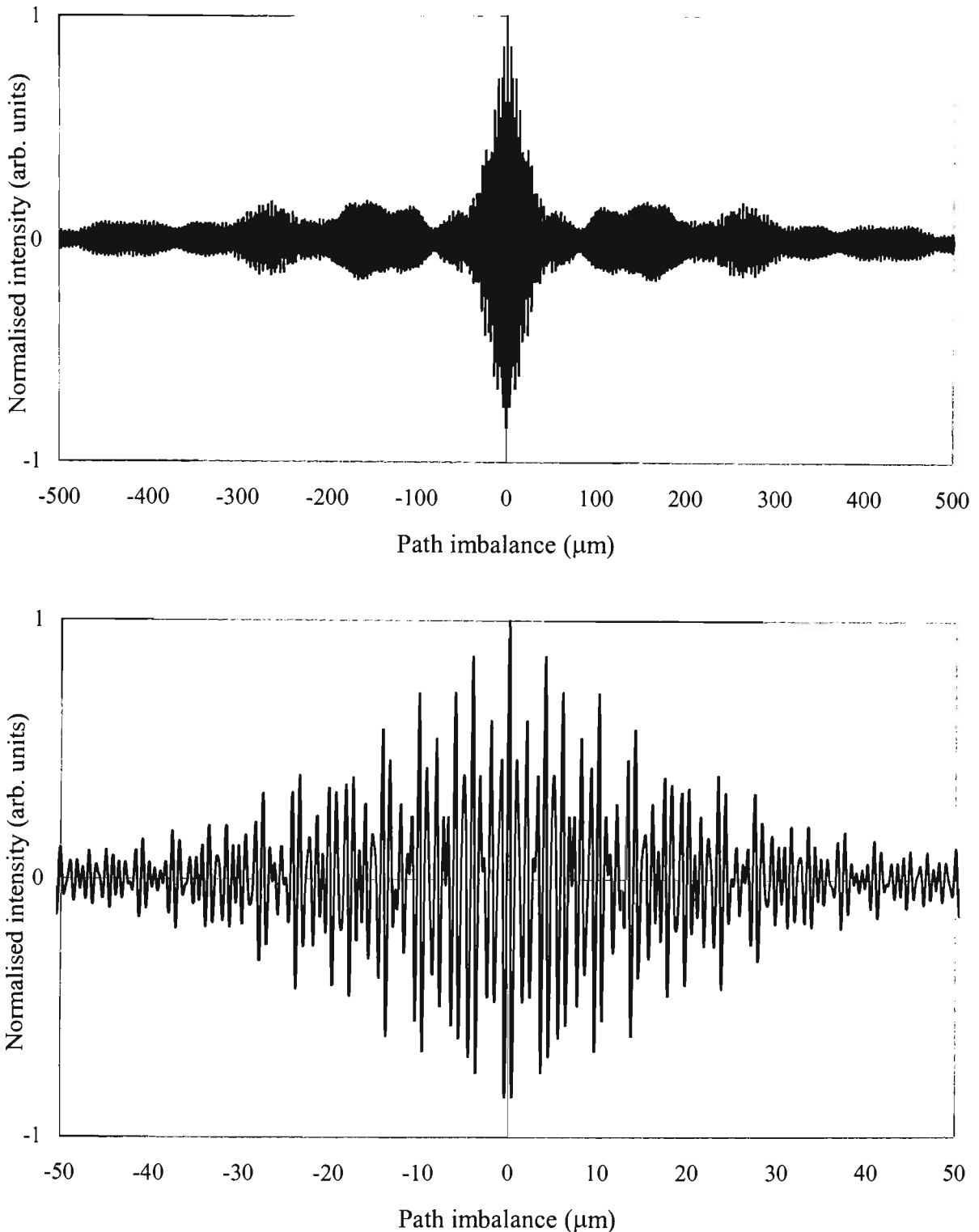


**Figure 3.17** *Modelled output white-light interference pattern produced by a sensor system using a chirped Bragg grating FP sensor and an optimised triple-wavelength combination source (central wavelengths 670, 833 and 1010 nm). Experimental data for spectral distribution of light reflected by the sensor cavity was used for obtaining the interferogram through a discrete Fourier transform of combined spectrum. The lower figure is a magnification of the central region (near the path-matching condition) of the interferogram shown in the upper figure.*

Analysis of the fringe pattern of Figure 3.17 gives a signal-to-noise ratio requirement of 18 dB. This figure suggests that for a chosen optimised combination of central wavelengths, a

significant spectral modification of source light on reflection from a non-ideal sensor element does not significantly increase the SNR requirement. This follows from the relatively low sensitivity of the fringe intensity distribution within the central fringe packet to the intensity of narrow-band spectral components of the source light. The optimisation of central wavelength combination remains useful even in the case of non-ideal FP mirrors as long as the overall mirror reflection bandwidth matches the emission bandwidth of light sources.

It is important to note that modelling of white-light fringe patterns in this section does not include the effects of dispersion in the fibre interferometer system. The effects of chromatic dispersion, stress-induced dispersion in fibre coils and polarisation-mode dispersion on LCI fringe patterns will be considered in detail in chapter 5.

### **3.7 Central fringe identification and processing of output fringe patterns.**

Measurements with low coherence interferometric systems rely on the correct determination of the position of zero optical path imbalance between the sensor interferometer and the receiver interferometer. The measurand information is extracted by analysing the output interference fringe pattern. This allows absolute determination of the optical path difference in the receiver interferometer matching that in the sensor.

For the system used in this work, the position of zero differential OPD corresponds to the centre of a bright fringe with maximum peak-to-peak amplitude and visibility in the output interference pattern. Since the overall structure of a white-light interference pattern is symmetric (in the absence of dispersion effects [Urbanczyk and Bock, 1994, Marshall *et. al.*, 1997]) with respect to the position of zero optical path imbalance, the fringe of maximum peak-to-peak amplitude is termed the central (or zero-order) fringe. During measurements, the central fringe must be identified reliably in the presence of noise in order to use data points from within this fringe for finding the position of its centre. Several signal processing algorithms have been devised to date to accomplish this task, since detection of central fringe through its maximum intensity amplitude can be unreliable in the presence of noise signals.

The choice of an optimum algorithm for fringe data processing depends on the character of the output interference pattern of a low coherence sensor and the signal-to-noise ratio in the output signal. An ideal data processing technique should involve minimum of computational

complexity for fast and reliable determination of the position of zero path imbalance. The effects of noise must be minimised through digital pre-processing of fringe data that filters out random noise peaks. Efficient algorithms for adaptive filtering of fringe data have been developed [Chen *et al.*, 1992, Rizk *et al.*, 1998]. The data filtering algorithm reported by Chen *et al.*, 1992 as a stage of data pre-processing before centroid determination discriminates between the signal peaks and the noise peaks in the captured data utilising the fixed spatial frequency of signal peaks. The noise peaks in the data have irregular (random) spatial frequency, and these can be filtered out efficiently, but at the cost of increased computational complexity. Successful implementation of this data pre-processing algorithm requires the value of a "tolerance" parameter  $t$  for the signal peak width to be chosen correctly. This parameter describes the maximum deviation in the width of detected signal peaks from its mean value, with which any peak in the sequence of data points can still be considered a signal peak.

### Centroid algorithm.

The centroid algorithm [Chen *et al.*, 1992] has been developed for the enhancement of measurement accuracy in electronically-scanned LCI systems. After the interference pattern data is acquired, the array of data points is normalised to ensure zero mean value and adaptively filtered using the technique described above. The centroid algorithm is then applied, which uses the following formula for the processing of pre-filtered normalised array of fringe data points  $a[i]$ :

$$c = \frac{\sum_{i=1}^N (i |a[i]|)}{\sum_{i=1}^N |a[i]|}, \quad (3.28)$$

where  $N$  is the number of points in the data array and  $c$  is the fractional index within this array corresponding to the estimate of the centre of the low coherence interference pattern (the centroid of the fringe pattern). The fringe nearest to this calculated centroid position in the data array is considered to be the central fringe.

The application of formula (3.28) allows determination of the central fringe with a good degree of noise tolerance, achieving misidentification rates of less than  $10^{-4}$  for patterns produced by single light sources with coherence lengths between 50-80  $\mu\text{m}$  at SNRs between 30-38 dB [Chen *et al.*, 1992a]. However, this algorithm is only valid mathematically for perfectly symmetric interference patterns not affected by the dispersion. The application of the centroid

algorithm to the processing of CCD-recorded data in electronically-scanned systems is only efficient for fringe patterns centered around the central line of the CCD frame [Rizk *et al.*, 1998]. An alternative data processing technique using a least-mean-square (LMS) regression algorithm has been reported to overcome difficulties related to the fringe pattern offset, offering sub-fringe resolution [Rizk *et al.*, 1998].

After the central fringe in the interference pattern is identified, for example, due to its superior visibility compared to side-fringes or through centroid analysis, intra-fringe resolution enhancement can be achieved by applying the centroid algorithm to the data points within the central fringe. This method of intra-fringe resolution enhancement is particularly suitable for systems using optimised multi-wavelength light sources offering easy identification of the central fringe by its visibility. Very little computational complexity is involved in the centroid processing of a small number of data points within the central fringe, resulting in the ability to process data quickly. This approach to data processing has been utilised during this study, and measurements with sub-fringe resolution have been performed successfully in the absence of external perturbations to the interferometers.

There are two modifications of the central fringe centroid algorithm, namely the bright-fringe centroid and the full-fringe centroid, with the latter reported to be significantly more noise-resistant and less sensitive to variations in the number of sample points per fringe [Chen *et al.*, 1992a].

The bright-fringe centroid algorithm uses only positive fringe voltage data points within the central fringe data array. The processing formula is the same as equation (3.28), except that  $N$  now equals to the number of points within the bright half-fringe of the central fringe and  $a[1]$  is considered to be the first (minimum-index in an original large array) data point within the bright half-fringe of the central fringe. An advantage of this method is that the processing time is a factor of two less than that in the case of the full-fringe centroid method. However, the bright-fringe centroid algorithm was reported to have its accuracy dependent on whether the number of sample points per fringe,  $S$ , is odd or even. Better performance of the bright-fringe method was reported for even values of  $S$  [Chen *et al.*, 1992a].

The full-fringe centroid algorithm uses the following formula for locating the centre of the central fringe:

$$c_{cf} = \frac{\sum_{i=u1}^{u2} [i(1 + a[i])]}{\sum_{i=u1}^{u2} (1 + a[i])}, \quad (3.29)$$

where  $u1$  is the index of the first data point within the original large data array  $a[i]$  that is considered to belong to the central fringe,  $u2$  is the index of the last data point of the central fringe, and  $c_{cf}$  is centroid index corresponding to the exact path-matching position.

During the experimental work in this project, the identification of the central fringe was performed by simple peak detection, since interference patterns generated by optimised source combinations ensured sufficiently dominant character of the central fringe in the absence of significant external perturbations to the fibre. In the case of fringe patterns generated by a triple-wavelength source, intra-fringe resolution was achieved by applying the full central fringe centroid algorithm. Fringe patterns obtained with chirped grating-based sensors proved a rather interesting subject for study, possessing unique features and imposing some limitations on the system performance. These are described in detail in chapters 5 and 6 of the thesis, after the discussion of Bragg gratings and sensor elements manufactured with this technology.

## In-fibre Bragg gratings and their applications in optical fibre sensors

### 4.1 Introduction.

This chapter is dedicated to the analysis of the properties and applications of in-fibre Bragg gratings (BGs) with particular emphasis on the design and fabrication of suitable broad bandwidth in-fibre reflectors for the Fabry-Pérot sensing elements in a white-light interferometer system. The spectral reflection and modal coupling properties of both uniformly periodic and chirped Bragg gratings are analysed using coupled-mode theory. A brief description of an alternative method for the analysis of arbitrary grating structures based on the scattering matrix approach is given. Fibre photosensitivity models and their application for the analysis of the dynamics of grating growth are discussed. From these considerations, the properties of superimposed chirped grating structures are predicted so that the reflection spectrum of a set of chirped gratings can be optimised. Several techniques for the manufacture of constant-periodicity and chirped Bragg gratings are analysed, including the novel prism interferometer technique for the production of wavelength-tunable broad bandwidth chirped gratings with controllable characteristics that was developed during this research program. The application of this technique for the production of broad bandwidth Fabry-Pérot cavities made of sets of superimposed chirped gratings is considered in detail.

## 4.2 Overview of properties and general theory of in-fibre Bragg gratings.

Photoinduced in-fibre Bragg gratings are periodic or quasi-periodic patterns of refractive index modulation inside the core of an optical fibre. In essence, a Bragg grating is a series of grating planes that acts as a one-dimensional diffraction grating inside the fibre core. A guided lightwave experiences Fresnel reflections from these planes that couple part of the wave into a backward-propagating mode. The fabrication of Bragg gratings in optical fibres relies on the photosensitivity observed when silica-based glasses are exposed to an interference pattern generated by ultraviolet (UV) irradiation having sufficient energy density. The exposure of the fibre core to the UV interference pattern leads to the formation of grating planes that appear as regions of increased refractive index at locations of interference maxima.

The principal feature of uniformly-periodic Bragg gratings is that the spectral distribution of the back-coupled light is resonant with a wavelength determined by the periodicity  $\Lambda$  of the core refractive index modulation according to the equation  $\lambda_B = 2n_{eff}\Lambda$ , where  $n_{eff}$  is the effective refractive index of the fibre core and  $\lambda_B$  is the Bragg resonance wavelength of the grating.

Bragg gratings of this type serve as narrow-bandwidth filters and are employed in a wide variety of applications including sensing applications based on wavelength-encoding schemes [Kersey *et al.*, 1992, Melle *et al.*, 1993, Rao *et al.*, 1995]. On the other hand, for a large range of applications, including the Fabry-Pérot strain sensor developed in this project, there is a need for in-fibre reflectors with a broad spectral reflection bandwidth. Fibre reflectors of this type can be provided by fusion splicing mirror-coated fibre ends or by writing broad bandwidth chirped gratings. The "chirp", or effective broadening of the Bragg reflection resonance, can be achieved by introducing a variation in the periodicity and/or amplitude of refractive index modulation along the grating length either during or after the UV exposure. The properties of uniformly-periodic and chirped Bragg gratings are considered throughout this chapter together with their production techniques and methods of their analysis and design.

### 4.2.1 General characteristics of fibre Bragg gratings. Approaches to the theoretical analysis of Bragg gratings.

The fundamental optical properties of in-fibre Bragg gratings that must be understood to enable the design, production and subsequent use of gratings are the peak reflection wavelength and spectral distribution of reflectivity. The properties of in-fibre Bragg gratings depend on the parameters of the optical fibre waveguide, the exposure technique, duration of exposure, and the characteristics of the UV beam used. The primary factors that determine the Bragg resonance wavelength of the grating, its peak reflectivity and reflection bandwidth are the periodicity of the UV interference pattern, the value of the induced core refractive index modulation, and the length of the exposed section of the fibre. Other principal parameters affecting the optical properties of gratings are: the presence (or absence) of a variation in either the grating period or the amplitude of index modulation along its length, the effective value of the core refractive index (RI), the degree of photosensitivity of the fibre, the index modulation profile, the method and geometry of exposure, and the temporal and spatial coherence properties of the writing UV beam. Many of the features of Bragg gratings related to their spectral and phase response are inter-dependent and are very sensitive to the fabrication conditions and design parameters. Thus, care is necessary in analysing and designing Bragg gratings in order to suit the specific application requirements.

The light reflected from a Bragg grating is a direct consequence of coupling between the forward-propagating and backward-propagating guided modes of the fibre initiated by the refractive index perturbations in the fibre waveguide. The spectral reflection and modal coupling properties of Bragg gratings may be analysed by coupled-mode theory [Yariv, 1973]. This method of analysis can also account for the effect of light coupling into the cladding and radiation modes [Katzir *et al.*, 1977]. Analytical solutions of the coupled-mode equations can be obtained in the case of a strictly periodic uniform grating structure, while numerical calculations can be applied to chirped Bragg gratings with axially non-uniform periodicity and/or index modulation depth. Throughout this chapter, coupled-mode analysis is applied to uniform and non-uniform Bragg grating structures including multiple superimposed non-uniform chirped grating structures.

A widely used alternative method for the analysis of chirped Bragg gratings is the scattering matrix method [Kim and Garmire, 1992] in which the nonuniform grating structure is subdivided into a series of small uniform segments, each characterised by its length  $L_i$ , core refractive index  $n_i$ , period  $\Lambda_i$ , and coupling coefficient  $k_i$ . In this method, the complex electric field amplitudes of the two counter-propagating guided modes of a fibre waveguide are

calculated at the input and output of every segment  $i$  of the grating structure and each segment is characterised by its own transmission matrix  $T^{(i)}$  defined as

$$\begin{bmatrix} b_i^{out} \\ a_i^{out} \end{bmatrix} = \begin{bmatrix} T_{11}^i & T_{12}^i \\ T_{21}^i & T_{22}^i \end{bmatrix} \begin{bmatrix} a_i^{in} \\ b_i^{in} \end{bmatrix}, \quad (4.1)$$

where  $a_i^{in}$ ,  $b_i^{in}$ ,  $a_i^{out}$ , and  $b_i^{out}$  are complex electric field amplitudes of the two waves  $a(z,t)$  and  $b(z,t)$  at the input and output of the section  $i$  of the grating structure. The transmission matrix of the whole grating in this method is calculated as a matrix product of all the individual transmission matrices of segments. The elements of the transmission matrix of each grating segment are obtained from the scattering matrix of segment  $S^{(i)}$  that is defined as follows:

$$\begin{bmatrix} b_i^{in} \\ b_i^{out} \end{bmatrix} = \begin{bmatrix} S_{11}^i & S_{12}^i \\ S_{21}^i & S_{22}^i \end{bmatrix} \begin{bmatrix} a_i^{in} \\ a_i^{out} \end{bmatrix}. \quad (4.2)$$

The elements of the scattering matrix of each uniform grating section are obtained using the analytical solutions of the coupled-mode equations for the uniform grating. For example,  $S_{11} = S_{22}$  since, from the above definition, the diagonal matrix elements  $S_{kk}$  are simply the grating reflection coefficients for each uniform section, and  $S_{12} = S_{21}$  since elements  $S_{kl}$  of the scattering matrix are the transmission coefficients of a grating section.

The elements of the transmission matrix are calculated from the scattering matrix in the following way [Yamada and Sakuda, 1987, Cruz *et al.*, 1996]:

$$\begin{aligned} T_{11}^i &= S_{21}^i - S_{22}^i S_{11}^i / S_{12}^i, & T_{12}^i &= S_{22}^i / S_{12}^i, \\ T_{21}^i &= -S_{11}^i / S_{12}^i, & T_{22}^i &= 1 / S_{12}^i. \end{aligned} \quad (4.3)$$

Therefore, the matrix method of grating analysis still relies on the coupled-mode theory and uses the exact analytical solutions of coupled-mode equations for each small segment of a nonuniform grating. The precision of this analysis depends ultimately on the number of segments chosen to represent the uniform sections of the grating.

Another method of nonuniform grating analysis that was used predominantly throughout this study involved the numerical solution of a modified set of coupled-mode equations [Okamoto *et al.*, 1993]. In this method, the set of coupled-mode equations is modified to account for the effects of variation in the periodicity of the grating and the amplitude of RI

modulation. This method uses the integration of phase changes acquired by the propagating modes over the length of the grating and avoids extensive calculations of the multiple matrix products whilst retaining the degree of precision similar to that of the matrix method. The accuracy of the numerical solution of coupled-mode equations depends on the size of integration step used during the calculations. The 5<sup>th</sup>-order Runge-Kutta method was used in this study to obtain the numerical solutions of a set of modified coupled-mode equations. The numerical calculations with this method produce values of real and imaginary parts of the electric field amplitude reflection coefficient for an arbitrary wavelength of light incident on the grating structure.

## 4.2.2 Coupled-mode theory analysis of uniform constant-periodicity Bragg gratings.

Constant-periodicity Bragg gratings are characterised by a cosine pattern of refractive index modulation within the optical fibre core. In general, the amplitude of this modulation is a function of position along the grating length and it is determined by the distribution of optical power within the writing UV beam, method of grating exposure and the degree of fibre photosensitivity. To simplify analysis, the non-uniformity of the index modulation amplitude is often ignored, and the visibility of the replicating interference pattern is often assumed unity. The grating is then characterised by a constant-amplitude cosine pattern of uniform index modulation. In order to analyse the nonuniform gratings in the subsequent parts of this chapter, we will use a more general description for the core refractive index modulation profile as represented by the equation [Mizrahi and Sipe, 1993]

$$n(z) = n_{eff} + \Delta n(z) \left\{ 1 + V \cos\left(\frac{2\pi z}{\Lambda}\right) \right\}, \quad 0 \leq z \leq L_G, \quad (4.4)$$

where  $n_{eff}$  is the effective refractive index of an unperturbed fibre,  $z$  is the position coordinate along the grating,  $\Lambda$  is the grating period,  $\Delta n(z)$  is the envelope function for the induced index change,  $L_G$  is the grating length and  $V$  is the visibility of the interference pattern used for producing the Bragg grating. In a more general case, the visibility factor must be replaced by the visibility profile function  $V(z)$  that is calculated by taking into account the geometry of exposure and the spatial coherence function characterising the UV writing beam. In order to obtain the exact analytic form of the solution of the coupled-mode equations, we will simplify the index modulation profile inside the constant-periodicity Bragg grating and use the following averaging approach to represent the RI modulation:

$$n(z) = n_{eff} + \Delta n \left[ 1 + \cos\left(\frac{2\pi z}{\Lambda}\right) \right], \quad 0 \leq z \leq L_G, \quad (4.5)$$

where  $\Delta n$  is the average value of the RI modulation amplitude that in this model is assumed constant over the grating length.

Figure 4.1 shows the modulated index of refraction according to model (4.4) for a constant-periodicity Bragg grating. The index modulation profile of model (4.4) is compared to the refractive index variation described by the simplified model of a uniform grating (4.5).

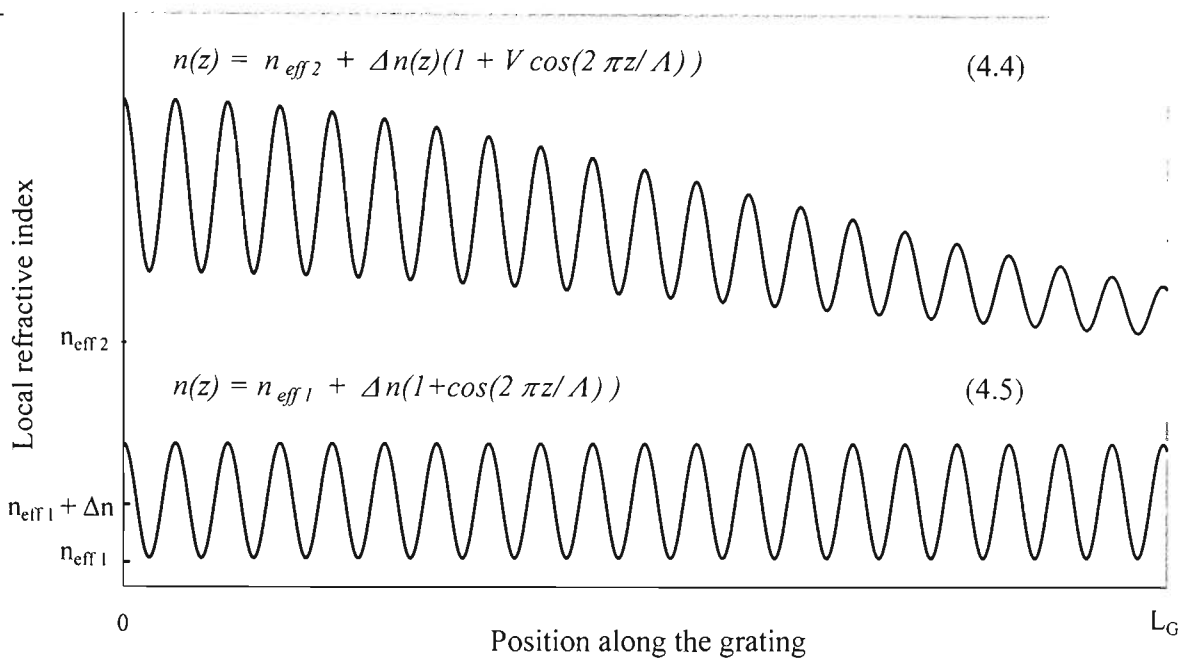


**Figure 4.1** Profiles (4.4) and (4.5) for the RI modulation inside a Bragg grating. The model (4.4) assumes a Gaussian function for the envelope of index modulation and a UV fringe visibility value  $V = 0.5$ .

The graph of index modulation profile predicted by model (4.4) shows the presence of a Gaussian envelope for the local RI modulation amplitude caused by the intensity distribution of the writing beam. The function of induced index change  $\Delta n(z)$  obtained assumed the index change was proportional to the local intensity value. Another important feature of the graph is the presence of an increase in the fibre refractive index caused by the non-ideal visibility value ( $V = 0.5$ ) for the fringe pattern. The sharpness of index modulation is always non-ideal in practice due to the effect of limited spatial coherence of the UV writing beam. A constant-periodicity Bragg grating with index modulation profile of (4.4) could be fabricated, for example, by using the prism interferometer technique (reported by Zhang *et al.*, 1994 and

illustrated in section 4.3.2), which utilises a folded beam with a Gaussian intensity profile. In order to produce a grating with a uniform index modulation profile (4.5), a diffraction phase mask method (reported by Hill *et al.*, 1993) could be used, and an apertured UV beam with a uniform top-hat intensity distribution would be required.

We will also assume for our grating analysis that the index perturbation exists only within the fibre core and consider only the process of energy exchange taking place between the forward-propagating and the backward-propagating LP<sub>01</sub> modes caused by the presence of a periodic index perturbation in the fibre waveguide. Therefore, we neglect the effects of lightwave energy being coupled into the cladding modes and radiation modes of the fibre. The process of contradirectional coupling between the guided LP<sub>01</sub> waveguide modes is responsible for the effect of grating reflectivity and is very well described by the coupled-mode formalism [Yariv, 1973]. Consider two counter-propagating electromagnetic waves in an unperturbed fibre waveguide, that are represented by the guided LP<sub>01</sub> fibre modes, and described by the equations

$$\begin{aligned} a(z,t) &= A(z) \exp[j(\omega_a t + \beta_a z)], \\ b(z,t) &= B(z) \exp[j(\omega_b t - \beta_b z)]. \end{aligned} \quad (4.6)$$

In this case the complex electric field amplitudes  $A$  and  $B$  of the two waves (eigenmodes of the unperturbed fibre waveguide) propagating in the region with no index perturbations can be considered constant. In the region of fibre with index perturbations present (within the Bragg grating), the complex electric field amplitudes will, however, become functions of the longitudinal coordinate  $z$  due to the process of energy exchange (coupling) between the two counter-propagating modes. According to coupled-mode theory, the complex field amplitudes of the two counter-propagating waves  $A(z)$  and  $B(z)$  obey the following relationships:

$$\begin{aligned} \frac{dA}{dz} &= k_{ab} B(z) \exp(-j \Delta z), \\ \frac{dB}{dz} &= k_{ab}^* A(z) \exp(j \Delta z), \end{aligned} \quad (4.7)$$

where  $k_{ab}$  is termed the coupling coefficient, and  $\Delta$  is the phase-mismatch constant given by  $\Delta = \beta_a - \beta_b - 2\pi m/\Lambda$ , where  $m$  is the diffraction order and is unity for the case of interest.

In order to analyse the spectral dependence of the grating power reflectivity, the set of equations (4.7) can be rewritten taking into consideration one incident LP<sub>01</sub> mode  $b(z,t)$  of frequency

$\omega$  corresponding to the vacuum wavelength  $\lambda$  and the wavevector  $\beta = 2\pi n_{eff}/\lambda$ , and a reflected mode  $a(z,t)$  characterised by the same frequency  $\omega$  and a wavevector  $(-\beta)$ . The value of the grating coupling coefficient is given by the relationship  $k = \pi \Delta n \eta / \lambda_B$ , where  $\eta$  is the fraction of the fundamental mode intensity contained within the fibre core and  $\lambda_B = 2n_{eff}\Lambda$  is the wavelength of the Bragg resonance [Meltz et al., 1989]. The wavevector detuning from the Bragg resonance  $\Delta\beta = \beta - \pi/\lambda$  is another parameter commonly used in this analysis in place of the phase mismatch constant  $\Delta$  from (4.7). The relationship between them is  $\Delta = 2(\Delta\beta)$ .

In order to define the boundary conditions for the solution of this system of differential equations, assume that the guided LP<sub>01</sub> mode of the fibre described by the function  $b(z,t)$  from (4.6) is incident at  $z = 0$  on the constant period Bragg grating which extends from  $z = 0$  to  $z = L_G$ . Since the counter-propagating mode  $a(z,t)$  is generated by the index perturbations within the grating, we have  $A(L_G) = 0$ .

The amplitude reflection coefficient  $r$  of a grating is a complex function defined in accordance with the above boundary conditions by the relationship

$$r = \frac{A(0)}{B(0)}, \quad (4.8)$$

where  $A(0)$  and  $B(0)$  are complex electric field amplitudes of the reflected wave and the incident wave at the point  $z = 0$ . The power reflection coefficient of the grating is given by

$$R = |r|^2 = \left| \frac{A(0)}{B(0)} \right|^2. \quad (4.9)$$

Using previously defined boundary conditions, the coupled-mode equations (4.7) have an analytical solution of the form [Yariv, 1973]

$$A(z) = B(0) \frac{2jk_{ab} \exp[-j(\Delta \times z/2)]}{-\Delta \times \sinh(SL_G) + 2jS \cosh(SL_G)} \sinh[S(z - L_G)] \quad (4.10)$$

and

$$B(z) = B(0) \frac{\exp[j(\Delta \times z/2)]}{-\Delta \times \sinh(SL_G) + 2jS \cosh(SL_G)} \times \{ \Delta \times \sinh[S(z - L_G)] + 2jS \cosh[S(z - L_G)] \},$$

where the following substitution was performed:

$$S = \sqrt{k^2 - \Delta^2 / 4}, \text{ and} \quad (4.11)$$

$$k \equiv |k_{ab}|.$$

Using equation (4.9) and the previously introduced definition for the wavevector detuning  $\Delta\beta$ , the spectral dependency of the power reflectivity can now be obtained from solutions (4.10) and expressed as a function of wavevector detuning:

$$R = \frac{\sinh^2(SL_G)}{\cosh^2(SL_G) - \left(\frac{\Delta\beta}{k}\right)^2} \quad \text{for } k^2 \geq \Delta\beta^2, \quad (4.12a)$$

$$R = \frac{\sin^2(\alpha L_G)}{\left(\frac{\Delta\beta}{k}\right)^2 - \cos^2(\alpha L_G)} \quad \text{for } k^2 < \Delta\beta^2, \quad (4.12b)$$

where  $S = (k^2 - \Delta\beta^2)^{1/2}$  equivalently to the definition in (4.11), and  $\alpha = (\Delta\beta^2 - k^2)^{1/2}$ .

In the case when the wavelength of incident light in the mode  $b(z,t)$  is equal to the Bragg reflection wavelength of the grating  $\lambda_B = 2n_{eff}A$ , the phase-matching condition occurs, which is characterised by the relationship  $\Delta\beta = 0$ , and then we have:

$$R_B = \tanh^2\left(\frac{\pi \Delta n \eta L_G}{\lambda_B}\right) \quad (4.13)$$

for the power reflectivity of the uniform constant-periodicity Bragg grating at the wavelength of Bragg resonance  $\lambda_B$ .

### 4.2.3 Spectral properties of uniform constant-periodicity Bragg gratings.

The analytic solutions (4.12) allow the spectral reflection response to be plotted for an arbitrary constant-periodicity Bragg grating provided the amplitude of index modulation is uniform. The effect of three principal design parameters for this type of grating (grating periodicity, length and amplitude of RI modulation) can therefore be considered. Understanding the role of these parameters is crucial for all applications and the simplest case of a uniform constant-periodicity grating provides the general basis for understanding the spectral behaviour of more complicated grating structures.

Typical spectral responses for the grating reflectivity calculated on the basis of coupled-mode theory and the dependency of grating reflectivity at the Bragg resonance wavelength on the amplitude of refractive index modulation are presented in this section.

Figure 4.2 shows the spectral reflection response of a 4 mm-long constant-periodicity Bragg grating at a wavelength of 1552.2 nm calculated using the solutions (4.12) of the system of coupled-mode equations (4.7).

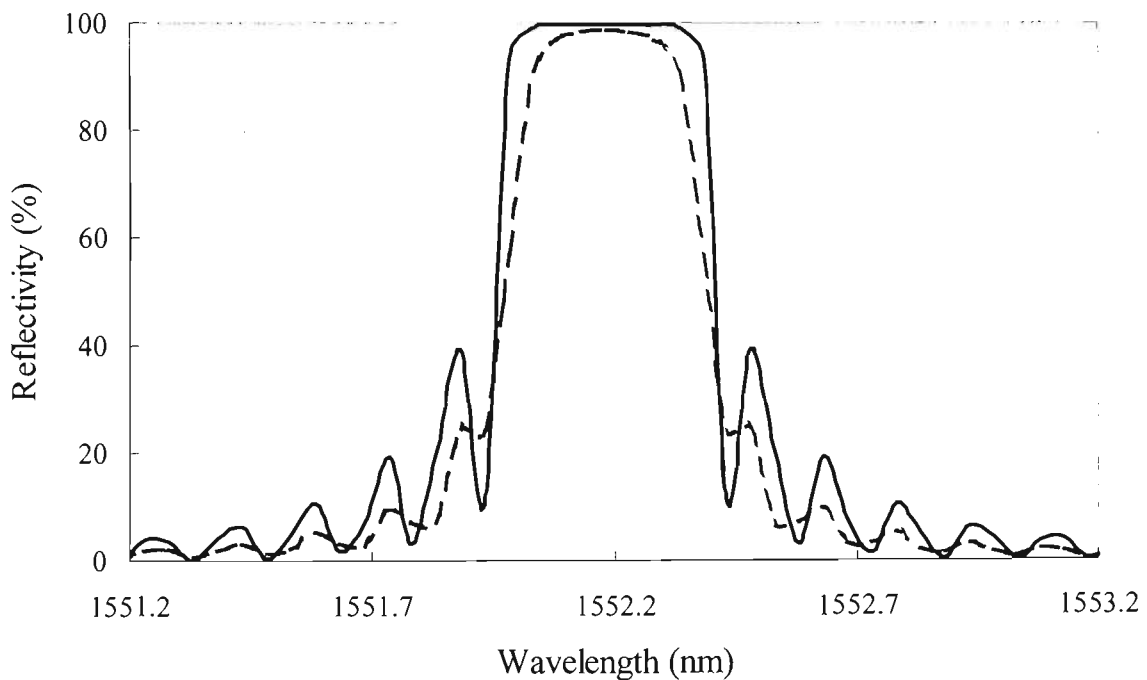


**Figure 4.2** *Calculated spectral responses for the reflectivity of a uniform constant-periodicity Bragg grating at 1552.2 nm (solid line) and of the same grating with apodization of index profile imposed (dashed line). The apodized grating is modelled assuming a Gaussian beam intensity distribution, the index change being proportional to the local intensity and exposure in a prism interferometer configuration. The maximum amplitude of RI change in an apodized grating is modelled equal to the uniform value of  $\Delta n = 0.0005$  and is decreased by a factor of  $e$  at  $z = L_G = 4$  mm.*

The effect of apodization (a smooth reduction in the amplitude of RI modulation, in this case, from  $z = 0$  towards  $z = L_G$ ) on the spectral reflection properties of this grating is also shown. Both plots have been obtained through numerical solution of coupled-mode equations accounting for variations in the value of local coupling coefficient in the case of an apodized grating. A Gaussian writing beam intensity profile is assumed in the model together with the proportional dependency of the local change in refractive index on the local UV intensity. The peak value of RI modulation (at  $z = 0$ ) for the apodized grating is assumed equal to the RI modulation amplitude of 0.0005 within the uniform grating. The apodization reduces the sidelobes of the spectral reflection response and slightly reduces the FWHM bandwidth thus improving the narrow-bandwidth filtering property of the grating.

The graphs in Figure 4.3 show the dependency of the grating reflectivity at the Bragg reflection peak on the amplitude of RI modulation for different values of the grating length. The amplitudes of RI modulation are assumed constant along the grating length for all three plots. In practical grating manufacturing situations, these dependencies can be used to evaluate the RI modulation amplitudes achieved within the uniform constant-periodicity gratings if the grating reflectivity is monitored during inscription.

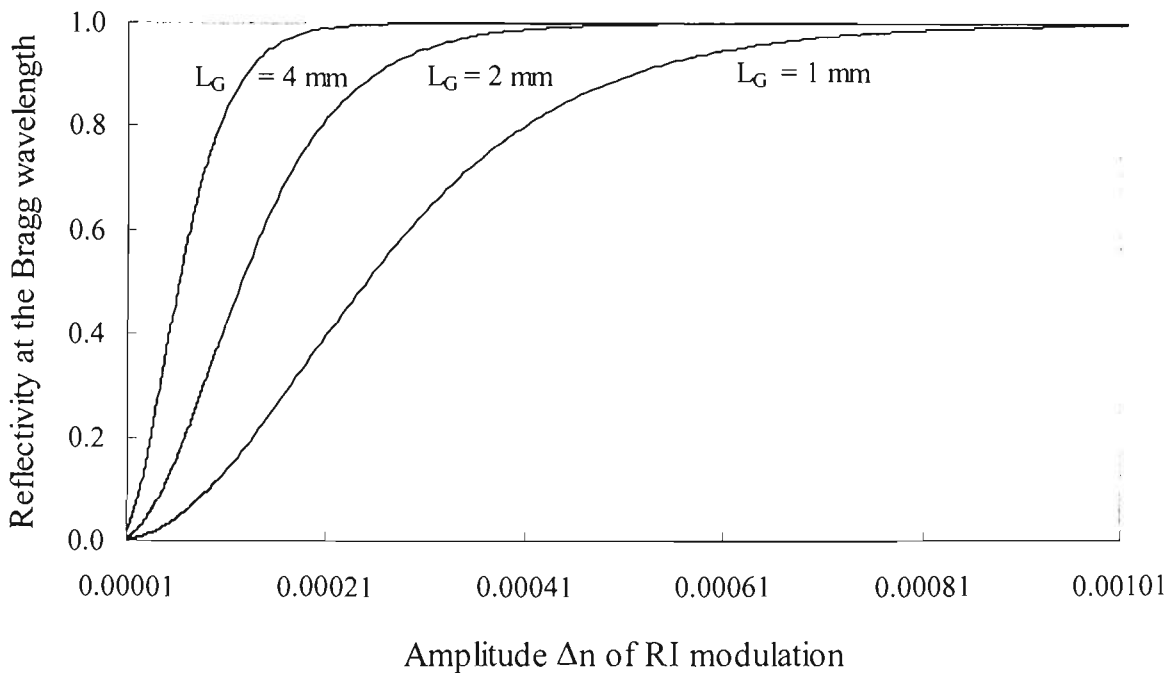


**Figure 4.3** *Dependency (4.13) of grating reflectivity at the Bragg resonance wavelength on the amplitude of RI modulation for a uniform constant-periodicity grating written at 800 nm.*

The spectral bandwidth of a Bragg grating is one of the most important properties that determines the suitability of a grating for a chosen application. It is characterised by the full width at half maximum of the spectral response (FWHM spectral bandwidth). This parameter in the case of a uniform constant-periodicity grating is given by [Russell *et al.*, 1993]:

$$\Delta\lambda_{FWHM} = \varepsilon\lambda_B \sqrt{\left(\frac{\Delta n}{2n_{eff}}\right)^2 + \left(\frac{1}{N}\right)^2}, \quad (4.14)$$

where  $N$  is the number of RI modulation planes and  $\varepsilon$  is a parameter that varies between approximately 0.5 for weak gratings ( $\Delta n < 10^{-3}$ ) and 1.0 for strong gratings. It is interesting to consider the two extreme cases of equation (4.14). In the case of a very long grating, when  $N \gg 2n_{eff}/\Delta n$ , the FWHM reflection bandwidth is approximated by the relationship

$$\Delta\lambda_{FWHM} \approx \varepsilon \Delta n \Lambda, \quad (4.15)$$

showing that the FWHM bandwidth is proportional to  $\Delta n$  but is independent of number of grating planes. Physically, in this case most of the incident optical power within the grating reflection bandwidth is reflected by a finite number of grating planes in the front section of the structure, thus rendering the spectral bandwidth of the device insensitive to further increase in the number of index modulation planes.

In the case of a short Bragg grating, when  $N \ll 2n_{eff}/\Delta n$ , the FWHM reflection bandwidth becomes

$$\Delta\lambda_{FWHM} \approx \frac{2\varepsilon n_{eff} \Lambda}{N}, \quad (4.16)$$

showing that the FWHM reflection bandwidth depends strongly on the number of grating planes and is independent of the RI modulation amplitude.

Analysis of relationships (4.15) and (4.16) shows that in the case of constant-periodicity Bragg gratings, the maximum FWHM spectral reflection bandwidth is limited to values of the order of magnitude of 1 nm, due to the limited achievable levels of RI modulation amplitudes and constraints regarding the typical values of grating periodicity and length. For example, if a strong 1 mm-long constant-periodicity grating is written at  $\lambda_B = 1550$  nm with a uniform index

modulation amplitude of  $\Delta n = 0.001$  and the effective index of fibre core is  $n_{eff} = 1.46$ , the FWHM bandwidth of this grating calculated from (4.14) will be  $\Delta\lambda_{FWHM} = 0.98$  nm, assuming  $\varepsilon$  is unity. Broader spectral reflection bandwidths are achievable if the grating is chirped, with either periodicity, index modulation amplitude, or waveguide shape varied along its length.

#### 4.2.4 Analysis of chirped Bragg gratings.

The reflectivity spectrum of an arbitrary chirped grating, a set of superimposed chirped gratings, or a Fabry-Pérot cavity formed by a pair of chirped Bragg gratings can be predicted using coupled-mode theory. We will consider a method [Okamoto *et al.*, 1993] for calculating the power reflectivity and the phase of reflection coefficient at any wavelength by solving numerically a differential equation derived from the system of coupled-mode equations. This is a modification of the set of coupled-mode equations (4.7) that takes into account the effects of variations in the grating periodicity and the amplitude of RI modulation. The spectral response of a chirped grating is calculated by incorporating the chirping profile function (variation of the local periodicity of RI modulation within the grating structure in the case of predominantly periodicity-induced bandwidth increase), and the amplitude profile of index modulation into the coupled-mode formalism. Index modulation variations are accounted for by having the local value of the coupling coefficient dependent on the local amplitude of the RI modulation. Throughout this study, broad reflection bandwidth chirped gratings produced by varying the grating periodicity have been used and characterised with this modified coupled-mode approach. The variation in the grating periodicity therefore had a dominant effect on the grating bandwidth, and, as in most practical cases, this was also affected by variations in the amplitude of the index modulation. This was accounted for by calculating the expected index modulation profile using the assumption of a Gaussian intensity distribution for the writing UV beam and a separate model for the dynamics of grating growth, described in section 4.3.5. The present approach also works for constant-periodicity Bragg gratings with uniform and non-uniform index modulation profiles.

Consider a chirped grating obtained by the periodicity chirping technique and having the chirping profile function  $A(z)$  describing the variation in local grating periodicity which is dependent on the geometry of exposure. We will also assume a known index modulation profile function  $\Delta n(z)$ .

Firstly, the reflectivity of an arbitrary chirped grating can be calculated using the following system of coupled mode equations [Okamoto *et al.*, 1993]

$$\frac{dA}{dz} = jk(z)B(z)\exp\left[-j\int_0^z(\beta_A(\xi) - \beta_B(\xi) - \Omega(\xi))d\xi\right], \quad (4.17a)$$

$$\frac{dB}{dz} = -jk(z)A(z)\exp\left[j\int_0^z(\beta_A(\xi) - \beta_B(\xi) - \Omega(\xi))d\xi\right], \quad (4.17b)$$

where  $A(z)$  is the complex electric field amplitude of the backward-propagating wave corresponding to a  $LP_{01}$  waveguide mode,  $B(z)$  is the complex electric field amplitude of the forward-propagating wave along the  $z$  direction, and  $k(z)$  is the local value of the grating coupling coefficient. The functions  $\beta_A(\xi)$  and  $\beta_B(\xi)$  are the local propagation constants of the waves  $A$  and  $B$ , and  $\Omega(\xi)$  is the function describing the local spatial frequency of the grating.

For the case of interest (periodicity chirping), when the variations in the index modulation amplitude along the grating length are slow, small and aperiodic, assuming a cosinusoidal modulation of the core refractive index, the local coupling coefficient can be represented by the function

$$k(z) = \pi\Delta n(z)\eta/\lambda_B(z), \quad (4.18)$$

where  $\eta$  is the fraction of the fundamental mode intensity contained within the fibre core,  $\Delta n(z)$  is the local amplitude of refraction index modulation and  $\lambda_B(z)$  is the local value of the Bragg reflection wavelength at point  $z$ .

In the general case (for the effective index and/or periodicity chirping), the  $z$ -dependencies of the propagation constants and the spatial frequency of the grating can be separated from the constant parts as

$$\beta_A(z) - \beta_B(z) - \Omega(z) = \beta_1 - \beta_2 - \frac{2\pi m}{\Lambda(z)} - \Theta(z), \quad (4.19)$$

where  $\beta_1$  and  $\beta_2$  are the constant parts of the propagation constants of the waves  $A$  and  $B$ ,  $m$  is the diffraction order and  $\Theta(z)$  is the function describing the  $z$ -dependencies of the propagation constants and the spatial frequency of the grating. For the first-order Bragg reflection,  $m = 1$ , and  $\beta_1 = -\beta_2 = 2\pi m_{\text{eff}}/\lambda$ .

For the case of periodicity chirping, when  $\Lambda(z)$  is known, the integral in equations (4.17) can be modified as follows:

$$\sigma(z) = \int_0^z [\beta_A(\xi) - \beta_B(\xi) - \Omega(\xi)] d\xi = \int_0^z [2\beta - 2\pi / \Lambda(\xi)] d\xi. \quad (4.20)$$

The function  $\sigma(z)$  represents the local phase difference between waves  $A$  and  $B$  accumulated due to propagation within a perturbed length of waveguide and the effect of diffraction from grating planes separated according to periodicity function  $\Lambda(z)$ . It has an equivalent representation of the form

$$\sigma(z) = 2\varphi z - \theta(z), \quad (4.21)$$

where the function  $\varphi(z)$  describes the local wavevector detuning from the Bragg resonance and  $\theta(z)$  is the integral of the function  $\Theta(z)$ :

$$\theta(z) = \int_0^z \Theta(\xi) d\xi, \quad (4.22)$$

$$\varphi(z) = \beta - \pi / \Lambda(z) = 2\pi n_{\text{eff}} / \lambda - \pi / \Lambda(z). \quad (4.23)$$

The system of coupled mode equations (4.17a, 4.17b) can now be simplified as follows:

$$\frac{dA}{dz} = -j k(z) B(z) \exp[j\sigma(z)] \quad (4.24a)$$

$$\frac{dB}{dz} = j k(z) A(z) \exp[-j\sigma(z)] \quad (4.24b)$$

The local complex amplitude reflection coefficient  $r(z)$  is defined as follows:

$$r(z) = \frac{A(z)}{B(z)}. \quad (4.25)$$

Now, differentiating (4.25) and using (4.24a) and (4.24b), we get:

$$\frac{dr}{dz} = \frac{1}{B} \frac{dA}{dz} - \frac{A}{B^2} \frac{dB}{dz} = jk(z) \left[ \exp[-j\sigma(z)] + r^2 \exp[j\sigma(z)] \right] \quad (4.26)$$

where  $\sigma(z)$  is defined by the relationship (4.20). This differential equation can be solved numerically using the 5<sup>th</sup>-order Runge-Kutta method. The boundary condition for the solution of this equation is

$$r(L_G) = 0, \quad (4.27)$$

since the grating extends from  $z=0$  to  $z=L_G$ , the incident wave is propagating in the positive  $z$  direction, and the reflected wave is generated by the waveguide perturbations that exist only within the grating. The complex reflection coefficient of the whole grating structure is determined by the value of  $r(0) = A(0)/B(0)$  and the power reflection coefficient of the grating is determined by the square of the absolute value of  $r(0)$ , that is:

$$R = |r(0)|^2 = \text{Re}^2[r(0)] + \text{Im}^2[r(0)] \quad (4.28)$$

The spectral response for the power reflectivity of any given periodicity-chirped grating with a known chirp function  $A(z)$  can now be calculated by solving equation (4.26) numerically under the boundary condition (4.27) for all wavelengths of interest. Calculations of the reflectivity spectra have been performed in this study with integration step sizes of the order of  $L_G/10000$ , yielding high numerical precision not affected by further reduction of step size. During calculations, the complex nature of the amplitude reflectivity function has been taken into account.

The spectral dependency of the phase (modulo  $\pi$ ) of the complex reflection coefficient can be found through the relationship

$$\varphi(\lambda) = \tan^{-1} \left[ \frac{\text{Im}[r(\lambda)]}{\text{Re}[r(\lambda)]} \right] \quad (4.29)$$

### ***Spectral reflection response of a linearly chirped Bragg grating.***

Consider the case of a Bragg grating with a linearly chirped RI modulation periodicity, with a known uniform amplitude of index modulation along the grating length. The chirping profile function of such a grating is represented by the function

$$A(z) = A_{max} - Cz, \quad (4.30)$$

where  $A_{max}$  is the maximum grating pitch (separation between the grating planes), and parameter  $C$  is the rate of (linear) variation of the grating pitch with length. This chirping profile function (4.30) corresponds to the following linear dependency of a local Bragg reflection wavelength on the position along the grating:

$$\lambda(z) = \lambda_{max} - bz, \quad (4.31)$$

where the chirp rate  $b$  (rate of variation in the local Bragg reflection wavelength with position along the grating) is related to parameter  $C$  in equation (4.30) by:

$$b = 2(n_{eff} + \Delta n)C, \quad (4.32)$$

accounting for the post-exposure rise in the effective fibre core refractive index.

Now the function  $\sigma(z)$  that corresponds to the linear chirping profile function as defined by (4.30) and (4.20) can be calculated:

$$\sigma(z) = \int_0^z \left[ 2\beta - \frac{2\pi}{A_{max} - Cz} \right] dz = \frac{4\pi(n_{eff} + \Delta n)z}{\lambda} + \frac{2\pi}{C} \ln \left( 1 - \frac{Cz}{A_{max}} \right). \quad (4.33)$$

Equation (4.33) is to be used when applying the 5<sup>th</sup>-order Runge-Kutta method for the numerical solution of (4.26) with the boundary condition (4.27).

Figure 4.4 shows the calculated spectral response for the reflectivity of a grating with the chirping function characterized by the equation  $\lambda(z) = 680 - 20z$  and a length of 1 mm. The calculation used the values of  $\eta = 0.9$  and the amplitude of refraction index modulation of  $\Delta n = 0.001$ .

The graph of Figure 4.4 represents a characteristic of spectral reflection properties typical of linearly chirped gratings with uniform index modulation profile written in any wavelength region. The relatively "flat" spectral response region for most wavelengths within the grating bandwidth is explained by the constant value of chirp rate (and consequently, the equal number of grating planes that reflect light resonantly within every nanometre of the total reflection bandwidth). The presence of "ripples" is due to the effect of multiple reflections within the grating structure and the slightly varying levels of back-coupling in different grating regions. The appearance of narrow spectral regions of slightly increased reflectivity at the edges of the spectral response function is a consequence of boundary effects created by the abrupt character of the start and end of the perturbed fibre region.

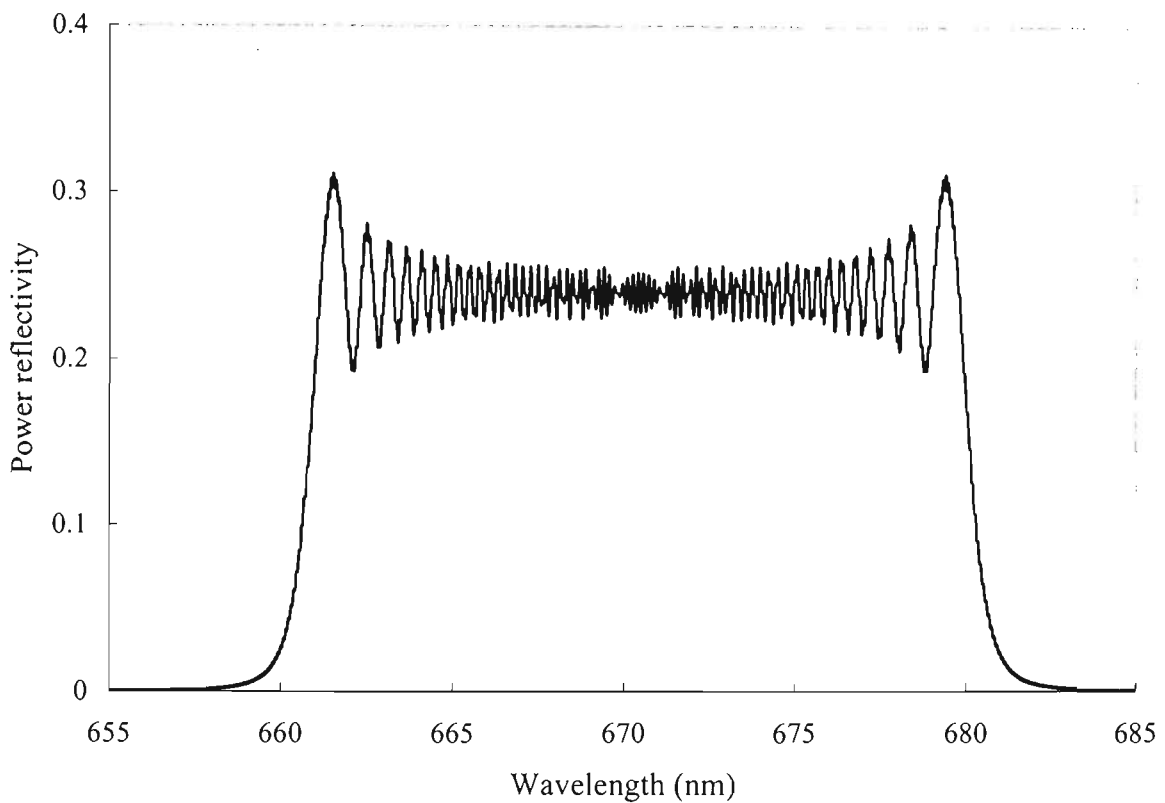


**Figure 4.4** *Calculated spectral distribution of the power reflectivity for a linearly chirped 1 mm-long Bragg grating. The maximum Bragg reflection wavelength is 680 nm and the chirping rate is 20 nm/mm. The value of RI modulation amplitude used in the calculations was  $\Delta n = 0.001$  and was assumed to be constant along the grating length according to the model (4.5). Numerical solution of a system of coupled-mode equations has been performed using an integration step size of  $L_G/10000$ .*

Linearly chirped Bragg gratings have found numerous applications in fibre communications technology, primarily due to their group velocity dispersion characteristics. For many optical fibre applications, their spectral response shape is also optimal since a nearly uniform reflectance can be achieved over a wide wavelength range. However, the technology for fabrication of linearly chirped gratings with uniform levels of reflectivity over a large

bandwidth is rather complicated and costly. For example, a linearly chirped diffraction phase mask can be used if the writing beam is translated along the sufficient length of the mask surface using a high-precision motorised translation stage.

### ***Spectral reflection response of a quadratically chirped Bragg grating.***

The broad reflection bandwidth chirped gratings produced during this research program and utilised in a low-coherence sensing application were manufactured with the prism interferometer technique. The chirping profile function of gratings manufactured in this way is quadratic (as is discussed in section 4.4.2 in more detail). Thus the case of a quadratic chirping function is now considered.

Chirped gratings produced with the right-angle prism interferometer have the following chirping profile function:

$$A(z) = A_{max} - Cz^2, \quad (4.34)$$

that corresponds to the following dependency of the local Bragg reflection wavelength on the position along the grating:

$$\lambda(z) = \lambda_{max} - bz^2, \quad (4.35)$$

where the relationship between parameters  $b$  and  $C$  is the same as in (4.31).

The function  $\sigma(z)$  is again calculated from (4.20) and has the following form:

$$\sigma(z) = \int_0^z \left[ 2\beta - \frac{2\pi}{A_{max} - Cz^2} \right] dz = \frac{4\pi(n_{eff} + \Delta n)z}{\lambda} - \frac{2\pi}{\sqrt{CA_{max}}} \operatorname{Arctanh} \left( z \sqrt{\frac{C}{A_{max}}} \right) \quad (4.36)$$

Equation (4.36) was used for the numerical solution of (4.26) under the boundary condition (4.27) in the case of a quadratic chirp described by (4.34). Figure 4.5 shows the calculated spectral response for a chirped grating characterized by the chirping function of the form  $\lambda(z) = 1552.18 - 1.565z^2$  produced by the right-angle prism interferometer method. The index modulation model (4.4) was used to describe the profile of RI change, with the visibility factor assumed to be unity. The following values of the grating design parameters were used in the

calculations:  $\eta = 0.75$ ,  $\Delta n_{max} = 0.001$  (index modulation amplitude at  $z = 0$ ),  $L_G = 4.1 \text{ mm}$ , half-divergence angle of the writing beam  $\alpha = 0.0624 \text{ rad}$ , distance between the prism hypotenuse face and the beam focus  $d = 35 \text{ mm}$ .

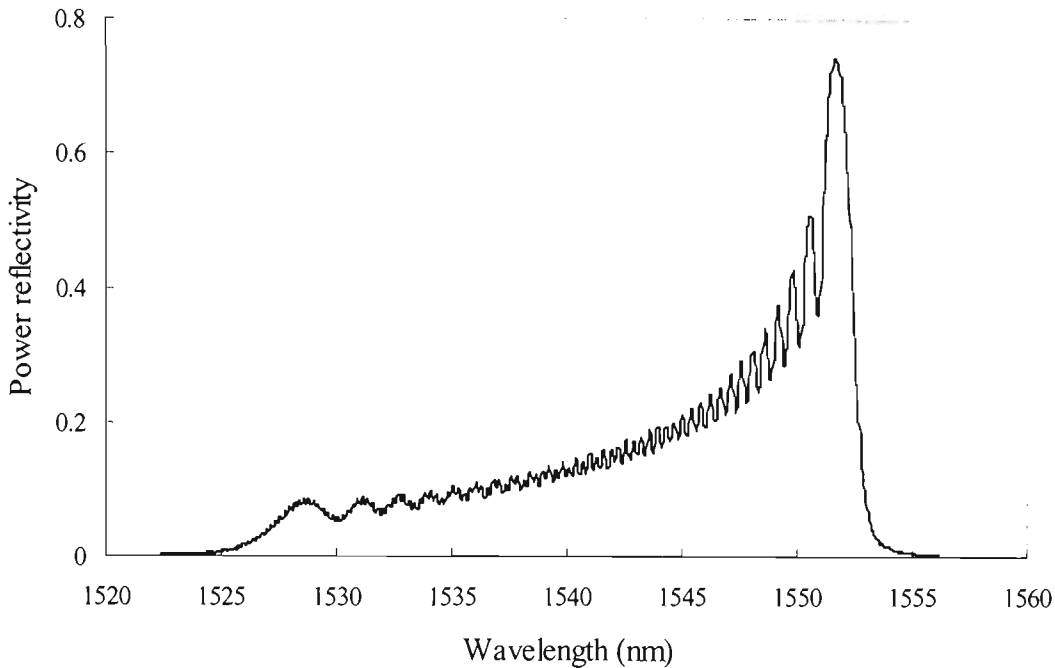


**Figure 4.5** *Calculated spectral distribution of the power reflectivity for a quadratically chirped 4.1 mm long Bragg grating produced with the prism interferometer technique. The maximum Bragg reflection wavelength is 1552.18 nm and the quadratic chirping rate is characterized by  $b = 1.565 \text{ nm/mm}^2$ . The value of RI modulation amplitude is assumed to be proportional to the local Gaussian beam intensity with the peak index modulation amplitude value of  $\Delta n = 0.001$ .*

The decrease of reflectivity in the low-wavelength region of the reflection spectrum observed from the graph of Figure 4.5 is typical for quadratically chirped gratings. The rate of this decrease is dependent on the value of chirping profile coefficient. For the geometry of exposure provided by the prism interferometer chirping technique, one reason for the lower reflectance at shorter wavelengths is that RI modulation amplitudes are smaller in the short wavelength region of the grating. This is caused by the decrease in intensity towards the edge parts of the writing UV beam. A second reason for this reflectivity decrease is common for all possible exposure geometries, since it is provided by the quadratic character of the chirp function which means that the local chirp rate  $d\lambda_B/dz$  is increasing linearly with position  $z$  along the grating. This leads to presence of a smaller number of grating planes for resonantly reflecting every subsequent nanometer of the total reflection spectrum determined by the chirp function and grating length. The reflectivity spectrum of quadratic chirped gratings produced with the prism interferometer technique (discussed in detail later in this chapter) depends strongly on the wavelength region in which the grating is written. This is caused by the dependency of the chirping profile

coefficient on the grating wavelength and exposure parameters. Therefore, there is a possibility of producing gratings with variable (and controllable) shapes of reflection response with the prism technique.

***Spectral reflection response of a Fabry-Pérot cavity formed by two chirped Bragg gratings in the case of coherent illumination.***

The method used above for calculation of reflectivity can be generalised to include the case of a Fabry-Pérot cavity formed inside an optical fibre by two identical chirped gratings with a known chirp function  $A(z)$  and separated by a distance  $d$ . The coupled-mode equations formalism will be applicable in this case if we assume a high degree of coherence for the light incident on the Fabry-Pérot cavity and introduce a generalised chirp function that treats a fibre Fabry-Pérot as an extended chirped grating. This approach to the numerical calculation of reflectivity is useful for the design of fibre Fabry-Pérot interferometers based on arbitrary Bragg grating structures and allows modelling of the spectral properties of fibre Fabry-Pérots for various applications. As discussed below, the Fabry-Pérot reflectivity spectrum obtained with this method can also provide useful information in the case when the structure is illuminated with incoherent light.

The geometry and boundary conditions for a chirped grating fibre Fabry-Pérot cavity are shown in Figure 4.6. According to the diagram, we denote the length of each Bragg grating as  $L_G$ , and the length of an unperturbed section of fibre (spacing between the gratings) as  $d$ . The complex electric field amplitudes for the incident and reflected waves at point  $z$  are denoted as  $A(z)$  and  $B(z)$  respectively.

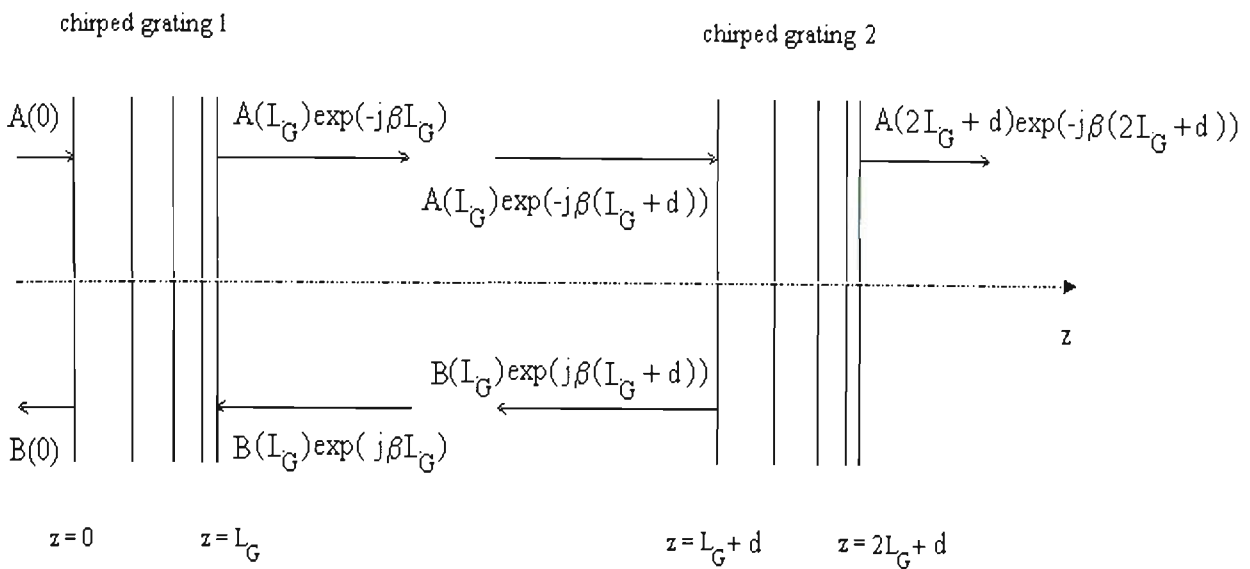


**Figure 4.6** *Contradirectional coupling for a Fabry-Pérot cavity formed by two identical chirped Bragg gratings. Illumination is from the left.*

The boundary conditions for the complex field amplitudes in this case are as follows:

$$A = A(0), \quad B = B(0) \quad \text{at} \quad z = 0,$$

$$A = A(L_G) \exp(-j\beta L_G), \quad B = B(L_G) \exp(j\beta L_G) \quad \text{at} \quad z = L_G, \quad (4.37)$$

$$A = A(L_G) \exp(-j\beta(L_G + d)), \quad B = B(L_G) \exp(j\beta(L_G + d)) \quad \text{at} \quad z = L_G + d,$$

$$A = A(2L_G + d) \exp(-j\beta(2L_G + d)), \quad B = 0 \quad \text{at} \quad z = 2L_G + d.$$

The local complex reflection coefficient of the structure is defined as  $r(z) = B(z)/A(z)$ , as usual. The boundary conditions (4.37) account for the change of phase of forward- and backward-propagating waves taking place in an unperturbed part of the fibre between the gratings. It is also assumed that there is no reflected wave for the region of  $z \geq (2L_G + d)$ .

The approach for calculating the spectral response of power reflectivity for this Fabry-Pérot structure is the same as that already used for the case of a single chirped grating. A generalised fringe periodicity function for the Fabry-Pérot structure is introduced in the following way:

$$A_{FP}(z) = \begin{cases} A(z), & \text{for } 0 \leq z \leq L_G, \\ \infty, & \text{for } L_G < z < L_G + d, \\ A(z), & \text{for } L_G + d \leq z \leq 2L_G + d, \end{cases} \quad (4.38)$$

where  $A(z)$  is the chirping profile function of gratings 1 and 2. This definition of the function  $A_{FP}(z)$  allows modification of the differential equation (4.26) so as to calculate the power reflectivity of a Fabry-Pérot structure in a similar way to the case of a single chirped grating. However, the function  $\sigma(z)$  from (4.20) has to be modified in order to account for the generalisation of the fringe periodicity function. The function  $\sigma(z)$  is replaced with the function  $\sigma_{FP}(z)$  which is defined as follows:

$$\sigma_{FP}(z) = \int_0^z \left[ 2\beta - \frac{2\pi}{\Lambda_{FP}(\xi)} \right] d\xi \quad (4.39)$$

Since the function  $A_{FP}(z)$ , by its definition, has only a finite number (two) of discontinuity points within the perturbed fibre region (at  $z = L_G$  and  $z = L_G + d$ ), the interval of integration in (4.39) can be subdivided into three intervals and  $\sigma_{FP}(z)$  can be calculated as follows:

$$\sigma_{FP}(z) = \int_0^z (2\beta) d\xi - \int_0^{L_G} \frac{2\pi}{\Lambda(\xi)} d\xi - \int_{L_G+d}^z \frac{2\pi}{\Lambda(\xi)} d\xi. \quad (4.40)$$

Equation (4.40) is used in numerical calculations for values of  $z$  between  $(L_G + d)$  and  $(2L_G + d)$  since it includes the effect of both chirped gratings on the change in phase of the forward-propagating and backward-propagating waves.

The last integral in (4.40) can be calculated using a different set of integration limits to simplify the calculation of the value of  $\sigma_{FP}(z)$ :

$$\sigma_{FP}(z) = 2\beta z - \int_0^{L_G} \frac{2\pi}{\Lambda(\xi)} d\xi - \int_0^{z-L_G-d} \frac{2\pi}{\Lambda(\xi)} d\xi. \quad (4.41)$$

The first term in (4.41) accounts for the change in phase due to propagation through the fibre core, the second term describes the phase change caused by the grating planes within grating 1, and the third integral stands for the effect of grating 2. Therefore, in numerical calculations, the

third integral term is only used for values of  $z$  between  $(L_G+d)$  and  $(2L_G+d)$ . The first two terms in (4.41) are used for calculations in the region of  $z$  values between  $z = L_G$  and  $z = (L_G+d)$  since the first integral accounts for the overall effect of chirped grating 1.

For values of  $z$  between  $z = 0$  and  $z = L_G$ , the function  $\sigma_{FP}(z)$  is taken to be identical in its form to the function  $\sigma(z)$  from equation (4.20) describing the effect of local periodicity of grating 1.

The complex reflection coefficient of the structure,  $r(z)$  can be found now, as before, by numerically solving the modified equation (4.26):

$$\frac{dr}{dz} = jk(z) \left[ \exp(-j\sigma_{FP}) + r^2 \exp(j\sigma_{FP}) \right] \quad (4.42)$$

starting from an initial condition of the form  $r(2L_G+d) = 0$  and taking into account the boundary conditions at the points  $z = L_G$  and  $z = (L_G+d)$  that give the following relationship for the complex reflection coefficient values  $r(L_G)$  and  $r(L_G+d)$ :

$$r(L_G) = r(L_G + d) \exp(-2j\beta d) \quad (4.43)$$

Relationship (4.43) shows that the unperturbed section of the fibre between the points  $z = L_G$  and  $z = (L_G+d)$  rotates the vector  $r(z)$  in the complex plane by the angle  $(-2\beta d)$  leaving its modulus unchanged due to the absence of grating planes in this region. The condition (4.43) is used for the numerical solution of (4.42). The other fact that is taken into account is the variation of the function  $\sigma_{FP}(z)$  between the three regions along the structure length.

The quantity of interest, namely the value of power reflectivity of the Fabry-Pérot structure for any wavelength of interest  $R(\lambda)$ , is represented by the square of the absolute value of  $r(0)$  and the spectral response can be obtained through evaluating the power reflectivity for all values of wavelength of coherent incident light in the spectral region of choice.

Figure 4.7 shows the result of numerical calculations for the reflection spectrum of a Fabry-Pérot cavity formed by two identical quadratically chirped Bragg gratings separated by a distance of  $d = 0.5$  mm. The comb-like character of the calculated spectral reflectivity (in the case of coherent incident light) is typical of a Fabry-Pérot structure under coherent illumination. The spectral response of this Fabry-Pérot structure under incoherent illumination is also shown and is calculated from the spectral response of a single chirped grating reflector by assuming that no multiple reflections occur within the cavity. Spectral properties of a Fabry-Pérot filter

fabricated with chirped Bragg gratings can therefore be studied with the help of coupled-mode theory.

The distribution of average reflectivity values for every fringe of the comb-like reflection function (in the coherent case) follows the shape of the spectral response of a Fabry-Pérot structure in the case of incoherent illumination.

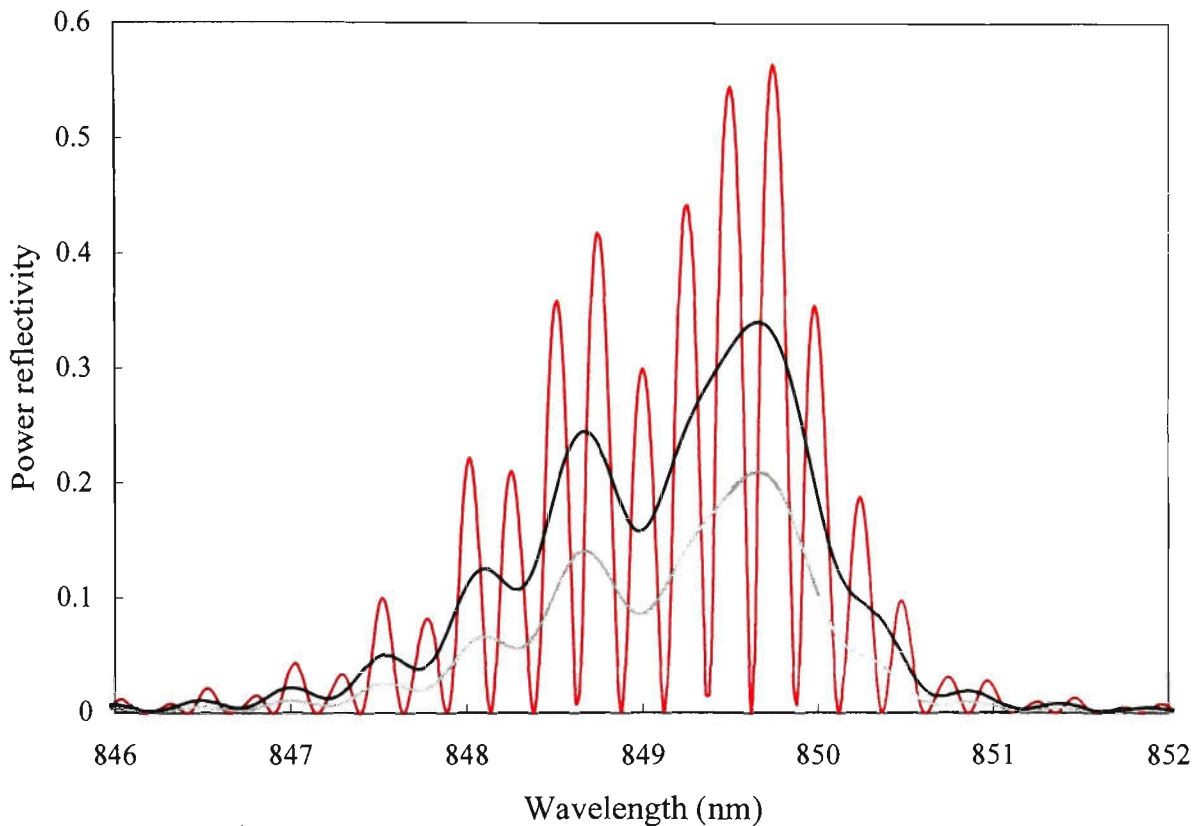


**Figure 4.7** *Spectral reflection responses (in cases of coherent and incoherent illumination) of a FP cavity formed by two identical quadratically chirped Bragg gratings. Grating separation is 0.5 mm, and grating parameters have the following values: maximum Bragg wavelength 850 nm, amplitude of RI modulation 0.0005, chirping coefficient  $b = 10 \text{ nm/mm}^2$ , and grating length 0.5 mm. Coherent illumination case is represented by the oscillating trace; solid line shows FP response in the case of incoherent incident light; dotted line shows the spectral response of a single chirped grating reflector.*

### **4.3 Manufacturing techniques and facilities for IFBG production.**

This section deals with the practical issues related to the fabrication of fibre Bragg gratings. The mechanisms of photosensitivity observed within germanosilicate glasses are discussed briefly since this is the basis for the grating fabrication process. The experimental arrangements used for grating fabrication during the course of this research are described in detail together with the techniques of grating exposure. Several methods for the production of chirped Bragg gratings reported to date are discussed, and the prism interferometer chirping technique is analysed in detail since this method was invented and patented during this research program. The fabrication of Fabry-Pérot sensor elements for the low-coherence interferometer relied on this new technique. Modelling of the grating growth process and the profile of refractive index modulation formed by the UV exposure is described since the results of this modelling are important for the design and fabrication of Bragg gratings and for predicting their optical properties.

#### **4.3.1 Photosensitivity in optical fibres.**

The phenomenon of photosensitivity observed within silica glasses with various doping materials has been studied extensively during recent years because of the many important applications based on UV-induced changes of refractive index in glass waveguides and optical fibres [Inoue *et al.*, 1995, Poumellec *et al.*, 1996]. Research efforts have concentrated on explaining the mechanisms of index change and ways of enhancing the degree of photosensitivity through glass sensitisation with different materials. Even though the complete theoretical description of the origins of refractive index change is yet to be obtained, significant progress has been made. Several models of photoinduced index change process have been proposed and tested experimentally [Sceats *et al.*, 1993], and glass co-doping techniques have been established [Williams *et al.*, 1993, Dong, *et al.*, 1995, Reekie and Dong, 1997] that result in highly photosensitive optical fibres designed specifically for grating fabrication.

The availability of photosensitive optical fibres is crucial for the production of Bragg gratings. For this reason, it is appropriate to discuss the techniques for fibre sensitisation and mechanisms responsible for photosensitivity enhancement.

The colour centre model of photosensitivity based on UV-bleaching of the germanium-oxygen deficiency centres present in germanium-codoped silica glasses has been the most widely

accepted model for the mechanism of index change. The germanium-related defects in the polycrystalline glass structure are known to absorb UV light near the 244 nm wavelength region. The absorption process transforms a structural defect in the glass into a colour centre characterised by the presence of a  $\text{Si}^+$  hole and a released electron that later could be trapped by a nearby Ge atom in the glass structure. The observed change in refractive index of glass is a result of the change in the spectral absorption properties caused by the redistribution of electrons in the material and is accounted for by the Kramers-Krönig relationship. Even though the mechanism of index change described by the colour centre model is commonly accepted, the application of this model leads only to rough estimates of the index change and it is yet to be determined if this model can account for all of the observed changes in the glass refractive index caused by the UV illumination [Poumellec *et al.*, 1996].

The compaction model for the mechanism of photoinduced refractive index change proposes that a densification of the glass structure occurs during the process of photolytic structural defect transformations [Sulimov *et al.*, 1995]. In this model, structural changes in the glass structure caused by the effects of UV absorption lead to local changes in the glass volume and this leads to a change in the refractive index.

Another model for the origin of the refractive index change is based on the suggestion that the UV-induced chemical bond breakages allow the relief of structural stress that was built into the fibre glass structure during the fibre drawing process due to mismatch of thermal expansion coefficients of the core and cladding glass materials [Sceats *et al.*, 1993]. The refractive index change is deduced in this model by characterising the photoelastic process of stress relief.

The dipole model for the photoinduced refractive index change proposes that the local RI changes are generated through a quadratic Pockels effect induced by the presence of electric fields of dipoles formed by the sites within the glass structure that act as traps for electrons and holes induced by irradiation. The dipoles are assumed to be weakly oriented along the direction of polarisation of the electric field of irradiating UV light. This model can probably explain only part of the refractive index change observed during the grating production.

At present time, it is believed that more than one type of process is responsible for the refractive index change observed during grating fabrication [Xie *et al.*, 1993], therefore, it is likely that the total change of fibre refractive index is provided by a combination of the mechanisms mentioned above.

The development of techniques for increasing the degree of fibre photosensitivity has been the subject of extensive research interest in recent years since this offers some exciting opportunities for gratings applications. The standard technique for increasing the photosensitivity of silica-based glass fibres used by most laboratories including OTRL is the hydrogen loading technique [Lemaire *et al.*, 1993, Atkins *et al.*, 1993]. It relies on the high pressure low temperature hydrogen treatment of optical fibre before the grating exposure that allows hydrogen molecules to diffuse into the fibre core region through the plastic jacket and the cladding region. It is believed that multiple mechanisms are responsible for the hydrogen-induced glass photosensitivity enhancement. The presence of hydrogen increases the concentration of UV-bleachable structural defects containing oxygen-deficient chemical bonds. Photolytic and thermally driven reactions occur between the hydrogen and germanium atoms that result in the formation of structural defects and increased absorption of UV light. The hydrogen loading technique is often applied to further increase the photosensitivity of fibres with enhanced photosensitivity provided by co-dopants such as boron or tin and has also been shown to increase the degree of photosensitivity in fibres without germanium [Liou *et al.*, 1997]. For example, at OTRL we fabricated Bragg gratings in hydrogen-loaded fluoride glass-based fibres.

A disadvantage of the hydrogen loading technique is that the presence of molecular hydrogen temporarily changes the effective refractive index of the fibre core, leading to a change in the spectral properties of Bragg gratings after their inscription [Malo *et al.*, 1994]. The magnitude of shift in the Bragg resonance wavelength of gratings caused by the hydrogen outgassing process is of the order of 0.1 nm. The exact values of this wavelength shift are difficult to predict since it is dependent on the initial hydrogen concentration and the exposure conditions. Therefore, the reproducibility of the Bragg reflection wavelength is compromised due to hydrogen loading, which limits the applicability of this technique in a number of manufacturing situations.

### 4.3.2 Experimental arrangements used for the production of Bragg gratings.

During the course of this study, in-fibre Bragg gratings have been produced using a variety of experimental arrangements and exposure techniques. The purpose of researching the properties of Bragg gratings was the development of a technique for the production of broad reflection bandwidth chirped gratings with controllable characteristics for their subsequent use as reflectors for the fibre Fabry-Pérot cavities. For this reason, most of experimental work was performed using the prism interferometer arrangement. However, the phase mask technique was also investigated and utilised experimentally to fabricate gratings for other OTRL applications. A diagram showing the general features of two experimental arrangements is shown in Figure 4.8.

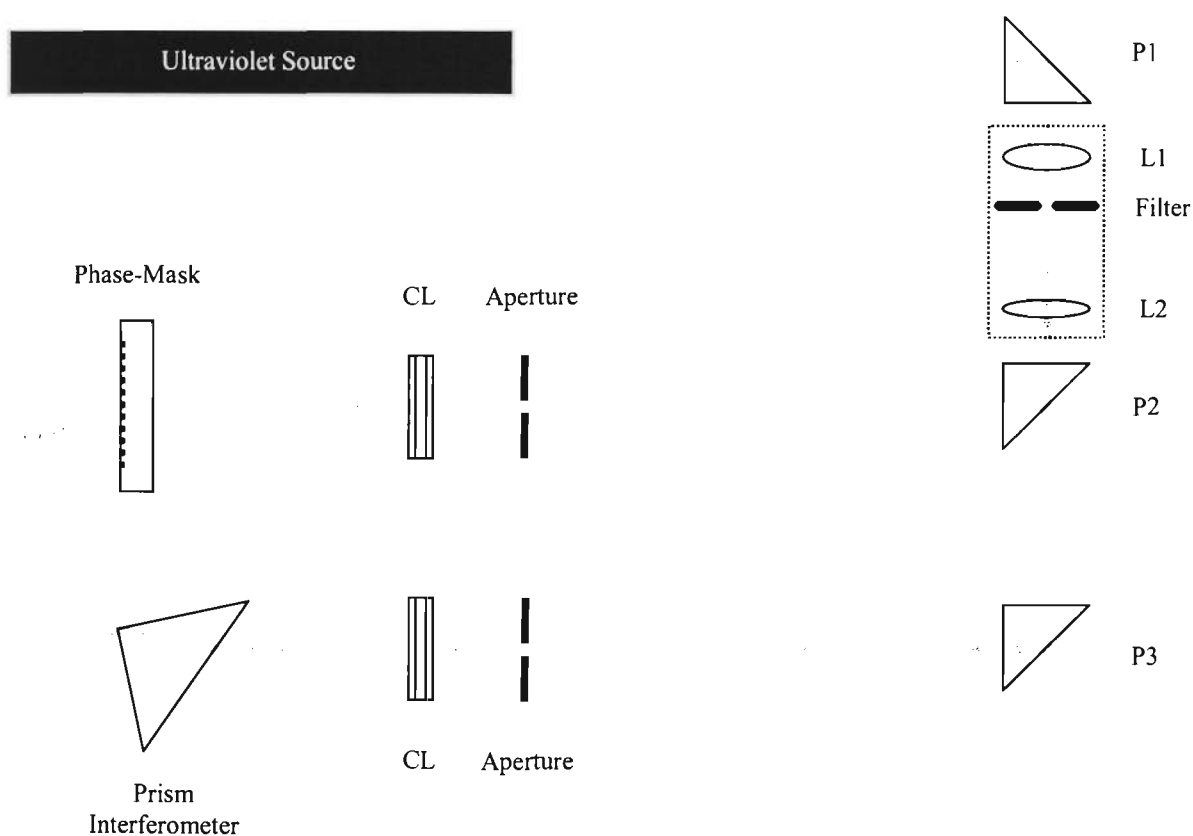


**Figure 4.8** *Diagram of the experimental arrangement used for the production of Bragg gratings with either phase mask or prism interferometer technique. (P1-P3: steering prisms; L1, L2: bi-convex spherical lenses; CL: cylindrical fused silica lens). The setup was mounted on a stabilised optical table; prism P2 is removable.*

Two different UV laser sources were used for grating production at different stages of this work. Initially, the source was a Spectra-Physics Master Oscillator - Power Oscillator (model MOPO-730) pumped with the internally frequency-doubled Nd:YAG (model GCR-250). The output radiation from the MOPO source had very good wavelength tuneability properties and was

adjustable between approximately 210 nm and 345 nm in the ultraviolet region of spectrum. It was operated for grating production at a wavelength of 245 nm which is near the wavelength band of peak UV absorption for germanosilicate glasses. The laser was pulsed at a repetition rate of 10 Hz with a pulse duration of approximately 2-4 ns and a pulse energy of about 5-10 mJ. The beam from the MOPO source has a Gaussian intensity distribution, horizontal polarization (extinction ratio >97%), and a coherence length of about 5 cm. A diagram of the experimental arrangement used for the production of chirped gratings with the MOPO source is shown in Figure 4.9. This was the original experimental arrangement used for the development of the prism interferometer chirping technique.

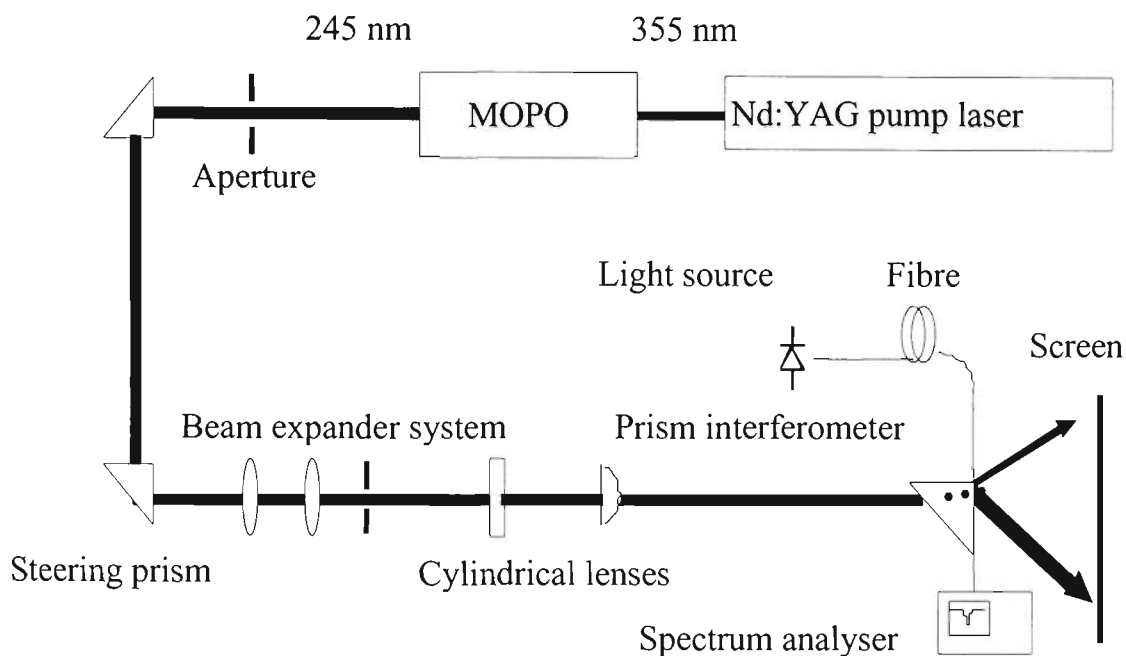


**Figure 4.9** Schematic diagram of an original experimental setup used for writing chirped gratings with a prism interferometer and MOPO UV source.

Later, during the course of this research, another ultraviolet laser source was commissioned which has superior beam characteristics to those of the MOPO. The Coherent internally frequency-doubled argon-ion laser (model FreD 300) has continuous-wave output at the wavelength of 244 nm with a nominal optical power of about 100 mW. The output beam of the FreD has very good uniformity, power and emission direction stability, temporal and spatial coherence properties and is horizontally polarised (extinction ratio of 100:1). The superior (compared to the MOPO system) spatial coherence properties of the output radiation from the FreD laser resulted in practically negligible values for the grating bandwidth reduction due to coherence-related decrease in the visibility of replicating interference pattern.

### 4.3.3 Techniques for the production of chirped Bragg gratings.

A large variety of experimental techniques have been proposed to date for the production of chirped Bragg gratings and for controlling the grating reflection bandwidth, shape of the reflection response and levels of reflectivity. Chirped gratings written inside the core of optical fibres can be divided into two broad categories, depending on the manner in which chirping is introduced. Amplitude chirping is created by varying the amplitude of refractive index modulation as a function of the grating length while the grating periodicity is kept constant. Periodicity chirping (which sometimes is referred to as wavelength or frequency chirping) is created by varying the periodicity of RI modulation along the grating length while keeping the depth of index modulation uniform. In the majority of practical chirped grating fabrication situations, however, both types of chirping are invariably present. Therefore, the two categories of fabrication techniques refer to the intended way of broadening of the spectral response utilised within a particular fabrication technique. Another category of chirping techniques exists for bulk-optic waveguide gratings, whereby induced waveguide corrugations (variations in the waveguide shape) can be used for obtaining Bragg gratings with desired characteristics of spectral response [Katzir *et al.*, 1977].

The chirp can be introduced either during the grating inscription process or after an initially unchirped grating has been produced. In the following subsections we will consider some of the principal experimental approaches to the fabrication of chirped gratings reported to date whilst concentrating mostly on the methods for introducing the periodicity chirp during the grating inscription process. Chirped gratings produced with methods from this category have most potential for the use in low-coherence applications since maximum reflection bandwidths can be obtained with those techniques.

#### ***Fabrication of chirped Bragg gratings with a non-uniform phase mask.***

The diffraction phase mask technique [Hill *et al.*, 1993] is one of the standard methods for the production of constant-periodicity Bragg gratings. The pattern of refractive index modulation in this technique is being replicated onto the optical fibre due to the process of photosensitivity through interfering the first order diffracted beams generated by the constant-periodicity phase mask. The principal feature of this technique is that the intensity of UV light in the interference pattern produced by the phase mask is described by a cosinusoidal function with the periodicity of exactly half the periodicity of the phase mask.

The use of “stepped-chirp” variable-periodicity phase masks for the production of linear and quadratic wavelength-chirped gratings with reflection bandwidths between 3 and 15 nm and reflectivities of 75-95% was first reported in [Kashyap *et al.*, 1994]. The method of fabricating the phase mask with nonuniform structure relies on the exposure of photoresist by electronic beams. This method builds the periodicity chirping function into the phase mask using short mask sections with each section differing in period from the previous one, and that allows the production of chirped gratings for a large range of wavelengths, chirp functions and bandwidths.

This method of chirped gratings fabrication is expensive but not very flexible since the Bragg wavelength and chirping function are built into the structure of the phase masks and a large number of expensive devices is necessary to facilitate production of chirped gratings in different wavelength regions with controllable chirp characteristics.

***Production of chirped gratings by fibre deformation during exposure.***

The holographic two-beam interferometer arrangement schematically represented in Figure 4.10 is one of the most popular standard configurations for the production of Bragg gratings. This experimental arrangement, with slight modifications, has been reported in a number of grating fabrication techniques, for the production of both uniformly-periodic and chirped gratings. This type of a two-beam interferometer can be used for the production of chirped gratings if the fibre is subject to deformation during exposure, as reported in [Sugden *et al.*, 1994]. In this method, a mechanical deformation of optical fibre is utilised, with a curved photosensitive fibre being placed in the two-beam interference field with a uniform fringe spacing  $\Lambda$ .

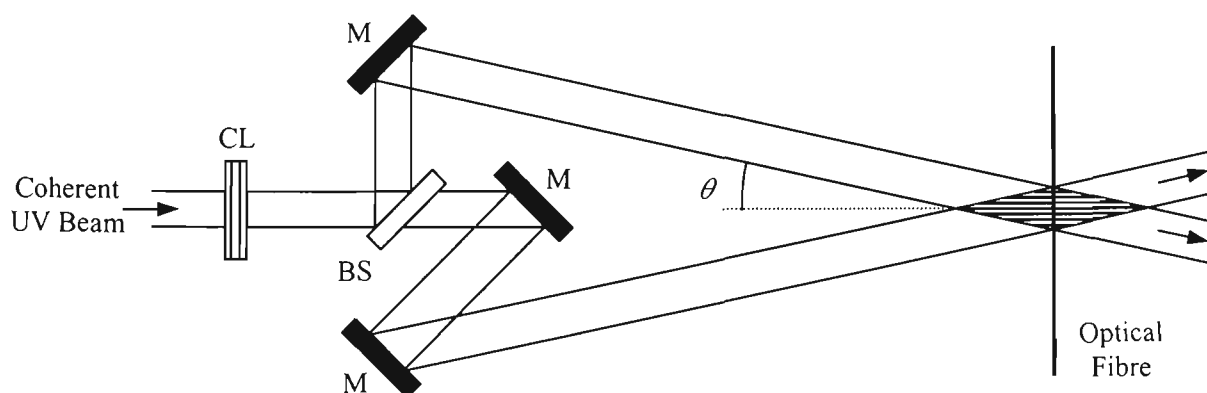


**Figure 4.10** *Holographic two-beam interferometer arrangement for the production of Bragg gratings. (CL: a cylindrical lens; BS: beam splitter; M: mirror.)*

The non-uniformity of the resultant periodicity of RI modulation is induced by the curvature of the fibre and can be controlled through exposure geometry. The periodicity  $\Lambda(z)$  of the grating produced in the fibre varies as  $\Lambda/\cos\phi(z)$ , where  $\phi(z)$  is the angle between the local direction of the longitudinal axis of the fibre and the normal to the exposing fringe pattern at position  $z$  along the grating. The resultant grating period varies continuously from a minimum value of  $\Lambda$  to a maximum value of  $\Lambda/\cos\phi(L_G)$ , and chirp magnitudes of 7.5 nm at 99% reflectivity have been obtained with this method.

The technique of curving the fibre is also compatible with the phase mask method. As reported in [Zhang *et al.*, 1995], by precisely specifying the curvature, it is possible to obtain linear, quadratic, and square-root chirped gratings. A segment of precurved bare fibre was positioned on a quartz plate, and a uniformly pitched phase mask was placed on top of the fibre. On exposure of the UV light through the phase mask, the resulting fringe periodicity imprinted on the fiber is expressed by the function  $\Lambda = \Lambda_0[1 + (df/dz)^2]^{1/2}$  where  $\Lambda_0$  and  $\Lambda$  are the fundamental periodicity of the unchirped gratings provided by a given phase mask and the projection of  $\Lambda_0$  onto the curved fibre. The fibre is curved according to the function  $f(z)$ .

The linearly chirped grating reported in [Zhang *et al.*, 1995] had a 65% reflectivity with a bandwidth of 6.76 nm. The main difficulty in application of this technique was in achieving the exact curvature profile, especially for the case of square root chirping.

### ***Writing of chirped-periodicity gratings using interfering wavefronts of dissimilar curvatures.***

Broad reflection bandwidth (up to 44 nm) gratings production with the use of curved wavefronts have been reported in [Farries *et al.*, 1994]. The holographic two-beam interferometry arrangement used in this method included two cylindrical lenses for the formation of the curved wavefronts, and a cylindrical lens was used to focus the interfering beams onto the fibre. By adjusting the relative positions of the cylindrical lenses, the bandwidth of the chirped gratings could be varied from zero chirp to over 100 nm with reflectivity values of over 90%.

### ***Chirped Bragg gratings in fibre tapers.***

Methods for the fabrication of chirped fibre Bragg gratings using a fibre taper have been reported in [Byron *et al.*, 1993, Cruz *et al.*, 1996]. The introduction of tapers alters the waveguide properties of the fibre and results in a change of the effective refractive index. The method described in [Byron *et al.*, 1993] involves tapering the fibre in the region of a grating initially produced by the holographic two-beam interference technique. The decreasing core size decreases the effective refractive index along the length of the taper, resulting in a grating chirp. This technique is well suited for relatively small chirp magnitudes (of the order of 2.9 nm). The tapers were designed such that the fibre diameter decreases smoothly from 125  $\mu\text{m}$  to 50, 75 or 100  $\mu\text{m}$  over a distance of 10 mm.

### ***Writing chirped gratings on pre-strained fibres.***

A method for producing broad reflection bandwidth chirped gratings using a uniform period phase mask has been reported in [Byron and Rourke, 1995]. In order to achieve controllable chirp, it has been proposed to write gratings in sections whilst applying strain to the fibre section under exposure. After each grating section is formed, the applied strain is either decreased or increased. The writing beam is then moved along the fibre for the production of next grating section exactly adjacent to the previous one. The spectral width of grating response that can be obtained by this method is reported to be limited by the length of the phase mask and the maximum strain that can be applied to the fibre. Chirped gratings with reflection bandwidths of up to 10 nm have been fabricated with this technique.

### ***Moving fibre/phase mask technique.***

Another approach to the fabrication of chirped Bragg gratings with controllable characteristics using a uniform-period phase mask has been reported in [Cole *et al.*, 1995]. In this method, the fibre, or alternatively, the phase mask, is slowly moved during exposure as the writing beam is being scanned. The motion of a fibre relative to the phase mask during the inscription process allows a phase shift to be added to the fibre grating being written. For uniform motion of the fibre, this results in a shift of the Bragg wavelength, the value of which is given by  $\delta\lambda = \lambda_0 v_f / v_{sc}$ , where  $\lambda_0$  is the unshifted Bragg wavelength,  $v_f$  is the speed of the fibre relative to the phase mask, and  $v_{sc}$  is the scanning speed of the beam. For a wavelength shift of the order of 1 nm,

the fibre speed should be only about 0.1% of the scanning speed. The maximum wavelength shift is reported to be dependent only on the diameter of the scanning beam. Only multi-frequency gratings with overall reflection bandwidth of about 5 nm were originally reported [Cole et al., 1995]. However, the authors suggest that this method can be used for writing continuously chirped gratings if the speed and acceleration of the fibre motion are specified precisely.

### ***Chirped gratings produced by tilting the fibre with respect to a phase mask.***

A modification of the phase mask method for the production of chirped gratings with controllable reflection bandwidth and central wavelength has been reported in [Painchaud *et al.*, 1995]. This technique uses tilting of the fibre with respect to the phase mask during exposure. A spherical or cylindrical lens is also required in this method to introduce a dependency of the angle of incidence of the writing beam on the position along the phase mask. The resultant periodicity of refractive index modulation is reported to be linearly dependent on the local angle of incidence of the writing beam when a phase mask of uniform period is used. The reflection bandwidth of chirped gratings is proportional to the tilting angle, the period of the phase mask, and the grating length. It also depends on the focal length of the spherical or cylindrical lens used, together with the distance between the lens and the phase mask. Fabrication of a chirped grating of 6 nm-wide reflection bandwidth has been reported, but the authors suggest that the chirp magnitude can be increased up to values exceeding 100 nm by the appropriate choice of experimental setup parameters [Painchaud *et al.*, 1995].

The application of fibre tilting method is limited by the fact that with the fibre positioned away from the phase mask surface, the contrast of interference fringes pattern on the core of fibre under exposure is drastically reduced. Efficient grating inscription is only possible with the fibre placed in physical contact or in close proximity of the phase mask surface. The degree of spatial coherence of the writing UV beam is of crucial importance for Bragg grating production, especially with the fibre positioned away from the phase mask [Othonos and Lee, 1995].

### ***Strain gradient chirp of fibre Bragg gratings.***

A grating packaging technique allowing dynamic control of the centre wavelength and spectral linewidth of fibre Bragg gratings has been reported in [Hill and Eggleton, 1994]. It uses the dependency of a local Bragg grating periodicity on the applied axial strain. When tension is applied to a fibre between two points, the resulting strain is constant throughout the fibre until the relief point is reached, producing a uniform Bragg wavelength shift without change in the shape of the reflection spectrum. This principle, generalised to strain gradients, is used in the method to change the local Bragg wavelength along the fibre. The grating chirp is a consequence of a strain gradient, which is realised by mounting the grating in a soft medium (glue) such that tension applied to one end of a fibre will be gradually relieved over a distance. This method is well suited for introducing a small chirp to the gratings, and requires a tension of about 1.5 N for a 30 mm-long uniform grating to have a bandwidth of 1 nm [Hill and Eggleton, 1994]. Another application of strain gradient chirping method for broadening of the reflection response in tapered gratings has been reported in [Putnam *et al.*, 1995].

## 4.4 The prism interferometer chirping technique.

A method for manufacturing broad reflection bandwidth, wavelength-tunable chirped Bragg gratings with a prism interferometer was developed during the present research program. The motivation was the need for broad bandwidth grating Fabry-Pérot sensing elements for use in a low-coherence sensing system. The development of this technique facilitated the production of sensing elements with the desired characteristics using a simple optical arrangement, with a limited number of components, having good mechanical stability and requiring simple alignment procedures only. The method also significantly reduced the cost of production of the required broadband grating Fabry-Pérots since no specialised equipment (e.g. variable-periodicity phase masks) was necessary. The overall complexity of grating production with the prism interferometer technique is significantly reduced compared to the holographic interferometry technique using dissimilar wavefronts. The flexibility and potential of the prism interferometer method, however, are similar to those of the holographic technique for many grating applications requiring wide bandwidth and wavelength tunability but not the exact linearity of the chirping profile. As will be shown theoretically and confirmed by the experimental data later in the chapter, the structures formed in the fibre as multiple superpositions of chirped Bragg gratings produced with a prism interferometer offer exciting potential for the design of custom-made Bragg reflectors suitable for various applications. This is possible due to the fact that the spectral response of a superposition of gratings can be predicted theoretically and tailored to suit particular requirements, and because quadratically chirped Bragg gratings produced using a prism interferometer are spectrally shaped unlike gratings provided by most other chirping techniques. A number of degrees of freedom exists for modifying the spectral shape and bandwidth of the prism interferometer gratings including most of the parameters related to the geometry of exposure, its duration, and the dynamics of refractive index change. Thus prism interferometer gratings are useful as "building blocks" of variable shape for the production of complicated grating structures with a custom-designed shape of the spectral response.

#### 4.4.1 Principle of the method.

The fabrication of chirped gratings with a prism interferometer relies on the periodicity chirping technique. The variation in the periodicity of refractive index modulation results from exposure of a photosensitive optical fibre to a UV interference pattern with variable fringe spacing. The prism interferometer chirping technique is an extension of a well-known prism interferometer method for the production of constant-periodicity Bragg gratings [Zhang *et al.*, 1994] that allows an interference pattern to be created with a variable fringe spacing. The variation in the periodicity of interference fringes is engineered in our technique by utilising the principle of holographic exposure, that is, the interfering wavefronts with dissimilar curvatures are generated. Therefore, the prism interferometer chirping technique is a novel method for the production of chirped Bragg gratings based on the combination of physical principles previously utilised for grating fabrication [Garchev *et al.*, 1998].

The generation of two interfering wavefronts in our method relies on the effect of beam splitting at the corner of a right-angle prism when a UV beam incident on the prism hypotenuse face is propagated through it [Garchev *et al.*, 1998]. The two interfering wavefronts are made dissimilar in their curvature by utilising the nonlinearity of the dependency of the angle of refraction on the angle of incidence for a range of angles of incidence within a divergent incident beam. The principal diagram of the technique showing the divergent beam pathways and the formation of the beam overlapping region is presented in Figure 4.11.

The variation of fringe spacing along the exit face of the prism can be obtained by considering the case of a divergent beam with half-divergence angle  $\alpha$  incident at an angle  $i$  (beam axial ray) on a 45-degree prism, as shown in Figure 4.11. If the axial ray is refracted into the vertex of the prism then the angles of incidence for the marginal rays are  $(i+\alpha)$  and  $(i-\alpha)$  and the corresponding refraction angles are  $\sin^{-1}[\sin(i+\alpha)/n]$  and  $\sin^{-1}[\sin(i-\alpha)/n]$ , where  $n$  is the refractive index of the quartz prism. Two divergent beams are produced by the prism; one each for rays having angles of incidence less than and greater than  $i$ . These beams overlap within the prism, on its surface and in the air. For simplicity it is assumed that the optical fibre is in direct contact with the prism, and refraction of the outgoing beams at the prism-air-fibre interface is not taken into account.



Thus for  $\alpha \neq 0$ , the interfering wavefronts are dissimilar and a variable fringe spacing is produced along the prism surface.

The grating length is limited by the common overlap region of the two beams given by  $L = \min(BC, BD)$ . The relative positions of points  $C$  and  $D$  depend upon the combination of parameters  $i$ ,  $\alpha$  and distance  $d$  from the focal point to the prism surface measured along the axial ray. For the case depicted in Figure 4.11 where  $BD < BC$ , the interference fringe spacing at point  $D$  is determined by the angles  $\theta_1$  and  $x$ . The local angle of incidence at point  $Z$ ,  $i + \alpha_0$  where  $0 < \alpha_0 < \alpha$ , is calculated as a solution of a trigonometric equation of the form  $BC(i + \alpha_0) = BD(i - \alpha)$ . The angle  $\alpha_0$  is found by solving

$$a - \frac{(AO - OM) \cos[\sin^{-1}(\sin(i + \alpha_0)/n)]}{\sin[\pi/4 + \sin^{-1}(\sin(i + \alpha_0)/n)]} = (a - LS) \tan(\theta_1), \quad (4.49)$$

where  $a = AB$  is the prism dimension. The angle  $x$  is calculated from

$$x = \pi/4 - \sin^{-1}[\sin(i + \alpha_0)/n]. \quad (4.50)$$

The local angles of intersection between the two interfering wavefronts and the dependency of these angles on position along the prism exit surface ( $z$ ) are readily calculated using the above equations by varying  $\alpha$  in small steps from zero to the actual half-divergence angle (thus moving point  $D$  along the exit face). The local chirped grating periodicity,  $\Lambda(z)$ , has the form

$$\Lambda(z) = \Lambda(\theta_1, x) = \frac{\lambda_{UV}}{n[\sin(\theta_1) + \sin(x)]}, \quad (4.51)$$

where both  $\theta_1$  and  $x$  are functions of  $z$ . The Bragg reflection wavelength is therefore a function of position along the grating and is given by  $\lambda_B(z) = 2n_{eff}\Lambda(z)$ , where  $n_{eff}$  is the effective refractive index of the fibre core. Analysis of the chirping profile function shows it has the approximate form

$$\Lambda(z) = \Lambda_{max} - bz^2, \quad (4.52)$$

where  $\Lambda_{max}$  is the fringe spacing at the prism vertex and  $b$  is the chirping profile coefficient. By varying parameters  $i$ ,  $\alpha$  and  $d$  the grating characteristics such as wavelength, chirping profile coefficient and grating length can be controlled.

#### 4.4.2 Analysis of the prism interferometer chirping technique.

Figure 4.12 shows graphs of dependency of the local Bragg resonance wavelength on the position along the grating for a chirped grating in the 670 nm wavelength region produced with the prism interferometer technique for three different values of parameter  $d$  (distance between the focus of divergence and the prism hypotenuse face measured along the axial ray). The chirping profile functions represented by the graphs were calculated numerically using equations presented in the section above and show the possibility of adjusting the shape of the chirp function (and consequently the chirping rate and grating reflection bandwidth for a given length) through varying distance  $d$ .

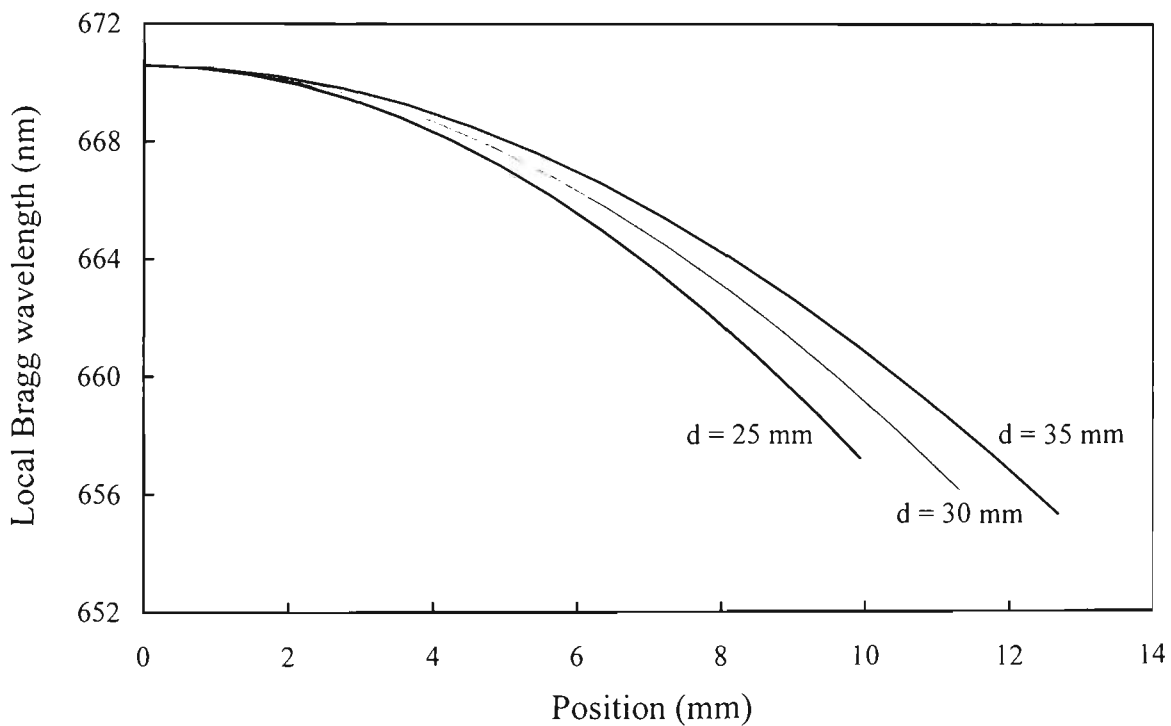


**Figure 4.12** *Calculated chirping profile functions for Bragg gratings produced with the prism interferometer technique in the 670 nm region for three different values of parameter  $d$ .*

The graphs show that quadratically chirped Bragg gratings produced with the prism interferometer are chirped very gradually at positions  $z$  close to  $z = 0$  (prism vertex). Consequently, their spectral reflection response near the maximum Bragg reflection wavelength

looks much like the spectral response of a constant-periodicity grating. However, large chirp magnitudes are achievable since the local value of the chirping rate increases rapidly with increased values of  $z$ . The ability to produce gratings with large values of reflection bandwidth is dependent in this technique on the maximum achievable grating length and on the wavelength region in which gratings are written. The values of the chirping profile coefficient  $b$  are strongly dependent on the wavelength region and are increasing rapidly with the increase in the maximum Bragg reflection wavelength of gratings. The dependencies of the value of the chirping profile coefficient on distance  $d$  for three different wavelength regions are presented in Figure 4.13.

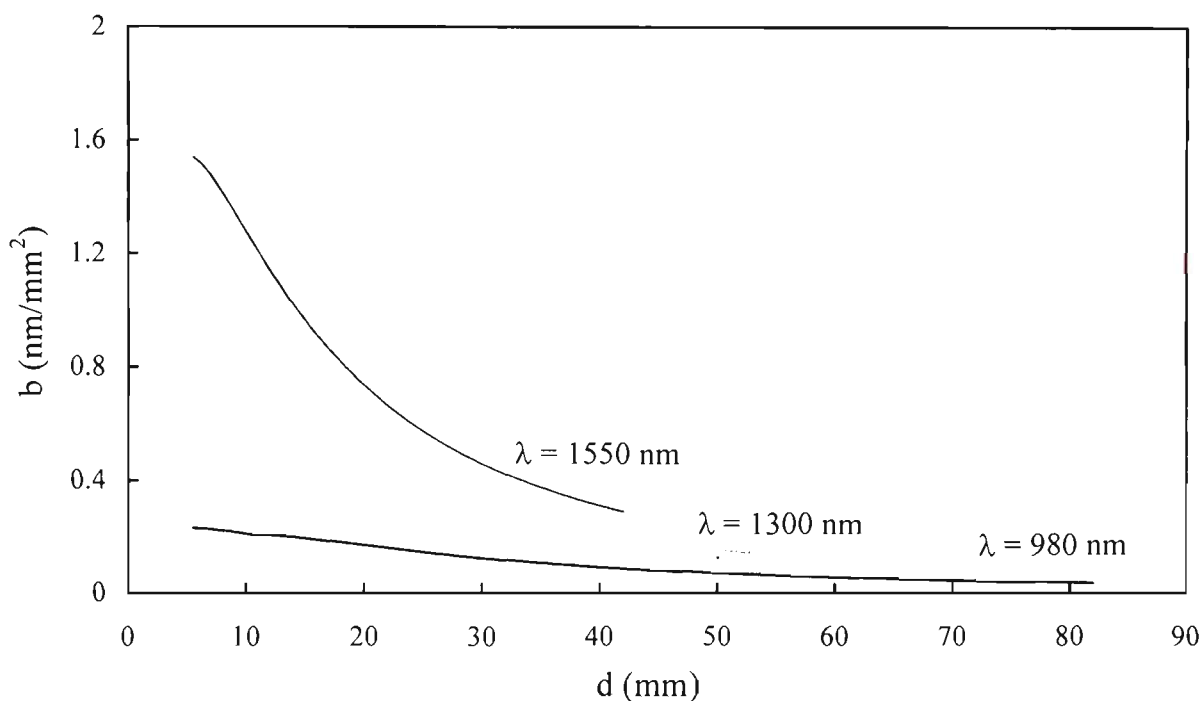
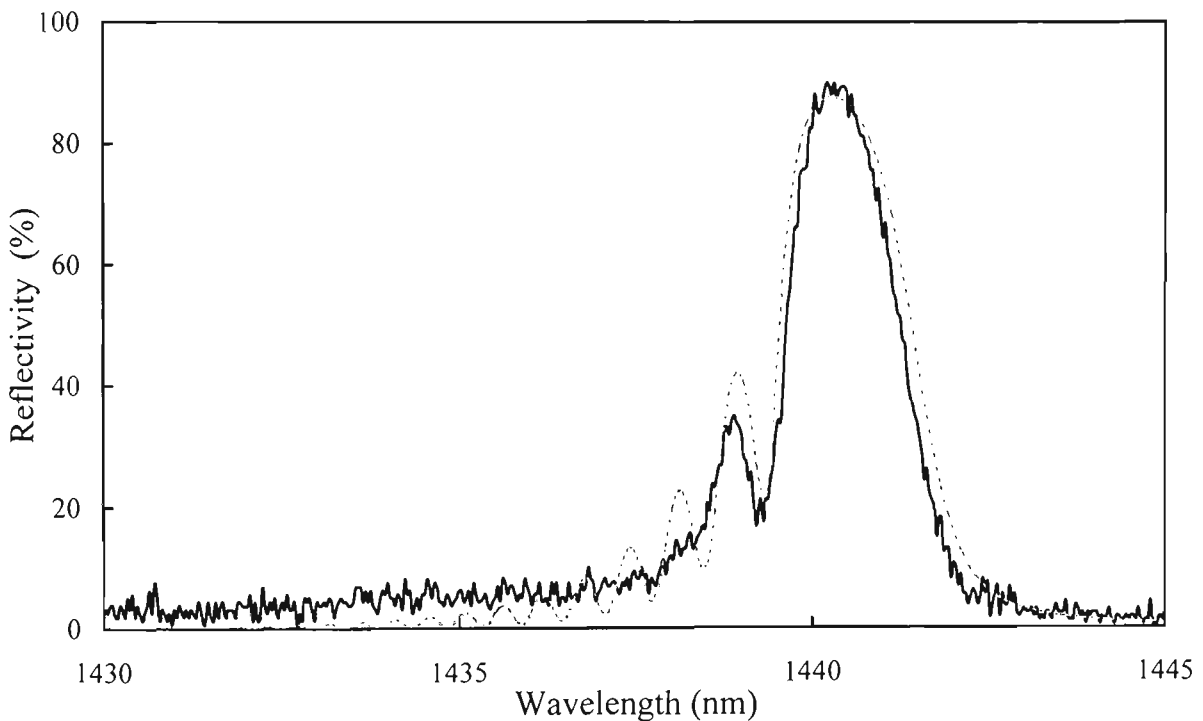


**Figure 4.13** Dependency of the chirp coefficient  $b$  on the distance  $d$  between the beam focus and prism surface for three different wavelength regions. Ranges of  $d$  values are limited by the prism dimension  $a = 50.8$  mm used in the calculations.

The graphs of Figure 4.13 demonstrate that the prism interferometer method allows the fabrication of gratings with much larger reflection bandwidths in the 1550 nm region compared to, for example, the 980 nm region, for a given value of grating length. The practical limitation on the achievable grating lengths is related to the spatial coherence properties of the writing UV beam, the size of the optical components used and the minimum energy density requirements for the replicating UV interference pattern that impose limitations on the beam expansion factor. The requirement of good spatial coherence properties for the writing beam follows from the geometry of grating exposure that dictates that regions of the grating close to  $z = L_G$  are

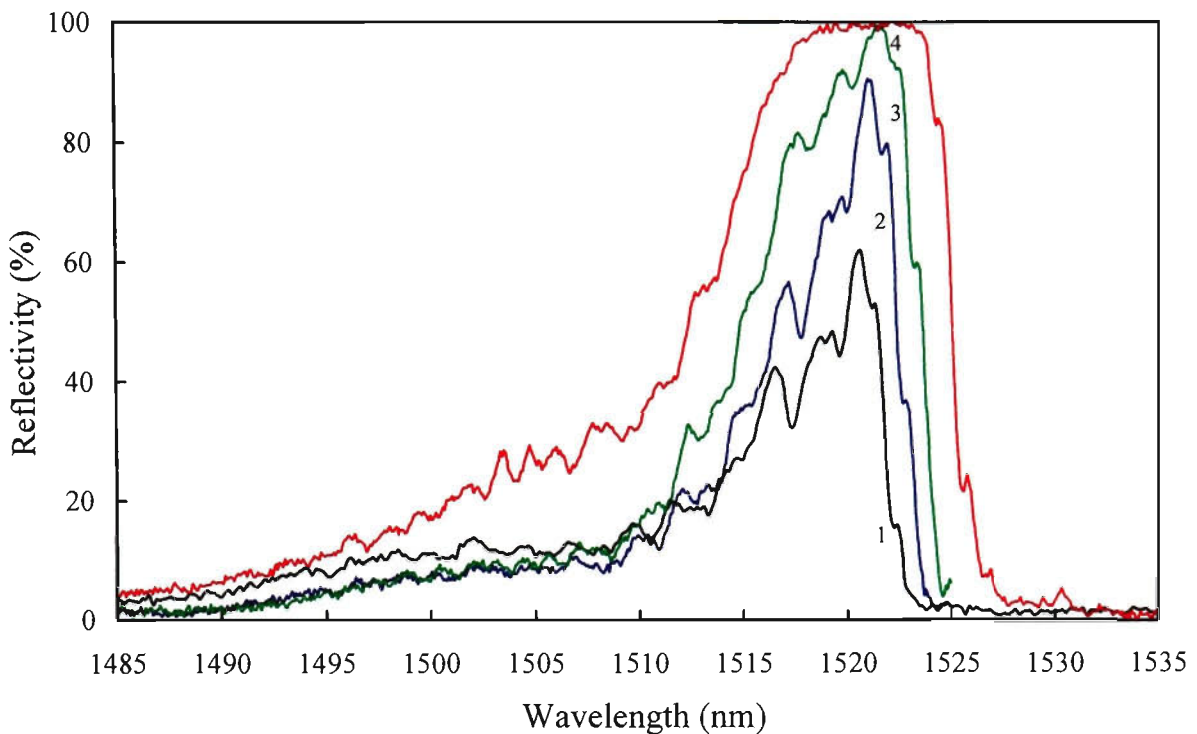
produced due to the interference of UV rays originating from the opposite peripheral regions of the UV beam.

Figure 4.14 shows the measured spectral reflection response for the first chirped Bragg grating fabricated at OTRL using the prism interferometer technique and the theoretically calculated spectral response of the same grating. The numerical calculations of spectral response used data of the exposure parameters for the solution of coupled-mode equations of Section 4.2.4 and a model of grating growth presented in the next section of this chapter. The decrease in the UV fringe visibility along the grating length was modelled assuming a Gaussian shape for the visibility profile with the rate of visibility decrease being the modelling parameter that was varied in obtaining the best fit.



**Figure 4.14** Experimental (solid) and calculated (dashed) spectral responses for a chirped grating ( $\alpha = 0.06$  radians,  $d = 20$  mm,  $\Delta n_{peak} \approx 1.4 \times 10^{-3}$ ,  $L_G \approx 3$  mm and  $b = 1.2$  nm/mm<sup>2</sup>).

Figure 4.15 shows the measured time evolution of the spectral reflection response for a broad bandwidth chirped grating produced with the prism interferometer including the stages of grating growth process close to RI saturation. The rapid decrease in reflectivity near the short wavelength side of the reflection response is due to the rapid increase of the local chirp rate with position along the grating. It is also due to the deterioration of the UV fringe visibility and UV light intensity with position along the grating, caused by the limited spatial coherence properties and the Gaussian decrease in the intensity of the writing beam from the MOPO source.



**Figure 4.15** *Spectral response time evolution of a chirped grating ( $\alpha = 0.06$  radians,  $d = 20$  mm,  $\Delta n_{peak} \approx 5 \times 10^{-3}$ ,  $L_G \approx 5$  mm.). Spectra are numbered to separate sequential measurements.*

An interesting feature of the prism interferometer chirping technique is the possibility of the production of broad bandwidth chirped gratings with a linearised quadratic chirp function. It is based on the fact that the most nonlinear region of chirp functions provided by this exposure technique is localised near the high reflection wavelength end of gratings (near the prism vertex exposure region). If this region of fibre is prevented from being exposed to the UV interference pattern during grating fabrication, then the resulting chirp function of a grating produced in this way will have only small nonlinearity and consequently, the spectral response of the resultant grating will have features similar to those of a linearly chirped Bragg grating. An example of this linearisation process was calculated and is shown in Figure 4.16.

Demonstration of this linearisation technique was not possible as the only fibres available (standard telecommunications fibres) would have required unduly long exposure times. A successful demonstration of gratings with linearised quadratic chirp function would have to rely on the exposure of fibre region positioned several millimetres away from the point of maximum fringe visibility (prism vertex), and therefore a high degree of fibre photosensitivity together with excellent spatial coherence of the UV beam are crucial. The demonstration of this linearisation technique would be best performed for gratings in the 1550 nm spectral region,

where the prism technique offers larger reflection bandwidths for a given grating length (compared to chirped gratings in the 670, 840 and 1000 nm regions required during the project).

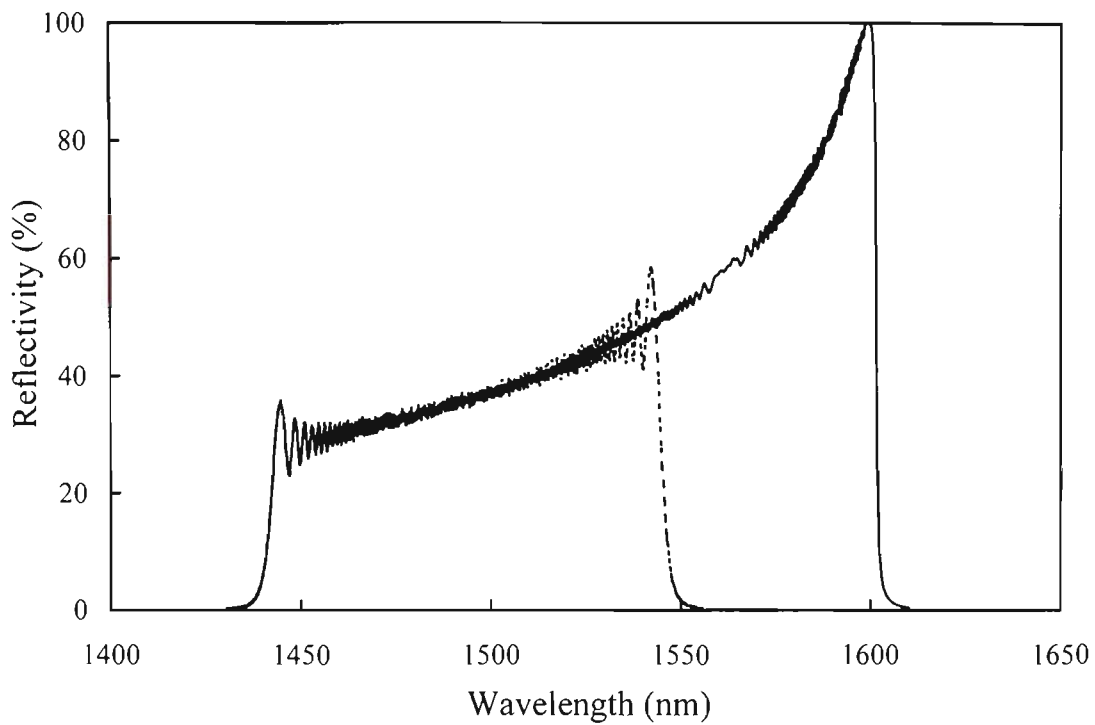


**Figure 4.16** *Calculated spectral responses of a 9 mm long chirped grating (solid) and the same grating produced with a 5 mm mask (dashed) near the prism vertex ( $\alpha = 0.19$  radians,  $d = 20$  mm and  $\Delta n_{peak} \approx 5 \times 10^{-3}$ ).*

## 4.5 Modelling of UV-induced refractive index change and index saturation effects.

Design and fabrication of all types of fibre Bragg gratings require knowledge of the parameters of index modulation profile that is to be produced inside the core of an optical fibre. It is very important for all grating manufacturing situations to be able to produce the desired patterns of index modulation since this ultimately determines the optical properties of Bragg gratings. A reliable theoretical model describing the process of photoinduced index change is necessary in order to design and fabricate gratings with controllable characteristics. This model must account for the fibre photosensitivity properties, the method and duration of exposure and the parameters of the writing UV beam. Up to date, the complete theoretical understanding of the phenomenon of fibre photosensitivity has not been achieved, yet it has been shown that several mechanisms of photoinduced refractive index change exist and several processes may be responsible for the index change observed within the fibre glass [Sceats *et al.*, 1993]. It is known from the literature [Poladian, 1993] and our own measurements that the parameters related to the dynamics of the refractive index change process are strongly dependent on the intensity of the irradiating UV light. The effect of index saturation also has its implications on both the achievable levels of index modulation and the rate of grating growth. Our experimental data suggest that the index saturation level is dependent on the writing beam intensity as well as on the degree of fibre photosensitivity.

Several models of the grating growth dynamics have been reported to date [Poladian, 1993, Patrick and Gilbert, 1993]. The most advanced model of RI change accounts for the effect of refractive index saturation and the dependency of the saturation level on local intensity by the following equation [Poladian, 1993]:

$$\frac{\partial n(z,t)}{\partial t} = \alpha [n_s(I(z,t)) - n(z,t)] I(z,t), \quad (4.53)$$

where  $n_s(I(z,t))$  is the local value of the saturation refractive index which, in a general case, is dependent on local UV illumination intensity  $I(z,t)$ . For the majority of practical examples it is convenient to consider the intensity distribution  $I(z)$  to be stationary, i.e.  $I(z,t) = I(z)$  for  $t > 0$ . Equation (4.53) should be solved with an initial condition of the form  $n(z,0) = n(z) = n_{eff}$  which sets the initial refractive index distribution in the fibre. Taking into account the convention regarding the stationary light intensity distribution, equation (4.53) can be rewritten as

$$\frac{\partial n(z,t)}{\partial t} = \alpha [n_s(I(z)) - n(z,t)] I(z). \quad (4.54)$$

The local amplitude of the RI change is obtained via the relationship

$$dn(z,t) = \frac{I}{2} (n(z,t) - n_{eff}). \quad (4.55)$$

Equation (4.54) can be solved for the general case and the value of local RI modulation amplitude at any given time is then easily obtained from (4.55) as long as the dependency of RI saturation level on intensity  $I(z)$  is known. To our knowledge, at present there are no reliable models of this dependency available, so the simplified case of the constant saturation level will be considered. Assume that for the range of UV intensities within the illuminated area the value of fibre RI at saturation is constant, i.e.  $n_s(I(z)) = n_s = const.$  The solution of equation (4.54) is then represented by the function

$$n(z,t) = n_s - e^{-[al(z)t + C(z)]}, \quad (4.56)$$

where the function  $C(z)$  can be obtained by applying the initial condition of the form  $n(z,0) = n_{eff}$  which leads to

$$C(z) = -\ln[n_s - n_{eff}]. \quad (4.57)$$

Combining equations (4.56) and (4.57), we obtain the solution for the RI modulation amplitude distribution at any given exposure time  $t$ :

$$n(z,t) = n_s + (n_{eff} - n_s) e^{-al(z)t}. \quad (4.58)$$

If the intensity-dependent saturation had been considered, then the general solution would have been obtained:

$$n(z,t) = n_s(I(z)) + [n_{eff} - n_s(I(z))] e^{-al(z)t}. \quad (4.59)$$

If a Gaussian UV beam is used for the production of chirped Bragg gratings with the prism interferometer, the envelope of the intensity distribution in the interference pattern will also be represented by a Gaussian function of the form  $I(z) = I_0 \exp(-z^2/(gL_G)^2)$ , where  $L_G$  is the grating length,  $I_0$  is the peak value of intensity at  $z = 0$  and  $g$  is a scaling factor for the Gaussian

distribution dependent on the size of an aperture used for beam conditioning. The variable fringe intensity value will cause the refractive index modulation amplitude to depend on position  $z$  along the grating. In order to account for this effect during the calculation of grating spectral response, the mechanism of refractive index change should be considered.

The refractive index change at the prism vertex (peak of the Gaussian) is maximum at any time and is given by:

$$dn(0,t) = \frac{1}{2} [n_s + (n_{eff} - n_s) e^{-\alpha I_0 t} - n_{eff}] = dn_{max}(t). \quad (4.60)$$

Assuming constant (time-independent) values of parameters  $I_0$  and  $\alpha$  in equation (4.60), their product ( $\alpha I_0$ ) can be estimated if the value of vertex RI modulation is known at some reference time  $t_0$ . This can be done by measuring the exposure time and evaluating the peak refractive index change using the value of peak reflectivity obtained from the grating reflection spectrum. In this way, the approximate value of the product of parameters ( $\alpha I_0$ ) is obtained via the equation

$$\alpha I_0 = -\frac{1}{t_0} \ln \left( \frac{2dn_{max} + n_{eff} - n_s}{n_{eff} - n_s} \right), \quad (4.61)$$

where  $dn_{max} = dn(0, t_0)$  is the peak RI change at the reference time  $t_0$  that is estimated from reflection spectrum data. Substituting the values of parameters  $t_0$ ,  $dn_{max}$  and the Gaussian function for the illumination profile  $I(z) = I_0 \exp[-z^2/(gL)^2]$ , we finally obtain the relationship for the profile of RI modulation amplitude at any exposure time  $t$ :

$$dn(z,t) = \frac{1}{2} [n_s + (n_{eff} - n_s) \left( \frac{2dn_{max} + n_{eff} - n_s}{n_{eff} - n_s} \right)^{\frac{1}{t_0} \exp(-z^2/(gL)^2)} - n_{eff}]. \quad (4.62)$$

The parameters required for this model are  $dn_{max}$ ,  $t_0$ ,  $g$  and  $n_s$ .

The sets of graphs in the following figures represent the results of calculations made on the basis of the gratings growth model being considered. Figure 4.17 shows the time evolution of the peak value of RI modulation amplitude observed within a Bragg grating exposed in a prism interferometer configuration. Different boundary conditions chosen for the solution of equation (4.54) correspond to the assumptions made regarding the degree of fibre photosensitivity and

the observed rate of index change. The chosen range of grating growth rates is determined by the range of experimentally observed rates of grating peak reflectivity increase for standard telecommunications fibres (hydrogen-loaded) and with UV laser sources used by OTRL.

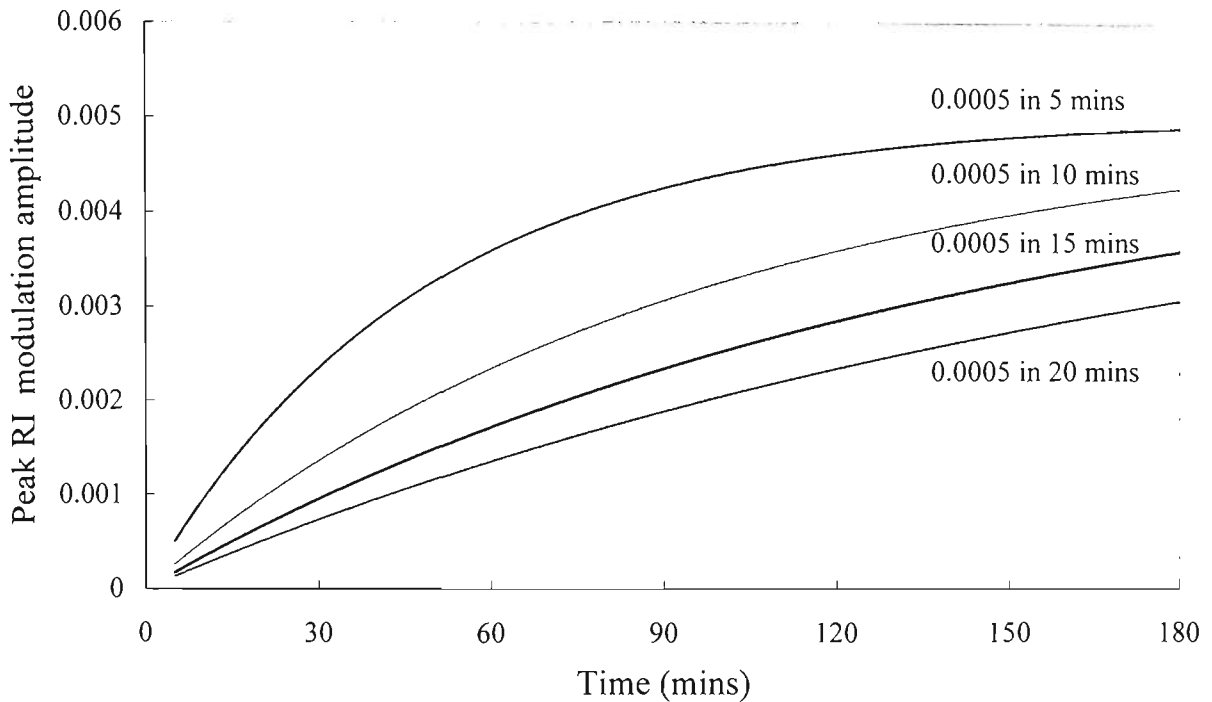


**Figure 4.17** *Modelled time evolution of the peak RI modulation amplitude for different rates of grating growth. The amplitude of RI modulation at saturation is assumed to be  $\Delta n_s = 0.0005$ .*

Figure 4.18 shows the results of application of the index modulation model for the calculation of the profiles of index modulation induced within Bragg gratings after a given exposure time. The amplitude envelopes of index modulation profiles are calculated using the assumption of the peak value of the RI modulation amplitude being equal to 0.0005 after 15 minutes of exposure. This corresponds closely to the observed moderate rates of grating growth for the chirped gratings produced with the prism interferometer. This rate depends upon the experimental apparatus used for the grating production, which contains several elements (including steering prisms and the interferometer prism itself) that introduce UV beam power loss through absorption and unwanted reflections. The graphs of time evolution of the index modulation envelope show that the effects of writing beam nonuniformity and index saturation effects lead to the increasing nonuniformity in the grating RI modulation profile with continued exposure.

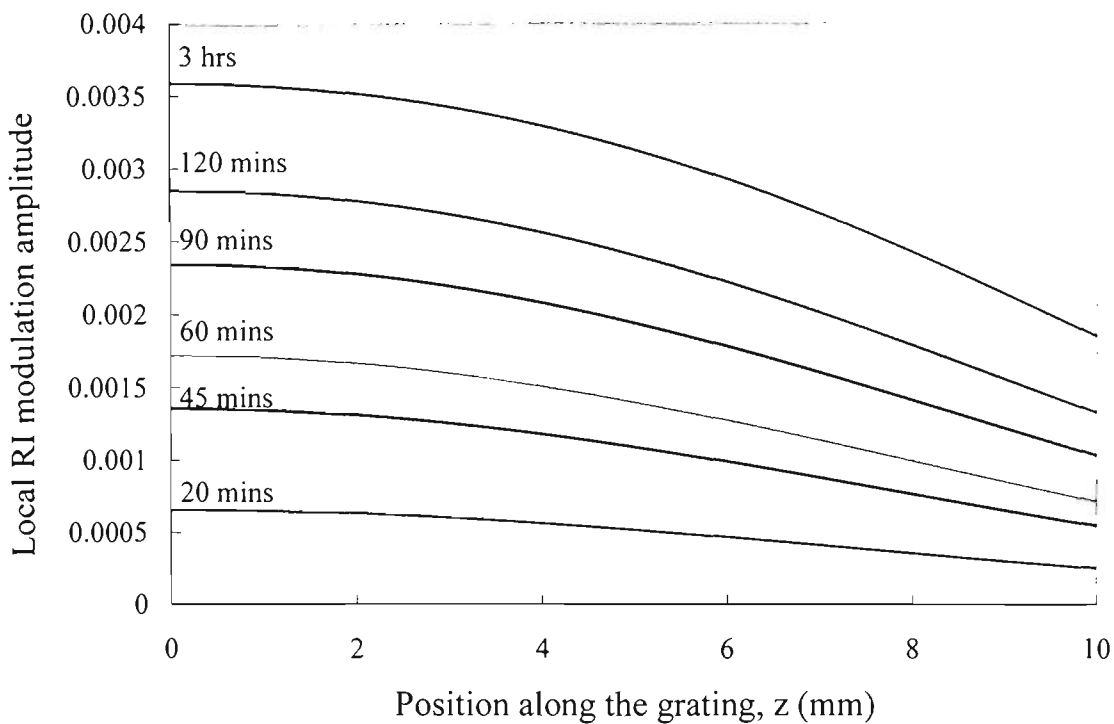


**Figure 4.18** *Modelled envelopes for the refractive index modulation profile. Calculations were based on the saturation model and the assumption of the peak index modulation value being equal to 0.0005 after 15 mins of exposure. The value of 0.005 was used for the RI modulation amplitude at saturation.*

## 4.6 Analysis of multiple superimposed chirped Bragg grating structures.

For many applications involving the use of broad reflection bandwidth chirped gratings, including this present low-coherence interferometry application, it is highly desirable to be able to control the shape of the spectral reflection response of chirped gratings. This goal can be achieved theoretically through the design of an appropriate chirping function in order to match the characteristics of chirped grating to those required for the application. However, some serious practical constraints may limit this approach because of technical difficulties related to the generation of an interference pattern with desired characteristics for grating production. A more practical approach to the fabrication of broad bandwidth chirped gratings with desired spectral response characteristics uses the technique of superimposing a number of chirped gratings in order to "build" the structure with appropriate spectral properties. This approach of superimposing chirped gratings was utilised during this study in order to fabricate broad bandwidth Fabry-Pérot reflectors using the prism interferometer chirping technique. Despite the fact that the quadratic nature of the chirping function limits the achievable FWHM spectral bandwidth of chirped gratings, the technique of superimposing gratings allows this difficulty to

be overcome easily, enabling grating structures to be fabricated with appropriate shapes of the reflectivity spectra. A large variety of grating structures with almost arbitrary shapes of the spectral reflection response can potentially be fabricated with the superimposing technique since the "building blocks" for the structure can have various chirp functions and index modulation levels. Provided that the fibre has sufficient photosensitivity, a large number (in excess of 10) of different chirped gratings can be written onto the same section of fibre, and even the dynamics of the index saturation process can be exploited in order to obtain the desired reflection response characteristics.

The coupled-mode equations can be used to describe the properties of sets of multiple superimposed chirped gratings with known chirp functions. In order to account for the combined effect of several superimposed gratings, the set of coupled-mode equations (4.19) can be modified as follows:

$$\begin{aligned}\frac{dA}{dz} &= -j \sum_{i=1}^N k_i(z) B(z) \exp[j\sigma_i(z)], \\ \frac{dB}{dz} &= j \sum_{i=1}^N k_i(z) A(z) \exp[-j\sigma_i(z)],\end{aligned}\tag{4.63}$$

where  $N$  is the number of gratings superimposed,  $k_i(z)$  is the local coupling coefficient of the grating number  $i$ , and  $\sigma_i(z)$  is the function describing the phase change due to propagation along the fibre and the effect of periodicity chirp for that grating. The relationships describing these functions are the same as considered above in this chapter for the case of a single chirped grating;

$$\sigma_i(z) = \int_0^z \left[ 2\beta - \frac{2\pi}{\Lambda_i(\xi)} \right] d\xi,\tag{4.64}$$

$$k_i(z) = \pi \Delta n_i(z) \eta / \lambda_{iB}(z).$$

In equations (4.64),  $\Lambda_i(z)$  is the fringe periodicity function for grating  $i$ ,  $\lambda_{iB}(z)$  is its local Bragg reflection wavelength, and  $\Delta n_i(z)$  is the local value of refractive index modulation amplitude produced by the exposure of that grating.

Each term of summation in (4.63) represents the effect of a particular grating on the local value of derivatives  $dA/dz$  and  $dB/dz$ . Mathematically, the set of superimposed gratings is treated here as a linear combination of individual gratings where it is assumed that gratings do not interact

with each other and do not affect each other's coupling properties. This assumption can be considered as viable at least for the case of a set of weak gratings with moderate levels of RI modulation amplitude. However, the grating writing sequence is accounted for through the calculation of  $\Delta n_i(z)$  profile functions for each grating, since each exposure alters the effective refractive index profile of the fibre core. From the grating growth dynamics model described in [Poladian, 1993] and considered in detail above, with each successive exposure the further growth of index modulation occurs at a slower rate as the local effective RI value of fibre is increased. As a consequence, the mean Bragg reflection wavelength of the structure is also increased.

The differential equation for the complex reflection coefficient in the case of a set of superimposed gratings can therefore be represented by the relationship:

$$\frac{dr}{dz} = j \sum_{i=1}^N k_i \left[ \exp(-j\sigma_i) + r^2 \exp(j\sigma_i) \right] \quad (4.65)$$

It can be solved numerically using the 5<sup>th</sup>-order Runge-Kutta method starting from the boundary condition of the form

$$r(L_{G_{max}}) = 0, \quad (4.66)$$

where  $L_{G_{max}}$  is the maximum grating length for the set of  $N$  superimposed gratings.

The numerical solution produces values of real and imaginary parts of the structure's electric field reflection coefficient at  $z = 0$  for any value of wavelength of the incident lightwave. These values are then used to calculate the spectral reflection response and phase response of a set of superimposed gratings.

## 4.7 In-fibre Fabry-Pérot cavities produced by writing chirped Bragg gratings.

In this project, broad reflection bandwidth Fabry-Pérot cavities were fabricated inside the core of optical fibres by writing of pairs of chirped Bragg gratings either simultaneously or sequentially. The low-coherence sensing application has required the production of pairs of three broadband reflectors at a specified set of central wavelengths with each set of three reflectors being effectively located at the same position along the fibre. This ensures the same effective value of the Fabry-Pérot cavity length for every spectral component of the propagating lightwaves provided by a multiwavelength combination source. Another requirement was that the reflectors should have suitable shapes of the spectral reflection response in order to not induce any significant additional highly coherent components in the reflected spectrum. At the same time, the reflectors of the triple-wavelength Fabry-Pérot cavity were required to have suitable values of mean reflectivity and FWHM bandwidth for each one of the three wavelength regions. The preferred shape for the spectral reflection response of grating mirrors was a rectangular one in order to ensure the uniformity of reflectivity levels for all wavelengths. This requirement is not critical for the application and is technically difficult to fulfil. However, it was possible to produce reflectors with spectral shapes that were nearly rectangular. This combination of technical challenges has been resolved using the prism interferometer technique for writing chirped gratings at desired wavelengths and by superimposing chirped gratings thereby enabling the fabrication of co-located reflectors with controllable spectral response. The prism interferometer chirping technique has proved effective for writing the "building blocks" of suitable (and variable) shapes, of which the more complicated grating structures with suitable spectral characteristics were made at all wavelengths of interest. The technique of superimposing chirped gratings has facilitated the production of the co-located chirped reflectors for three different wavelength regions and also the ability to "build" the grating structures with required spectral characteristics within each of the required wavelength regions. The task of fabricating suitable Fabry-Pérot cavities for use as a sensor element in a low-coherence interferometer system has necessitated extensive research into Bragg gratings during this study.

### **4.7.1 Methods of fabrication of Fabry-Pérot cavities formed by pairs of superimposed chirped grating structures.**

Two principal techniques of fibre exposure were used to fabricate broad reflection bandwidth Fabry-Pérot cavities, the simultaneous exposure method and the method of sequential exposure of grating pairs.

The simultaneous exposure technique was employed when a large diameter (about 1 cm) UV output beam was available with levels of optical power that did not require any additional focussing of the beam in the vertical plane to increase the power density. Pairs of chirped gratings were written simultaneously with both sections of fibre under exposure positioned symmetrically with respect to the diameter of the writing beam to ensure similar (or preferably identical) distributions of UV power density along each of the exposed fibre sections.

The method of sequential exposure was employed with the FreD source since in this case gratings could only be effectively written with the writing beam being focussed in the vertical plane onto the fibre. It could be focussed onto two fibre sections positioned in parallel close together but in that case the power density in the replicating UV interference pattern would be insufficient for obtaining suitable grating growth rates and it would have been harder to ensure the same UV intensity distribution along each of the fibre sections. Each one of the pairs of superimposed gratings was written in sequence by adjusting the position of the vertical focussing lens in order to "switch" exposure from one fibre section to another. Identical values of exposure time were used and care was taken to position two parallel fibre sections close to each other, so that only very slight adjustment was necessary in order to move the beam focus onto another fibre without introducing any large changes to the UV interference pattern.

With both of these methods, the fibre was bent in a loop before being fixed with clamps in a fibre holder, in such a way as to ensure the same direction of chirp for gratings written for each of the two reflector mirrors of the Fabry-Pérot cavity. The diagrams in Figure 4.19 illustrate the details of fibre positioning and exposure-switching techniques used for the production of fibre grating Fabry-Pérot cavities.

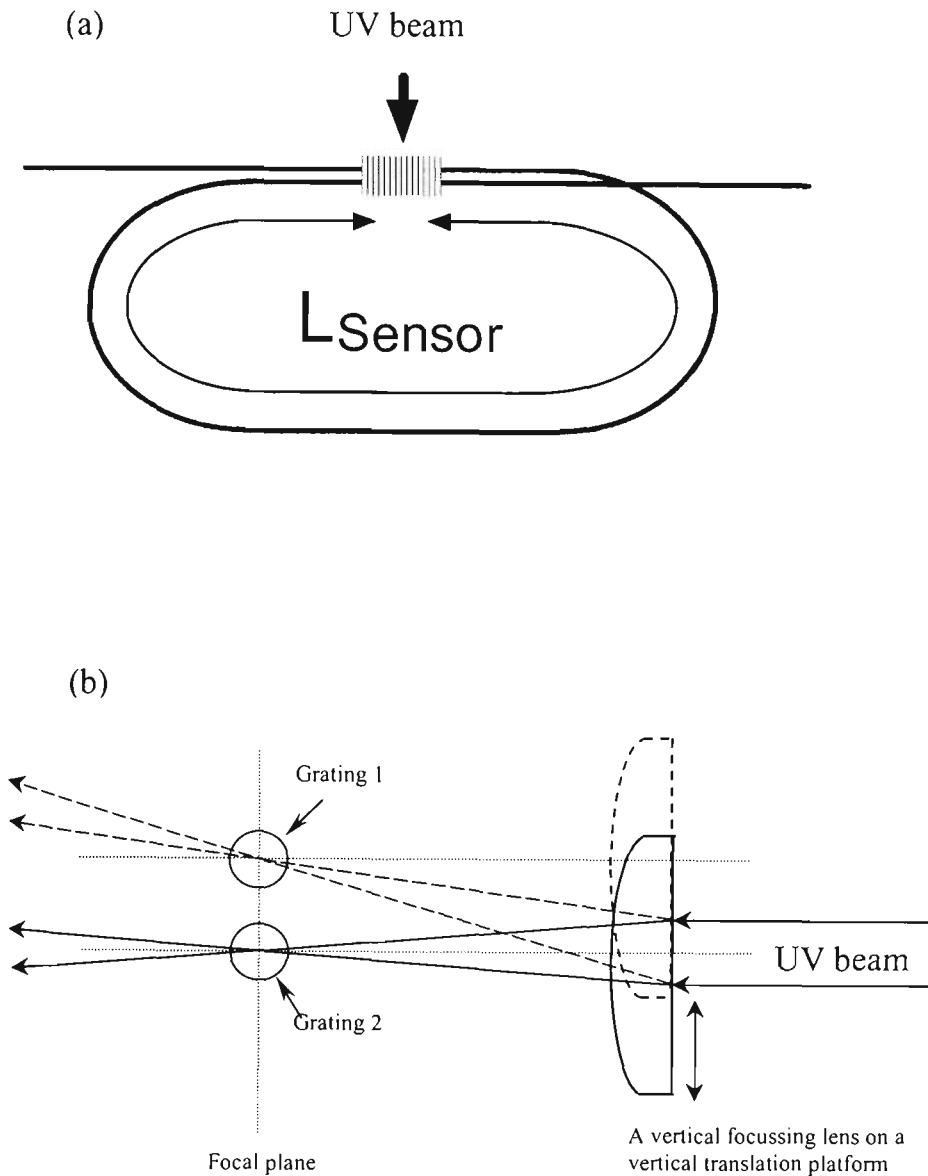


**Figure 4.19** Techniques used for the fabrication of fibre Fabry-Pérot cavities. (a) fibre positioning and (b) technique used for exposure switching.

The starting point ( $z = 0$ ) of each grating in a multi-wavelength set of superimposed gratings is the prism vertex position since the fibre remains positioned against the prism surface in the fibre holder during the entire process of triple FP manufacture with only the prism being turned (with fibre attached) for wavelength tuning. This ensures that each spectral component of incident light on reflection from the FP structure experiences the same value of phase delay between the waves reflected from the first and second grating mirror. The additional phase change on reflection from chirped gratings is different for every wavelength due to the spectral dependency of the phase of grating reflection coefficient but this effect is small compared to the

value of phase change provided by the FP cavity. Since the Fabry-Pérot structure is made of a set of superimposed chirped gratings with overlapping chirp functions, each spectral component of incident light is effectively reflected from a set of points within each reflector structure. The overall effect, however, is effectively identical to that of the two point mirrors separated by the FP cavity length since care was taken to ensure identical properties of reflectors in each pair. This was done by either positioning fibres symmetrically relative to the UV beam diameter (equalising the UV intensities) during simultaneous writing of grating pairs, or through exposing fibres for the same time intervals without changing the illumination conditions during the sequential exposure experiments.

#### **4.7.2 Fabry-Pérot cavities formed by multiple superimposed sets of chirped Bragg gratings.**

Now some examples of the results of application of fibre Fabry-Pérot fabrication technology are considered. A number of broad reflection bandwidth multiwavelength Fabry-Pérot structures with co-located reflectors were fabricated at OTRL. These fibre Fabry-Pérots were used as sensor elements in a white-light interferometer system with a multi-wavelength combination source. The primary factors affecting the Fabry-Pérot fabrication process and the suitability of Fabry-Pérot cavities for the sensing application were the quality of the output beam from the ultraviolet source and the achievable levels of photosensitivity for the hydrogen-treated Corning Flexcore 780 fibre. The best fabrication results have been achieved with the FreD laser and when using fibres with good photosensitivity achieved due to hydrogen soaking for several days. The importance of these factors is based on the fact that the faster grating growth rates allow better control over the properties of reflectors being formed, often reducing the number of gratings needed to be superimposed, thus reducing the fabrication time. The issue of photosensitivity is of primary importance for the production of structures with a large number of superimposed gratings. In general, the more small-size "building blocks" are used in a controlled fashion during the structure fabrication, the better the overall flexibility of the technique, but this approach also increases the fabrication complexity. The quality of the UV beam, especially its spatial coherence, is also crucial since it limits the achievable spectral reflection bandwidth and growth rates of chirped gratings, therefore possibly necessitating the fabrication of a larger number of superimposed gratings for the required spectral response.

Figure 4.20 shows a plot of measured spectral transmission for a FP cavity composed of two sets of superimposed chirped gratings fabricated by simultaneously writing pairs of gratings. The UV light source used was the frequency-quadrupled Spectra-Physics GCR-250 providing a

pulsed (10Hz repetition rate) output at 266 nm. Simultaneous writing of grating pairs was possible with this source since the output UV beam had a diameter of about 1 cm and did not need to be focussed onto fibres in the vertical plane due to the level of available UV optical power of about 1 W. Two fibre sections were positioned against the prism surface in parallel at equal small distances to the horizontal diameter of the incident beam to ensure the gratings being formed had identical (or very similar) properties. Since the combined reflectivity of two sets of gratings is low (about 25% mean reflectance), the reflectivity of each set of gratings is approximately half that of the Fabry-Pérot structure. As described in the previous section, all gratings were written with codirectional chirp and every chirp function had a common starting point being  $z = 0$  at the prism vertex in order to ensure an identical (within manufacturing precision) effective Fabry-Pérot reflector separation for every spectral component of the incident light. For this Fabry-Pérot cavity, better uniformity of reflectivity level was achieved in the low-wavelength part of the reflected spectrum.

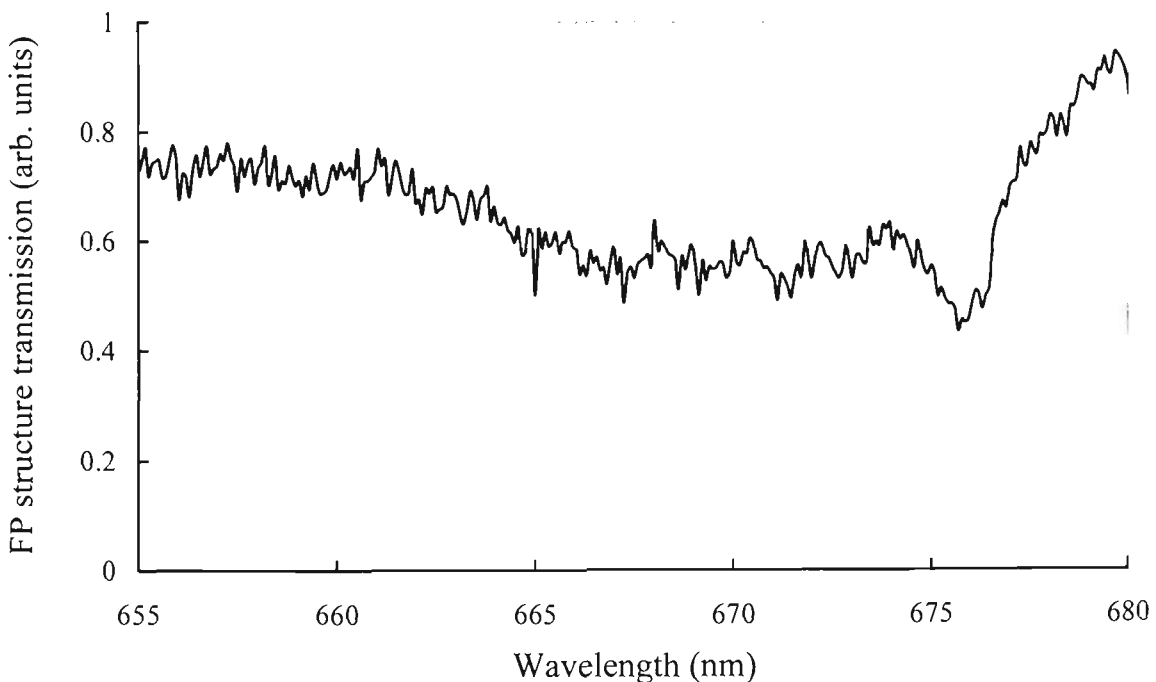


**Figure 4.20** *Spectral transmission of a FP cavity fabricated in the 670 nm region by simultaneously writing pairs of chirped gratings and superimposing seven gratings in each of the 4 mm-long fibre sections. FP cavity length is 25.2 cm.*

Figure 4.21 shows the measured transmission spectrum of a Fabry-Pérot written in the 830 nm spectral region. This set of broad bandwidth reflectors was superimposed onto reflectors of the FP cavity of Figure 4.20, and also was produced by simultaneous writing of grating pairs with the same starting point for all gratings as in the 670 nm region. In fact, this Fabry-Pérot was written immediately after producing a 670 nm FP in the same fibre. Better degree of uniformity of the levels of reflectivity is achieved in this case due to a larger number of gratings being

superimposed (10 gratings). No significant reduction in the grating growth rates was noticed after writing a large number of superimposed gratings in the same sections of fibre (all gratings of Figures 4.20 and 4.21), even though the grating growth rate was initially moderate due to UV wavelength not being optimum for absorption in the glass (266 nm).

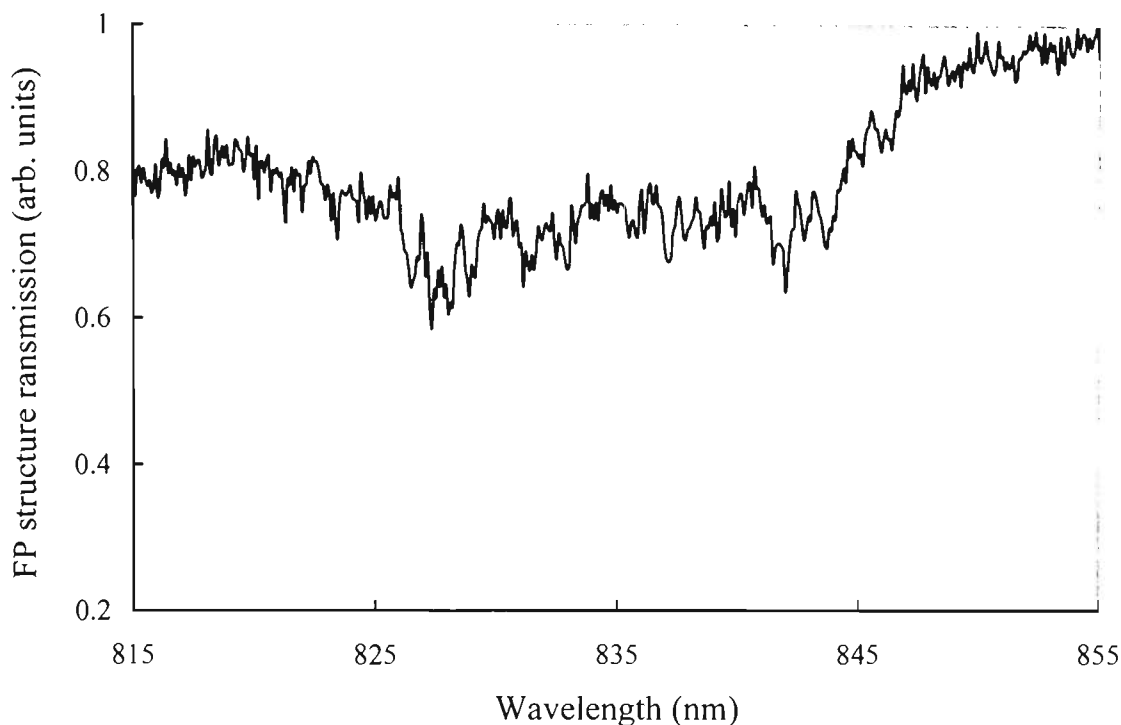


**Figure 4.21** *Spectral transmission of a broadband FP cavity fabricated in the 830 nm region with multiple superimposed gratings. Grating pairs were written simultaneously. All of the chirped gratings in the 830 nm region were superimposed on top of the previously written set of gratings in the same sections of fibre in the 670 nm region shown in Figure 4.19. The number of gratings superimposed is 10.*

Figures 4.22 and 4.23 show spectral transmission plots for another multi-wavelength Fabry-Pérot formed by writing grating pairs sequentially using the FreD laser source. A smaller number of chirped gratings needed to be superimposed in this case in order to achieve suitable spectral characteristics for the resultant structure. This was due to the better grating growth rates achieved with this 244 nm CW source and also due to the superior spatial coherence properties of the UV beam that ensured little reduction in visibility of the replicating interference pattern along the grating length. Sequential grating writing with equal exposure times of about 15 minutes for each grating in every grating pair ensured approximately identical properties for both reflectors of the Fabry-Pérot cavity.

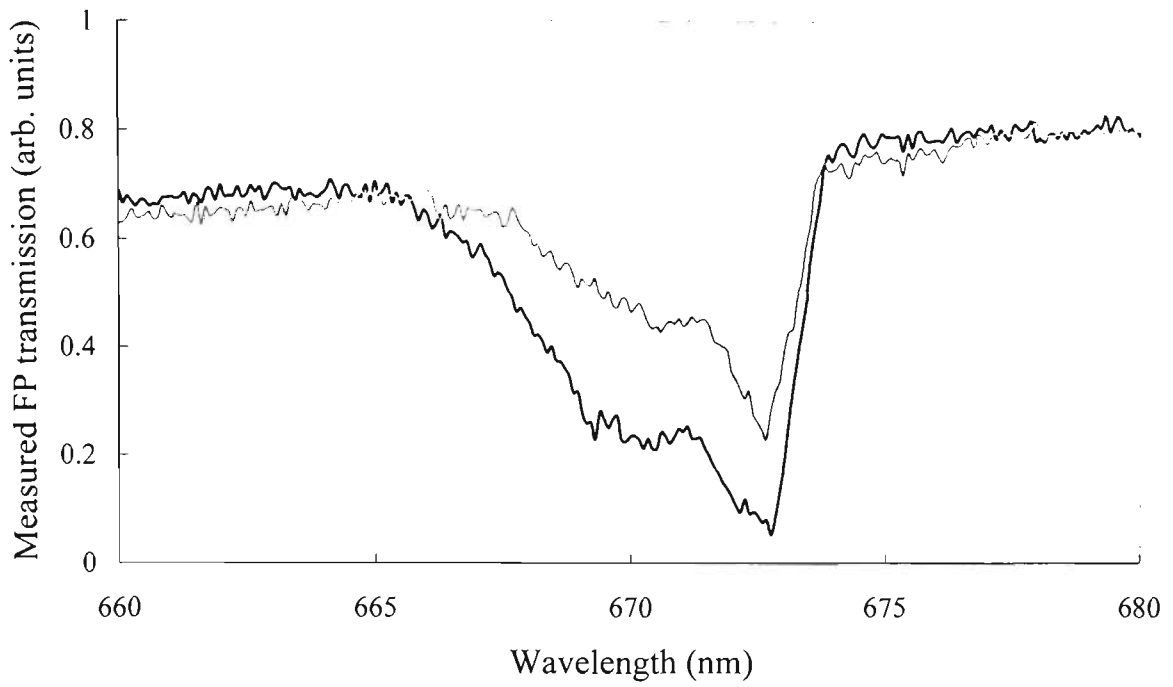


**Figure 4.22** *Spectral transmission of a FP cavity fabricated in the 670 nm region by sequentially writing a pair of sets of three superimposed chirped gratings. The reflector length is about 4 mm, separation of reflectors in a cavity is 230 nm.*

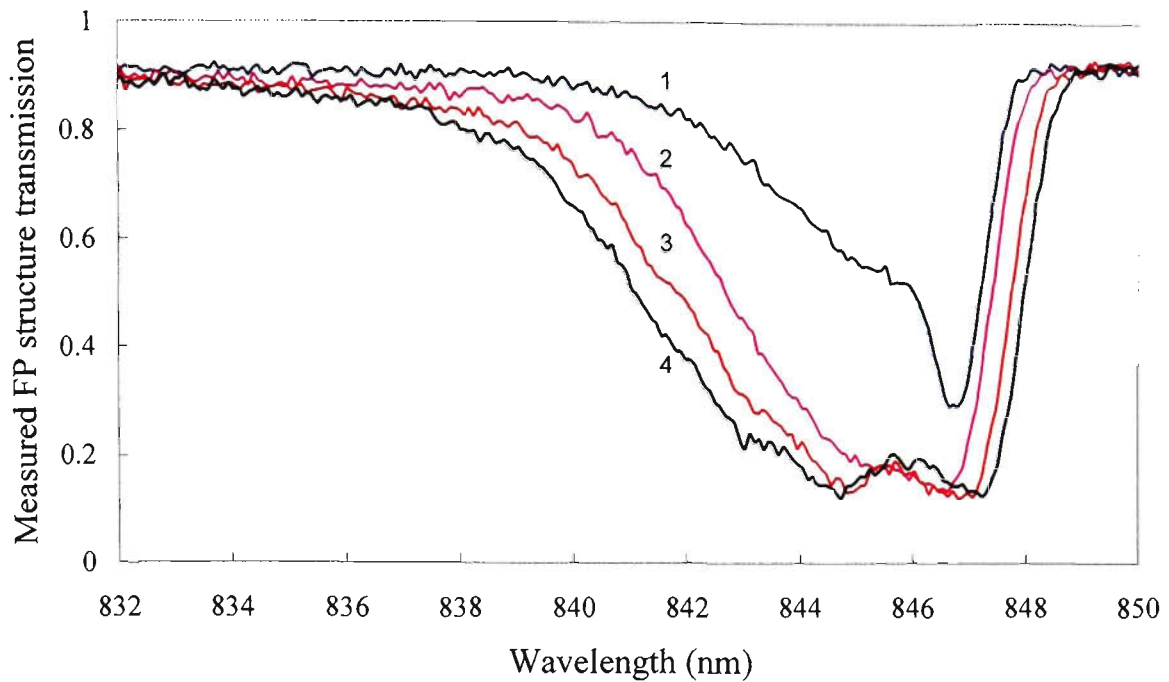


**Figure 4.23** *Time evolution of the spectral transmission of a FP cavity fabricated in the 840 nm region by sequentially writing a pair of sets of three superimposed chirped gratings. This FP structure was superimposed onto the previously fabricated structure of Figure 4.22. Top trace: one chirped grating in each reflector section; second trace: two chirped gratings superimposed in each reflector section; third trace: three superimposed gratings in one reflector section and two gratings in another one; fourth trace: three superimposed gratings in each reflector section.*

Figure 4.23 shows the intermediate stages of a Fabry-Pérot fabrication process. All gratings written in the 840 nm region were superimposed onto previously written gratings that formed a Fabry-Pérot of Figure 4.22.

## **Development of low-coherence optical fibre Fabry-Pérot sensor systems**

### **5.1 Introduction.**

This chapter describes the principal features of low coherence interferometers developed during this project. The sensor configuration and all system components are considered from a technical point of view. The properties of the output interferometric signal obtained with multi-wavelength sensor systems are considered and compared to the predictions made within Chapter 3. Specific issues related to system configuration and performance are addressed. In particular, the effects of stress-optic dispersion induced in the fibre coils, lead sensitivity in the receiver interferometer, and the influence of chromatic dispersion on the output signal properties are considered. The summary section presents an overview of technical issues related to the system performance and brings together the comparative effects of the phenomena affecting the system operation, in order to characterise the sensor's measurement potential and its limiting factors.

## 5.2 Scheme and description of a practical low-coherence sensing system.

A diagram of the white-light fibre Fabry-Pérot sensors built during this project is shown in Figure 5.1.

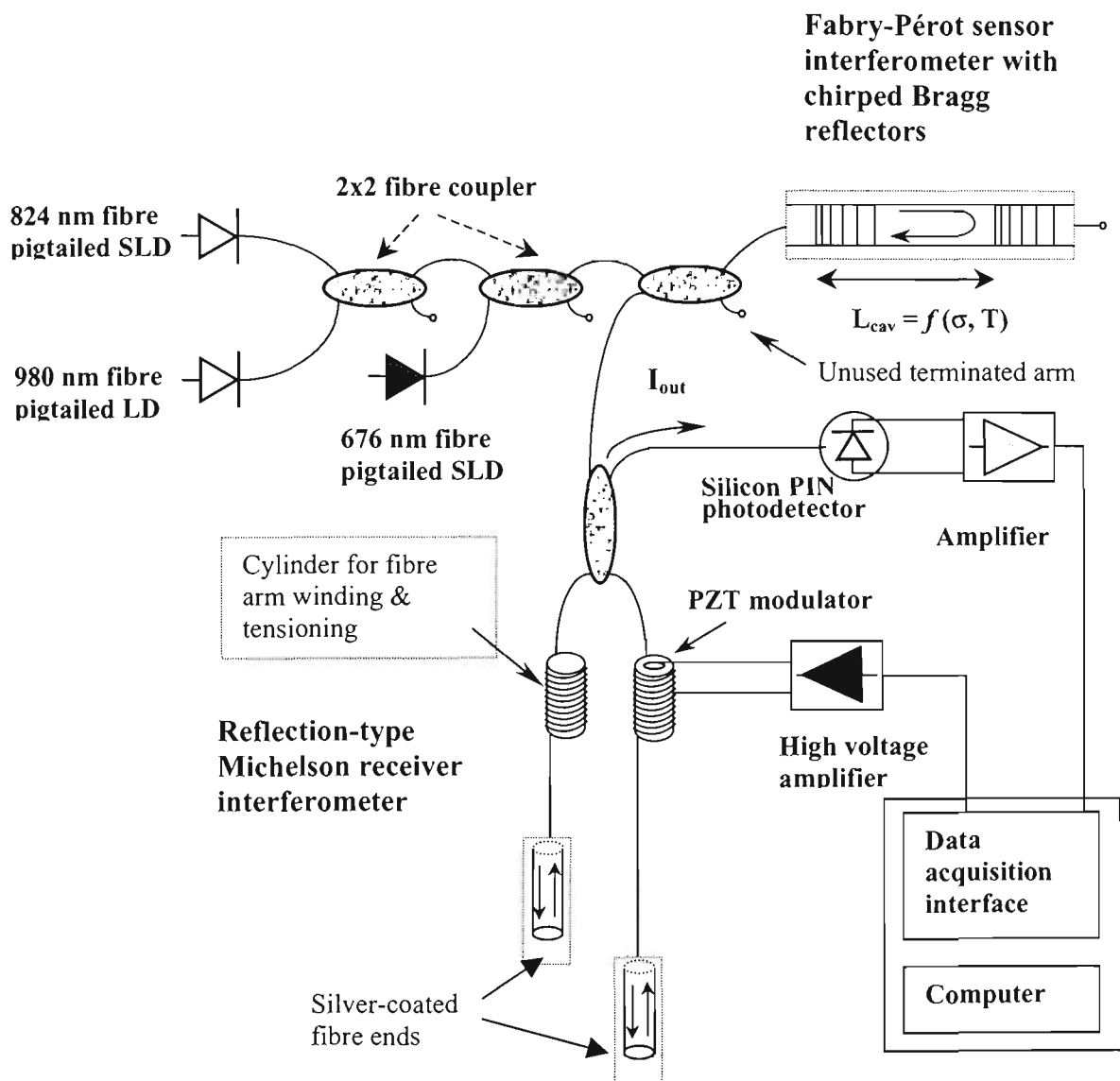


**Figure 5.1** *The low-coherence strain monitoring system.*

The overall structure of this sensor system can be functionally subdivided into four sub-systems, each of which can be considered separately.

Firstly, the sub-system of light sources includes three low-coherence sources with their power supplies and electronic driver circuitry. An arrangement of two four-port couplers was used to produce the combined source and then direct light to the sensor interferometer.

The sensor interferometer sub-system performs encoding of the measurand signal through splitting the incident light into two reflected beams with the optical path difference between them affected by the measurand during operation. The performance characteristics of two types of Fabry-Pérot sensing elements (based on either mirror-coated fibre ends or superimposed chirped Bragg grating structures) have been tested during laboratory measurements.

The receiver interferometer sub-system performs the function of decoding the measurand-induced path difference of beams split within the sensor. Phase domain processing has been implemented, with the temporal fringe formation technique used. The optical path difference of the receiver was scanned with a PZT stretcher during operation to generate the fringe pattern and recover the measurand information. A Vernitron PZT-5H cylindrical piezoelectric tube of 50 mm diameter wound with coils of fibre was used. The number of turns varied from 50 to 250 in various implementations of the interferometer, with the fibre under slight tension to eliminate sagging effects.

The position of the centre of the output white-light fringe pattern was tracked during repeated scanning of the receiver path difference within the range of fibre extension provided by the PZT modulator. This scanning operation was controlled by the data processing and control sub-system. The latter includes receiver electronics (a silicon p-i-n photodiode and a transimpedance amplifier followed by a voltage amplifier stage), data acquisition interface (National Instruments AT-MIO-16 E10 12-bit data acquisition card), a computer for running the sensor operation software, and a Lutz-Pickelman high voltage amplifier. The software interface used for sensor operation and fringe data processing was National Instruments LabView 4.1 installed on a Pentium computer.

### 5.3 Low-coherence optical sources.

The choice of an appropriate combination of optical sources is of critical importance for the design of any successful multi-wavelength low-coherence sensor system. The characteristics of light sources directly affect the properties of the output interference signal and the achievable signal-to-noise ratio. During this project, two triple combinations of sources were tested with the sensor system.

In the initial stages of this work, a source combination of two laser diodes operated below threshold (central wavelengths of 670 nm and 1  $\mu\text{m}$ ) and one superluminescent diode (central wavelength 833 nm) was used. The characteristics of these sources are summarised in the following table:

Light source	Emitted power	Central wavelength	FWHM bandwidth	Operation mode
Toshiba TOLD 9225 LD	75 $\mu\text{W}$ (just below lasing threshold)	670 nm	5 nm	Below threshold
Hamamatsu L3302 SLD	3.3 mW (max)	833 nm	8.9 nm	
E-Tek 980 nm LD pump module, fibre pigtailed	100 $\mu\text{W}$ (in pigtail)	1 $\mu\text{m}$	45 nm	Below threshold, temperature-stabilised

The emission spectra of all three sources installed initially in the system were presented in Figure 3.14 in Chapter 3.

A hybrid-optic coupling arrangement using microscope objectives was necessary for coupling light from two of the above sources into the fibre (arms of Acrotec four-port couplers using fibre with 850 nm cut-off wavelength). Low coupling efficiencies of 7-9% were achieved experimentally and coupling instability limited the amounts of optical power reaching the photodetector and led to signal-to-noise problems during signal processing. This bulk-optic coupling arrangement also made it difficult to transport the measurement system to the testing location. For these reasons, two medium-power fibre-coupled SLD sources have been purchased from Superlum Ltd. (Moscow) to replace the 670 nm and 833 nm light sources used initially.

The characteristics of this second light source combination with improved characteristics (used for obtaining measurement data in the final stages of this work) are summarised in the following table:

<b>Light source</b>	<b>Emitted power</b>	<b>Central wavelength</b>	<b>FWHM bandwidth</b>	<b>Operation mode</b>
Superlum SLD-261-MP, fibre pigtailed	0.31 mW at I=130 mA (in pigtail)	676.3 nm	12.9 nm	Driving current and temperature-stabilised
Superlum SLD-381-MP3, fibre pigtailed	0.81 mW at I=130 mA (in pigtail)	824.3 nm	23.3 nm	Driving current and temperature-stabilised
E-Tek 980 nm LD pump module, fibre pigtailed	100 $\mu$ W (in pigtail)	1 $\mu$ m	45 nm	Below threshold, temperature-stabilised

The spectral emission characteristics for these sources are shown in Figure 5.2. All three light sources were temperature-controlled with Peltier elements and temperature stabilisation circuits incorporated into the driving electronics modules. SLD source driving modules (Superlum Pilot-2 Driving Sets) also featured stabilisation of the driving current.

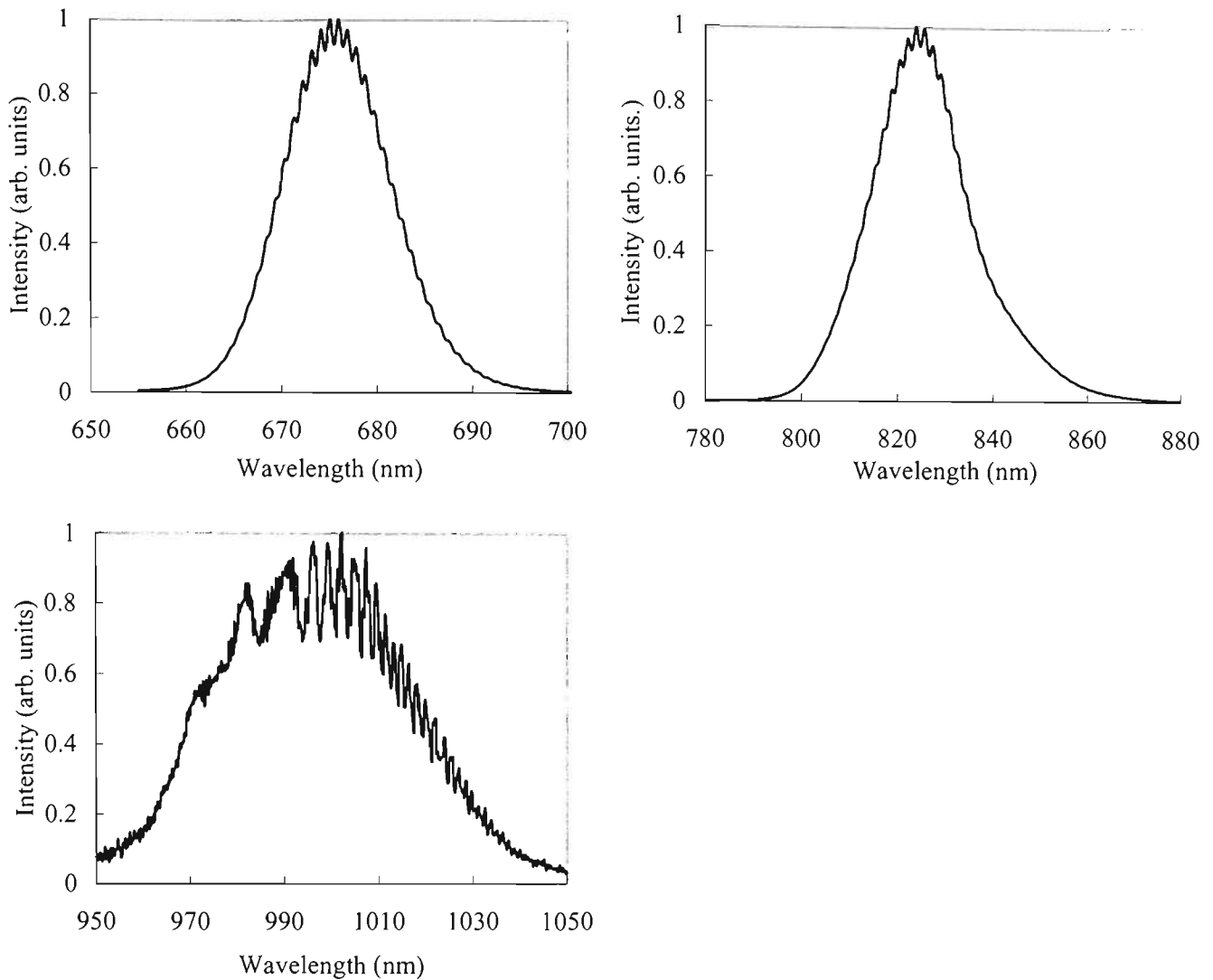


**Figure 5.2** Emission spectra of three low-coherence light sources used in the sensor system.

The values of self-coherence length for these three light sources calculated according to formula  $L_c = \lambda^2 / \Delta\lambda_{FWHM}$  were  $L_c(676) = 35.5 \mu\text{m}$ ,  $L_c(824) = 29 \mu\text{m}$ , and  $L_c(1000) = 22.2 \mu\text{m}$ .

The output of the SLD sources was launched into fibre pigtailed, made of single-mode polarisation-maintaining fibre, at  $45^\circ$  to its principal birefringence axes, enabling depolarisation of the launched light through the exchange of power between the two polarisation modes along the pigtail (length  $\sim 1$  m). According to the manufacturer's figures, the degree of polarisation of the output light was 4.8% for the 676 nm source and 3.7% for the 824 nm source.

## **5.4 Sensor Fabry-Pérot properties. Advantages and disadvantages of sensing elements produced with the prism interferometer technique.**

Fibre Fabry-Pérots utilised in this work were manufactured to suit the specific requirements dictated by the low-coherence sensing scheme and the source coherence synthesis method. They represent a novel type of sensing element for white-light interferometry, since the use of multiple superpositions of co-located quadratically chirped gratings designed for sensor interferometers with synthetic white-light sources has not been reported in the literature. The technology for producing fibre Fabry-Pérot cavities for broad bandwidth multi-wavelength interrogation based on superimposing chirped Bragg gratings has been proven to be generally successful. However, the method has advantages and disadvantages.

One of the major advantages of this novel type of sensing element is its intra-core reflectors achieved without breaking the fibre thereby providing superior mechanical strength properties (compared to in-fibre Fabry-Pérots formed using fusion-splicing technology [Kaddu, 1995] and fibre end coatings). This significantly increases the potential achievable dynamic range for intrinsic fibre Fabry-Pérot strain sensors.

Another advantage of superimposed chirped gratings is the ability to fabricate intrinsic fibre Fabry-Pérots that are specifically designed to be interrogated by an optimised multi-wavelength white-light source. The reflection spectra of cavity mirrors can be matched to a desired spectral content and shape, thus enabling efficient output signal processing. This flexibility is provided by the technique of superimposing co-located sets of chirped gratings, with each set being optimised to reflect light from each particular white-light source. The apparent limitation of this technology is dictated by the available degree of fibre photosensitivity that limits the number of gratings that can be superimposed. The prism interferometer chirping technique in combination with the grating superposition technology provides an efficient and economic way of fabricating spectrally tunable broadband reflectors for fibre Fabry-Pérots.

Reflection spectra of a Fabry-Pérot cavity used for sensing strain in the final stages of this project are shown in Figure 5.3.

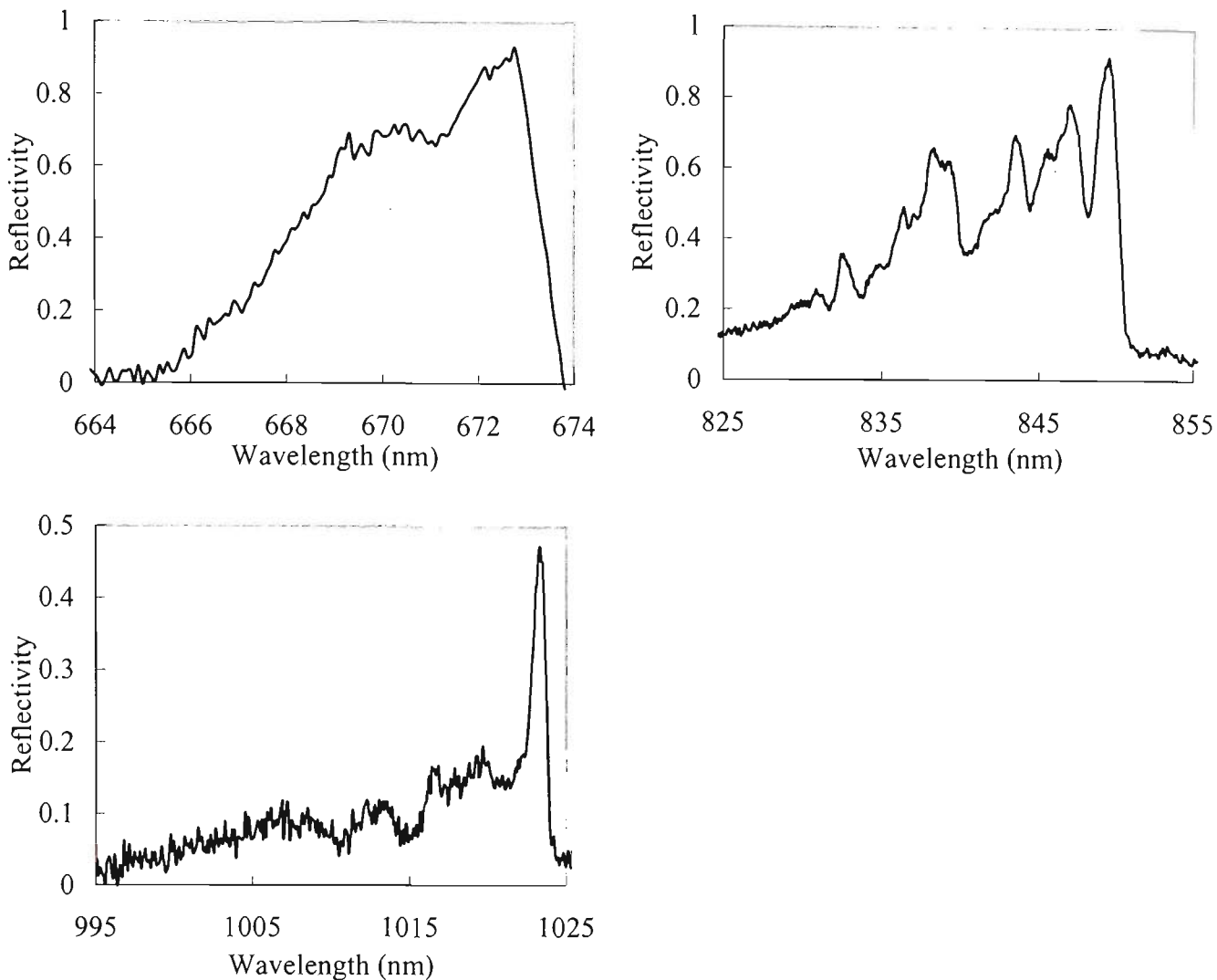


**Figure 5.3** Reflection spectra of the fibre Fabry-Pérot sensor cavity produced by superimposing chirped Bragg gratings at three different wavelength ranges.

One disadvantage of this type of sensor is that the reflection spectra of cavity mirrors contain narrow-band spectral features, which effectively increases the degree of coherence of the incident light due to spectral filtering. It is difficult to produce a perfectly flat reflection spectrum without ripple when using superimposed quadratic chirped gratings. Also, limitations on the achievable spectral widths of reflectors are imposed by the degree of fibre photosensitivity and the writing UV beam characteristics. The limited spectral width of the grating reflectors affects the output signal power when the emission bandwidth of an optical source exceeds the reflection bandwidth of the sensor.

Another specific feature of grating-based fibre Fabry-Pérot interferometers is that the cavity mirrors are in fact distributed reflectors. It is very important to produce sensing cavities with identical grating mirrors for practical sensing applications. Effectively, the grating-based fibre Fabry-Pérots behave as multiple sets of interferometers which leads to the formation of elongated white-light fringe patterns. The dispersion characteristics and birefringence of the

grating mirrors also contribute to the non-ideal character of the fringe patterns observed at the output of white-light systems that employ these sensing elements. The degree to which the structures of the grating mirrors are identical is the most important quality characteristic of these sensors. The better the manufacturing precision of grating reflectors, the more pronounced the central fringe is in the output interference pattern. A fully automated computer-controlled grating exposure system could be built using precision multi-axis translation stages for controlling the position (vertical and horizontal) of the grating exposure region with an accuracy of tens of nanometres. This positioning accuracy is well within the size of one grating fringe, and a range of suitable precision translation stages is available. In addition, these positioning devices would allow control of the UV power density within the replicating interference pattern through controlling the distance from the beam focus location to the fibre. The duration of exposure of each superimposed grating could also be computer-controlled to within milliseconds using a shutter with an actuator driven by LabView software.

The quality of the fibre Fabry-Pérot sensors fabricated using the writing system described in Chapter 4 was limited by the angular deviations in the writing UV beam, which led to the generation of an extra source of chromatic dispersion in the system (wavelength dependency of the sensor cavity length, discussed further in section 5.7). In the future, the use of automated grating writing systems employing precision translation stages (and possibly, custom-designed chirped phase masks) will certainly reduce the chromatic dispersion caused by the imperfections of grating superposition to levels not affecting the system performance.

The writing method used during the production of grating-based fibre Fabry-Pérots effectively removed all first-order variations in the effective locations of superimposed gratings due to the fibre being positioned in contact with the prism and the fibre holder being rotated on the same platform of the rotation stage. Therefore, a cluster of superimposed gratings starting from the same point (the prism vertex location) was produced in both reflector sections of fibre. The spread of starting reflection wavelengths within each pair of successively written gratings of each sub-interferometer was limited by the writing beam wander and the wobble of the translation stage during adjustments. These random variations in the starting wavelength between each successively written pair of superimposed grating reflectors resulted in dispersive shifting of the central fringes produced by each sub-interferometer in a compound Fabry-Pérot structure with respect to the structure's mean effective central fringe position. The magnitudes of these shifts were limited to a maximum of several interference fringes (calculated within section 5.7), and their distribution was Gaussian with the mean value being zero.

The coherent reflections (caused by the existence of narrow-linewidth features in each of the superimposed gratings) originating from throughout the grating length, and the spectral instabilities of the optical sources also complicated signal processing. These effects led to the elongation of the interference patterns, the appearance of parasitic groups of fringes causing asymmetric side-lobes in the fringe pattern, and an increase in the optical noise level during measurements, which caused some of the central fringe misidentifications. The output power variations of about 10% of the peak value and some narrow-linewidth (less than 1 nm) unstable spikes have been measured during the characterisation of the sources' emission spectra with a spectrum analyser.

Measurements of strain with chirped grating-based Fabry-Pérots in this study (discussed in Chapter 6) have shown that in the realistic case of mirror structures being not perfectly identical, the central fringe is still enhanced due to optimisation of source combination, even in the case of elongated white-light fringe patterns.

## 5.5 Receiver electronics.

The output white-light fringe patterns generated in the time domain during scanning of the receiver interferometer OPD have been detected with an electronic circuit incorporating a silicon p-i-n photodiode and a transimpedance amplifier, the output of which was further amplified with a one-stage voltage amplifier. The circuit diagram is shown in Figure 5.4.

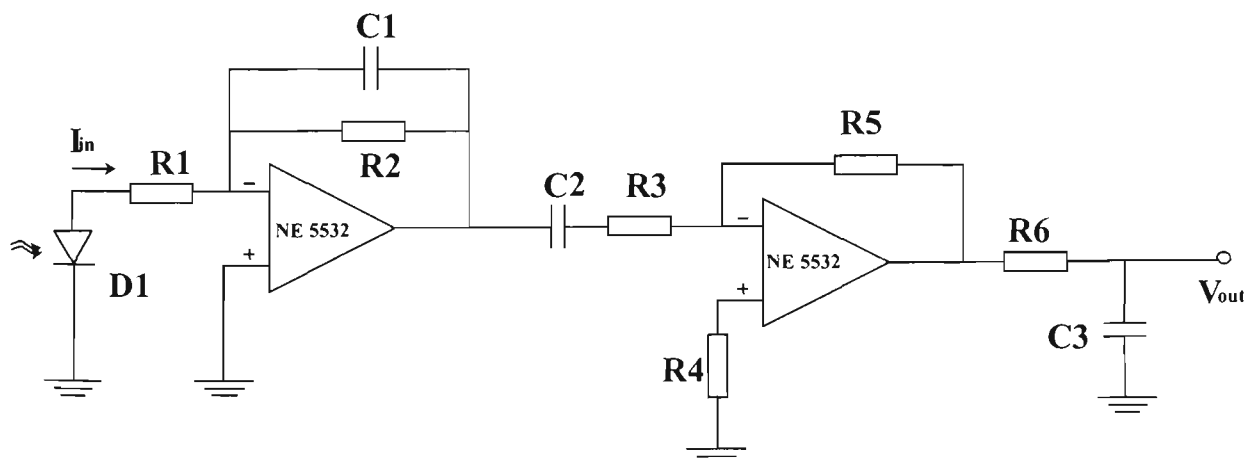


**Figure 5.4** Diagram of receiver electronics circuitry.

The characteristics of the electronic components used are summarised in the following table:

Component	Value	Description
R1	100 $\Omega$	Used for suppressing high-frequency oscillations in the input-stage amplifier.
R2	220 k $\Omega$	Feedback resistor (transimpedance stage)
R3	4.7 k $\Omega$	Biasing resistor
R4	4.7 k $\Omega$	Input resistance of the voltage amplifier stage
R5	1.2M $\Omega$	Feedback resistor (voltage amplifier stage)
R6	15 k $\Omega$	Resistor in the output low-pass filter
C1	33 pF	Feedback capacitor for limiting amplification bandwidth
C2	47 nF	Capacitor of intermediate high-pass filter
C3	1 nF	Capacitor in the output low-pass filter

The photodetector used in the circuit had dimensions of 1×1 mm, enabling efficient coupling of light exiting the fibre system. From its data specifications, its responsivities at the wavelengths used were:  $R(670 \text{ nm}) = 0.4 \text{ A/W}$ ,  $R(830 \text{ nm}) = 0.56 \text{ A/W}$ , and  $R(1000 \text{ nm}) = 0.39 \text{ A/W}$ . The manufacturer stated that the diode's maximum dark current was 5 nA (typical value of about 1 nA) and the noise equivalent power (NEP) was  $3.3 \times 10^{-14} \text{ WHz}^{-1/2}$  at 900 nm.

A Philips NE 5532 IC amplifier was used in the circuit in both the transimpedance stage and the voltage amplifier stage. The receiver bandwidth was limited by using an intermediate high-pass filter between the two amplification stages (a RC-chain providing a 3-dB low-frequency cut-off at 720 Hz) and an output low-pass filter (3-dB high-frequency cut-off at 10.6 kHz). This configuration of filters enabled the limitation of receiver bandwidth to approximately 10 kHz, allowing noise reduction and detection of signal waveforms generated with various rates of receiver interferometer scanning.

This electronic receiver circuit enabled the conversion of each 10 nA of input photodiode current into approximately 560 mV of output voltage within its operation bandwidth. The maximum practical peak-to-peak amplitude of electronic noise voltage measured did not exceed 30 mV. With input light powers producing a range of 0.5 V - 1.6 V of signal voltage peak-to-peak amplitudes during measurements (dependent on the combination of light sources and type of sensing element used), the working range of signal-to-noise ratios achieved with this circuit was about 24 dB to 34.5 dB.

## 5.6 Properties of the interferometer output signal and dispersion-induced signal distortion effects.

The properties of the output fringe signal of any low coherence fibre sensor depend on the characteristics of the sensing element employed and the propagation characteristics of the fibre components used. Of all fibre system characteristics, one of the most important ones for the performance of combination-source white-light systems is the magnitude of dispersion from all sources present in the system components. In the following sections, the influence of dispersion on the properties of the output white-light interferograms is discussed. Several sources of dispersion are considered, and their effect on the output fringe signals illustrated.

### 5.6.1 Effect of stress-optic dispersion.

The effect of wavelength dispersion in the stress-optic coefficient of fibre can lead to serious measurement problems in low-coherence fibre interferometry systems using combination sources with widely separated central wavelengths. This effect can be especially detrimental in the case of a receiver interferometer with long fibre arm lengths subjected to different levels of total strain. In the case when one of the arms in the receiver interferometer is wound tightly around a PZT cylinder, and the fibre in the second arm is free from tension, stress-optic dispersion will cause the optical length of the strained arm to depend on the light source wavelength. This would cause the path matching condition in the receiver interferometer to depend on the source wavelength and therefore complicate the operation of sensors utilising a combination source. The effect of stress-optic dispersion effectively shifts the positions of central fringes in the white-light fringe patterns generated by sources with different central wavelengths, making it difficult to identify the path matching condition. This effect has been observed experimentally during strain measurements in this project.

Consider the system in Figure 5.1, with the omission of the fibre winding cylinder in the constant-length arm of the Michelson receiver interferometer. Also assume that the other receiver arm contains  $L = 40$  m of fibre wound under uniform tension around a PZT cylinder, so that this wound length of fibre is subjected to uniform strain of  $\varepsilon = 10^{-4}$  (100 microstrain). For a combination low-coherence source with a minimum central wavelength of  $\lambda_1 = 670$  nm and a maximum central wavelength of  $\lambda_2 = 1000$  nm used in the system (maximum source wavelength separation of  $\Delta\lambda = \lambda_2 - \lambda_1 \approx 300$  nm), the dispersion due to the stress-optic coefficient can be shown to significantly affect the properties of output interferometer signal, as follows.

Using the published data on the Young's modulus of fused silica fibre [Hocker, 1979] ( $Y = 7.0 \times 10^{10} \text{ N/m}^2$ ), the mechanical stress in the wound fibre is  $\sigma = \epsilon Y = 7.0 \times 10^6 \text{ N/m}^2$ . From Barlow and Payne, 1983, the value of the stress-optic coefficient of germanium-doped silica fibre is  $C = -3.22 \times 10^{-11} \text{ m}^2 \text{ kg}^{-1}$  at the wavelength of 1064 nm, and its wavelength dispersion is  $dC/d\lambda = 2.34 \times 10^{-15} \text{ m}^2 \text{ kg}^{-1} \text{ nm}^{-1}$  at the same wavelength. The stress-induced decrease in the effective core refractive index of a wound length of fibre is therefore dependent on the wavelength of propagating light, and at 1064 nm this change in refractive index is  $\Delta n(\sigma)_{1064} \approx C\sigma \approx -2.2 \times 10^{-5}$ . The variation in the stress-induced RI change with wavelength can be estimated using

$$d\Delta n(\sigma, \lambda) \cong \sigma \frac{dC}{d\lambda} \Delta\lambda. \quad (5.1)$$

From equation (5.1), for a wavelength difference of  $\Delta\lambda \approx 300 \text{ nm}$  and fibre strain of 100 microstrain, the dispersion-induced variation in the stress-optic RI change is approximately equal to  $\Delta n(980) - \Delta n(670) \approx 4.9 \times 10^{-7}$ . Consequently, the dispersion-induced variation in the double-pass optical path length of the strained arm of the receiver interferometer is about  $\Delta(2nL) = 2L(\Delta n(980) - \Delta n(670)) \approx 3.92 \times 10^{-5} \text{ m} \approx 39 \mu\text{m}$ . As a result of the stress-optic dispersion effect, the position of the central fringe in the pattern generated by the 1000 nm light will be shifted by about 39  $\mu\text{m}$  with respect to the position of central fringe within the pattern generated by 670 nm light. This implies that correct determination of the central fringe in the combined white-light fringe pattern will be practically impossible if fibre arms in the receiver interferometer are not matched with respect to applied strain.

The influence of stress-optic dispersion on the output fringe signal of a white-light interferometer is illustrated in Figures 5.5 and 5.6. Figure 5.5 shows the interference pattern generated by a triple-wavelength combination source with an assumption that the positions of the centres of the individual 830 nm and 1000 nm patterns are shifted by 2  $\mu\text{m}$  and 4  $\mu\text{m}$  respectively relative to the middle of the 670 nm fringe pattern. The position of a fringe with maximum peak-to-peak intensity in this case is not coincident with the position of zero relative path imbalance for any of the three interferograms. The overall interference pattern is not symmetric, and the relative intensity difference between the largest fringe and other fringes is increased compared to the zero dispersion case. Further deterioration of interferometer signal in the case of larger dispersion shifts of 830 nm and 1000 nm patterns by values of 10  $\mu\text{m}$  and 20  $\mu\text{m}$  with respect to the centre of 670 nm pattern is shown in Figure 5.6.

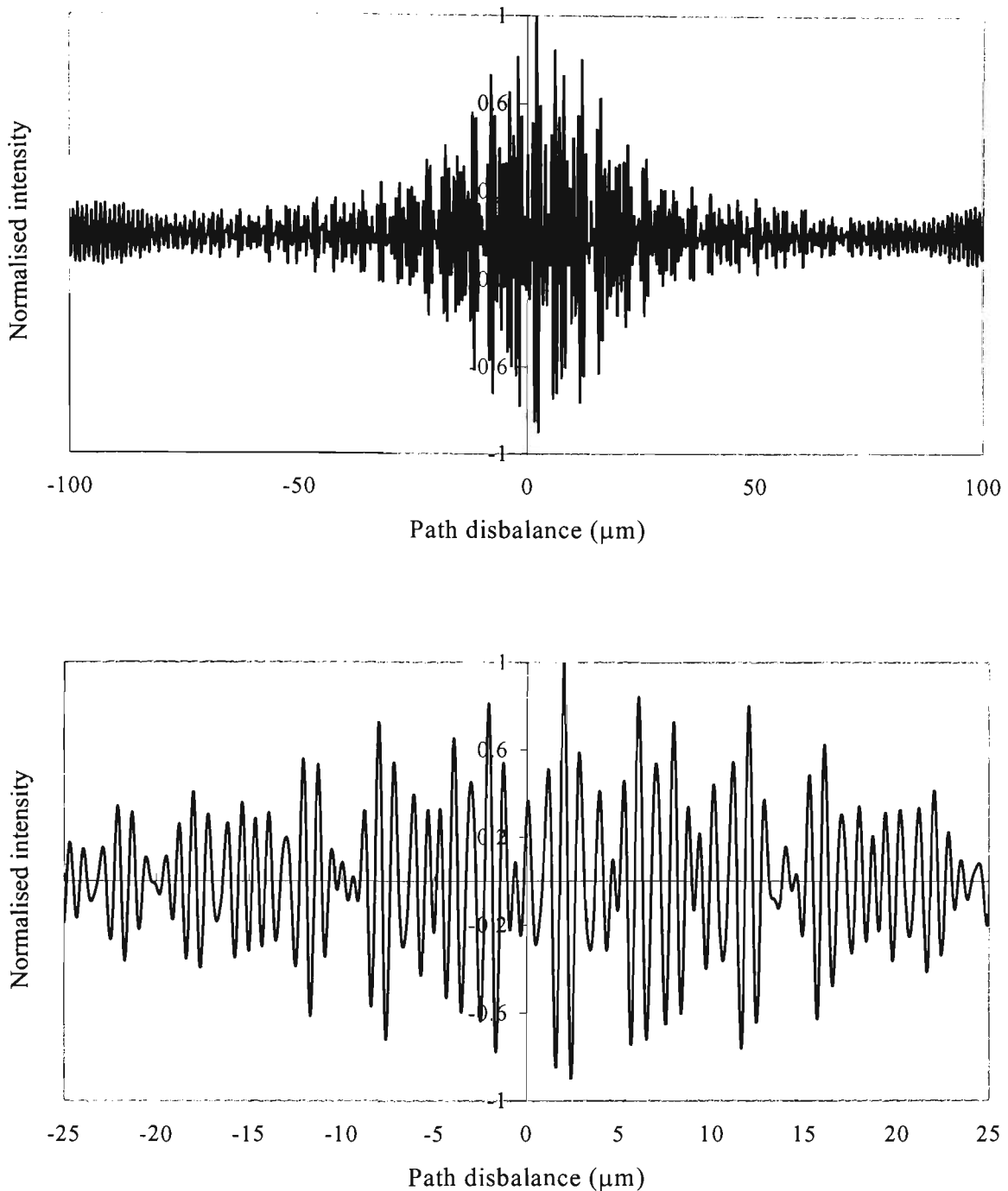


**Figure 5.5** *Modelled output white-light fringe signal distorted by stress-optic dispersion. Spectral data for a real triple combination source (central wavelengths 670 nm, 830 nm and 1000 nm) and a Bragg grating FP sensor was used for calculating the interferogram through the Fourier transform of the combined source spectrogram. The dispersion effect is incorporated in the model by assuming shifts of 2 μm and 4 μm for the position of central fringes generated by 830 nm and 1000 nm light with respect to the centre of the 670 nm source interferogram. An expanded view of the central region of interferogram is shown below.*

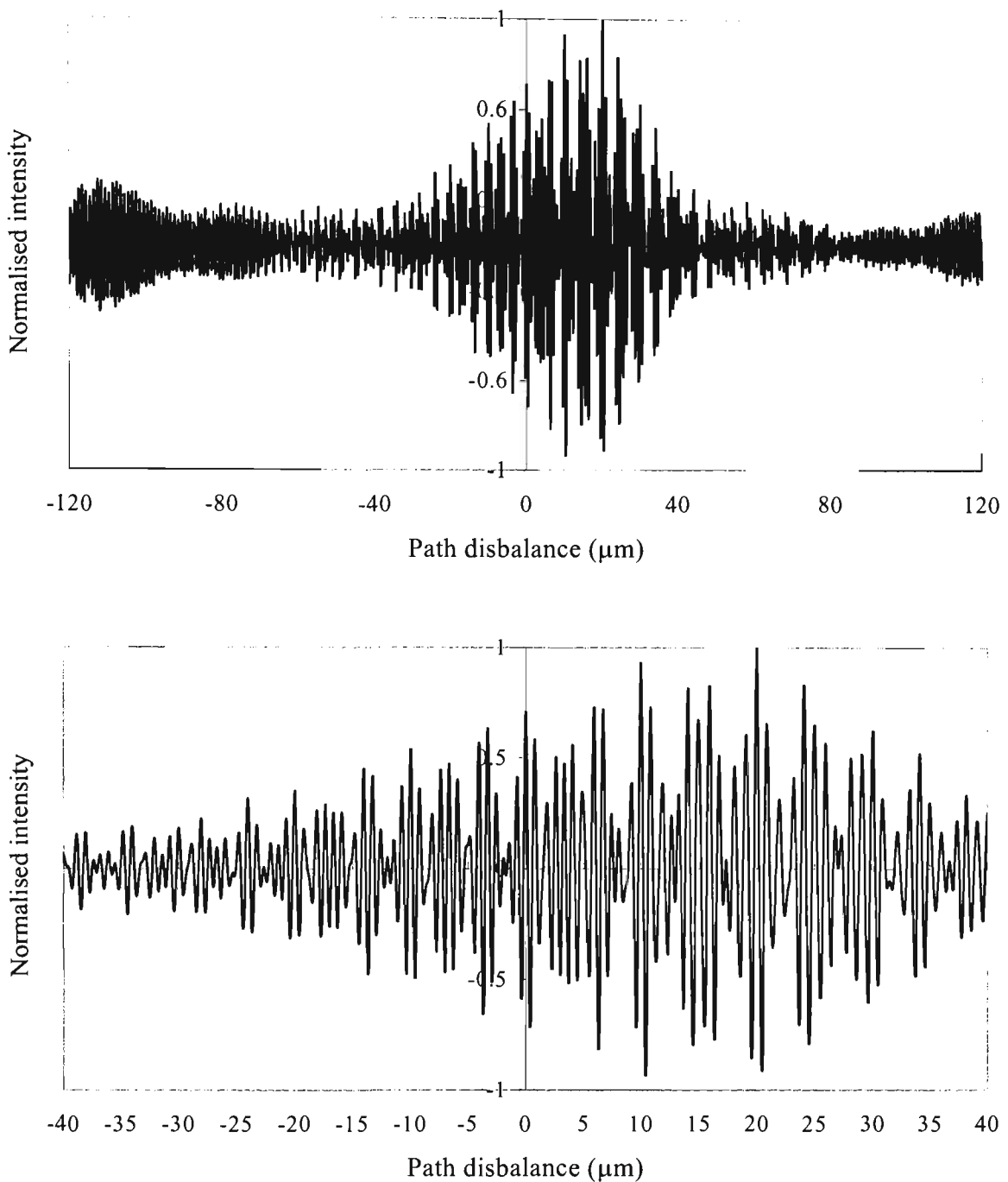


**Figure 5.6** *Modelled output white-light fringe signal significantly distorted by the effect of stress-optic dispersion. Spectral data for a real triple combination source (central wavelengths 670 nm, 833 nm and 1000 nm) and a Bragg grating FP sensor was used for calculating this interferogram through the Fourier transform of the combined source spectrogram. The dispersion effect is modelled by assuming shifts of 10  $\mu\text{m}$  and 20  $\mu\text{m}$  for the positions of central fringes generated by 833 nm and 1000 nm light with respect to the centre of the 670 nm source interferogram.*

Clearly, it is necessary to minimise the influence of the stress-optic dispersion in order to perform reliable measurements based on identification of the path matching condition. The shifting of white-light interferograms produced by sources of different central wavelengths can be minimised (or eliminated) by winding equal numbers of fibre turns under the same tension

around cylinders of identical diameter in both arms of the receiver interferometer. Since it is difficult to control tension precisely in the fibre during winding, accurate dispersion compensation, in principle, can be achieved by varying the number of fibre turns in the passive cylinder arm whilst observing the movement of the positions of central fringes provided by different light sources during the system operation. This dispersion compensation operation must be performed with the sensor element isolated from strain and temperature variations and under conditions of minimised lead sensitivity in the receiver interferometer in order to reliably identify the individual positions of path matching condition for all sources. Superposition of three central fringes with maximum precision can be achieved if the signal-to-noise ratio in the system is sufficient for the correct identification of central fringes provided by each individual light source.

### **5.6.2 Effect of chromatic dispersion in the system components.**

The presence of chromatic dispersion in any of the components of low coherence fibre interferometers leads to significant changes in the appearance of the output fringe interferograms. In particular, in fibre systems employing multi-wavelength combinations of sources with widely separated central wavelengths, great care must be taken to eliminate any chromatic dispersion effects.

The influence of chromatic dispersion on the properties of the output fringe signal in optical fibre LCI systems is illustrated in the following figures 5.7-5.9.

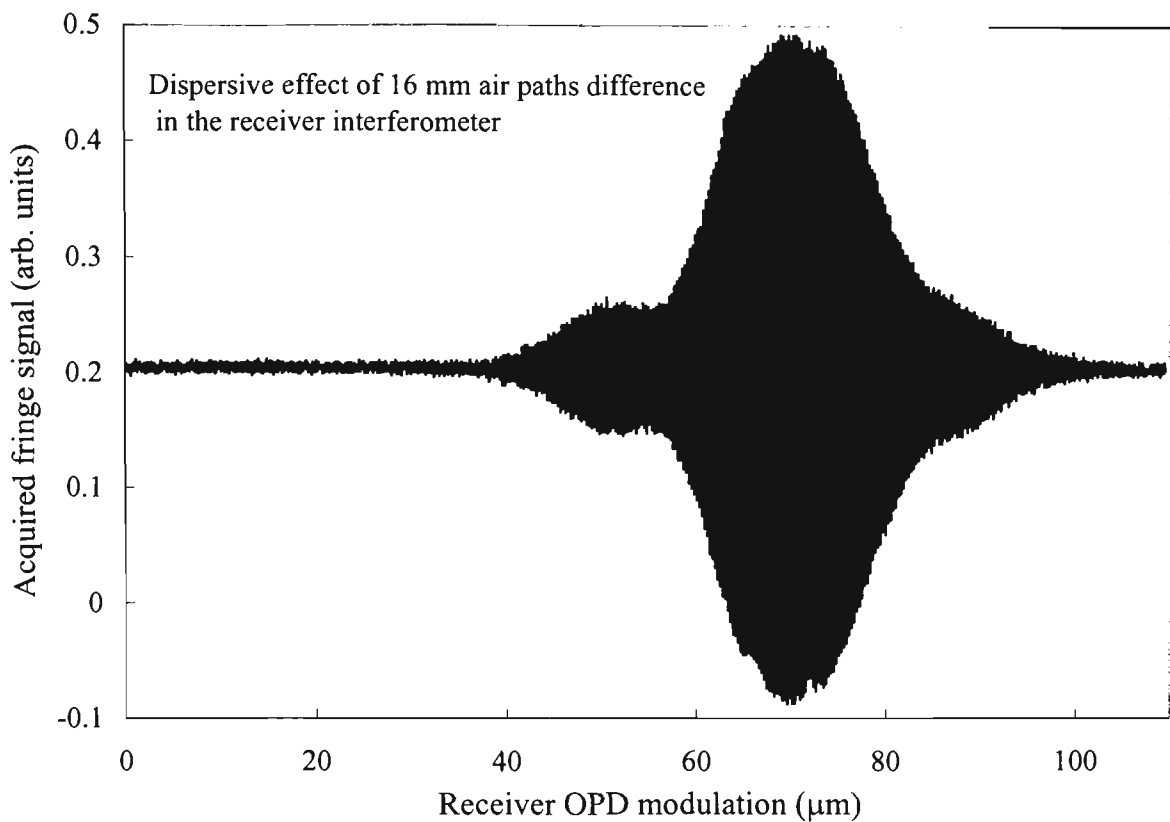


**Figure 5.7** *Elongation of a WLI fringe pattern generated at the output of a balanced Michelson interferometer illuminated with a single 676 nm source. The dispersion is caused by a difference of 16 mm in the air paths of the arms balanced with external mirrors.*

Clearly, if a small amount of chromatic dispersion can significantly distort a LCI fringe pattern from a single light source, this problem becomes particularly aggravated if several different light sources with widely separated central wavelengths are used. This situation is shown in the following figures 5.8 and 5.9.

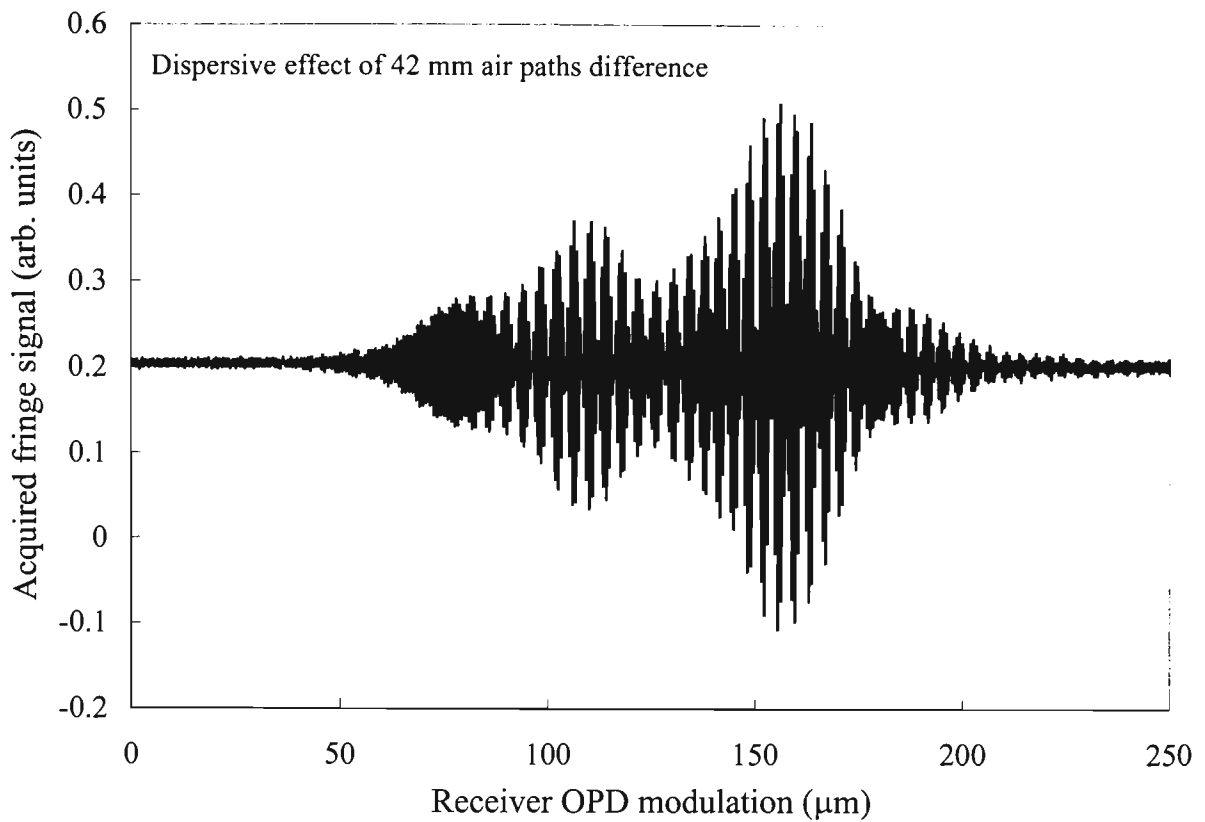


**Figure 5.8** *An effect caused by the presence of a dispersion mismatch between the arms of a balanced Michelson receiver interferometer with external mirror reflectors due to optical paths in its arms being different by a 42 mm air propagation path. A source combination of 676 nm and 824 nm was used.*

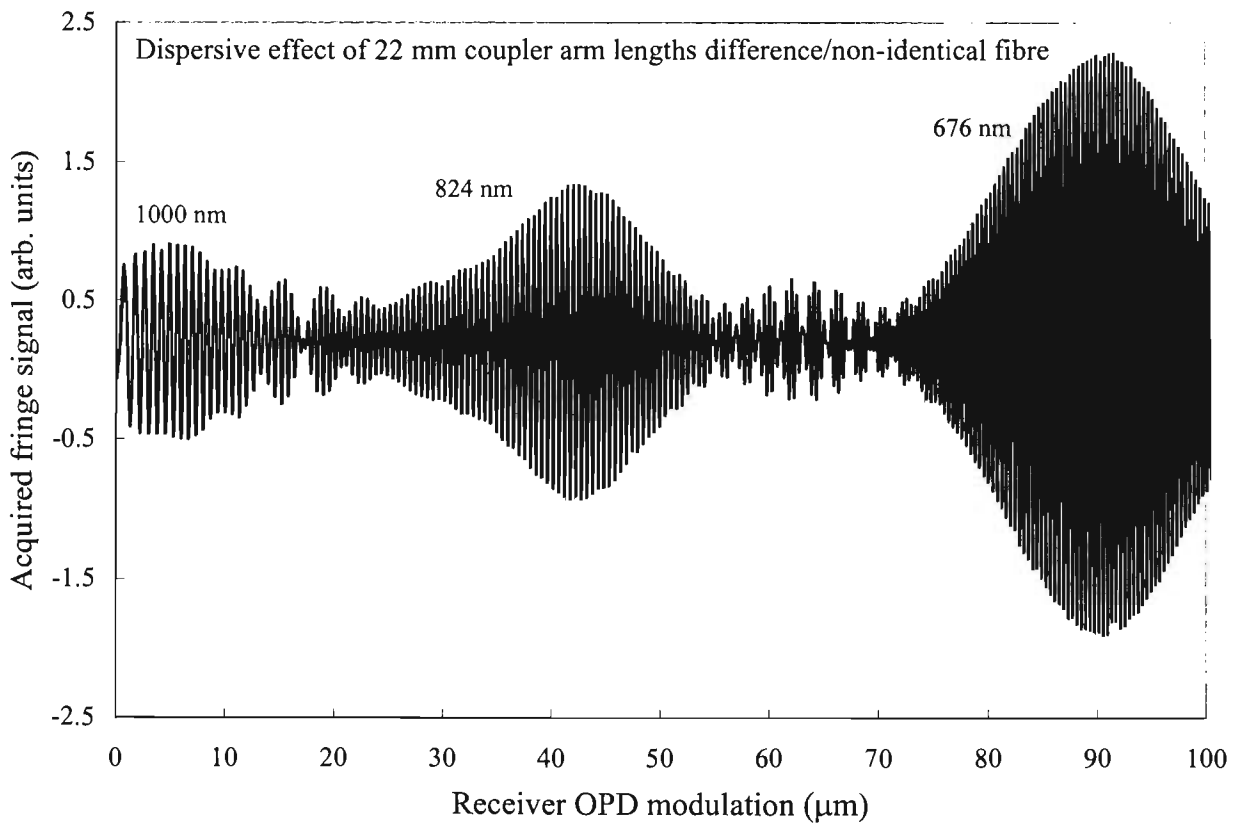


**Figure 5.9** *A dispersive effect observed in an all-fibre balanced Michelson interferometer due to light propagating through fibre arms having a non-common path of 22 mm of different fibre.*

## **Effects of modal dispersion, induced birefringence and polarisation mode dispersion.**

In systems using three wavelengths with wide spectral separation and fibre allowing two-mode or multimode propagation at the shortest wavelength, the effects of modal dispersion and noise will affect the stability of the output signal and its noise levels. In addition, the light propagating at the longest wavelength will be sensitive to bending-induced loss. These effects have been observed during measurements with the sensor system, especially when fibre of the receiver interferometer was not packaged sufficiently well to shield the effects of mechanical and thermal environmental disturbances. In the extreme cases of manually applying bending to the interferometer fibre (and therefore inducing energy exchanges between the guided modes), substantial amounts of signal fading prohibiting measurements were observed. These effects were present in both two-source (676 nm and 824 nm) and three-source (676, 824 and 1000 nm) interferometers. This indicates the presence of noise and signal instability contribution from two-mode propagation at the lowest wavelength. However, significant energy exchanges between the guided fibre modes did not occur during the unperturbed operation of well-packaged interferometers. The differences in the values of propagation constants of the guided fibre modes were limited to a maximum of several parts in a thousand, which could not lead to any significant instabilities in the position of the central fringe. On the other hand, energy exchanges between the two polarisation modes occurring at splices and fibre bends, together with the microphonic pick-up of acoustic noise by the sensor element were the major source of the central fringe position instability and optical phase noise during measurements. Another optical noise contribution was from spectral and power instabilities in the fibre-coupled optical sources. During measurements with a well-packaged receiver interferometer and undisturbed coupler fibre, modal noise effects were suppressed to levels allowing correct identification of the central fringe by its visibility in about 90% of measurement scans made with the double combination source system using end-coated Fabry-Pérot cavities. The measurements and fringe misidentification events are reported in quantitative detail in Chapter 6.

In systems using non-polarisation-maintaining single-mode optical fibre, a special type of modal dispersion can be present due to birefringence induced by environmental perturbations and in the fibre coils due to applied tension. If polarisation modes having different propagation constants due to birefringent elements in the system can exchange energy on propagation through optical fibre, this can lead to an increase in optical phase noise levels. Separation of LCI fringe patterns formed by two different polarisation modes can be observed in the output

interferogram if an increase in birefringence occurs in the system, for example, if a fibre is wound around a small diameter coil. This effect is illustrated in Figure 5.10.

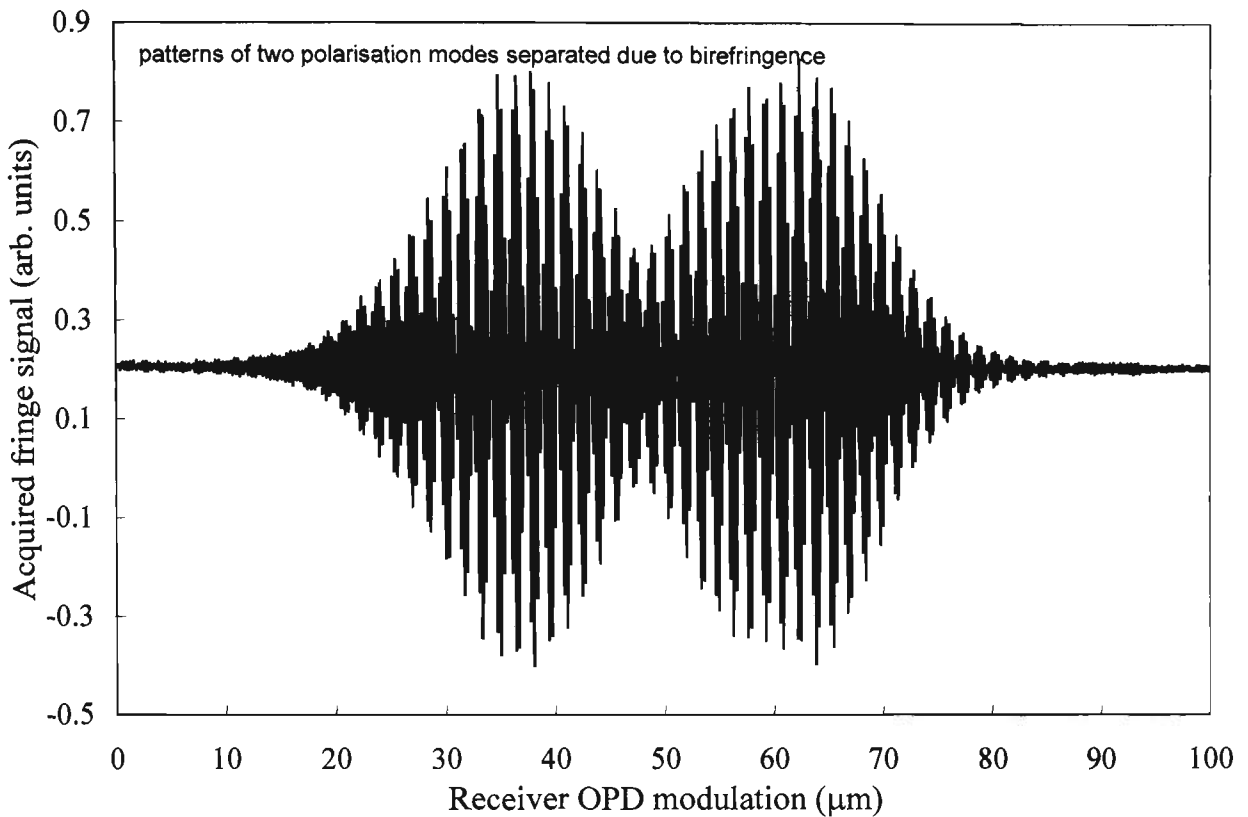


**Figure 5.10** *The effect of polarisation mode dispersion.*

Polarisation mode dispersion was found to be the major contributor to the levels of optical phase noise in the system. It affected the system through the formation of unwanted polarimeters in parts of the system, produced by the environmentally-induced splitting and recombination of optical paths followed by two polarisation modes. This indicates the necessity to develop improved interferometer packaging techniques and to consider building future low-coherence systems with specially designed (possibly highly birefringent) low-wavelength single-mode cut-off optical fibre, high-power fibre-coupled stable SLD sources, and with fibre couplers using the same fibre as all system components. These major improvements in the design of low-coherence systems are likely to result in the development of high-performance industrial strain and temperature sensors in the future.

## 5.7 Summary.

The research conducted during this study highlights several important technical issues that need to be addressed carefully during the development of low coherence grating-based Fabry-Pérot sensors with multi-wavelength interrogation. In order to utilise fully the advantages of this novel approach in low coherence fibre sensing, each of the sub-systems of the measurement system must be designed to minimise the influence of phenomena leading to a decrease in the quality of the output fringe signal. In order to optimise the performance of the measurement system as a whole, several trade-offs must be considered between, for example, the achievable measurement range, resolution, and the overall system cost target.

The principal technical challenges that need to be taken into account during the development of the described type of systems are:

1. Fabrication of the Fabry-Pérot sensor elements with chirped Bragg gratings superimposed with maximum positioning accuracy.
2. Minimisation of the effect of chromatic dispersion in all parts of the system caused by the wide spectral separation of light sources and the properties of the fibre components used.
3. Minimisation of the effect of modal dispersion (including polarisation mode dispersion) through making careful choice of the fibre and fibre components to be installed in the system.

The superimposed chirped gratings used as Fabry-Pérot mirrors of the sensing element were written sequentially onto two sections of fibre separated by the effective length of the Fabry-Pérot cavity. The importance of grating superposition accuracy lies in the necessity to ensure the identical effective mirror separation for every spectral component of incident light. If the effective FP lengths of, for example, 676 nm, 824 nm and 1000 nm reflectors are different, the overall effect on the fringe pattern will be similar to that caused by the stress-optic dispersion (wavelength-dependent receiver interferometer path length imbalance). In addition, the problem is complicated by the fact that each of the three main reflectors is formed by several superimposed gratings. The superposition accuracy achievable during the production of chirped grating-based fibre Fabry-Pérots is in principle limited to a fraction of the grating fringe period, if high-precision computer-controlled motorised translation stages are available and the angle of incidence of the writing UV beam onto the prism surface is controlled to within microradians using active beam steering systems external to the laser source. If chirped phase masks are used, then this accuracy is limited by the achievable positioning accuracy (and wobble) of the translation stage, which is 25-50 nm for current state-of-the-technology stages.

During the production of the sensing elements, the Fabry-Pérot manufacturing accuracy was limited by the degree of control over the incident writing beam angle, since the wobble of the vertical translation stage carrying the focussing lens was less than 1  $\mu\text{m}$  over about 100  $\mu\text{m}$  of translation required to shift the beam focus from one fibre core to another. The starting point for both grating sections at every wavelength was fixed at the position of the prism vertex. However, the starting local reflection wavelength was affected slightly by the amount of incident beam wander. The angular sensitivity of the Bragg reflection wavelength in the prism technique at 800 nm is about 5 nm/degree. The long-term (several hours observation time) amount of angular beam deviation (beam wandering) in the system was typically within 1 mrad (0.057 deg.), which would cause a shift in the starting-point Bragg wavelength of about 0.29 nm for a nominal local reflection wavelength of 800 nm. Therefore, for  $\lambda_1 = 800$  nm and  $\lambda_2 = 800.29$  nm, the difference in the FP cavity lengths will be about 29  $\mu\text{m}$  at a grating (linearly approximated) chirp rate of 10 nm/mm. Approximately the same cavity length difference will apply to every other wavelength within the grating, since the chirp function is fixed by the distance from beam focus to prism and the beam divergence, which do not change when switching exposures. Since the exposure time of every chirped grating was about 10-15 minutes, and gratings were written sequentially, the short-term angular deviations were at least a factor of 10 smaller in magnitude, producing an estimate of the superposition accuracy of within several microns (much smaller than the overall FP cavity length of about 240  $\mu\text{m}$ ). Therefore, the slight grating inscription inaccuracy during the fabrication of sensor elements leads to the appearance of an extra source of dispersion in the system – the chromatic dispersion caused by the wavelength-dependent sensor cavity length. Like other dispersion sources, this effect leads to the elongation of the output fringe patterns, combined with reduction of the central fringe visibility. Minimisation of this dispersive effect is achieved by superimposing the minimal number of gratings necessary to produce the FP sensor with desired spectral properties, which requires highly photosensitive fibre.

In low coherence systems employing multi-wavelength source combinations with wide spectral separation of sources, minimisation of the detrimental effect of chromatic dispersion in all parts of the system becomes a crucial design consideration. It is necessary to estimate the magnitudes of dispersive effects arising from all sources. Two principal causes of chromatic dispersion affect the receiver interferometer sub-system, namely the presence of unbalanced amounts of strain applied to the receiver interferometer arms, and the presence of dissimilar optical fibre paths. The dispersion caused by the stress-optic effect is difficult to cancel, especially in systems with long arm lengths in the receiver. To superimpose the central fringes produced by sources with 300 nm spectral separation with sub-fringe accuracy, the accuracy required in

matching the total integrated applied strain in the arms of the receiver must be less than  $1\mu\epsilon$  for an arm length of 40 m (from calculations in section 5.6.1). This leads to the necessity of choosing a trade-off between the ability to optimise the fringe signal (and therefore facilitate accurate measurements) and the measurement range (limited by the number of fibre turns wound around the PZT). The practical way of dispersion balancing was found to be the iterative optimisation of the combined-source fringe signal performed while varying the number of fibre turns wound onto the strain-compensating cylinder, followed by determination of the individual positions of central fringes produced by each source.

In systems in which the receiver interferometer has fibre couplers made of fibre different from that in the interferometer arms, a special case of chromatic dispersion is observed. The dispersive degradation of the output signal will be present, caused by fibre paths with non-common wavelength-dependent propagation properties, if the coupler arm lengths joined to the receiver arms are different in length. The ability to balance the coupler arm lengths precisely is limited by the accuracy of fibre length measurement and the performance of the fibre cleaver used. From measurements of the magnitude of this effect in this study, for couplers made using Acrotec fibre with 850 ( $\pm 50$ ) nm single-mode wavelength cut-off joined to receiver arms using Corning Flexcore 780 fibre, the 22 mm difference in coupler arm lengths lead to the 86  $\mu\text{m}$  separation of central fringes produced by light at 676 nm and 1000 nm. This produces an estimate of fibre cutting accuracy required to cancel or minimise this dispersive effect. In order to bring the two central fringes together to within 0.5  $\mu\text{m}$ , a length matching accuracy of about 0.125 mm is required.

# *Chapter 6*

## **Measurements of temperature and strain with low-coherence fibre Fabry-Pérot sensors**

### **6.1 Introduction.**

This chapter provides a detailed description of experimental work involving several multi-wavelength low coherence sensor systems and analyses the results of laboratory tests. Experimental techniques used for calibration and testing of sensors performance are described. Data obtained during laboratory measurements are presented to provide full characterisation of the potential and performance of the multi-wavelength white-light interferometers constructed during this study. A critical analysis of the performance of sensing systems is provided, and the results of measurements are compared to the performance characteristics predicted by theory. The practical limitations of this type of measurement systems in terms of achievable resolution, range and speed of measurement are characterised.

## 6.2 Temperature monitoring with end-coated Fabry-Pérot sensors.

Fibre Fabry-Pérot sensors with plane mirrors provided by partially reflective silver-coated cleaved fibre ends were constructed during this study and used for temperature monitoring. Construction of these sensors enabled comparison of the white-light fringe patterns produced with sensing elements using plane mirrors and chirped Bragg grating reflectors.

Fibre Fabry-Pérot cavities were connected to the lead-in fibre using Siecorm mechanical splices. Partially reflective mirrors were formed on cleaved ends of the sensing cavity fibre by depositing thin layers of silver using a chemical process from a saturated solution of silver. Despite the low mechanical strength of these sensing elements due to mechanical splice connection, they were found suitable for monitoring temperature and provided proof of the advantages of using an optimised triple-wavelength source combination.

Two systems with plane-mirror Fabry-Pérots were constructed and tested. The first system was based on Spectran fibre with single-mode cut-off wavelength of 633 nm and utilised a double source combination with central wavelengths of 676 nm and 824 nm. Identification of the central fringe was facilitated by a signal processing algorithm based on peak detection. However, environmental disturbances in the system that lead to polarisation mode hopping effects limited the achievable sensing resolution due to the relatively small intensity difference between the central fringe and its adjacent side-fringes.

The second system based on semi-reflective plane mirrors was constructed using Corning Flexcore fibre with single-mode cut-off wavelength of  $720 \pm 50$  nm. An optimised triple wavelength source combination (central wavelengths of 676 nm, 824 nm and  $1 \mu\text{m}$ ) was used, which resulted in fringe patterns with a prominent central fringe, enabling its easy identification by maximum visibility and the application of the central fringe centroid resolution enhancement technique. The stability of measurements was significantly better in the case of a triple-source system. However, the effects of environmental thermally-induced signal drift and modal noise caused by polarisation-mode cross-coupling were not completely eliminated during measurement. The output of the low-coherence SLD sources was not 100% depolarised, and so the presence of birefringence induced in the fibre coils and polarisation-mode cross-coupling effects caused by environmental disturbances in the receiver interferometer meant that fringe misidentifications did sometimes occur. However, it was possible to achieve intra-fringe resolution in the absence of significant disturbances to the receiver interferometer fibre.

## 6.2.1 Measurements with a double combination source interferometer.

A double-source interferometer system utilised an 86 mm long fibre Fabry-Pérot cavity. The reflectivities of cavity mirrors were  $R_1 \cong 20\%$  (front mirror) and  $R_2 \cong 25\%$  (rear mirror effective reflectance as obtained from power measurements). The sensing cavity was attached to the surface of an electrical hot plate ensuring good thermal contact and the position of the central fringe was monitored during repeated scanning of the receiver interferometer path difference. A white-light interferogram obtained with this system is shown in Figure 6.1.

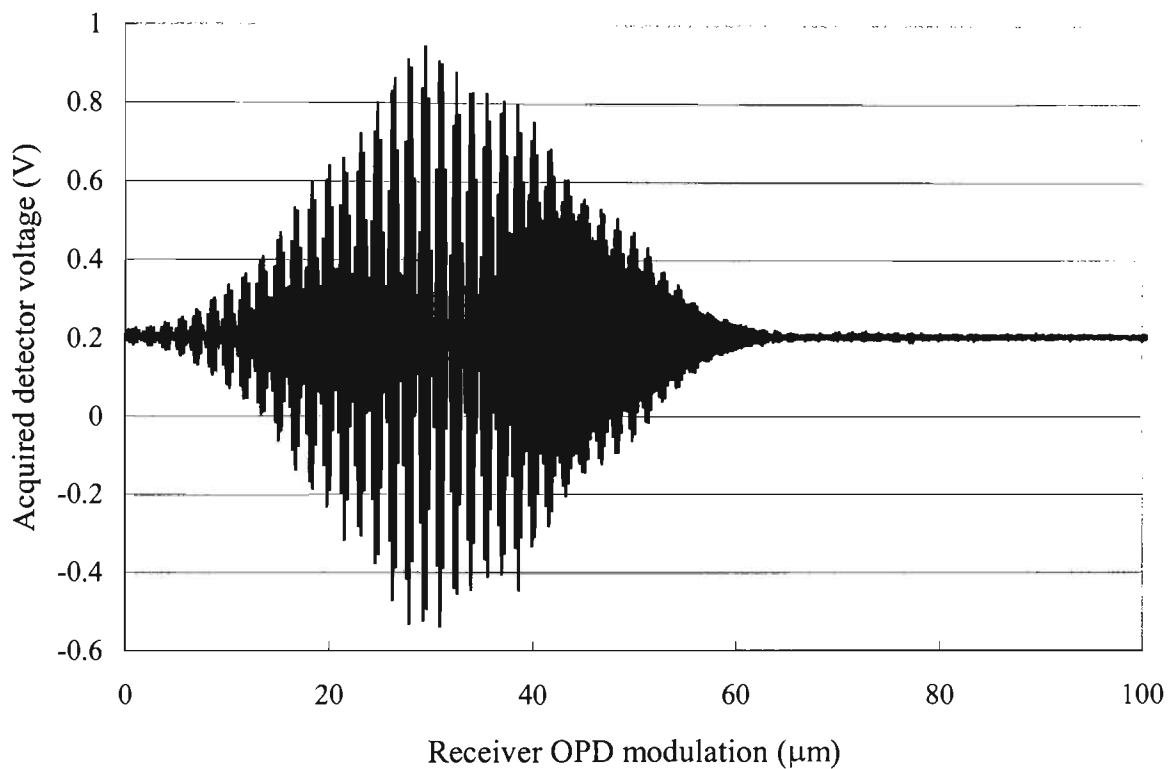


**Figure 6.1** *Measured white-light interference pattern generated by a double combination source (central wavelengths 676 nm and 824 nm) used in a temperature monitoring experiment.*

The receiver interferometer was constructed using Spectran single-mode fibre (633 nm cut-off), with a PZT stretcher containing 100 turns of fibre. The fibre coupler in the receiver interferometer also used 633 nm cut-off fibre, manufactured by Gould. The calibration of the PZT transducer using the fringe pattern from the 676.3 nm source provided the figure of 2.878 fringes/V for the modulation of optical path difference within the linear extension range (0 V to 200 V of applied voltage). This corresponds to the full linear range of OPD modulation of 575.6 fringes at the output (133.7  $\mu\text{m}$  of maximum fibre arm extension).

A waveform used for fringe pattern generation and scanning of the receiver OPD was generated by the computer-controlled data acquisition system running LabView 4.1 software. The shape of the applied voltage waveform measured at the output of the analog output data channel is shown in Figure 6.2. This waveform was generated during sensor operation, performing scans of 0.1 s duration containing 5000 voltage output points within each up-ramp and down-ramp cycle (update rate of 50 kHz). This voltage was directed to the input of a Lutz-Pickelman high voltage amplifier (providing voltage gain of 100), the output of which was used for driving the Vernitron PZT cylinder of diameter 50 mm.

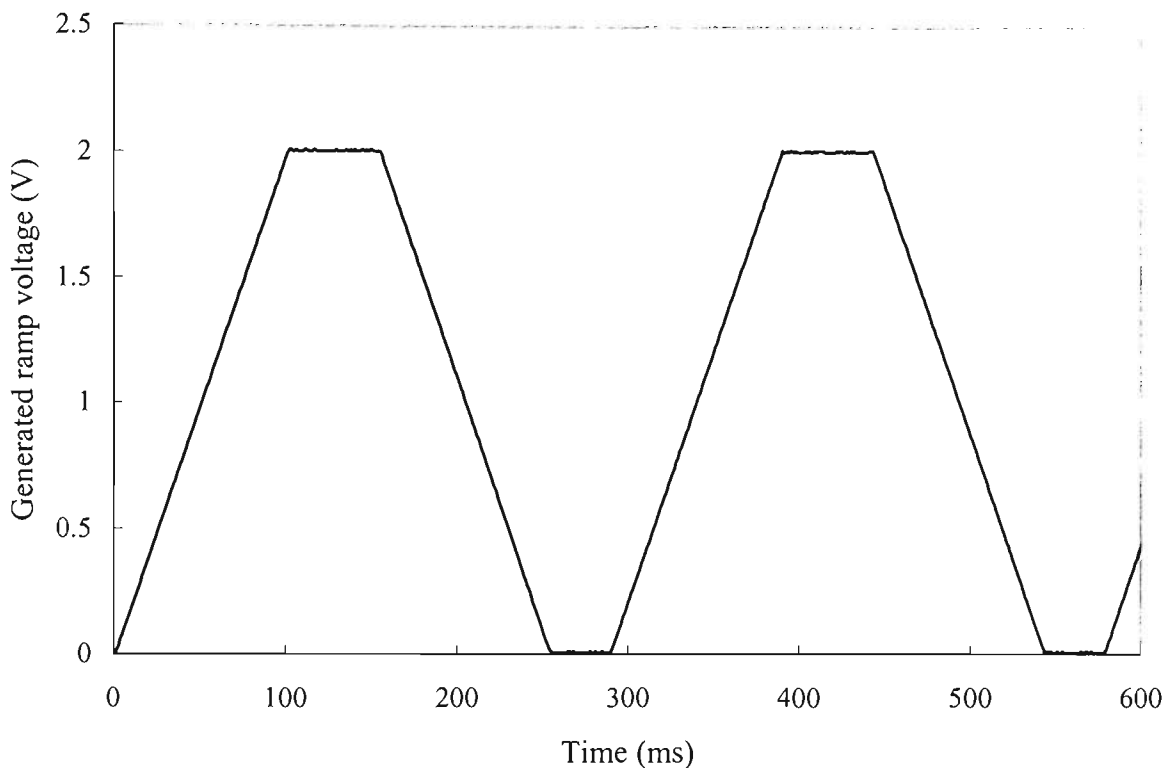


**Figure 6.2** *A voltage waveform generated by the data acquisition card for driving the PZT transducer. Fringe pattern acquisition was performed during up-ramp cycles only. A delay at maximum voltage is due to data processing and DAQ channels re-initialisation.*

Acquisition of the fringe pattern data was performed during up-ramp cycles of this waveform. Typically, 10000 output voltage data points were generated during the up-ramp lasting 0.125 s, with the identical number of fringe voltage data points acquired simultaneously during this time interval. Data acquisition and generation operations were synchronised with both operations starting simultaneously due to the application of hardware triggering, which required an external TTL signal input. The scan rate and update rate figures for data acquisition and generation were typically both equal to 80 kHz. The fringe pattern was sampled at 17.3 data points per fringe during temperature monitoring.

After performing a scan of the receiver OPD, data processing to detect the peak fringe voltage data point was performed using LabView software. The PZT voltage is kept constant during data processing at 200 V. In Figure 6.2 showing 0.1 s-long scans, the delay due to data processing and DAQ channels re-configuration for performing a down-ramp is 54 ms. Finding an array maximum and the corresponding PZT voltage takes only 18 ms, since the measured delay time of 36 ms at 0 V level corresponds to the time necessary for memory buffer and DAQ channels re-configuration only. The latter is required to improve the computer performance characteristics and avoid memory allocation errors during continued operation. The down-ramp cycle was performed with the same parameters as the up-ramp, in order to avoid sharp changes in voltage applied to the PZT that could cause ringing effects due to the broad frequency spectrum of the applied voltage waveform. No fringe data were acquired during down-ramp cycles to avoid possible PZT hysteresis effects.

During temperature monitoring, the data acquisition software was running continuously, with the PZT voltage corresponding to the position of the maximum acquired voltage data point being plotted on screen and stored in a file.

Figure 6.3 shows the sensor output (PZT voltage corresponding to the maximum generated fringe voltage) during operation at constant temperature with the effects of environmental thermal drift and fringe misidentifications caused by the exchange of power between the two polarisation modes. The horizontal scale is “measurement number”; it was used instead of “time” as the data were only required for calculating the percentage of noise-induced fringe misidentifications (the separation between each pair of successive measurements in time is approximately 0.34 s). It was possible to stabilise the receiver interferometer for performing sensor calibration. However, environmental disturbances have significantly affected measurements with a double-source system due to the central fringe not being dominant in the interferogram. The voltage SNR (electronic noise component only) during temperature monitoring with a double-source interferometer was 33.7 dB with equalised central fringe intensities produced by each source.

The fibre sensor element was sealed from air currents during temperature measurements by positioning the hot plate with attached sensor inside a small cardboard box with foam insulation attached to its inside walls. However, this did not prevent some weak air currents caused by convection inside the enclosure from affecting measurements and causing slow drift of the fibre temperature. The temperature at the fibre core was mostly affected by the hot plate, since a good thermal contact between the fibre and aluminium plate surface was established during fibre attachment with tape. The systematic character of fringe misidentifications observed

(substantially lower than average sensor signal levels recorded during misidentifications) is explained by the slight asymmetry of the output fringe pattern and the presence of modal noise in the interferometer.

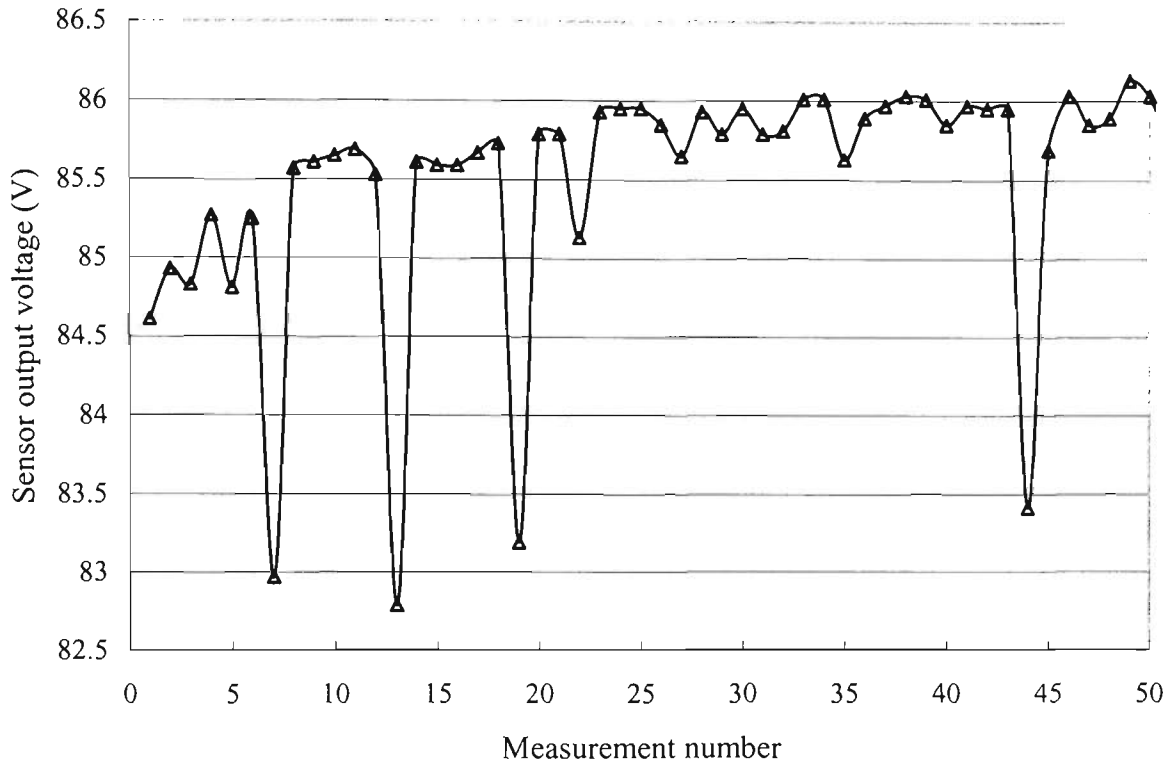


**Figure 6.3** *Output signal of a double-wavelength temperature sensor at constant sensor temperature with modal noise causing fringe misidentifications. Environmental drift also affects the signal stability.*

In Figure 6.3, the maximum signal voltage deviation caused primarily by modal noise has amplitude 2.82 V, which corresponds to an error of 8.1 fringes (maximum error in absolute OPD determination of about 1.9  $\mu\text{m}$ ). However, during undisturbed operation (with receiver interferometer sealed from air currents), the typical amplitude of signal voltage deviations was about 0.38 V, corresponding to an average error of about 1.1 fringes generated by a 676 nm source (absolute error in the sensor OPD determination of about 255 nm). The interferometer performance was not affected by a power switch-off.

Figure 6.3 shows five significant fringe misidentifications out of a set of 50 measurements. Hence, 90% of the identifications of the central fringe through its visibility were performed correctly. The instability in the measured position of the central fringe was a real effect caused by the imperfections in the insulation of the sensor element from air currents.

The calibration of the interferometer response was performed using a Fluke 52 digital thermocouple monitoring the temperature of the sensing fibre. The thermocouple temperature data were read manually as the sensor temperature was increased slowly. Figure 6.4 shows the result of sensor calibration, featuring good response linearity. The calibration was performed in the range of temperatures from room temperature (23°C) to nearly 90°C.

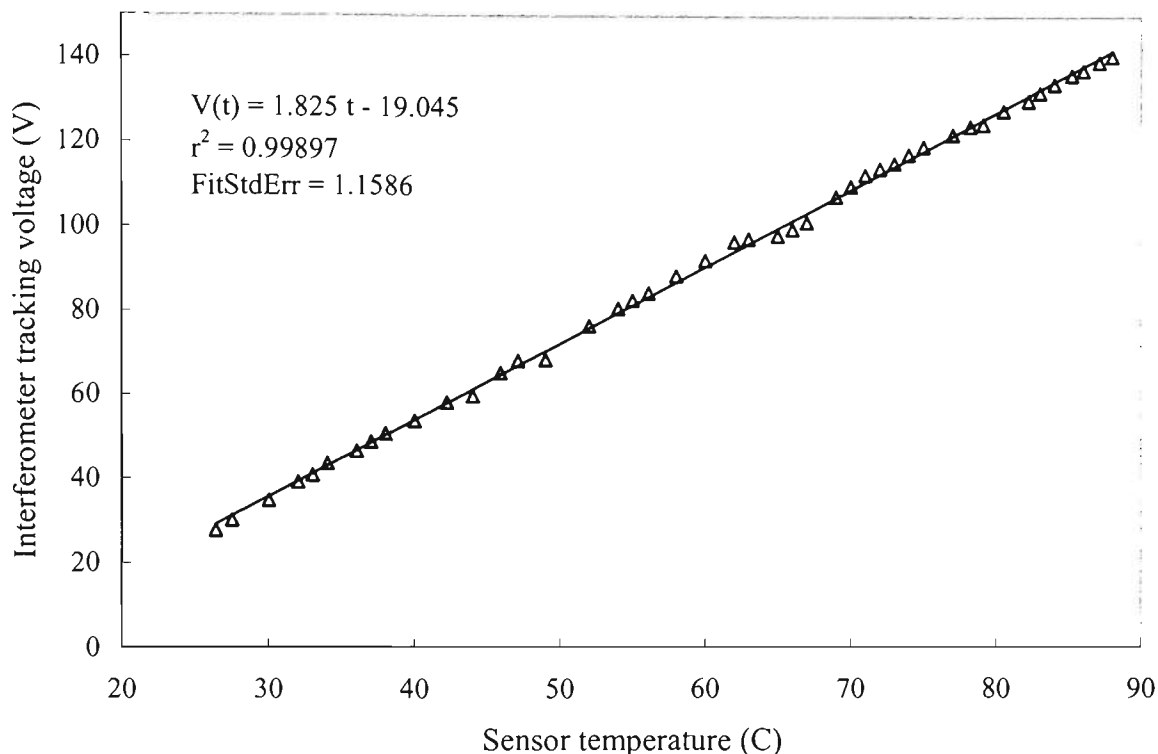


**Figure 6.4** Calibration curve of double-source temperature sensor (86 mm-long fibre FP) employing peak detection signal processing.

The analysis of calibration data and parameters of a linear fit shows a worst-case error of calibration at any measured point of 1.29 °C, with the overall accuracy of calibration (corresponding to a fit standard error of 1.15866 and gradient 1.825 V/°C) being equal to  $\langle \Delta T \rangle = 0.635$  °C. The maximum range of temperature measurement with this system was 109.6 °C, limited by the linear range of fibre extension in the receiver interferometer.

The slope of this linear calibration allows determination of the fractional round-trip phase change per unit temperature change of the fibre FP cavity. Using the figures of  $\lambda = 676.3$  nm,  $n_{co} = 1.456$ ,  $L_{cav} = 86$  mm,  $dV/dT = 1.825168$  V/°C and a PZT calibration factor of 2.878 fringes/V, a fractional FP round-trip phase-temperature sensitivity figure of  $\Delta\phi_T / (\phi_T \Delta T) \approx 1.415 \times 10^{-5}$  °C<sup>-1</sup> was obtained. This figure is in good agreement with the theoretically expected value for FP temperature sensitivity as predicted in Chapter 2 ( $\Delta\phi_T / (\phi_T \Delta T) \approx 1.6 \times 10^{-5}$  °C<sup>-1</sup> from equation 2.24).

## 6.2.2 Measurements with a triple combination source interferometer.

A fibre interferometer system using an optimised triple source combination was built using Corning Flexcore 780 fibre (single-mode propagation cut-off at  $720 \pm 50$  nm). The previously developed system based on fibre with 633 nm cut-off (core diameter of only 4  $\mu\text{m}$ ) did not allow the use of the third source (central wavelength of 1  $\mu\text{m}$ ), due to light of that wavelength travelling mostly through the fibre cladding and suffering high loss. This triple-source interferometer system employed a 54 mm long fibre Fabry-Pérot cavity with partially-reflective cleaved-end mirrors. The cavity mirror reflectances were  $R_1 \cong 16\%$  (front mirror) and  $R_2 \cong 22\%$  (rear mirror).

A white-light fringe pattern obtained with the triple-source interferometer is shown in Figure 6.5.

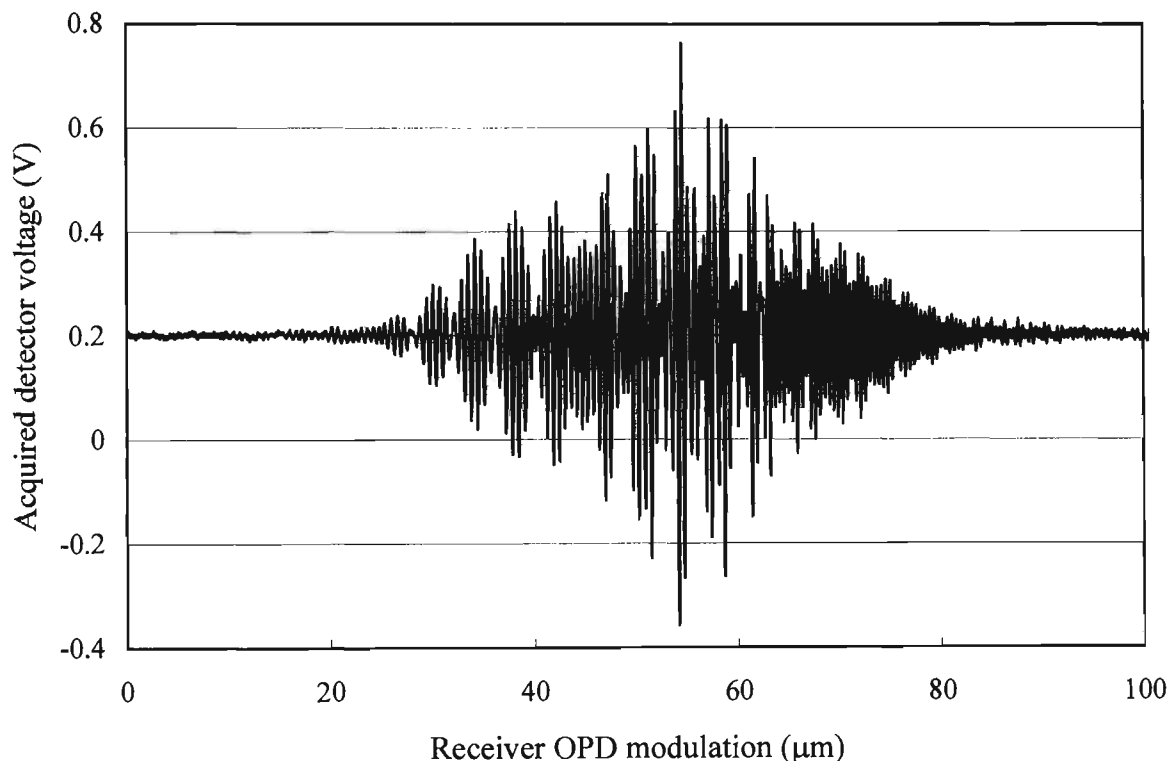


**Figure 6.5** *Measured white-light interference pattern generated by a triple combination source (central wavelengths 676 nm, 824 nm and 1000 nm) used in a temperature monitoring experiment with improved resolution.*

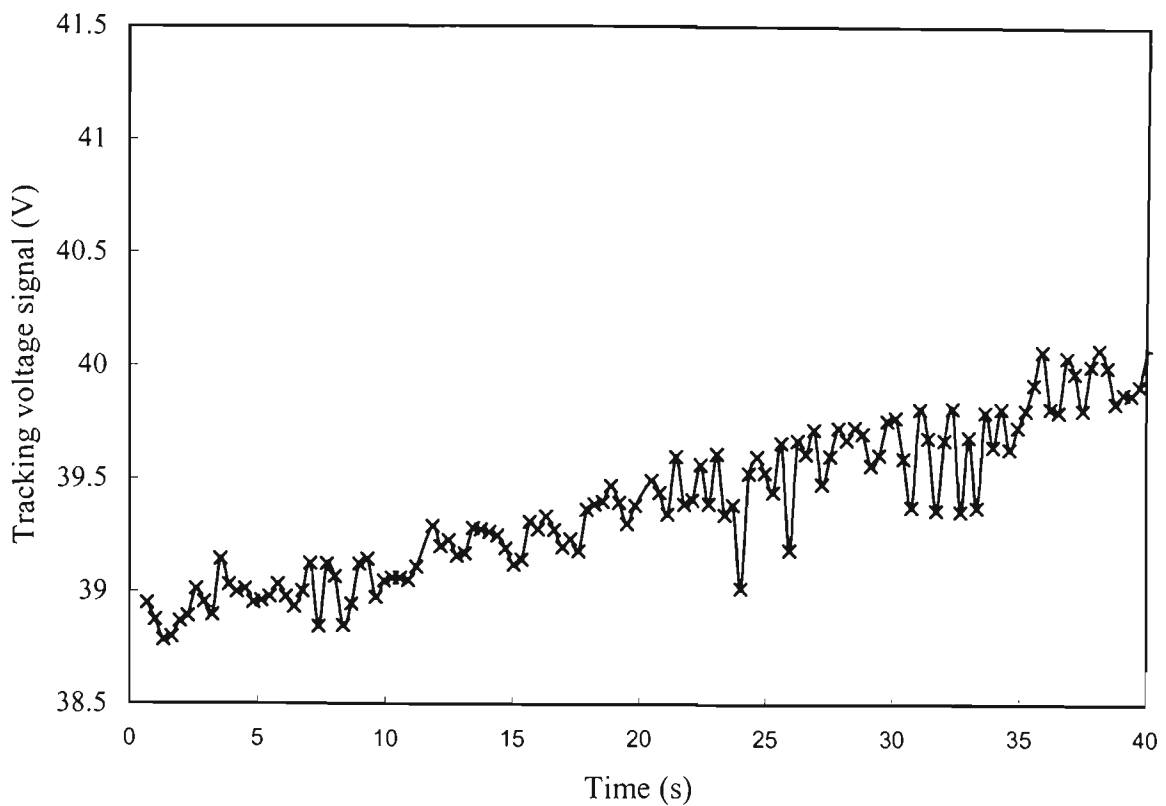
The SNR required for the identification of the central fringe through direct peak detection is only about 16.7 dB for this fringe pattern (this calculation is based on the peak intensity difference between the central fringe peak and the largest side-peak in the measured pattern). During experiments, a voltage SNR of about 31 dB (calculated using the ratio of rms peak signal voltage to the rms measured detector noise voltage) was obtained after equalising the

central fringe amplitudes obtained with each individual light source. However, measurements with this source combination were also affected by environmentally induced signal perturbations that led to the appearance of modal noise due to polarisation mode effects.

The approach used for data acquisition and receiver OPD scanning with this triple-source system was the same as described for the double-source interferometer, with identification of the central fringe also performed through peak detection. The intra-fringe resolution enhancement technique using the full central fringe centroid algorithm was applied for the determination of the position of the centre of the central fringe. To facilitate the application of this technique, peak detection software subroutines were employed for finding the "valley points" located around the peak detected voltage data point. After locating the two central fringe minima, all points lying within the full central fringe in-between these minima were used in the central fringe centroid formula.

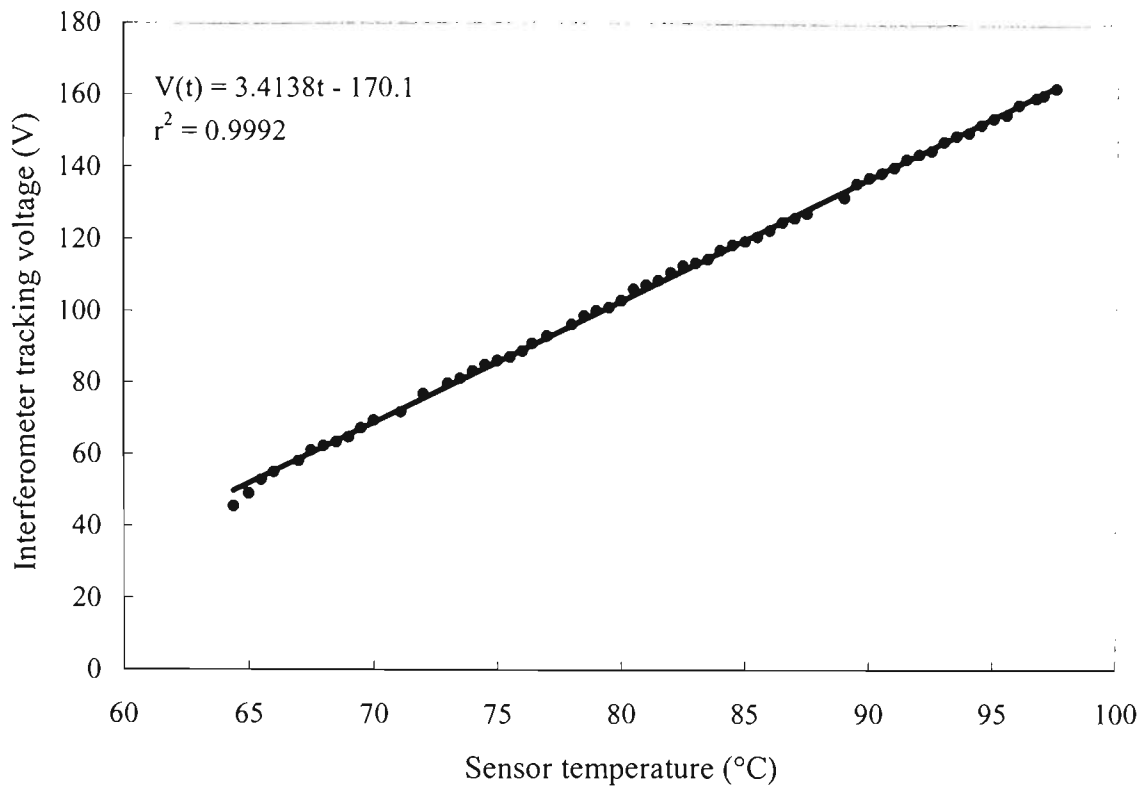
The PZT transducer in the receiver interferometer contained only 60 turns of fibre, in order to minimise the effects of induced birefringence and stress-optic dispersion. The PZT expanded at 1.18 fringes/V (measured with fringes from 676.3 nm source), providing a total fibre arm physical extension range of about 54.8  $\mu\text{m}$  in the linear regime. This corresponds to the total range of receiver OPD modulation of 109.6  $\mu\text{m}$ .

Figure 6.6 shows how the processed sensor output (PZT scanning voltage corresponding to the calculated centroid position) over 40 seconds of operation at constant temperature experiences the effects of environmentally induced signal variation.



**Figure 6.6** *Output signal of the triple-wavelength temperature sensor during 40 seconds of operation at constant sensor temperature in the presence of environmental thermal drift affecting the arms of the receiver interferometer.*

For the data presented in Figure 6.6, the maximum signal voltage deviation caused by all noise sources is about 0.6 V, which corresponds to an error of 0.7 of a fringe (maximum error in absolute OPD determination of about 163 nm). Typical values of noise-induced centroid position deviations during measurement were about  $\pm 0.2$  V, which corresponds to 0.23 of a fringe from a 676 nm source, or is equivalent to a typical average error in OPD determination of about 55 nm. During this measurement, the value of thermal drift in the position of zero path imbalance was about 350 nm. This corresponds to a variation in the sensor temperature of about 0.2°C. During 40 seconds of operation, 121 data points were acquired, of which a maximum of 14 measurements were based on incorrectly identified central fringe. This corresponds to 88.4% of correct central fringe identifications performed at a measurement frequency of 3.025 Hz. The maximum range of temperature measurement with this system was 59 °C, limited by the linear range of fibre extension in the receiver interferometer.



**Figure 6.7** Calibration curve of a triple-wavelength temperature monitoring system employing peak-amplitude central fringe identification and central-fringe centroid data processing algorithm.

Figure 6.7 shows the calibration graph of the fibre interferometer with a triple combination source. In this experiment, the fibre sensor cavity was attached initially to an already warm surface of the hot plate at about 65 °C, which caused temperature measurement errors during the initial heat transfer process between the hot plate and the fibre. The measurement range of 65-97 °C was chosen to minimise the errors caused by the difference in temperature between the surface of the hot plate and the fibre, since the warming-up rate of the heated aluminium surface is smaller at higher temperatures. A very good degree of linearity was obtained for this set of data through curve fitting, with a calibration accuracy achieved of about 0.19 °C. The linear fit to the measured data was obtained using Microsoft Excel software.

Using the figures of  $\lambda = 676.3$  nm,  $n_{co} = 1.456$ ,  $L_{cav} = 54$  mm,  $dV/dT = 3.4138$  V/°C and a PZT calibration factor of 1.18 fringes/V, a fractional round-trip phase-temperature sensitivity figure of this FP sensor  $\Delta\phi_T/(\phi_T\Delta T) \approx 1.733 \times 10^{-5}$  °C<sup>-1</sup> is obtained. This result agrees well with the theoretically expected value for the cavity phase-temperature sensitivity (about  $1.6 \times 10^{-5}$  °C<sup>-1</sup>).

Figure 6.8 shows the results of real-time temperature monitoring obtained with a triple-wavelength sensor system during 30 minutes of continuous measurement.

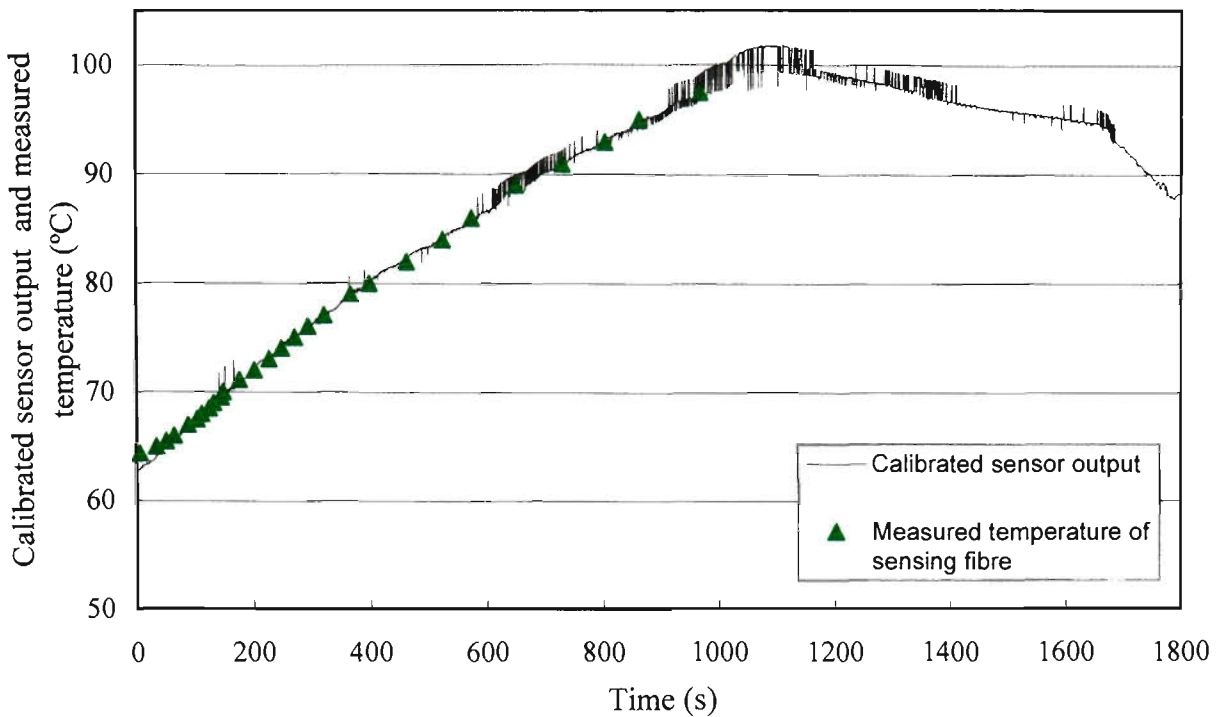


**Figure 6.8** *Measured output (calibrated) of the triple-wavelength sensor during 30 mins of a continuous temperature monitoring experiment and thermocouple temperature data .*

During the first 1100 seconds of this experiment, the sensor was heated slowly from about 60 °C to just over 100 °C. During this heat-up process, the sensing cavity was thermally insulated from the environment. After the sensor temperature reached 100 °C, the heater was switched off and gradual cooling occurred. The increase in the cooling rate after approximately 1700 s is due to a layer of thermal insulation being removed from the sensor cavity, enabling faster cooling.

### 6.3 Methods of calibration and testing used for strain monitoring.

The strain sensor system developed during this project was calibrated and tested using a fibre Fabry-Pérot sensor element embedded into an aluminium beam with dimensions 500 mm × 60 mm × 6 mm. The optical fibre containing a 230 mm long Fabry-Pérot sensor cavity was installed into the host structure by gluing the fibre (with its jacket unstripped) into a U-shaped groove machined on the beam's surface. Loctite Liquid Steel epoxy was chosen for embedding the fibre sensor into the host structure due to its excellent mechanical properties (hardness in the solidified state and good degree of surface attachment to both the fibre jacket and aluminium). Industrial sensing simulations have been performed with the system by applying controllable periodic deformations to the aluminium beam (with an embedded sensor element) using an Instron 8501 universal testing machine (Figure 6.9).

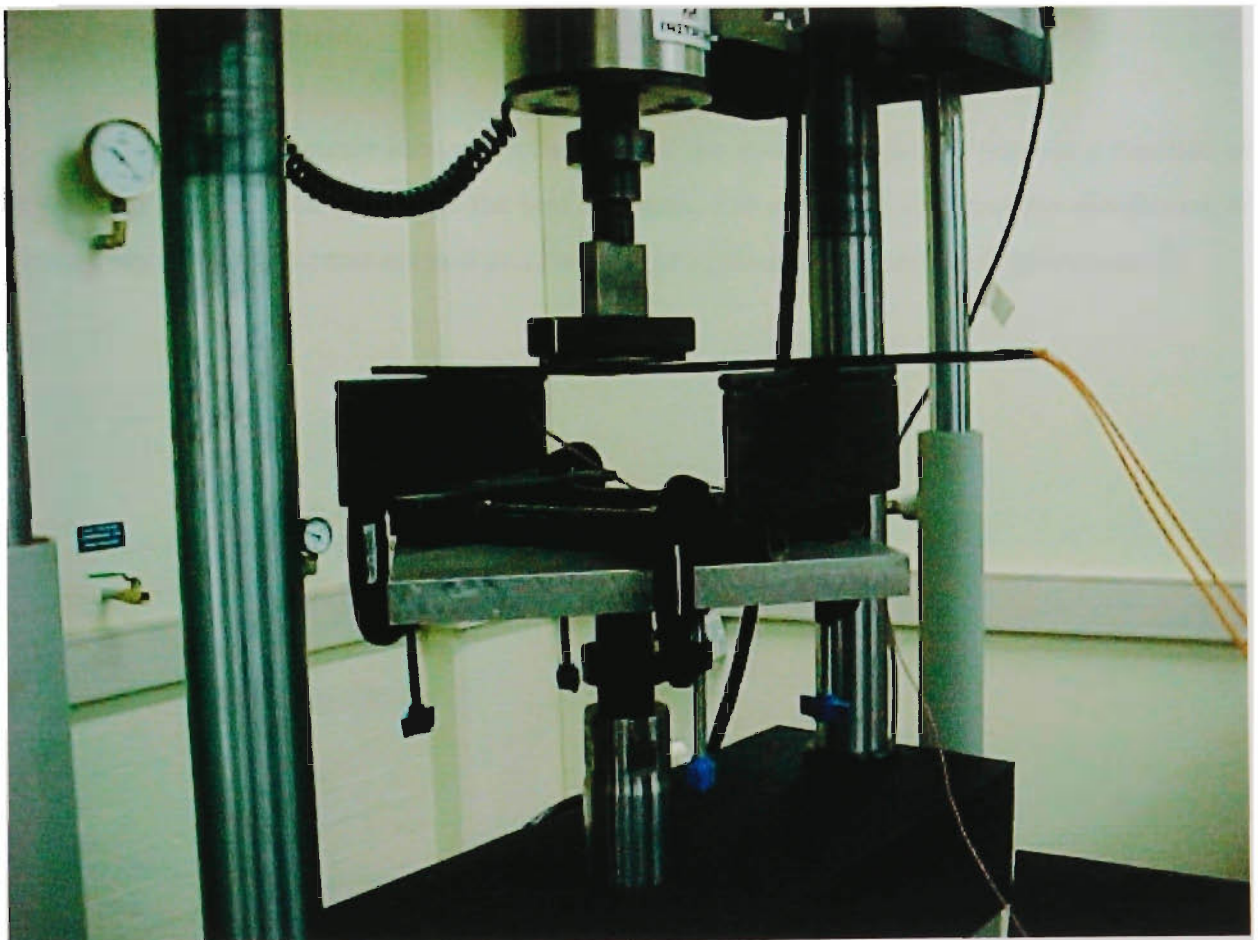


**Figure 6.9** *Experimental arrangement used for testing the strain sensor performance. The Instron 8501 testing machine applies periodic deformations to the aluminium beam structure containing an embedded fibre Bragg grating Fabry-Pérot.*

### 6.3.1 Mechanical characterisation of testing method.

In the following the geometry of the sensor testing arrangement is considered and applied to the mechanics of the solid beam with rectangular cross-section when deformed during testing. Figures 6.9 and 6.10 illustrate the principle of applying deformations to the aluminium beam host structure and the geometry of mechanical arrangement used for sensor characterisation. An aluminium beam is positioned onto a frame with two steel rods of circular cross-section that establish lines of supporting contact with the bottom surface of the beam. The distance along the beam between these supporting lines is  $L = 300$  mm and is fixed due to the geometry of the frame used. The supporting frame is attached to the testing machine's actuator shaft that can perform vertical displacements, with the displacement waveforms being programmable from the Instron 8501 control panel. A third line of mechanical contact is located on the top flat surface of beam, symmetrically in between the two support lines and is used for loading the beam during actuator movements.

In order to derive the strain induced in the core of the embedded optical fibre as a function of mechanical deformation applied to the host structure, it is necessary to derive the distribution of strain within the beam cross-section as a function of applied load (actuator displacement  $d$ ).

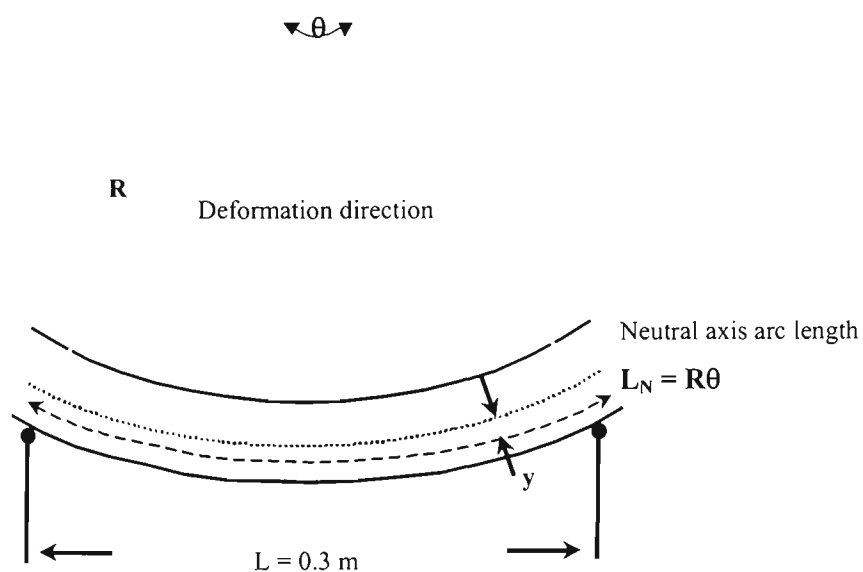


**Figure 6.10** Geometry of mechanical arrangement used for sensor testing. The front cross-sectional view of a deformed beam is shown with a fibre sensor installed at depth  $y$  below the beam's neutral plane.

From theoretical mechanics, when a beam of rectangular cross-section resting on two lines of support is loaded due to application of force to its top surface, the top surface of the beam experiences compression, whereas the strain on the bottom surface is tensile. A neutral plane with zero strain at all points exists within the beam, which coincides with its horizontal plane of symmetry in an unloaded state and remains parallel to the loaded surface when deformation is applied. For small deformations applied to the centre of the beam's top surface ( $d \ll L/2$ ), the shape of a deformed cross-section of beam is approximately circular. Therefore, the distribution of strain within the deformed vertical cross-section of the beam can be found by considering circular arcs limited by radii drawn from the centre of curvature towards points of support that remain fixed during loading (Figure 6.10). Let us denote the radius of curvature of the neutral plane  $R$  and the arc angle between the fixed support points  $\theta$ . The arc length of the deformed neutral plane is therefore  $L_N = R\theta = 0.3$  m, since it experiences zero strain. The arc length in a plane of fibre sensor (installed at a depth  $y$  below the neutral plane) is  $L_S = (R + y)\theta$ . In the zero load case, both lengths considered are equal to the separation of the support lines (0.3 m). Therefore, strain in the plane of sensor installation is given by the relationship

$$\varepsilon(y) = \frac{(R + y)\theta - R\theta}{R\theta} = \frac{y}{R}. \quad (6.1)$$

Relationship (6.1) shows that within the cross-section of a deformed beam, strain in any plane parallel to loaded surface is linearly proportional to its distance from the neutral plane. Compressive strain is observed if the sensor is installed above the neutral plane and tensile strain in the opposite case.

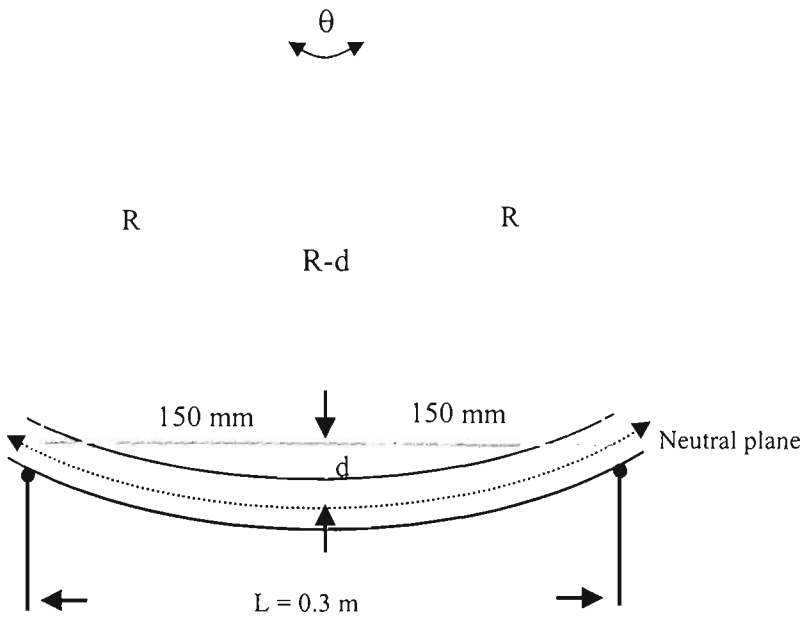


**Figure 6.11** *Determination of the curvature radius of the neutral plane in a deformed beam using the approximation of small central deformations. The base of a triangle shows the original position of the neutral plane.*

Figure 6.11 illustrates the calculation of the radius of curvature  $R$  of the deformed section of beam for any small displacement  $d$  of the centre of the beam's loaded surface. Assuming the beam is absolutely rigid, the displacement  $d$  of the testing machine's actuator is equal to the displacement of the centre of the neutral plane. By considering a right-angle triangle formed by the undeformed position of the neutral plane, the vertical plane of symmetry, and the radius of curvature, the following relationship is obtained:

$$R = \frac{L^2/4 + d^2}{2d}. \tag{6.2}$$

Since the present model assumes small actuator displacements ( $d \ll L/2$ ), the relationship (6.2) can be simplified to give

$$R = \frac{L^2}{8d}. \tag{6.3}$$

Equations (6.1) and (6.3) allow characterisation of the strain distribution within the cross-section of a loaded beam for any small deformation applied to the beam's top surface. By combining the two equations, we obtain:

$$\varepsilon(d, y) = \frac{8yd}{L^2}, \quad (6.4)$$

where it is assumed that values of  $y$  are positive for planes of interest lying below the neutral plane (experiencing tensile strain). If we denote the beam thickness  $t$ , the relationship (6.4) can be re-written in a more convenient form in terms of the sensor installation depth parameter  $D$ :

$$\varepsilon(d, D) = \frac{8d(D - t/2)}{L^2}, \quad (6.5)$$

where  $D = t/2 + y$ .

Substituting the dimensions (in mm) of the test equipment used, we obtain the following relationship for strain (in microstrain) within the horizontal plane of the beam containing the core of optical fibre installed at depth  $D$ :

$$\varepsilon(d, D) = \frac{8d(D - 3)}{90000} \times 10^6. \quad (6.6)$$

An important feature of this relationship (6.5) is the linearity of induced strain as a function of actuator displacement (central deformation of beam  $d$ ) for small deformations. According to equation (6.6), the compressive strain induced at the top surface of the beam ( $D = 0$ ) equals  $266.67 \mu\varepsilon$  per millimeter of actuator displacement. Figure 6.12 shows graphs of surface strain calculated from equation (6.6) and surface strain measured with a resistive strain gauge versus the displacement  $d$  of the machine's actuator. The measured strain data is in good agreement with theory predictions.

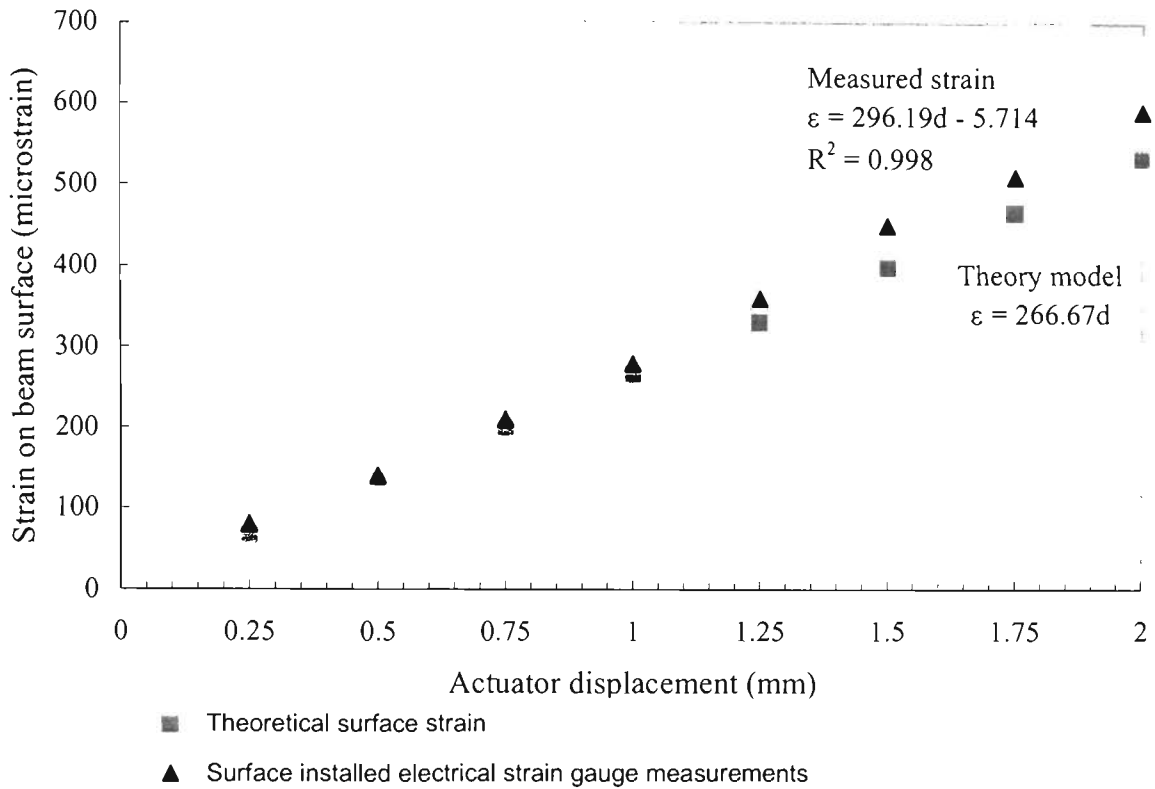


**Figure 6.12** *Strain of the beam surface measured by a surface-attached resistive strain gauge, and theoretical surface strain versus actuator displacement calculated from (6.6).*

For a range of actuator displacements of up to 1 mm, the agreement between the theory predictions and measured data is excellent, with discrepancies within the error margins set by the accuracy of the reference strain gauge and variations in beam thickness and symmetry along the beam length. For larger actuator displacements, slight deviation of measured data from the model can be explained by systematic errors arising from the precision of the Instron's actuator and deviations of the beam deformation from the assumed circular shape.

### 6.3.2 Monitoring of dynamic strain with grating-based Fabry-Pérot sensors.

Embedded fibre Fabry-Pérot sensors based on superimposed chirped gratings were used for monitoring strain in real time. Two low-coherence fibre interferometers were used in these experiments. The first system employed the receiver interferometer with long ( $\sim 40$  m) Corning Flexcore 780 fibre arms and significant uncompensated dispersion due to the large number (230) of turns in the PZT winding and unequal arm lengths of the Acrotec coupler used. The sensing cavity was 230 mm long, with superimposed chirped reflectors fabricated using the sequential writing technique described in chapter 4. The sensor element was embedded into an aluminium beam at a depth  $D = 1.9$  mm below the surface (at a distance of 1.1 mm from the neutral plane). The orientation of the host structure during bending was chosen to provide stretching of the sensing element.

The output fringe signal obtained with this system was significantly elongated, with fringes observed at relative path imbalances approaching the length of grating reflectors (about 4 mm). Interference patterns generated by each source of the optimised triple-wavelength combination were elongated due to the combined effect of dispersion, coherent components in the grating reflection spectrum and the distributed character of the cavity reflectors. However, the middle region of the interference pattern contained sharp features, the position of which could be tracked during scanning of the receiver interferometer OPD. The group of interference fringes with maximum peak-to-peak intensity (relative to other nearby groups of fringes) near the middle of the interferogram was used for tracking the changes in the sensor interferometer OPD. The central region of the interferogram obtained with this system is shown in Figure 6.13. A large degree of irregularity observed within this interferogram was primarily due to the presence of uncompensated dispersion (of the stress-optic and chromatic origin) in the receiver interferometer. The principal character of the output fringe pattern did not change when the sensing element was replaced by another chirped grating-based Fabry-Pérot.

However, despite the reduced quality of the output interferogram, it was possible to perform monitoring of strain with this system within a limited range (about 100  $\mu\text{m}$  of OPD modulation). This limitation of the operating range was dictated by significant changes in the overall envelope of the output fringe pattern occurring due to strain affecting the structure of cavity reflectors during measurement. Combined with the effect of dispersion in the receiver interferometer, this led to a significant increase in the level of optical noise.

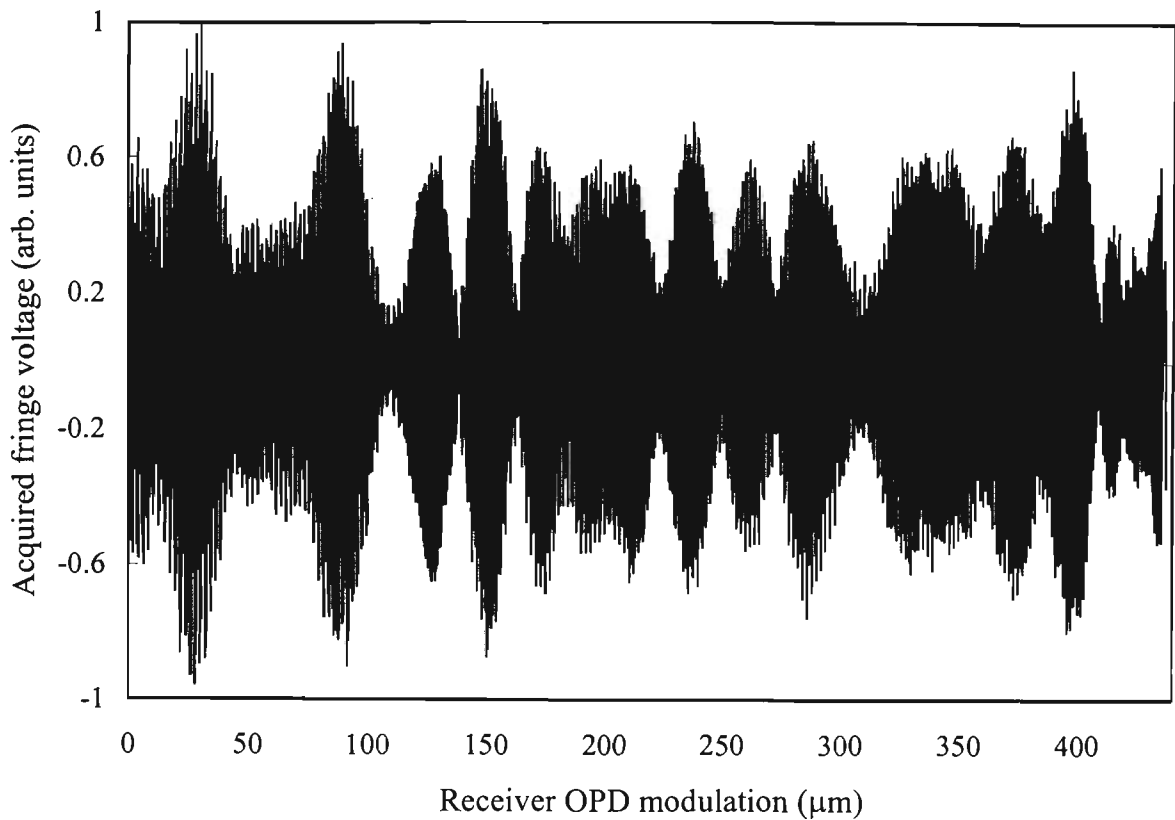


**Figure 6.13** *Low coherence fringe pattern, distorted and elongated due to the spurious effects of dispersion and non-identical distributed-reflector structures of chirped grating mirrors of a Fabry-Pérot sensor generated during the scan of the receiver interferometer. The leftmost group of fringes with maximum peak-to-peak intensity represents the centre of this elongated interferogram.*

Some strain waveforms monitored with this system are shown in Figures 6.14 and 6.15. The peak detection technique was used for data processing during these experiments. A typical resolution achieved during tracking of applied strain waveforms with this system was about  $\pm 3$  fringes.

The PZT transducer was scanned over its entire expansion range of approximately 198  $\mu\text{m}$  during operation, with data acquisition performed on the up-ramp cycles lasting 0.1 s. Despite the limited resolution and range of measurements achieved, these experiments reproduced the applied strain waveforms thereby confirming the applicability of these chirped Bragg grating sensors for strain measurement. These experiments also emphasise that it is necessary to cancel dispersive effects in the receiver interferometer. The effective linearity of strain transduction from the metallic host structure to the fibre core material has also been confirmed qualitatively, proving the suitability of the chosen method of fibre embedding.

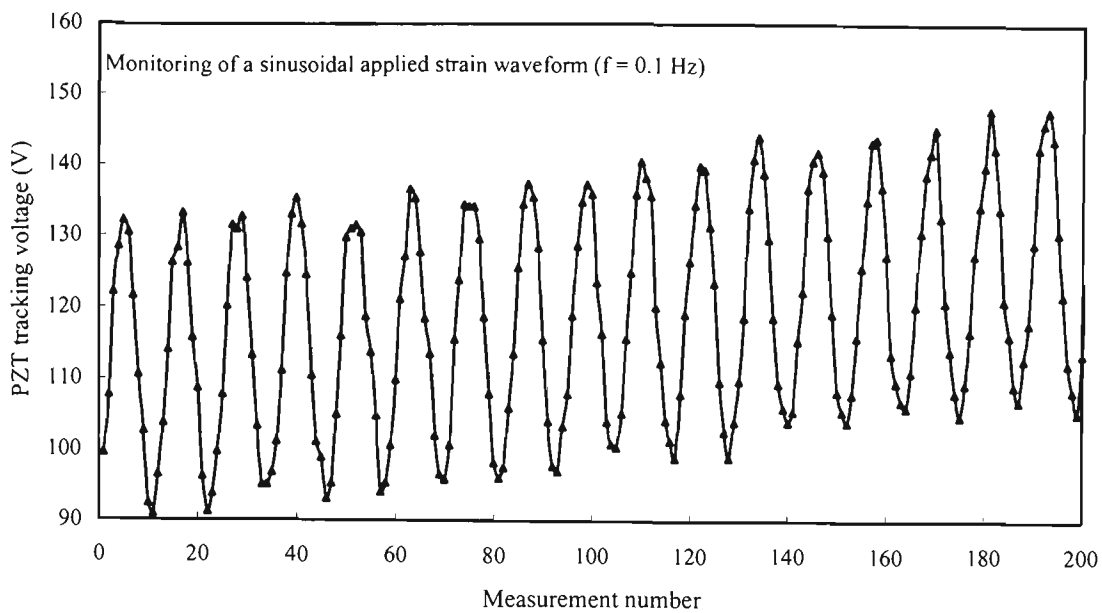


**Figure 6.14** *PZT tracking voltage corresponding to the peak voltage data point in the case of a sinusoidal beam deformation with frequency 0.1 Hz.*

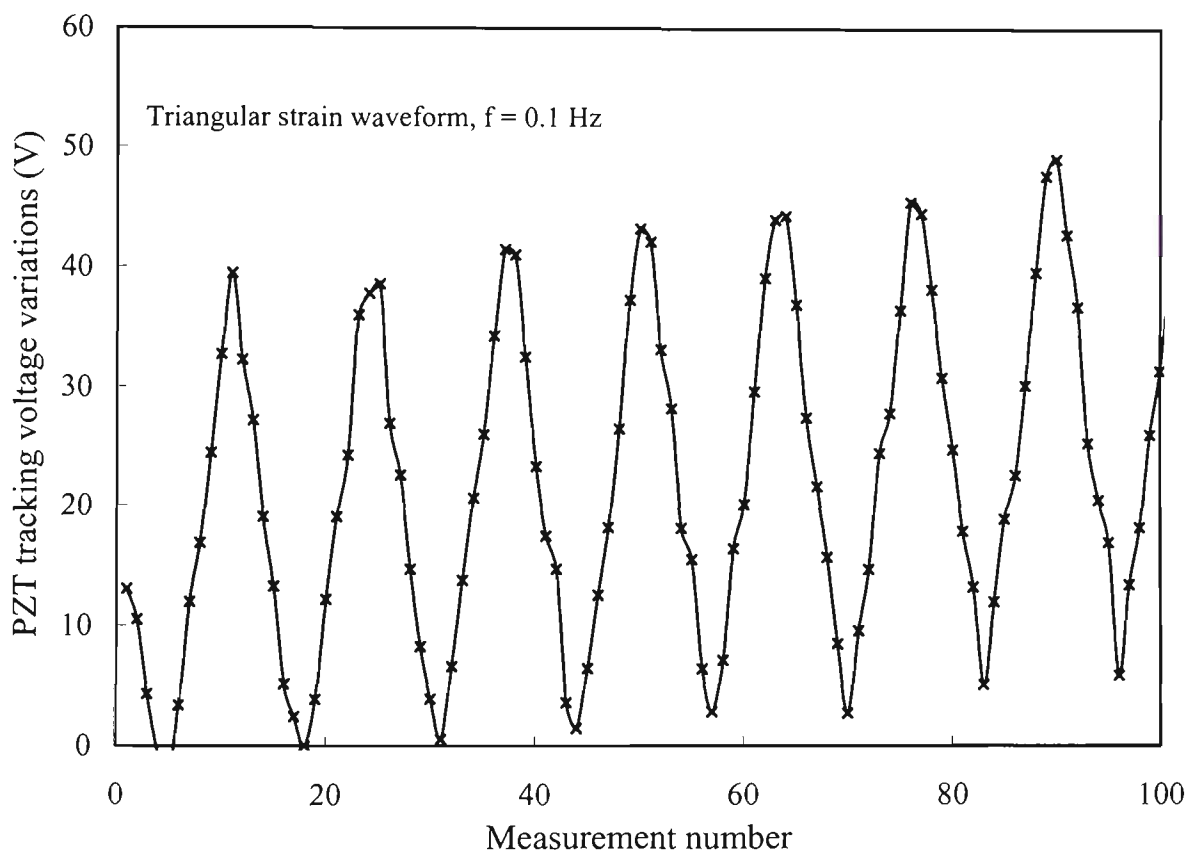


**Figure 6.15** *Monitoring of a triangular-shape strain waveform with frequency 0.1 Hz.*

The phase-strain sensitivity of the chirped grating Fabry-Pérot deduced from the system calibration and tracking voltage output was  $\Delta\varphi(\varepsilon)/\varphi_\varepsilon \varepsilon \approx 0.878$ , which is close to the figure of  $\Delta\varphi_\varepsilon/(\varphi_\varepsilon \varepsilon) \approx 0.80$  predicted in Chapter 2.

A triple-wavelength fibre sensor system with minimised dispersion in the receiver interferometer (the system described in section 6.2.2 used previously for monitoring temperature variations) was used for further strain monitoring experiments with chirped grating-based Fabry-Pérot sensors. A sensing cavity of length 245 mm based on triple superposition of broad reflection bandwidth chirped mirrors fabricated using the simultaneous writing method was installed into the beam host structure at a distance from the neutral axis of  $y = 0.3$  mm. Due to the effort devoted to minimising chromatic dispersion in the receiver interferometer and a low number (only 60) of turns in the PZT winding, the interference pattern generated by this system proved suitable for efficient signal processing. As was the case previously, the overall spatial extent of the output fringe pattern was long (about 4 mm), but in the case of a system with minimised dispersion the central region of the output interferogram contained a single central fringe group, with the central fringe being identifiable through peak detection. Furthermore, during strain monitoring the perturbations applied by the measurand to cavity reflectors did not lead to substantial increase in the phase noise. Due to the optimisation of the wavelength combination, it was possible to monitor strain in real time with sub-fringe resolution (achieved when the receiver interferometer was well sealed from air currents) possible due to application of the central fringe centroid algorithm.

The central region of the output interferogram obtained with this strain monitoring system is shown in Figure 6.16.

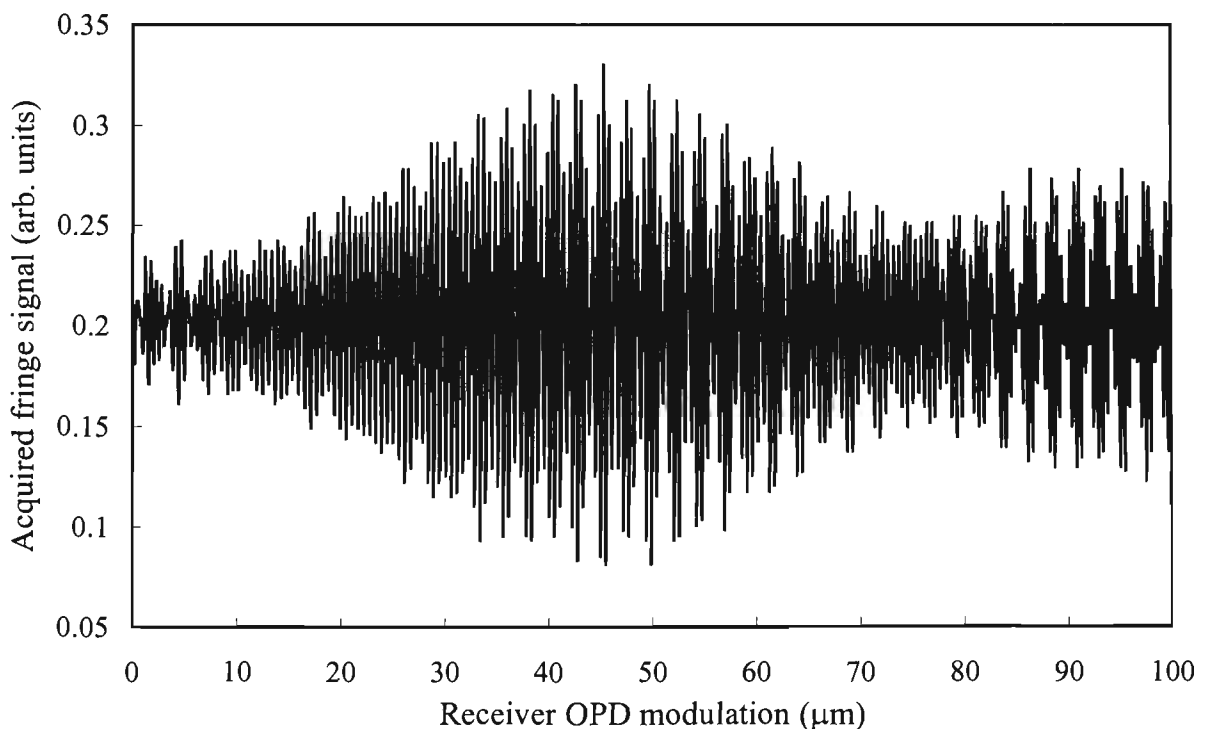


**Figure 6.16** *Central fringe region in a low coherence fringe pattern generated by an interferometer using a chirped grating Fabry-Pérot sensor and a triple-wavelength combination source.*

Some degree of asymmetry is present in the interferogram due to the non-ideal structures of grating mirrors. However, in the immediate vicinity of the centre of this pattern, side-fringes were symmetrical with respect to the central fringe. Figures 6.17 and 6.18 show the results of high-resolution real-time strain monitoring experiments conducted with the chirped grating-based fibre Fabry-Pérot sensor. The strain signal waveform was inferred from the calibrated analogue output of the Instron 8501 which was proportional to the displacement of the machine's actuator. Strain variations at the fibre installation depth were inferred from the model presented in section 6.3.1 and the measured actuator displacement signal.

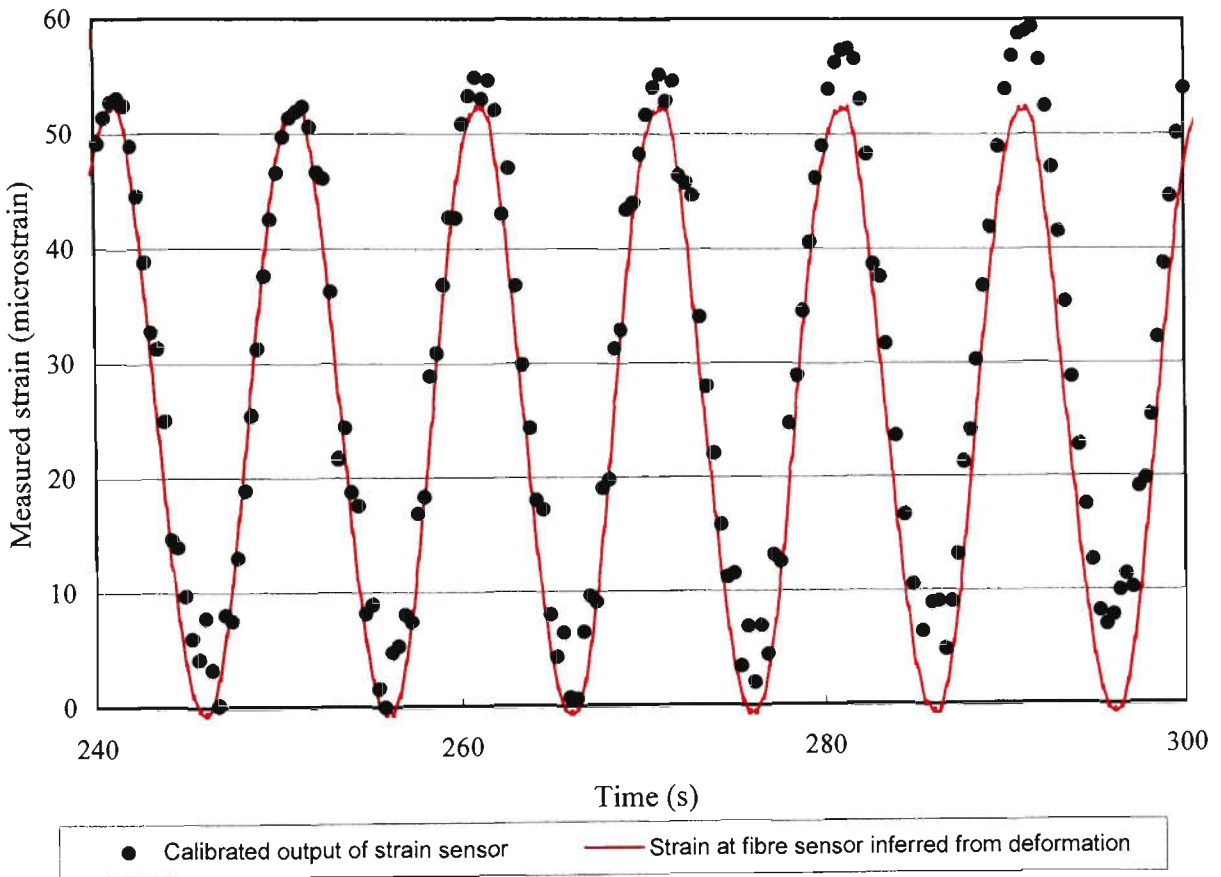


**Figure 6.17** *Dynamic strain data obtained during real-time monitoring of a sinusoidal strain waveform of frequency 0.1 Hz. The peak-to-peak amplitude of applied deformations was 2 mm.*

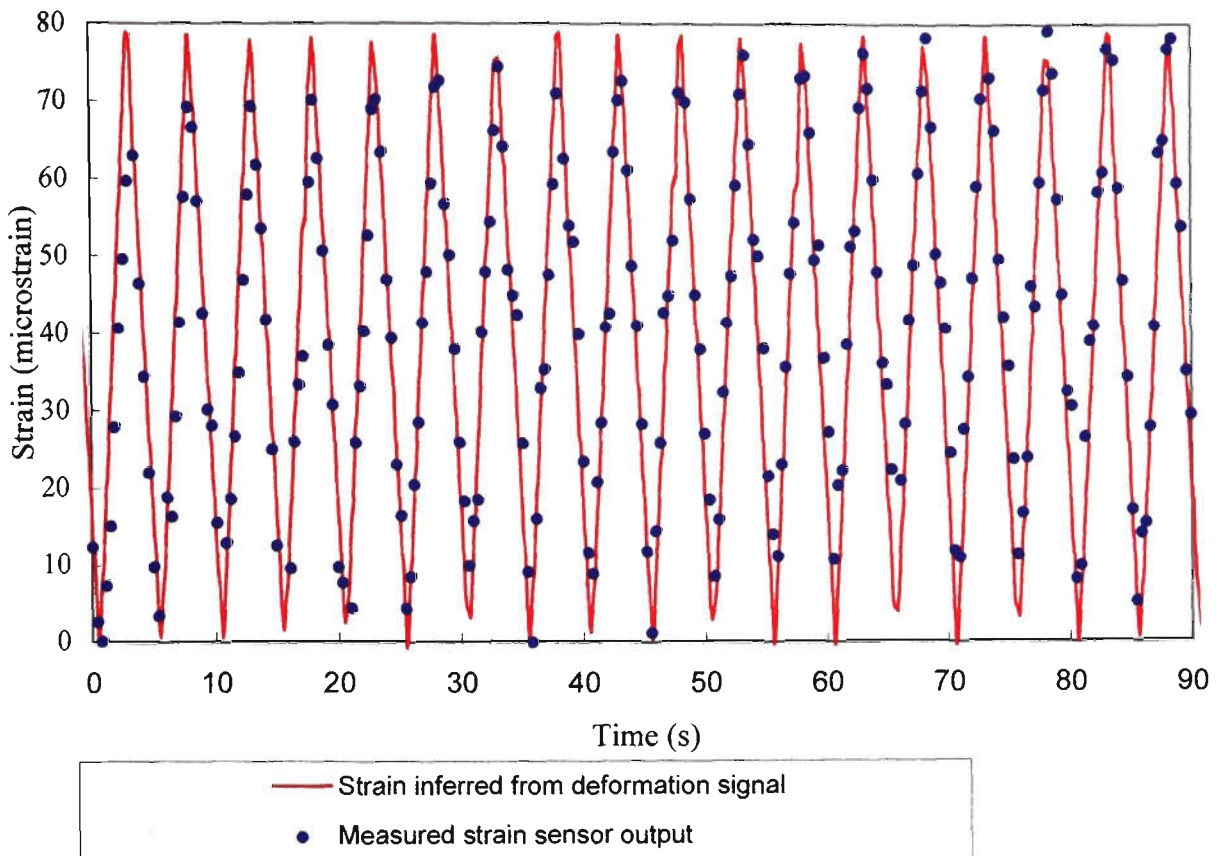


**Figure 6.18** *Dynamic strain data obtained during real-time monitoring of a triangular strain waveform of frequency 0.2 Hz. The peak-to-peak amplitude of applied deformations was 3 mm.*

Figures 6.17 and 6.18 demonstrate the suitability of the chirped grating-based Fabry-Pérot sensors for the monitoring of strain with low-coherence interrogation. The speed of measurement during the strain monitoring experiment illustrated in Figure 6.18 was 2.6 measurements/second.

Figure 6.19 shows the data from the initial quarter of a period of the waveform of Figure 6.18. A high degree of correlation between the calibrated sensor output and the strain signal waveform is evident. Also present is an indication of the fact that the fibre core material experiences smaller strain than the surrounding matrix, due to the elastic properties of the plastic fibre coating. The existence of this effect, together with its measurements, have been reported by Yuan and Zhou, 1998. In their experiments, the core of optical fibre experienced approximately 87% of the strain in the surrounding matrix.

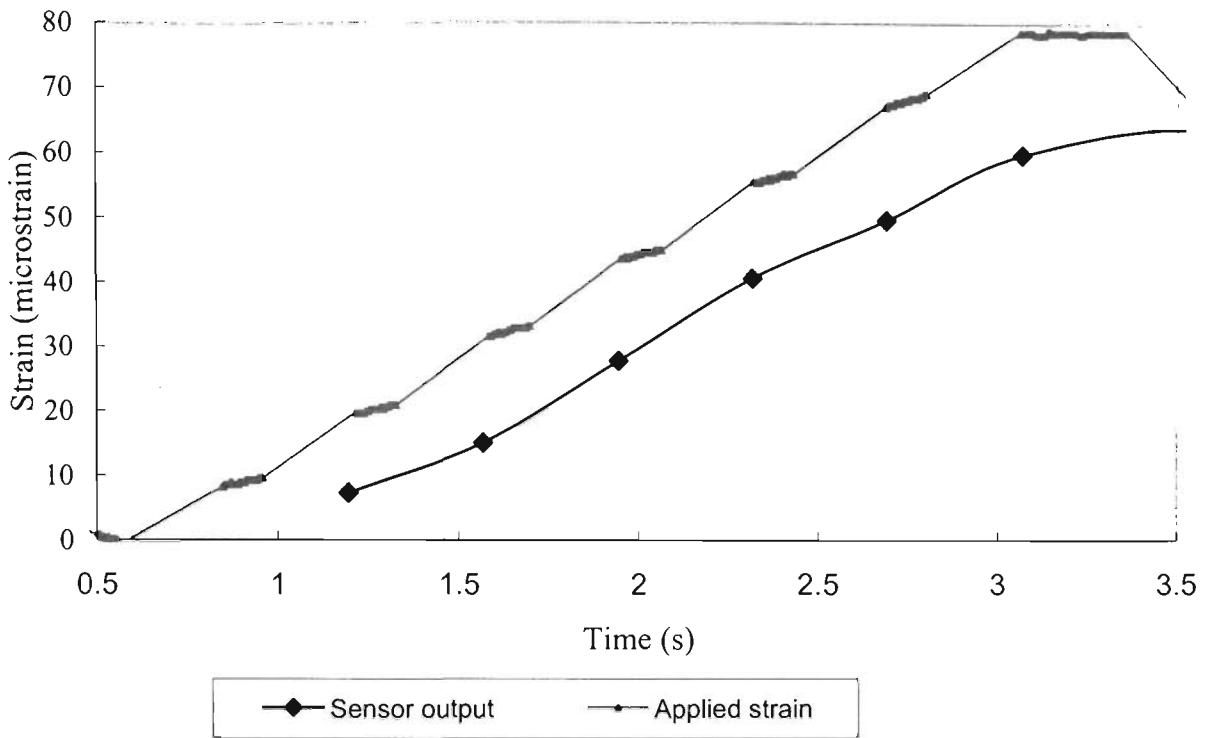


**Figure 6.19** *Correlation between the sensor output signal and strain at the sensor installation depth during a quarter of the triangular waveform period. Irregularities in the applied strain signal are associated with the analogue output from Instron 8501.*

The analysis of the data presented in Figure 6.19 reveals interesting details regarding the mechanism of strain transduction from the stressed beam structure to the fibre core through layers of epoxy and plastic coating. The fraction of actual strain sensed at the fibre core is low (about 50%) at very small levels of applied strain, but it stabilises above  $45 \mu\epsilon$  at a value of  $74.5\% \pm 1.5\%$  (worst-case error that includes the error of strain measurement) within the range of  $48\text{--}79 \mu\epsilon$ . This confirms that in embedded fibre sensors, the plastic fibre coating can absorb a significant fraction of an applied deformation (for small deformations), but after a certain strain threshold is reached, the strain transduction effect becomes constant.

Analysis of the correlation in the sensor signal and applied strain waveforms of Figure 6.18 shows that sub-microstrain resolution of strain measurement was achieved. Using the estimated 1.5% figure for the maximum error of strain measurement within the range of  $48\text{--}79 \mu\epsilon$ , it is easy to derive the worst-case and average (mid-range) strain measurement errors within this range. The former is  $\Delta\epsilon_{max} = 1.185 \mu\epsilon$  and the latter  $\langle\Delta\epsilon\rangle = 0.975 \mu\epsilon$ .

## 6.4 Results summary.

It is interesting to summarise the results of laboratory tests performed with several different versions of the multi-wavelength low coherence measurement system developed during this study. The performance characteristics of three interferometers employing different combinations of optical sources, fibre components, and signal processing techniques are compared in Table 6.1.

System characteristics, measurement type and method of signal processing	Performance characteristics: measurement accuracy, range and speed (data points/second)
<ul style="list-style-type: none"> <li>• <i>Double-source system (676 and 824 nm) using an 86 mm FP with end-coated mirrors.</i></li> <li>• Real-time temperature monitoring.</li> <li>• Simple peak detection through visibility, no intra-fringe data processing.</li> </ul>	<p>Maximum error 1.29 °C            Average error: <math>\langle \Delta T_{err} \rangle = 0.635</math> °C            Range: <math>\Delta T_{max} = 109.6</math> °C            Speed: 2.94 pts/s</p>
<ul style="list-style-type: none"> <li>• <i>Triple-source system (676, 824 and 1000 nm) using a 54 mm FP with end-coated mirrors.</i></li> <li>• Real-time temperature monitoring.</li> <li>• Central fringe detection by visibility followed by full fringe centroid processing.</li> </ul>	<p>Maximum error 0.56 °C            Average error: <math>\langle \Delta T_{err} \rangle = 0.19</math> °C            Range: <math>\Delta T_{max} = 59</math> °C            Speed: 3.025 pts/s</p>
<ul style="list-style-type: none"> <li>• <i>Triple-source system (676, 824 and 1000 nm) using a 245 mm FP with superimposed chirped Bragg gratings embedded in structure under test.</i></li> <li>• Real-time strain monitoring.</li> <li>• Central fringe detection by visibility followed by full fringe centroid processing.</li> </ul>	<p>Average error: <math>\langle \Delta \epsilon_{err} \rangle &lt; 1</math> <math>\mu\epsilon</math>            Speed: 2.6 pts/s            Range: <math>\Delta \epsilon_{max} &lt; 100</math> <math>\mu\epsilon</math>,            limited by signal distortions induced environmentally in the testing arrangement (increased vibration and air circulation during large deformations of the host structure)</p>

**Table 6.1** Comparative performance of the three multi-wavelength low coherence measurement systems tested during this project.

It is also interesting to compare the performance characteristics of systems built during this study with those of previously reported fibre sensing schemes. For example, the reported values of resolution of Bragg grating strain sensors based on the detection of strain-induced wavelength shift are 4.12 microstrain [Jackson *et al.*, 1993], and 2.6 microstrain in a system

using interferometric detection of the Bragg wavelength shift [Song *et al.*, 1997]. In other systems (for example, employing a tunable in-fibre Fabry-Pérot filter for grating wavelength detection [Kersey and Berkoff, 1993]), the reported strain sensing resolution is better than  $0.3 \mu\epsilon$ . The measurement resolution of grating-based strain sensors is limited by the finite spectral width of the grating reflection peak, whilst the measurement range is limited typically by the detection system to values of several hundred microstrains (corresponding to a 0.6 nm maximum wavelength shift detected by Kersey and Berkoff). In the field of Bragg grating temperature sensors, a typical measurement resolution of  $0.2 \text{ }^\circ\text{C}$  was reported [Ball *et al.*, 1994] in a system using a tunable laser as a light source, limited by the spectral width of the grating reflection.

## 6.5 Conclusion.

Measurements of temperature and strain performed with multi-wavelength low coherence fibre sensors in this study have demonstrated the high degree of applicability of the described type of measurement systems. Of principal importance is the demonstration of the viability of using novel chirped grating-based fibre Fabry-Pérot sensors in systems with low-coherence interrogation. In particular, the use of optimised multi-wavelength combination sources opens up new possibilities for the processing of interferometric fringe patterns which are non-ideal in terms of large spatial extent, such as those produced by distributed-reflector cavity mirrors. The results of measurements performed with low coherence systems indicate a potentially large number of industrial and laboratory applications, provided care is taken during the design of practical systems in terms of protecting the fibre components from environmental perturbations. Sub-microstrain resolution was achieved during measurements with a system employing a non-ideal chirped Bragg grating-based sensing element, with the chirped Bragg grating mirrors being subjected to strain variations during measurement. The measurement results achieved suggest that implementation of these types of sensors in civil engineering and safety control industries is possible in the near future.

## Conclusion and future work

### 7.1 Conclusion.

An in-depth investigation of the low-coherence sensing scheme and optical fibre sensors utilising novel chirped grating-based Fabry-Pérot sensing elements has been performed. Methods of optimisation of central wavelength combinations for low coherence systems employing multiple light sources have been fully investigated, and measurement systems utilising light source combinations based on the results of this study have been built and characterised. The properties of output fringe signals generated by systems using optimised white-light sources have allowed improvements in signal processing to be demonstrated during real-time monitoring of temperature and strain. The objectives of this study of multi-wavelength low coherence fibre interferometry, outlined in Chapter 1, have been realised.

A significant aspect of this project was the study of optical fibre Bragg gratings. This resulted in the successful development of a novel technique for the production of broad reflection bandwidth chirped gratings suitable for application in low coherence fibre sensors. Techniques for the economically efficient fabrication of in-fibre Fabry-Pérot interferometers based on multiple superpositions of chirped gratings have been developed. The technique of writing superimposed chirped grating structures with a prism interferometer was proven to be suitable for the production of wideband in-fibre reflectors with a custom-designed spectral response, which has been utilised in other OTRL projects. It is hoped that the results of this study of Bragg gratings will find applications in various fields of optical technology, from the

construction of new types of fibre sensors to the design of dispersion compensators and mirrors for fibre amplifiers in the field of optical communications.

The performance characteristics of fibre Fabry-Pérot sensors with chirped grating reflectors have been modelled theoretically and tested experimentally. Modification of the source spectrum due to the non-ideal spectral response of gratings was shown to affect the properties of output fringe signals obtained from low coherence interferometers, leading to the formation of elongated fringe patterns. The distributed structure of cavity reflectors provided by chirped gratings has been shown to also contribute significantly to the non-ideal spatially-extended character of the output fringe patterns, limiting the performance characteristics of fibre sensors. However, the principal applicability of these types of sensors in the case of illumination with optimised multi-wavelength sources, has been demonstrated during real-time monitoring of strain.

The effects of dispersion in the system components, originating from propagation through non-identical fibre paths and the mismatch in the mechanical strain applied to the fibre arms of the receiver interferometer have been shown to affect measurements, with the importance of minimising these effects demonstrated during the study of white-light systems response.

Practical all-fibre Fabry-Pérot sensor systems utilising low coherence interferometry with multi-wavelength source interrogation were designed and tested. The potential of the source optimisation approach for the generation of improved output fringe patterns suitable for efficient real-time processing has been demonstrated. An efficient computer-aided signal processing approach suitable for real-time measurement has been implemented, with the intra-fringe resolution enhancement technique based on the centroid algorithm applied to the processing of low coherence fringe patterns. Monitoring of temperature and strain waveforms in real time has been performed with low coherence fibre sensors employing multi-wavelength sources.

In conclusion, the performance and potential of all-fibre low coherence interferometers utilising multi-wavelength light sources and Fabry-Pérot sensing elements based on either reflective-film mirrors or superimposed chirped Bragg gratings has been investigated. The approaches for the optimisation of light source combinations and system configuration have been studied. The principal applicability of a novel type of sensing element based on chirped grating Fabry-Pérot structures has been shown for fibre sensors employing low-coherence interrogation. Measurement systems employing these sensing elements have been built which can serve as prototypes for future industrial sensors with applications in safety control and monitoring of displacement, strain and temperature.

## 7.2 Future work.

In the future various efforts can be undertaken to further bridge the gap between the laboratory application of low coherence fibre interferometers and the commercial utilisation of such systems. These will necessarily involve improvements in the light source, the sensing element and the overall system configuration.

A multi-wavelength combination light source can be provided by filtering the broad bandwidth output of a superfluorescent rare-earth-doped fibre source, as has already been reported by Brady *et al.*, 1997a for a low-coherence system using dual-wavelength quasi-heterodyne processing. The use of a fibre source makes the system more compact and robust, eliminating the loss of light power on coupling from source to fibre.

The design of fibre Fabry-Pérot sensors based on chirped gratings can be improved by reducing the grating length and increasing the reflection bandwidth, if a highly photosensitive fibre is available. In the case of short grating reflectors with sufficient reflection bandwidth, reduced sharpness of spectral features and minimised induced birefringence, effective shortening of the overall spatial extent of output white-light fringe patterns can be expected. This would make the grating-based cavity mirrors perform nearly as well as reflection-coated plane mirrors and extend the useful dynamic range and resolution of low-coherence measurement systems. It would be interesting to compare the performance of mirrors with superimposed sets of chirped gratings versus single linearly chirped gratings.

In order to minimise the sensitivity of the output fringe signal to environmental perturbations, an attempt could be made to construct the overall fibre interferometer system using a polarisation-maintaining fibre to prevent the exchange of power between polarisation modes and minimise the effects of induced birefringence and polarisation mode dispersion. This new implementation, however, would make the system more costly and more complicated from the technical point of view, since polarisation controllers or polarisation-selective filters will be necessary.

# References

- Al-Chalabi, S.A., Culshaw, B., and Davies, D.E.N.**, “Partially coherent sources in interferometric sensors”, *Proc. 1<sup>st</sup> Conf. Optical Fiber Sensors*, London, pp. 132-135, 1983.
- Atkins, R.M., Lemaire, P.J., Erdogan, T., and Mizrahi, V.**, “Mechanisms of Enhanced UV Photosensitivity via Hydrogen Loading in Germanosilicate Glasses”, *Electron. Lett.*, **29**(14), pp. 1234-1235, 1993.
- Ball, G.A., Morey, W.W., Cheo, P.K.**, “Fiber Laser Source/Analyzer for Bragg Grating Sensor Array Interrogation”, *J. Lightwave Technol.*, **12** (4) pp. 700-703, 1994.
- Barlow, A.J., and Payne, D.N.**, “The Stress-Optic Effect in Optical Fibers”, *IEEE J. Quantum Electron.*, **19**(5), pp. 834-839, 1983.
- Belleville, C., and Duplain, G.**, “White-Light Interferometric Multimode Fibre-Optic Strain Sensor”, *Opt. Lett.*, **18**, pp. 78-80, 1993.
- Bertholds, A. and Dändliker, R.**, “Determination of the individual strain-optic coefficients in single-mode optical fibers”, *J. Lightwave Technol.*, **6**(6), pp. 17-20, 1988.
- Bhatia, V., Jones, M.E., Grace, J.L., Murphy, H.A., Claus, R.O., Greene, J.A., Tran, T.A.**, “Applications of Absolute Fiber Optic Sensors to Smart Materials and Structures”, *Proc. OFS-10*, Glasgow, p. 171, 1994.
- Bock, W.J., Urbanczyk, W., Wojcik, J., and Beaulieu, M.**, “White-Light Interferometric Fiber-Optic Pressure Sensor”, *IEEE Trans. Instrum. Meas.*, **44**(3), pp. 694-697, 1995.
- Born, M., and Wolf, E.**, “Principles of Optics”, *Oxford University Press, Oxford*, 1980.
- Bosselman, Th., and Ulrich, R.**, “High accuracy position sensing with fiber-coupled white light interferometers”, *Proc. 2nd Int. Conf. Optical Fiber Sensors*, Stuttgart, pp. 361-365, 1984.
- Brady, G.P., Kalli, K., Webb, D.J., Jackson, D.A., Reekie, L., and Archambault, J.L.**, “Simultaneous Measurement of Strain and Temperature Using the First and Second-Order Diffraction Wavelengths of Bragg Gratings”, *IEE Proc. Optoelectron.*, **144**(3), pp. 156-161, 1997.
- Brady, G.P., Kalli, K., Webb, D.J., Jackson, D.A., Zhang, L., and Bennion, I.**, “Extended-Range, Low Coherence Dual Wavelength Interferometry Using a Superfluorescent Fibre Source and Chirped Fibre Bragg Gratings”, *Optics Commun.*, **134**, pp. 341-348, 1997a.

- Brooks, J.L., Wentworth, R.H., Youngquist, R.C., Tur, M., Kim, B.Y., and Shaw, H.J.,** "Coherence Multiplexing of Fiber-Optic Interferometric Sensors", *J. Lightwave Technol.*, **3**(5), pp. 1062-1072, 1985.
- Butter, C.D. and Hocker, G.B.,** "Fiber Optics Strain Gauge", *Appl. Opt.*, **17**(18), pp. 2867-2869, 1978.
- Byron, K.C., and Rourke, H.N.,** "Fabrication of Chirped Fibre Gratings by Novel Stretch and Write Technique", *Electron. Lett.*, **31**(1), pp. 60-61, 1995.
- Byron, K.C., Sugden, K., Bricheno, T., and Bennion, I.,** "Fabrication of Chirped Bragg Gratings in Photosensitive Fibre", *Electron. Lett.*, **29**(18), pp. 1659-1660, 1993.
- Chen S., Grattan K.T.V., Meggitt B.T., and Palmer, A.W.,** "Instantaneous Fringe-Order Identification Using Dual Broadband Sources With Widely Spaced Wavelengths", *Electron. Lett.*, **29**(4), pp. 334-335, 1993.
- Chen S., Meggitt, B.T., and Rogers, A.J.,** "Electronically-Scanned White Light Interferometry With Enhanced Dynamic Range", *Electron. Lett.*, **26**(20), pp. 1663-1665, 1990.
- Chen, S., Palmer, A.W., Grattan, K.T.V., and Meggitt, B.T.,** "Fringe Order Identification in Optical Fibre White-Light Interferometry Using Centroid Algorithm Method", *Electron. Lett.*, **28**(6), pp. 553-555, 1992.
- Chen, S., Palmer, A.W., Grattan, K.T.V., and Meggitt, B.T.,** "Digital Signal-Processing Techniques for Electronically Scanned Optical-Fiber White-Light Interferometry", *Appl. Opt.*, **31**(28), pp. 6003-6010, 1992a.
- Chen, S., Rogers, A.J., and Meggitt, B.T.,** "Electronically Scanned Optical-Fiber Young's White-Light Interferometer", *Optics Lett.*, **16**(10), pp. 761-763, 1991.
- Cole, M.J., Loh, W.H., Laming, R.I., Zervas, M.N., and Barcelos, S.,** "Moving Fibre/Phase Mask - Scanning Beam Technique for Enhanced Flexibility in Producing Fibre Gratings With Uniform Phase Mask", *Electron. Lett.*, **31**(17), pp. 1488-1490.
- Cruz, J.L., Dong, L., Barcelos, S., and Reekie, L.,** "Fiber Bragg gratings with various chirp profiles made in etched tapers", *Appl. Opt.*, **35**(34), pp. 6781-6787, 1996.
- Culshaw, B., and Dakin, J.,** *Optical Fiber Sensors: Principles and Components/Systems and Applications, Vol. 1 & 2*, Artech House, Inc., 1988/1989.
- Dakin, J.P., Ecke, W., Rothardt, M., Schauer, J., Usbeck, K., and Willsch, R.,** "New Multiplexing Scheme for Monitoring Fiber Optic Bragg Grating Sensors in the Coherence Domain", *Proc. 12th Int. Conf. on Optical Fiber Sensors (OFS-12)*, Williamsburg, USA, pp. 1473-1477, 1997.

- Dändliker, R., Zimmermann, E., and Frosio, G.**, “Noise-Resistant Signal Processing For Electronically Scanned White-Light Interferometry”, *Proc. 8th OFS Conf.*, Monterey, Calif., pp. 53-56, Jan 29-31, 1992.
- Davis, M.A., Kersey, A.D.**, “Application of a Fiber Fourier Transform Spectrometer to the Detection of Wavelength-Encoded Signal from Bragg Grating Sensors”, *J. Lightwave Technol.*, **13** (7), pp. 1289-1295, 1995.
- Dong, L., Cruz, J.L., Reekie, L., Xu, M.G., and Payne, D.N.**, “Enhanced Photosensitivity in Tin-Codoped Germanosilicate Optical Fibers”, *IEEE Photonics Technol. Lett.*, **7**(9), pp. 1048-1050, 1995.
- Farries, M.C., Sugden, K., Reid, D.C.J., Bennion, I., Molony, A., and Goodwin, M.J.**, “Very Broad Reflection Bandwidth (44 nm) Chirped Fibre Gratings and Narrow Bandpass Filters Produced by the Use of an Amplitude Mask”, *Electron. Lett.*, **30**(11), pp. 891-892, 1994.
- Garchev, D.D., Vasiliev, M., and Booth, D.J.**, “Wavelength-Tunable Chirped In-Fiber Bragg Gratings Produced With a Prism Interferometer”, *Optics Comm.*, **148**, pp. 254-258, 1998.
- Gerges, A.S., Farahi, F., Newson, T.P., Jones, J.D.C., and Jackson, D.A.**, “Interferometric Fibre-Optic Sensor Using a Short-Coherence-Length Source”, *Electron Lett.*, **23**(21), pp. 1110-1111, 1987.
- Giallorenzi, T.G., Bucaro, J.A., Dandridge, A., Sigel, G.H., Cole, J.H., Rashleigh, S.C., and Priest, R.G.**, “Optical Fiber Sensor Technology”, *IEEE J. Quantum Electron.*, **18**(4), pp. 626-665, 1982.
- Giovannini, H.R., Huard, S.J., and Lequime, M.R.**, “Influence of Chromatic Dispersion on a Dual-Wavelength Passive-Homodyne Detection Method for Fiber-Coupled Interferometers”, *Appl. Opt.*, **33**(13), pp. 2721-2733, 1994.
- Grattan, K. T. V., and Sun, T.**, “Fiber optic sensor technology: an overview”, *Sensors and Actuators A*, **82**, pp 40-61, 2000.
- Grattan, K.T.V, and Meggitt, B.T.**, *Optical Fiber Sensor Technology, Chapter 9*, Chapman & Hall, 1995.
- Guenther, R.D.**, *Modern Optics*, 1990.
- Hill, K.O., Malo, B., Bilodeau, F., Johnson, D.C., and Albert, J.**, “Bragg Gratings Fabricated in Monomode Photosensitive Optical Fiber by UV Exposure Through a Phase Mask”, *Appl. Phys. Lett.*, **62**(10), pp. 1035-1037, 1993.
- Hill, P.C., and Eggleton, B.J.**, “Strain Gradient Chirp of Fibre Bragg Gratings”, *Electron. Lett.*, **30**(14), pp. 1172-1174, 1994.

- Hocker, G.B.**, “Fiber-Optic Sensing of Pressure and Temperature”, *Appl. Opt.*, **18**(9), pp. 1445-1448, 1979.
- Huang, D., et al.**, “Optical Coherence Tomography”, *Science*, **254**, pp. 1178-1181, 1991.
- Inoue, A., Shigehara, M., Ito, M., Inai, M., Hattori, Y., and Mizunami, T.**, “Fabrication and Application of Fiber Bragg Grating - A Review”, *Optoelectronics - Devices and Technologies*, **10**(1), pp. 119-130, 1995.
- Jackson, D., Lobo, A.B., Ribeiro, L., Reekie, L., Archambault, J.L.**, “Simple Multiplexing Scheme for a Fibre-Optic Grating Sensor Network”, *Optics Lett.*, **18** (14), pp. 1192-1193, 1993.
- Jeunhomme, L.B.**, Single-mode fiber optics: principles and applications, 2nd edn., Marker Dekker, New York, U.S.A. 1990.
- Jin, X.D., and Sirkis, J.**, “Optical Fiber Sensors for Simultaneous Measurement of Strain and Temperature”, *SPIE J.*, **3042**, pp. 120-127, 1997.
- Kaddu, S.C.**, “Low Coherence Fibre Optic Fabry-Pérot Sensors Suitable for Multiplexed Strain Measurement”, *PhD Thesis, Victoria Univ. of Technol.*, 1995.
- Kaddu, S.C., Booth, D.J., Garchev, D.D., and Collins S.F.**, “Intrinsic Fibre Fabry-Pérot Sensors Based on Co-Located Bragg Gratings”, *Optics Comm.*, **142**, pp. 189-192, 1997.
- Kaddu, S.C., Collins, S.F., and Booth, D.J.**, “Multiplexed Intrinsic Optical Fibre Fabry-Pérot Temperature and Strain Sensors Addressed Using White-Light Interferometry”, *Meas. Sci. Technol.*, **10**, pp. 416-420, 1999.
- Kashyap, R., McKee, P.F., Campbell, R.J., and Williams, D.L.**, “Novel Method of Producing All Fibre Photoinduced Chirped Gratings”, *Electron. Lett.*, **30**(12), pp. 996-997, 1994.
- Katzir, A., Livanos, A.C., Shellan, J.B., and Yariv, A.**, “Chirped Gratings in Integrated Optics”, *IEEE J. Quantum Electron.*, **13**(4), pp. 296-304, 1977.
- Kersey, A.D., and Berkoff, T.A.**, “Multiplexed Fiber Grating Strain-Sensor System With a Fabry-Pérot Wavelength Filter”, *Optics Lett.*, **18** (16), pp. 1370-1372, 1993.
- Kersey, A.D., Berkoff, T.A., and Morey, W.W.**, “High-Resolution Fibre-Grating Based Strain Sensor with Interferometric Wavelength-Shift Detection”, *Electron. Lett.*, **28**(3), pp. 236-238, 1992.
- Kim, B.G. and Garmire, E.**, “Comparison Between the Matrix Method and the Coupled Wave Method in the Analysis of Bragg Reflector Structures”, *J. Opt. Soc. Am. A*, **9**, pp 132-136, 1992.
- Koch, A., and Ulrich, R.**, “Displacement Sensor With Electronically Scanned White Light Interferometer”, *Proc. SPIE*, **1267**, pp. 126-133, 1990.

- Koch, A., and Ulrich, R.**, "Fiber-Optic Displacement Sensor with 0.02  $\mu\text{m}$  Resolution by White-Light Interferometry", *Sensors and Actuators A*, **25-27**, pp. 201-207, 1991.
- Lagakos, N., Bucaro, J.A., and Jarzynski, J.**, "Temperature-induced optical phase shifts in fibres", *Appl. Opt.*, **20**(13), pp. 2305-2308, 1981.
- Lee, C.E., and Taylor, H.F.**, "Sensors for smart structures based upon the Fabry-Pérot interferometer", *Fiber Optic Smart Structures*, edited by E. Udd (New York: Wiley), pp. 249-269, 1995.
- Lee, C.E., and Taylor, H.F.**, "Fibre-Optic Fabry-Pérot Temperature Sensor Using a Low-Coherence Light Source", *J. Lightwave Technol.*, **9**, pp. 129-134, 1991.
- Lee, C.E., and Taylor, H.F.**, "Interferometric Optical Fiber Sensors Using Internal Mirrors", *Electron. Lett.*, **24**, pp. 193-194, 1988.
- Lefevre H.C.**, "White Light Interferometry in Optical Fibre Sensors", *Proc. 7th Int. Conf. on Optical Fibre Sensors (Sydney)*, pp. 345-351, 1990.
- Legoubin S., Fertein, E., Douay, M., Bernage, P., Niay, P., Bayon, F., and Georges, T.**, "Formation of M $\acute{o}$ ire Gratings in Core of Germanosilicate Fiber by Transverse Holographic Double Exposure Method", *Electron. Lett.*, **27** (21), pp. 1945-1946, 1991.
- Lemaire, P.J., Atkins, R.M., Mizrahi, V., and Reed, W.A.**, "High Pressure H $_2$  Loading as a Technique for Achieving Ultrahigh UV Photosensitivity and Thermal Sensitivity in GeO $_2$  Doped Optical Fibres", *Electron. Lett.*, **29**(13), pp. 1191-1193, 1993.
- Lesko, J.J., Carman, G.P., Fogg, B.R., Miller, W.V., Vengsarkar, A.M., Reifsnider, K.L., and Claus, R.O.**, "Embedded Fabry-Pérot Fiber Optic Strain Sensors in the Macromodel Composites", *Opt. Eng.*, **31**(1), pp. 13-22, 1992.
- Liou, C.L., Wang, L.A., Shih, M.C., and Chuang, T.J.**, "Characteristics of Hydrogenated Fiber Bragg Gratings", *Appl. Phys. A (Materials Science & Processing)*, **64**, pp. 191-197, 1997.
- Liu, T., Fernando, G., Rao, Y., Jackson, D.A., Zhang, L., and Bennion, I.**, "Simultaneous Strain and Temperature Measurements in Composite Using a Multiplexed Fiber Bragg Grating Sensor and an Extrinsic Fabry-Pérot Sensor", *SPIE J.*, **3042** pp. 203-212, 1997.
- Liu, T., Wu, M., Rao, Y., Jackson, D.A., and Fernando, G.F.**, "A Multiplexed Optical Fibre-Based Extrinsic Fabry-Pérot Sensor System for In-Situ Strain Monitoring in Composites", *Smart Mater. Struct.*, **7**, pp. 550-556, 1998.
- Malo, B., Albert, J., Hill, K.O., Bilodeau, F., and Johnson, D.C.**, "Effective Index Drift From Molecular Hydrogen Diffusion in Hydrogen-Loaded Optical Fibres and its Effect on Bragg Grating Fabrication", *Electron. Lett.*, **30**(5), pp. 442-444, 1994.
- Marillier, C., and Lequime, M.**, "Fiber-Optic White Light Birefringent Temperature Sensor", *Proc. SPIE*, Vol. **798**, pp. 121-130, 1987.

- Marshall, R.H., Ning, Y.N., Palmer, A.W., and Grattan, K.T.V.**, “Dispersion in an Electronically-Scanned Dual-Wavelength Low-Coherence Interferometer”, *Optics Commun.*, **138**, pp. 136-142, 1997.
- Marshall, R.H., Ning, Y.N., Palmer, A.W., and Grattan, K.T.V.**, “Simultaneous Measurement of a.c. and d.c. Stresses Using a Fibre-Optic Electronically Scanned White-Light Interferometer”, *Sensors and Actuators A*, **64**, pp. 225-229, 1998.
- Measures, R.M.**, “Advances Toward Fibre Optic Based Smart Structures”, *Opt. Eng.*, **31**(1), pp. 34-47, 1992.
- Meggitt, B.T.**, “Fiber Optic White-Light Interferometric Sensors”, *Chapter 9 in Optical Fiber Sensor Technology*, edited by K.T.V. Grattan and B.T. Meggitt, Chapman & Hall, London, 1995.
- Melle, S.M., Liu, K., and Measures, R.M.**, “Practical Fiber-Optic Bragg Grating Strain Gauge System”, *Appl. Opt.*, **32**(19), pp. 3601-3609, 1993.
- Meltz, G., Morey, W.W., and Glenn, W.H.**, “Formation of Bragg Gratings in Optical Fibers by a Transverse Holographic Method”, *Optics Lett.*, **14**, pp. 823-825, 1989.
- Mitchell, G.L.**, “Intensity-Based and Fabry-Pérot Interferometer Sensors”, Chapter 6, *Fiber Optic Sensors: An Introduction for Engineers and Scientists*, edited by Eric Udd, John Wiley & Sons, Inc., 1991.
- Mizrahi, V. and Sipe, J. E.**, “Optical Properties of Photosensitive Fiber Phase Gratings”, *IEEE J. Lightwave Technol.*, **11**(10), pp 1513-1517, 1993.
- Morey W.W., Dunphy, J.R., and Meltz, G.**, “Distributed and Multiplexed Fibre Optic Sensors”, *Proc. SPIE*, **1586**, p. 216, 1991.
- Murphy, D.F., and Flavin, D.A.**, “Dispersion-Insensitive Measurement of Thickness and Group Refractive Index by Low-Coherence Interferometry”, *Appl. Opt.*, **39**(25), pp. 4607-4615, 2000.
- Murphy, K.A.**, “Extrinsic Fabry-Pérot Optical Fiber Sensor”, *Proc. OFS-8*, Monterey, Calif., p. 193, 1992.
- Ning, Y., Grattan, K.T.V., Meggitt, B.T., and Palmer, A.W.**, “Characteristics of Laser Diodes for Interferometric Use”, *Appl. Opt.*, **28**(17), pp. 3657-3661, 1989.
- Ning, Y.N., and Grattan, K.T.V.**, “White Light Interferometric Optical Fiber Sensing Techniques”, *Optical Fiber Sensor Technology, Vol. 4*, edited by K.T.V. Grattan and B.T. Meggitt, Chapter 10, Kluwer Academic Publishers, London, 1998.
- Okamoto, K., Hibino, Y., and Ishii, M.**, “Guided-Wave Optical Equalizer with a-Power Chirped Grating”, *IEEE J. Lightwave Technol.*, **11**(8), pp. 1325-1330, 1993.
- Othonos, A., and Lee, X.**, “Novel and Improved Methods of Writing Bragg Gratings with Phase Masks”, *IEEE Photonics Technol. Lett.*, **7**(10), pp. 1183-1185, 1995.

- Painchaud, Y., Chandonnet, A., and Lauzon, J.,** “Chirped Fibre Gratings Produced by Tilting the Fibre”, *Electron. Lett.*, **31**(3), pp. 171-172, 1995.
- Patrick, H., and Gilbert, S.L.,** “Growth of Bragg Gratings Produced by Continuous-Wave Ultraviolet Light in Optical Fiber”, *Optics Lett.*, **18**(18), pp. 1484-1486, 1993.
- Peters, K., Pattis, P., Botsis, J., and Giaccari, P.,** “Experimental Verification of Response of Embedded Optical Fiber Bragg Grating Sensors in Non-Homogeneous Strain Fields”, *Optics and Lasers in Engineering*, **33**, pp. 107-119, 2000.
- Poladian, L.,** “Models of the Growth Dynamics of Holographically Written Bragg Gratings”, *Proc. Australian Conf. on Optical Fibre Technol. (ACOFT)*, pp. 55-58, 1993.
- Poumellec, B., Niay, P., Douay, M., and Bayon, J.F.,** “The UV-Induced Refractive Index Grating in Ge:SiO<sub>2</sub> preforms: Additional CW Experiments and the Macroscopic Origin of the Change in Index”, *J. Phys. D: Appl. Phys.*, **29**, pp. 1842-1856, 1996.
- Putnam, M.A., Williams, G.M., and Friebele, E.J.,** “Fabrication of Tapered, Strain-Gradient Chirped Fibre Bragg Gratings”, *Electron. Lett.*, **31**(4), pp. 309-310, 1995.
- Rao, Y., and Jackson, D.A.,** “Recent Progress in Fibre Optic Low-Coherence Interferometry”, *Meas. Sci. Technol.*, **7**, pp. 981-999, 1996.
- Rao, Y.J.,** “Recent Progress in Applications of In-Fibre Bragg Grating Sensors”, *Optics and Lasers in Engineering*, **31**, pp. 297-324, 1999.
- Rao, Y.J., and Jackson, D.A.,** “Improved Synthesized Source for White-Light Interferometry”, *Electron. Lett.*, **30**, pp. 1440-1441, 1994.
- Rao, Y.J., Jackson, D.A., Jones, R., and Shannon, C.,** “Development of Prototype Fibre-Based Fizeau Pressure Sensors with Temperature Compensation”, *J. Lightwave Technol.*, **12**, pp. 1685-1695, 1994.
- Rao, Y.J., Kalli, K., Brady, G., Webb, D.J., Jackson, D.A., Zhang, L., and Bennion, I.,** “Spatially-Multiplexed Fibre-Optic Bragg Grating Strain and Temperature Sensor System Based on Interferometric Wavelength-Shift Detection”, *Electron. Lett.*, **31**(12), pp. 1009-1010, 1995.
- Rao, Y.J., Ning, Y.N., and Jackson, D.A.,** “Synthesized Source for White-Light Sensing Systems”, *Optics Lett.*, **18**, pp. 462-464, 1993.
- Reekie, L., and Dong, L.,** “Material Considerations for Bragg Fibre Gratings”, *Proc. SPIE*, **2998**, pp. 2-10, 1997.
- Rizk, M.S., Romare, D., Grattan, K.T.V., and Palmer, A.W.,** “Adaptive Filtering of White-Light Interferometry Fringe Patterns”, *IEEE Trans. Instrum. Meas.*, **47**(3), pp. 782-787, 1998.
- Russell, P.S.J., Archambault, J., and Reekie, L.,** “Fibre Gratings”, *Physics World*, pp. 41-46, Oct. 1993.

- Sandoz, P. and Tribillon, G.**, “Profilometry by Zero-Order Interference Fringe Identification”, *J. Modern Opt.*, **40**(9), pp. 1691-1700, 1993.
- Santos, J.L., and Jackson, D.A.**, “Coherence Sensing of Time-Addressed Optical-Fibre Sensors Illuminated by a Multimode Laser Diode”, *Appl. Opt.*, **30**, pp. 5068-5076, 1991.
- Sceats, M.G., Atkins, G.R., and Poole, S.B.**, “Photolytic Index Changes in Optical Fibers”, *Annu. Rev. Mater. Sci.*, **23**, pp. 381-401, 1993.
- Singh, H., and Sirkis, J.**, “Simultaneous Measurement of Strain and Temperature Using Optical Fiber Sensors: Two Novel Configurations”, *Proc. OFS-11 Conf.*, Japan, pp. 108-111, May 1996.
- Sinha, P.G., and Yoshino, T.**, “Acoustically Scanned Low-Coherence Interrogated Simultaneous Measurement of Absolute Strain and Temperature Using Highly Birefringent Fibers”, *J. Lightwave Technol.*, **16**(11), pp. 2010-2015, 1998.
- Sirkis, J., Berkoff, T.A., Jones, R.T., Singh, H., Kersey, A.D., Friebele, E.J., and Putnam, M.A.**, “In-Line Fiber Etalon (ILFE) Fiber Optic Strain Sensors”, *IEEE J. Lightwave Technol.*, **13**, p. 1256, 1995.
- Snyder, A.W. and Love, J.D.**, *Optical Waveguide Theory*, Chapman & Hall, London, 1983.
- Song M., Lee, B., Lee, S.B., and Choi, S.S.**, “Interferometric Temperature-Insensitivity Strain Measurement With Different-Diameter Fiber Bragg Gratings”, *Optics Lett.*, **22** (11), pp. 790-792, 1997.
- Sugden, K., Bennion, I., Molony, A., and Copner, N.J.**, “Chirped Gratings Produced in Photosensitive Optical Fibres by Fibre Deformation During Exposure”, *Electron. Lett.*, **30**(5), pp. 440-442, 1994.
- Sulimov, V.B., and Sokolov, V.O.**, “Photosensitivity and Quadratic Non-linearity in Glass Waveguides: Fundamentals and Applications”, *Portland, OR: Optical Society of America*, 1995.
- Taplin, S.R., Podoleanu, A.Gh., Webb, D.J., and Jackson, D.A.**, “White-Light Displacement Sensor Incorporating Signal Analysis of Channeled Spectra”, *Proc. SPIE*, Vol. **2292**, pp. 94-100, 1994.
- Timoshenko, S.P., and Goodier, J. N.**, *Theory of Elasticity*, 3rd edn., McGraw-Hill, 1970.
- Trouchet, D., Desforges, F.X., Graindorge, P., and Lefevre, H.C.**, “Remote Fibre Optic Measurement of Air index with White Light Interferometry”, *Proc. 8th Int. Conf. on Optical Fibre Sensors (Monterey, Calif.)*, pp. 57-60, 1992.
- Urbanczyk, W. and Bock, W.J.**, “Analysis of Dispersion Effects for White-Light Interferometric Fiber-Optic Sensors”, *Appl. Opt.*, **33**(1), pp. 124-129, 1994.
- Uttam, D., Culshaw, B., Ward, J.D., and Carter, D.**, “Interferometric Optical Fibre Strain Measurement”, *J. Phys. E: Sci. Instrum.*, **18**, pp. 290-293, 1985.

- Velluet, M.T., Graindorge, P., and Arditty, H.J.**, “Fiber-Optic Pressure Sensor Using White Light Interferometry”, *Proc. SPIE*, Vol. **838**, pp. 78-83, 1987.
- Wang, D.N., Ning, Y.N., Grattan, K.T.V., Palmer, A.W., and Weir, K.**, “The Optimized Wavelength Combinations of Two Broadband Sources for White Light Interferometry”, *J. Lightwave Technol.*, **12**(5), pp. 909-915, 1994.
- Wang, D.N., Ning, Y. N., Grattan, K. T. V., Palmer, A. W., and Weir, K.**, “Optimized Multiwavelength Combination Sources for Interferometric Use”, *Appl. Opt.*, **33**(31), pp 7326-7333, 1994a.
- Weber, M.J.**, *Optical Crystals, CRC Handbook of Laser Science and Technology, Volume 4: Optical Materials*, CRC Press, Florida, 1986.
- Weir, K., Boyle, W.J.O., Meggitt, B.T., Grattan, K.T.V., and Palmer, A.W.**, “A Novel Adaptation of the Michelson Interferometer for the Measurement of Vibration”, *J. Lightwave Technol.*, **10**, pp. 700-703, 1992.
- Weir, K., Palmer, A.W., and Grattan, K.T.V.**, “Accurate Measurement of Small Displacement Using Optical Techniques”, *Internat. J. Optoelectron.*, **9**(6), pp. 449-455, 1994.
- Williams, D.L., Ainslie, B.J., Kashyap, R., Maxwell, G.D., Armitage, J.R., Campbell, R.J., and Wyatt, R.**, *Proc. SPIE*, **2044**, p. 55, 1993.
- Xie, W.X., Niay, P., Bernage, P., Douay, M., Bayon, J.F., Georges, T., Monerie, M., and Poumellec, B.**, “Experimental Evidence of Two Types of Photorefractive Effects Occurring During Photoinscriptions of Bragg Gratings within Germanosilicate Fibres”, *Optics Comm.*, **104**(1-3), pp. 185-195, 1993.
- Xu, M.G., Archambault, J.-L., Reekie, L., and Dakin, P.**, “Discrimination Between Strain and Temperature Effects Using Dual-Wavelength Fibre Grating Sensors”, *Electron. Lett.*, **30**(13), pp. 1085-1087, 1994.
- Yamada, M., and Sakuda, K.**, “Analysis of Almost-Periodic Distributed Feedback Slab Waveguides via a Fundamental Matrix Approach”, *Appl. Opt.*, **26**, pp. 3474-3478, 1987.
- Yariv, A.** “Coupled-Mode Theory for Guided-Wave Optics”, *IEEE J. Quantum Electron.*, **9**(9), pp. 919-933, 1973.
- Yoffe, G.W., Krug, P.A., Ouelette, F., and Thorncraft, D.A.**, “Passive Temperature-Compensating Package for Optical Fiber Gratings”, *Appl. Opt.*, **34**, pp. 6859-6861, 1995.
- Yoshino, T., Kurosawa, K., Itoh, K., and Ose, T.**, “Fiber-Optic Fabry-Pérot Interferometer and Its Sensor Applications”, *IEEE J. Quantum Electron.*, **18**(10), pp. 1624-1633, 1982.
- Youngquist, R.C., Carr, S., and Davies, D.N.**, “Optical Coherence Domain Reflectometry: a New Optical Evaluation Technique”, *Optics Lett.*, **12**, pp. 158-160, 1987.

**Yuan, L., and Zhou, L.,** “1×N Star Coupler as a Distributed Fiber-Optic Strain Sensor in a White-Light Interferometer”, *Appl. Opt.*, **37**(19), pp. 4168-4172, 1998.

**Zhang, Q., Brown, D.A., Reinhart, L., and Morse, T.F.,** “Simple Prism-Based Scheme for Fabricating Bragg Gratings in Optical Fibers”, *Optics Lett.*, **19**(23), pp. 2030-2032, 1994.

**Zhang, Q., Brown, D.A., Reinhart, L.J., and Morse, T.F.,** “Linearly and Nonlinearly Chirped Bragg Gratings Fabricated on Curved Fibers”, *Optics Lett.*, **20**(10), pp. 1122-1124, 1995.

**Zhang, S., Lee, S.B., Fang, X., and Choi, S.S.,** “In-Fiber Grating Sensors”, *Optics and Lasers in Engineering*, **32**, pp. 405-418, 1999.

# *Publications*

Vasiliev M., Garchev D.D., and Booth D.J., “Production of Wavelength-Tunable Chirped In-Fibre Bragg Gratings With a Simple Prism Interferometer”, *Proc. XI Australian Optical Society Conference*, p. FP22, 1997.

Garchev D.D., Vasiliev M. and Booth D.J., “Wavelength-Tunable Chirped In-Fibre Bragg Gratings Produced With a Prism Interferometer”, *Optics Communications*, vol. 148, pp. 254-258, 1998.

Garchev D.D., Vasiliev M. Booth D.J. and Tapanes E.E., “A Method of Providing In-Situ Chirped Gratings in Waveguides and Waveguides Made By That Method”, International Patent Number PCT/AU98/00081.

Vasiliev M., Garchev D.D., and Booth D.J., “Production of Broadband Wavelength-Tunable In-Fibre Bragg Gratings with a Prism Interferometer”, *Proc. of School of Communications and Informatics Collaborative Research Forum (SCIRF '99), Faculty of Engineering and Science, Victoria University of Technology*, p. 79, 1999.

Vasiliev, M., Stevenson, A.J., and Collins, S.F., “Low-coherence strain monitoring system using an optimised triple-wavelength combination source and chirped Bragg grating-based Fabry-Pérot sensor”, *Congress Abstracts and Posters Summaries*, p. 24, 14th National Congress of the Australian Institute of Physics, Adelaide University, December 10-15, 2000.

Vasiliev M., Stevenson A.J. and Collins S.F., “Low coherence interferometric strain and temperature sensing using a triple-wavelength synthesised source”, submitted for publication in the *Proc. OECC/IOOC*, Sydney, 2001.

## A.1 List of symbols

Symbol	Description
$\alpha$	Coefficient of thermal expansion
$\beta$	Propagation constant of a guided fibre mode
$\Delta$	Phase mismatch constant in coupled-mode theory
$\Delta\beta$	Wave vector detuning from Bragg resonance
$c$	Speed of light in vacuum
$d$	Distance
$\gamma(\tau)$	Degree of coherence (autocorrelation function)
$\Delta\phi$	Optical phase change
$\Delta\lambda$	Linewidth of the source
$\Delta\lambda_{\text{opt}}$	Optimised central wavelength separation of two sources
$\Delta L$	Change in length
$\Delta X$	Relative optical path imbalance between the sensing and receiving interferometers
$n$	Index of refraction
$n_{\text{eff}}$	Effective core refractive index
$n_s$	Refractive index at saturation
$\Delta n$	Refractive index modulation
$r$	Amplitude reflection coefficient
$R$	Intensity reflection coefficient
SNR	Signal-to-noise ratio
$\Delta T$	Temperature change
$D$	Fibre diameter
$I$	Optical intensity
$\varepsilon$	Axial strain

$E$	Electric field
$k$	Coupling coefficient
$L_c$	Temporal coherence length
$L_{cav}$	Fabry-Pérot cavity length
$L_\epsilon$	Fraction of the Fabry-Pérot cavity length subjected to strain
$L_T$	Fraction of the Fabry-Pérot cavity length subjected to temperature change
$L_G$	Bragg grating length
$\Lambda$	Fringe periodicity (pitch of a Bragg grating)
$\lambda$	Wavelength of light in vacuum
$\mu$	Poisson's ratio
$\lambda_B$	Bragg resonance wavelength
$\eta$	Fraction of fundamental mode power within the fibre core
$r_{co}$	Fibre core radius
$R_B$	Reflectivity at Bragg wavelength
$\sigma$	Mechanical stress
$\tau$	Propagation time delay
$\omega$	Circular frequency
$V$	Visibility
$V$	Normalised frequency
$Y$	Young's modulus
$z$	Distance along the fibre